DISS. ETH NO. 22892

Bang-bang Control of a Trapped-Ion Oscillator

A thesis submitted to attain the degree of

DOCTOR OF SCIENCES of ETH ZURICH
(Dr. sc. ETH Zurich)

presented by

FLORIAN MICHAEL LEUPOLD

Dipl.-Phys., Freie Universität Berlin
BSc (Hons), Victoria University of Wellington

born on 27.12.1981
citizen of Germany

accepted on the recommendation of

Prof. Dr. J. P. Home
Prof. Dr. C. Ospelkaus

2015

Abstract

Trapped atomic ions are currently among the most advanced systems for quantum state engineering and quantum information processing. In the quest for a useful quantum computer, all of the required operations on quantum bits stored in the internal states of ions have been demonstrated in small-scale implementations. Full scalability, however, remains a challenge and requires transport of information throughout the processor. In the proposed architecture of a quantum charge-coupled device, this means physically shuttling the ions, which has been limited to long timescales compared to the natural frequency of the ion oscillation.

This thesis describes experiments performed with a new setup in which we realize bang-bang control of a trapped-ion oscillator by switching the trapping potentials on nanosecond timescales, much faster than the ion can respond. Technically this involves a novel method of placing CMOS electronics in our cryogenic vacuum system close to the trap itself. In a first exploration of this technology, we have demonstrated control of coherent states with up to 10 000 quanta of energy and have used these displaced states to verify the Franck-Condon coefficients for the light–atom interaction far outside the usual regime for trapped-ion work. Sub-nanosecond timing control of the switching process allows us to verify the coherence of the excited cites by returning them to the ground state of motion. A similar scheme is expected to facilitate ion transport over distances comparable to trap electrode dimensions within less than one period of oscillation.

The experiments were carried out on an entirely new apparatus for experiments with trapped $^{40}Ca^{+}$ ions built at ETH Zurich. The centerpiece is a microfabricated surface-electrode trap mounted in an ultra-high-vacuum chamber inside a pulse-tube cryostat. Light for photoionization, cooling, manipulation, and detection of ions is derived from diode lasers. Relevant lasers are frequency-stabilized and computer-controllable via acousto-optic modulators. Ions are imaged through a custom-designed cryo-compatible achromatic in-vacuum objective. Experimental sequences are executed in real time by a field-programmable gate array.

Besides describing the main experiments and the experimental setup, this thesis reviews the trapping of ions in a linear radio-frequency trap with a planar electrode geometry; addresses interaction of lasers with atoms; presents basic experimental techniques specific to our setup and routine calibration methods; and discusses the possibility for applying bang-bang control to speed up transport in trapped-ion quantum processing and other opportunities for quantum state engineering.

Zusammenfassung

Gefangene Ionen gehören derzeit zu den vielversprechendsten physikalischen Systemen auf dem Gebiet der Quanteninformationsverarbeitung. Auf dem Weg zu einem vollwertigen Quantencomputer wurden mit in Ionen kodierten Quantenbits bereits alle fundamentalen Operationen exemplarisch durchgeführt. Eine fortbestehende Herausforderung dabei ist jedoch die Skalierbarkeit hin zu vielen Quantenbits und die Informationsübertragung zwischen ihnen innerhalb eines Quantenprozessors. In einer möglichen quantenladungsgekoppelten Architektur ("quantum charge-coupled device") würde dies durch das physische Bewegen von Ionen durch eine Matrix von Mikrofallen geschehen, was bislang auf lange Zeitskalen im Vergleich zu der Eigenfrequenz der Ionenschwingung beschränkt war.

Die vorgelegte Arbeit beschreibt Experimente, in denen die Schwingungszustände von Ionen durch abrupte Änderungen der Fallenpotentiale ("bang-bang") manipuliert werden. Dies wird ermöglicht durch die Integration von elektrischen CMOS-Schaltern in die Spannungsversorgung der Fallenelektroden in unmittelbarer Nähe zu dem Ionenfallenchip. Im Rahmen erster Erkundungen dieser Technologie haben wir kohärente Zustände mit bis zu 10 000 Energiequanten kontrolliert erzeugt. Mit ihrer Hilfe liessen sich die Franck-Condon-Koeffizienten für die Wechselwirkung zwischen Laserlicht und Ionen weit ausserhalb des üblichen Regimes nachweisen. Sub-Nanosekunden-Auflösung in den Schaltvorgängen erlaubt uns, die Kohärenz der angeregten Zustände durch Rückführung in den Grundzustand der Bewegung zu bestätigen. Ein ähnliches Schema sollte den Ionentransport über mit den Elektrodenabmessungen vergleichbare Entfernungen innerhalb von weniger als einer Schwingungsperiode ermöglichen.

Die beschriebenen Versuche wurden in einem an der ETH Zürich neu errichteten Aufbau für Experimente mit gefangenen $^{40}Ca^{+}$-Ionen durchgeführt. Das Herzstück ist eine mikrogefertigte Oberflächenelektroden-Falle in einer Ultrahochvakuumkammer, die von einem Pulsröhrenkryostaten gekühlt wird. Licht zur Photoionisation, Kühlung, Manipulation und Detektion von Ionen wird aus Diodenlasern gewonnen. Relevante Laser sind frequenzstabilisiert und über akusto-optische Modulatoren verstimm- und schaltbar gemacht. Die Ionen werden durch ein selbst designtes, kryo-kompatibles, vakuumtaugliches Objektiv abgebildet. Versuchssequenzen werden in Echtzeit mittels eines "Field Programmable Gate Arrays" gesteuert.

Neben der Beschreibung der Bang-bang-Experimente und des Versuchsaufbaus werden in dieser Dissertation das Speichern von Ionen im elektrischen Wechselfeld einer linearen Paul-Falle mit ebener Elektrodengeometrie beschrieben, die Wechselwirkung von Lasern mit Atomen theoretisch dargelegt, für unseren Aufbau spezifische Techniken und Kalibri-

erverfahren erläutert und die Möglichkeit der Nutzung abrupter Potentialverschiebungen zum schnellen Ionentransport in der Quanteninformationsverarbeitung diskutiert.

Acknowledgements

The past four and a half years I spent at ETH Zurich have been fabulous. I had the opportunity to work with and learn from many bright and skilled people, pursue my own projects and at the same time contribute to some nice achievements. For that I am grateful towards many people (I apologize in advance for leaving anyone or anything out), specifically:

Jonathan Home for letting me join his group, which was still in its infancy at that time, being the most the approachable and involved professor I have ever met, and always finding the time to discuss experimental and theoretical problems that bugged me;

Joseba Alonso for a very enjoyable collaboration on our project, tediously fabricating our trap in the cleanroom and all other contributions and advancements along the way, being open for and often initiating intellectual sparring sessions, and the very few victories he let us snatch at kicker;

Ben Keitch for setting up the whole computer-control architecture, being patient and eager to help with all electronics and engineering (coil winding, ripping off glued mirrors, etc.) issues, and not letting go at the other end of the rope;

Daniel Kienzler for the air-conditioning in our lab, his expertise with mostly anything in the lab, helping us time and again with taming calcium ions, where he was always a few steps ahead of us, and setting up a bedroom wardrobe without a ladder;

Hsiang-Yu for his professional advice on optics, many discussions about laser–matter interactions and Bloch equations, and my first and best Chinese hot pot;

Ludwig de Clercq for his EVILs and (reluctantly) making them really useful, some pestiferous soldering of stubborn in-vacuum wires, reliably punctual lunch calls, and rather sleeping in skiing garment than closing the window;

Frieder Lindenfelser for his initial work on the stabilization cavities, putting together many parts of our shared laser setup (a.k.a. the greatest mess on a bread board), the design of and help with AOM drivers, putting up with our many interferences with his setup, his outstanding willingness to help (and glue things), and some fun sailing with zero wind;

Vlad Negnevitsky for everything he has done for the computer-control system (I frankly lost oversight), creating the DDS system, constantly fixing GIT-related problems, his openness to enter philosophical discussions, and the many “Oh, man!”s when we got lost in the snow and had to climb another hill;

Matteo Marinelli for substantially improving Ionizer, embodying the Ionizer helpdesk and complaining about but eventually fixing a ton of bugs, and being a fun desk neighbor;

David Nadlinger for a much needed overhaul of the computer-control system and the integration of previously stand-alone devices therein;

Ursin Solèr for his sympathetic “do it properly”-approach towards all kinds of engineering;

Felix Krauth for simulations of the electric potential in our surface-electrode trap;

Dominik Wild, Roland Hablützel, and Matteo Fadel for their work on ovens, the resonator, and switching electronics;

Karin Fisher, Martin Sepiol, and Christa Flühmann for their contribution to the quadrupole-laser stabilization;

Andreas Stuker, Bernhard Morath, Willy Staubli from the institute’s workshop for manufacturing uncountably many pieces big and tiny for our apparatus based on my sometimes not-so-technical drawings;

Lutz Bachmann for his much appreciated input on several engineering problems;

Lisa Artel and Mirjam Bruttin, our group secretaries, for battling and knowing their way around bureaucracy, and freeing us from many burdens;

my parents, Regina and Michael, for raising a curious mind, making me susceptible to the wonders of Nature, and always helping me to achieve my goals;

my wife Anna for being there for me, making every aspect of life better, and heroically carrying our lively son.

Contents

Abstract iii

Zusammenfassung v

Acknowledgements vii

List of Figures xiii

List of Tables xvii

List of Acronyms xix

1. Introduction 1

2. The Harmonic Oscillator 5
2.1. Trapping ions in a Paul trap . . . 6
2.1.1. Solutions to the Mathieu equation . . . 7
2.1.2. Physical interpretation . . . 9
2.2. Electric potentials in SETs . . . 11
2.3. The quantum harmonic oscillator . . . 15
2.3.1. Number states . . . 15
2.3.2. Coherent states . . . 16
2.3.3. Squeezed states . . . 17
2.3.4. Thermal states . . . 19

3. Laser–Ion Interactions 21
3.1. The calcium ion . . . 21
3.2. Coherent interaction . . . 22
3.3. Rabi oscillations . . . 26
3.4. Optical Bloch equations . . . 28
3.4.1. The two-level system . . . 29
3.4.2. The three-level Lambda-system . . . 30
3.5. Evaluation of Rabi frequencies . . . 31
3.5.1. Rabi frequency for dipole transitions . . . 32
3.5.2. Rabi frequency for quadrupole transitions . . . 33
3.5.3. Choice of qubit . . . 34

3.6. Laser cooling . . . 35
3.6.1. Doppler cooling . . . 36
3.6.2. EIT cooling . . . 38
3.6.3. Final state after cooling . . . 40
3.7. State analysis . . . 40
3.7.1. Spin-state analysis . . . 40
3.7.2. Oscillator-state analysis . . . 41
3.8. Spin coherence and Ramsey interferometry . . . 43
3.8.1. Ramsey interferometry . . . 43
3.8.2. Discrete noise . . . 44

4. Experimental Apparatus **47**
4.1. Ion-trap apparatus . . . 49
4.1.1. Surface-electrode ion trap . . . 49
4.1.2. Cryo-electronics board and fast switches . . . 52
4.1.3. Resonator . . . 54
4.1.4. Atom source . . . 57
4.1.5. Ultra-high-vacuum chamber . . . 59
4.1.6. Cryostat . . . 63
4.2. Lasers . . . 68
4.2.1. Frequency stabilization . . . 69
4.2.2. Acousto-optic modulation . . . 71
4.2.3. Beam delivery . . . 74
4.3. Imaging system . . . 76
4.3.1. Schwarzschild-type objective . . . 76
4.3.2. Imaging system outside the cryostat . . . 80
4.4. Control system . . . 81

5. Calibration Experiments and Techniques **85**
5.1. First steps . . . 85
5.1.1. Imaging system . . . 85
5.1.2. Beam pointing . . . 86
5.1.3. Neutral atom fluorescence . . . 87
5.1.4. Ion loading . . . 87
5.1.5. Calibrating the dipole lasers . . . 88
5.2. Coherent manipulation of the qubit . . . 89
5.2.1. Spin polarization . . . 89
5.2.2. Quantum jumps . . . 90
5.2.3. Rabi spectroscopy and Rabi oscillations . . . 90
5.2.4. Calibrations based on Rabi oscillations . . . 92

5.3. Control over trap potential . . . 93
5.3.1. Understanding the trapping potential . . . 94
5.3.2. Determining the rf voltage amplitude . . . 96
5.4. Micromotion . . . 96
5.4.1. Parametric driving . . . 97
5.4.2. Micromotion compensation . . . 100
5.5. EIT cooling . . . 101
5.6. Heating rate . . . 102
5.7. Detection efficiency . . . 104
5.8. Fidelity of spin polarization . . . 105
5.9. Spin-coherence measurement . . . 106

6. Quantum Control **109**
6.1. Oscillator in a moving potential . . . 109
6.2. Quasi-instantaneous displacements . . . 111
6.3. Tracking oscillations . . . 112
6.4. Catching in the ground state . . . 115
6.5. Large coherent states and laser–ion interaction . . . 117
6.6. Conclusion . . . 121

7. Fast Ion Transport **123**
7.1. Transport protocol . . . 124
7.2. Effect of trap anharmonicity . . . 125
7.3. Switch timing . . . 126
7.4. Finite switching time . . . 127
7.5. Extended transport throughout an array . . . 129
7.6. Conclusion . . . 130

8. Summary and Outlook **131**
8.1. Future plans and improvements . . . 133

A. Time-Evolution Pictures in QM **135**
A.1. Schrödinger picture . . . 135
A.2. Heisenberg picture . . . 136
A.3. Interaction picture . . . 136
A.4. General unitary transformation . . . 137

B. Density Matrix Formalism **139**
B.1. Fidelity for mixed quantum states . . . 139
B.2. Closed-system dynamics . . . 140
B.3. Open-system dynamics . . . 140

C. Wigner Distribution **143**
C.1. Examples of Wigner functions 144

D. Gaussian Beam Propagation **145**

E. Data Analysis and Error Estimation **149**

F. Useful Formulas **151**

Bibliography **155**

List of Figures

2.1. Stability chart for Mathieu functions. 8
2.2. Solutions to the Mathieu equation. 9
2.3. Schematic layout of the SET used in this dissertation. 12
2.4. Electric potential and field from rf electrodes. 13
2.5. Equipotential lines of the total electric potential in the radial plane. 14
2.6. Wigner function and number-state distribution of a coherent state. 17
2.7. Wigner function and number-state distribution of a squeezed state. 18
2.8. Number-state distributions of displaced thermal states. 19

3.1. Level diagram of the $^{40}Ca^{+}$ ion. 22
3.2. Energy levels and transitions of the spin-oscillator system. 25
3.3. Franck-Condon coefficients as functions of Fock state number. 26
3.4. Bloch vector and Rabi oscillations on the Bloch sphere. 27
3.5. Energy diagrams for a driven two-level system. 28
3.6. Solutions to the optical Bloch equations for the three-level system. 30
3.7. Geometry-dependent coupling strength of a quadrupole transition. 34
3.8. Spectral lines on the $S_{1/2} \leftrightarrow D_{5/2}$ quadrupole transition. 35
3.9. Atomic resonance line and transition rates for Doppler cooling. 37
3.10. Three-level system and absorption profile for EIT cooling. 39
3.11. Photon count probabilities for both qubit states. 41
3.12. Pulse sequence in Ramsey interferometry. 44
3.13. Ramsey fringes for constant detuning. 45

4.1. Overview of the experimental setup in the laboratory. 48
4.2. Overview of the ion trap and imaging systems. 48
4.3. Microscope images of the SET chip. 50
4.4. Mounted SET chip and Faraday cage. 51
4.5. Cryo electronics board mounted on OFHC carrier. 52
4.6. Schematics of filtered and switched voltage lines to the control electrodes. . 53
4.7. Helical resonator and schematic of a series-LCR circuit. 54
4.8. Resonance frequency and Q value of the resonator versus temperature. . . . 56
4.9. Atom oven designs for laser desorption. 57
4.10. Images of atom oven tests. 58
4.11. Resistively heated oven and trap assembly. 59

4.12. UHV chamber, mounted to the cryostat and inside view. 60
4.13. Cryogenic vacuum sealing with indium O-rings. 61
4.14. Low-stress vacuum viewports. 62
4.15. Micro-D type and SMA connectors laser-welded into stainless steel flanges. 63
4.16. Cross-section view and schematic of the cryostat. 64
4.17. Cryostat stand and equipment sledge. 66
4.18. Assemblies for helium supply and isolation vacuum. 67
4.19. Temperature curves during the cooling process. 67
4.20. Schematic of a PDH locking setup. 69
4.21. Transmission (blue) and PDH (orange) signal from a low-finesse cavity. . . 70
4.22. AOM double-pass setup with changing beam polarization. 71
4.23. AOM double-pass setup with constant beam polarization. 72
4.24. AOM and fiber setup of all laser-beam lines. 73
4.25. Diffraction power spectra for the DDS-driven 397 nm AOM. 74
4.26. Beam delivery to the experimental chamber. 75
4.27. Outcoupling setup for the PCF beams. 76
4.28. Cross section and image of the Schwarzschild objective. 77
4.29. Simulated RMS spot size 78
4.30. Imaging system outside the cryostat. 81
4.31. Overview of the computer-control system. 82
4.32. Pulse sequence for switching the electrode voltages. 83

5.1. Images of the SET and beam pointing using the imaging system. 86
5.2. Laser pulse and PMT detection sequence for ion loading. 87
5.3. Spectral profiles of the driven $S_{1/2} \leftrightarrow P_{1/2} \leftrightarrow D_{3/2}$ system. 88
5.4. Experimental sequence for rough calibration of the SP laser. 89
5.5. Experimental sequence for observing and signature of quantum jumps. . . . 90
5.6. Laser-pulse sequence for Rabi spectroscopy and driving Rabi oscillations. . 91
5.7. Rabi spectroscopy on the quadrupole transition. 92
5.8. Chevron-like curve of probability oscillations. 93
5.9. Experimental sequence and signal for scanning the 854 nm repump laser. . . 94
5.10. Illustrations of the trap potential for different experimental parameters. . . 95
5.11. Simulated micromotion for different ion positions in the radial plane. 97
5.12. Effect of micromotion on ion fluorescence. 98
5.13. Circuitry for generating a modulated rf signal for parametric driving. 99
5.14. Parametric resonance spectrum. 100
5.15. Micromotion compensation via detection of parametric resonance. 101
5.16. Pulse sequence and signal for optimizing EIT cooling. 102
5.17. Two methods for thermal-state estimation after EIT cooling. 103
5.18. Heating-rate measurement data. 104
5.19. Measuring the detection efficiency of the imaging system. 105

5.20. Pulse sequence and transitions for measuring the Spin Polarization (SP) fidelity. 105
5.21. Pulse sequences for Ramsey experiments. 106
5.22. Experimental and evaluated data from Ramsey experiments. 107

6.1. Evolution after a quasi-instantaneous harmonic-well displacement. 111
6.2. Evolution of displaced Wigner functions in phase space. 112
6.3. Protocol for tracking the coherent state evolution in a displaced potential. . 113
6.4. Experimental sequence and data of the coherent-state-tracking experiment. 113
6.5. Coherent state evolution in the displaced potential. 114
6.6. Comparison of ground and returned state. 115
6.7. Sequence for creating coherent states and Franck-Condon coefficients. . . . 117
6.8. Experimental and simulated data for the laser–ion interaction. 118
6.9. Calculated AC Stark shifts and fitted displacement distances. 119
6.10. Fourier spectrum of the measured probability P_S. 120

7.1. Sketch of the fast "throw-catch" transport routine. 124
7.2. Fidelities of the transported state versus trap potential anharmonicity. . . . 126
7.3. Effect of finite switching times. 128
7.4. Schematic wiring and protocol for extended transport through an array. . . 129

8.1. Squeezing a ground state by nonadiabatic changes to the trap frequency . . 134

D.1. Gaussian beam diverging away from its waist. 146

List of Tables

3.1. Natural lifetimes and spontaneous emission rates in $^{40}Ca^{+}$. 22
3.2. Landé factors and Zeeman splittings for the relevant levels in $^{40}Ca^{+}$. 22
3.3. Laser polarization for dipole-allowed transitions. 33

4.1. Performance data of the switching IC at room and cryogenic temperature. . 53
4.2. List of the laser sources used. 68
4.3. Surface parameters from ZEMAX for the three design steps of the SO. . . . 79
4.4. Expected SO detection efficiency. 80

5.1. Fitted noise components for Ramsey experiments. 107

6.1. Best fit values for the data in Figure 6.6. 116
6.2. Best fit values for the coupling constants and detuning offsets. 120

List of Acronyms

AOM	Acousto-Optic Modulator (p. xiv, 69, 71–74, 82, 87, 107, 131)
AR	Anti-Reflection (p. 78, 80)
CAD	Computer-Aided Design (p. 54, 59)
CCD	Charge-Coupled Device (p. 86)
CEB	Cryo-Electronics Board (p. 47, 51, 52, 54, 56, 59, 60, 62, 63, 66, 67, 82)
CM	Coherent Manipulation (p. 89, 106)
CMOS	Complementary Metal–Oxide–Semiconductor (p. 52, 54, 131, 133)
CW	Continuous-Wave (p. 57)
DAC	Digital-to-Analog Converter (p. 82, 123, 133)
DC	Doppler Cooling (p. 87–90, 97, 101, 104)
dc	Direct Current (p. 11, 12, 85, 87, 93–96)
DDPG	Digital Delay and Pulse Generator (p. 82, 114)
DDS	Direct Digital Synthesizer (p. xiv, 69, 72, 74, 81, 82, 99, 101, 107, 131)
EIT	Electromagnetically Induced Transparency (p. xiii, xiv, 21, 30, 36, 38–40, 85, 101–104, 131, 133)
EMCCD	Electron-Multiplying Charge-Coupled Device (p. 48, 49, 76, 80–83, 85, 86)
EOM	Electro-Optic Modulator (p. 70)
EVIL	Electronically Variable Interactive Lockbox (p. 71)
FPGA	Field-Programmable Gate Array (p. 71, 81)
FWHM	Full Width at Half Maximum (p. 55, 70)
GUI	Graphical User Interface (p. 81, 82)
HR	High-Reflection (p. 78, 80)

HWP Half-Wave Plate (p. 73, 75)

IC Integrated Circuit (p. xvii, 52–54)

IR InfraRed (p. 58, 75, 76)

ITO Indium Tin Oxide (p. 134)

KILL Keitch Integrated Laser Lock (p. 69, 71)

NA Numerical Aperture (p. 76–78)

OFHC Oxygen-Free High-Conductivity (p. xiii, 51, 52, 54, 55, 59, 61)

PBS Polarizing Beam Splitter (p. 71–73, 75)

PCB Printed Circuit Board (p. 52)

PCF Photonic-Crystal Fiber (p. xiv, 69, 74–76, 86, 89, 90, 131)

PD Photo Diode (p. 69, 71)

PDH Pound-Drever-Hall (p. xiv, 69, 70)

PEEK PolyEther Ether Ketone (p. 51)

PI PhotoIonization (p. 68, 73, 74, 86–88, 131)

PIC Proportional-Integral Controller (p. 69, 71)

PL Programmable Logic (p. 81, 82)

PM Polarization-Maintaining (p. 69, 74)

PMT PhotoMultiplier Tube (p. xiv, 48, 49, 76, 80–82, 86, 87, 131)

PPKTP Periodically Poled potassium Titanyl Phosphate (p. 68)

PS Processing System (p. 81, 82, 93, 94)

PTFE PolyTetraFluoroEthylene (p. 54, 59)

PTV Peak-To-Valley (p. 78, 79)

QWP Quarter-Wave Plate (p. 71, 72, 76, 89)

rf Radio Frequency (p. xiii, xiv, 5, 6, 10–14, 47–49, 51–54, 59, 60, 63, 65, 71, 72, 74, 82, 86, 87, 93–99, 104, 115)

RMS Root-mean-square (p. xiv, 78, 124, 125)

RWA Rotating Wave Approximation (p. 24, 35)

SET Surface-Electrode ion Trap (p. xiii, xiv, 5, 6, 9, 11–13, 47–52, 54–57, 59, 60, 75, 79, 80, 85–87, 93, 97, 99, 103, 104, 111, 114, 123, 126)

SHG Second-Harmonic Generation (p. 68)

SM Single-Mode (p. 69)

SMA SubMiniature version A (p. xiv, 60, 63, 64)

SNR Signal-to-Noise Ratio (p. 86, 89)

SO Schwarzschild-type Objective (p. xvii, 77–81, 83, 85–87, 105)

SP Spin Polarization (p. xiv, xv, 89, 90, 92, 102, 105, 106, 113)

SPI Serial Peripheral Interface (p. 82)

SPST Single-Pole-Single-Throw (p. 52, 53, 82)

SPTT Single-Pole-Triple-Throw (p. 52)

TA Tapered Amplifier (p. 68)

TMP TurboMolecular Pump (p. 65–67)

TTL Transistor-Transistor Logic (p. 80, 82)

UHV Ultra-High Vacuum (p. xiv, 47–49, 54, 59–65, 67, 76, 79, 80, 85, 131, 133, 134)

UV UltraViolet (p. 50, 62, 75, 76, 78, 86)

1. Introduction

As late as in the middle of the last century, many years after the invention of quantum theory, Erwin Schrödinger argued that "we are not experimenting with single particles, any more than we can raise Ichthyosauria in the zoo" and doubted whether "one is allowed to pick one's 'initial state' arbitrarily as composed of pure energy states" [Sch52]. Only a few decades later, owing to modern technologies as computers and lasers, such experiments became possible and complete control over single quantum systems was obtained. Physicists can nowadays confine individual particles (atoms, photons, ...) in small regions of space, prepare them in well-defined states, and follow their evolution. This has enabled the investigation of many predicted peculiarities of quantum mechanics (such as superposition, entanglement, and nonlocality) and led to the emergence of numerous new fields of research. One of them is quantum information science, which seeks to gain advantage from storing, transmitting, and processing information encoded in systems that exhibit unique quantum properties, with the ultimate goal of building a quantum computer [Lad10].

The principal requirements for a quantum computer are a scalable physical system with well characterized qubits[1], state initialization, robust qubit storage, a universal set of quantum gates, qubit readout, and the ability to transmit qubits between separate locations in the processor [DiV00]. One possible experimental implementation of a quantum information processor uses qubits stored in the internal states of trapped atomic ions [Cir95; Mon95; Sch03; Bar04; Lei03b; Ben08]. By trapping the ions in vacuum with electromagnetic forces, the qubits are decoupled from the environment and robustly stored with long coherence times. Through precisely controlled interactions with strong laser fields, they can be prepared, manipulated and measured with nearly unit efficiency. Two-qubit gates are realized by transient, state-dependent excitations of the coupled mechanical motion, mediated via the Coulomb interaction. While small-scale quantum computation protocols have been demonstrated, the outstanding challenge is the scaling to large numbers of qubits [Bla08; Häf08; Mon13].

A possible scalable architecture for quantum computing with trapped ions consists of a large number of interconnected ion traps in a complex array with dedicated zones for storage, logic gates and detection [Kie02]. Planar electrode geometries simplify the construction of such multiplexed ion traps and provide the possibility to apply standard microfabrication techniques [Chi05]. Information would be shared between the zones by physically moving the ions via time-varying voltages on the electrodes. In order to reduce processing time

[1] In extension of the classical terminology, the informational building blocks in a quantum computer are called *quantum bits* or "qubits".

and thereby decoherence of the qubits, such transport should be fast. On the other hand, motional excitation after the transport should be minimal because it increases errors in multi-qubit quantum logic gates. Motional excitation can be removed after transport, for example by means of sympathetic cooling [Bar03], but that takes extra time [Hom09a, supplement]. Initial experiments on ion transport therefore operated in the adiabatic regime, where the harmonic trapping potential is moved sufficiently slowly for maintaining the ion near the motional ground state throughout the process [Row02]. The adiabatic constraint, however, limits transport to timescales long compared to the motional period of oscillation. Faster, diabatic transport within a few oscillation periods was recently enabled by using low-noise, high-speed digital-to-analog converters. Despite transient motional excitation during the transport, the ions were returned to the motional ground state of the potential well at the end by appropriately timing the locomotion of the potential well [Bow12; Wal12]. In all cases, the electrode voltage waveforms were generated outside the vacuum system and had to run through low-pass noise filters on the way to the ion trap, which prevented more sudden accelerations.

We have implemented time-dependent control of the trapping potential using active electronic switches inside the vacuum system. Digital signals control closing and opening the electric connections of noise-filtered voltage supply lines to the trap electrodes. Changes to the trapping potential can thereby be made on the nanosecond timescale, much faster than the ion's period of oscillation. This would allow for ion transport without vibrational heating at the ultimate speed limit of half an oscillation cycle [Che11; Alo13].

Such *bang-bang control* of the trapping potential can also be used for quantum state engineering of trapped-ion oscillator states. Control operations on these primarily make use of resonant effects using optical or microwave fields, which are limited to long timescales compared to the natural frequency of the oscillator [Mee96; Zäh10; Osp11; Kie15b; Lo15]. Fast motional-state control has been performed using short trains of picosecond laser pulses [Miz13] but is likewise restricted to small momentum transfers. A non-adiabatic shift of the trap center, on the other hand, creates quasi-instantaneously a nearly arbitrarily large coherent harmonic oscillator state [Lei03a, p. 308]. We explore this method by creating coherent states of phase-space amplitudes up to more than $|\alpha| = 100$, which involve vibrational states above 10 000 quanta of energy. We have used these states to characterize the matrix elements describing the interaction of light with atoms far outside the usual regime of operation.

Before these experiments could be performed, the by far largest amount of work, shared mostly between Joseba Alonso and the author, was spent on equipping an entirely new laboratory, and designing, fabricating and implementing a complex experimental apparatus. The central part of the setup is a microfabricated planar ion-trap chip mounted inside an ultra-high-vacuum chamber, which is attached to and cooled to 4 K by a liquid-helium recondenser cryostat. Operating the ion trap at liquid-helium temperature suppresses outgassing from otherwise not vacuum-compatible materials, which allows us to put commercially

available integrated circuits for fast potential switching in the immediate vicinity of the ion trap. Other components essential for the trapped-ion experiments described here are a system of several lasers to address relevant atomic transitions, electronics to create the dynamic and static trapping potentials, an imaging system, and flexible computer control to run experimental sequences.

The remainder of this thesis covers all aspects of the setup, relevant theoretical background, experimental techniques and the main results, and is structured as follows:

Chapter 2 introduces how ions can be trapped by dynamic electric fields and how the trapping potential of a surface-electrode trap can be calculated analytically. A brief overview of the quantum harmonic oscillator formalism and relevant oscillator states is given.

Chapter 3 reviews the interaction of lasers with atoms by the example of a calcium ion. The basic coupling Hamiltonian is derived as well as the coherent and dissipative evolution of driven few-level systems. Laser cooling and the analysis of the internal and motional states of a trapped ion are discussed. Finally, Ramsey interferometry is presented as tool to characterize noise that leads to loss of qubit coherence.

Chapter 4 gives an overview of the experimental setup that was designed and built and presents details of all relevant components: the ion trap apparatus including the surface-electrode trap, in-vacuum electronics, the vacuum chamber, and the cryostat; the laser system and beam deliver setup; the imaging system built around a custom-designed in-vacuum objective; and the computer-control system.

Chapter 5 discusses a selection of experimental techniques from first steps when putting a new ion trap into operation to routine calibration methods applicable for manipulating trapped ions with lasers. It illustrates how electrode voltages are programed and how moving the static potential affects the position and motional modes of an ion. Aspects of micromotion compensation and heating rate measurements are addressed. The photon-detection efficiency of the imaging system is measured. The fidelity of qubit-state initialization and decoherence of the qubit are determined.

Chapter 6 presents a short introduction into and results of bang-bang quantum control experiments. Besides the controlled creation of small and large coherent states, the matrix elements for the laser–ion interaction are mapped out for sidebands up to fifth order. And the ability to de-excite a coherent state by a well-timed second displacement of the potential well is investigated.

Chapter 7 proposes the application of bang-bang control to ion transport in multiplexed trap arrays and discusses possible sources of error.

Chapter 8 summarizes the results and provides an outlook on future work.

2. The Harmonic Oscillator

An ion is an atom or molecule with a net electrical charge. In the context of quantum information experiments, ions are often singly positively charged atoms from the group of the alkaline earth metals (Be – beryllium, Mg – magnesium, Ca – calcium, Sr – strontium, Ba – barium). Electric and magnetic fields couple directly to such net charges and can hence be used for "trapping" ions, that is stably confining them in free space.

A consequence of Maxwell's first equation, $\boldsymbol{\nabla} \cdot \boldsymbol{E} = \rho/\epsilon_0$, however, is that a source-free ($\rho = 0$) electric field is divergenceless. As a result, charged particles cannot be maintained in a stable stationary equilibrium configuration with stationary electric fields alone, which is known as *Earnshaw's theorem*. The combination of static electric fields with static magnetic or oscillating electric fields, techniques for which Hans Georg Dehmelt and Wolfgang Paul were awarded the Nobel Prize in 1989, can overcome this constraint.

Radial confinement in a linear Radio Frequency (rf)[1] *Paul trap* [Pau90] is provided by an oscillating quadrupole potential. At any given moment in time, this potential has a saddle point at the trapping position, which means it is confining in one direction (say along y) and anti-confining in the other (then z). The equations of motion are examples of the *Mathieu equation*, as we shall see below, and have solutions that are stable in all directions. The motion in the effective *pseudopotential* is that of a three-dimensional harmonic oscillator. Linear rf traps have, for example, paved the way for quantum information processing experiments and optical frequency standards with trapped ions [Bla08].

The central building block of the experiments in this thesis is a linear rf trap, which is realized by gold electrodes on the surface of a quartz substrate, a so-called *Surface-Electrode ion Trap* (SET) [Sei06]. Linear rf traps are often used in quantum information processing applications because, as we shall see, they have a line along which the *micromotion* is eliminated and the motion is purely harmonic. Displacements, transport, and state squeezing will be considered for the corresponding motional mode.

This chapter begins with an introduction to Paul traps, illustrating how and for which trapping parameters they can be used to confine ions (Section 2.1). Next, computer-assisted calculations of the electric potential above SETs are discussed in Section 2.2. It is also shown that the total potential for the ion is harmonic with non-degenerate eigenmodes. Finally, relevant harmonic-oscillator states, namely the number, coherent, squeezed and thermal states, are reviewed and useful formulas for describing them are derived for later use (Section 2.3).

[1] Typical drive frequencies fall into the radio frequency range (30 kHz to 300 MHz).

2.1. Trapping ions in a Paul trap

At the center of an ideal Paul trap, the net force on an ion vanishes and the electric potential, consisting of a static and an oscillating part at frequency ω_{rf}, is to leading order quadratic in the Cartesian coordinates,[2]

$$\Phi(\boldsymbol{r}, t) = \frac{1}{2} \sum_i u_i r_i^2 + \frac{1}{2} \sum_i v_i r_i^2 \cos(\omega_{\mathrm{rf}} t), \tag{2.1}$$

where sums are over $i = x, y, z$. The curvatures u_i and v_i (in units of $1\,\mathrm{V/m^2}$) are proportional to the applied voltages and depend on the electrode geometry. In the case of more complicated structures, such as SETs, they need to be computed from simulations (next section). Nonetheless, valuable insights can be gained from an analytic treatment.

Being an electric potential, $\Phi(\boldsymbol{r}, t)$ fulfills Laplace's equation at every instant in time,

$$\boldsymbol{\nabla}^2 \Phi(\boldsymbol{r}, t) = 0 \qquad \Longrightarrow \qquad \sum_i u_i = \sum_i v_i = 0, \tag{2.2}$$

which excludes the generation of a momentary local minimum. Thus the potential can only trap in a dynamical way. In the following, we seek to find suitable parameter ranges for the applied voltages and rf drive frequency.

Given the constraints in Equation (2.2), different electrode geometries can realize a trap. In a linear Paul trap, confinement along one direction, here and henceforth along the x-axis, comes purely from the static part of the potential, which implies $u_x = -u_y - u_z > 0$. The oscillating potential confines only in the radial y, z-plane and has no effect along the trap axis, so $v_y = -v_z$.[3]

The classical equations of motion for a particle with mass m and charge e subject to the potential above are

$$\frac{\mathrm{d}^2 r_i}{\mathrm{d}t^2} = -\frac{e}{m} \frac{\partial \Phi}{\partial r_i} = -\frac{e}{m} \Big(u_i r_i + v_i r_i \cos(\omega_{\mathrm{rf}} t) \Big).$$

In terms of the dimensionless parameters

$$\tau = \frac{\omega_{\mathrm{rf}} t}{2} + \frac{\pi}{2}, \qquad a_i = \frac{4 e u_i}{m \omega_{\mathrm{rf}}^2}, \qquad q_i = \frac{2 e v_i}{m \omega_{\mathrm{rf}}^2}, \tag{2.3}$$

[2] Note that I have assumed here that the Cartesian axes are aligned with the eigenaxes of the static and dynamic potentials, despite the fact that the eigenaxes of the two potentials in many ion traps do not align in the first place (which is, to my knowledge, completely disregarded in the literature). This simplification decouples the equations of motion and is justified insofar as it does not invalidate the pseudopotential approximation or calculations based thereupon.

[3] In a trap of finite dimensions, this is true to a good approximation.

these can be rewritten in the standard form of the Mathieu equation,

$$\frac{\mathrm{d}^2 r_i}{\mathrm{d}\tau^2} + \Big(a_i - 2q_i \cos(2\tau)\Big)\, r_i = 0, \tag{2.4}$$

which is a well-studied differential equation. In the next two subsections, I will first outline solutions of interest to the general Mathieu equation, and then relate those to relevant experimental parameters.

2.1.1. Solutions to the Mathieu equation

The following analysis and conclusions are based on the book on Mathieu equations by McLachlan [McL64]. We start by noting that the Mathieu equation

$$\frac{\mathrm{d}^2 y}{\mathrm{d}\tau^2} + \Big(a - 2q \cos(2\tau)\Big)\, y = 0, \tag{2.5}$$

writing y for r_i in this section, is a particular case of a linear second-order differential equation with a periodic coefficient. One can hence expect that there are solutions with period π or 2π in τ. For a given q, this is the case for particular numbers of a.

When $q = 0$, the solutions of Equation (2.5) reduce to $\cos m\tau$ or $\sin m\tau$ if we set $a = m^2$ with $m \in \mathbb{N}$. For $q \neq 0$, a and y are functions of q. Assuming

$$\begin{aligned} a &= m^2 + \alpha_1 q + \alpha_2 q^2 + \alpha_3 q^3 + \ldots, \\ y &= \cos m\tau + q c_1(\tau) + q^2 c_2(\tau) + q^3 c_3(\tau) + \ldots, \end{aligned}$$

one can find the cosine-elliptic Mathieu functions $\mathrm{ce}_m(\tau, q)$ as solutions with *characteristic numbers* $a_m(q)$. Analogously, the other periodic solutions are sine-elliptic Mathieu functions $\mathrm{se}_m(\tau, q)$ with characteristic numbers $b_m(q)$. For even (odd) m, the Mathieu functions have period π (2π) in τ [McL64, p. 11ff]. The characteristic numbers are plotted as functions of q in Figure 2.1. Their curves divide the a, q-plane into regions of stability and instability [McL64, p. 76ff].

We now seek a general solution to the Mathieu equation. It can be shown that a formal solution is given by $y_1(\tau) = \mathrm{e}^{\mu\tau}\phi(\tau)$ where $\mu = \alpha + \mathrm{i}\beta$ is a complex number with $\alpha, \beta \in \mathbb{R}$ being functions of a and q, and $\phi(\tau)$ is periodic in τ with period π [McL64, p. 57ff]. Since Equation (2.5) is unchanged if $-\tau$ is written for τ, $y_2(\tau) = y_1(-\tau)$ is a second independent solution. Hence the complete solution of the Mathieu equation may be expressed in the form

$$y(\tau) = A\mathrm{e}^{\mu\tau} \sum_{r=-\infty}^{\infty} C_{2r}\mathrm{e}^{\mathrm{i}2r\tau} + B\mathrm{e}^{-\mu\tau} \sum_{r=-\infty}^{\infty} C_{2r}\mathrm{e}^{-\mathrm{i}2r\tau}, \tag{2.6}$$

A, B being arbitrary constants, and μ, C_{2r} functions of a, q.

A solution is defined to be stable if it tends to zero or remains bounded as $\tau \to \infty$. This

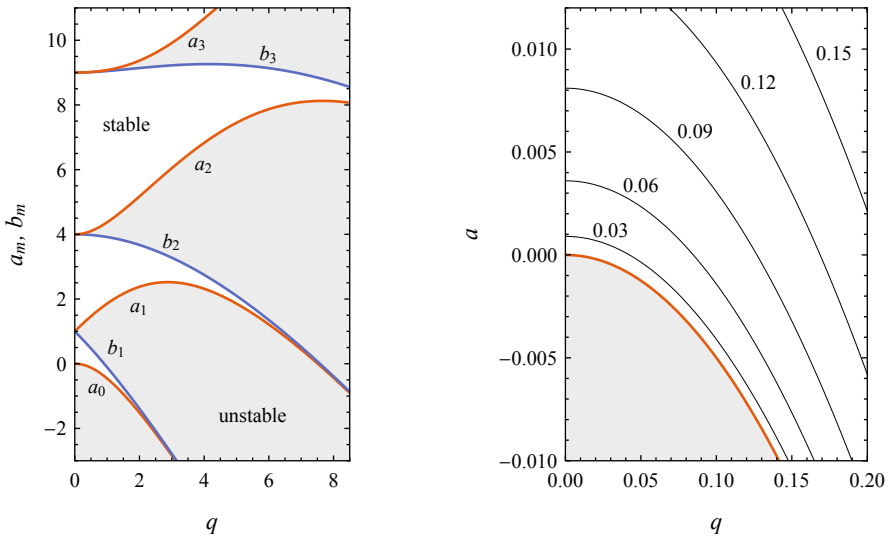

Figure 2.1: (left) Stability chart for Mathieu functions. The characteristic curves a_m, b_m for Mathieu functions of integral order divide the plane into regions of stability and instability [McL64, p. 40, 76f]. (right) Region of the stability chart for small a, q. Thin black lines are iso-β curves; the red line corresponds to a_0 and marks $\beta = 0$.

requires $\alpha = 0$ and is fulfilled when the parameter combination (a, q) falls into a region of stability in the stability chart (Figure 2.1). Usually, and also in the work described here, ion traps are operated at small Mathieu parameters a, q, that is $|a|, q^2 \ll 1$. So how does the motion look like in that case? By inserting Equation (2.6) into (2.5), we find the recursion relation

$$0 = \left[a - (2r + \beta)^2\right] C_{2r} - q \left(C_{2r+2} + C_{2r-2}\right).$$

Setting $\gamma_{2r} = [a - (2r + \beta)^2]/q$, we can write this as

$$\frac{C_{2r}}{C_{2r\pm2}} = \gamma_{2r\pm2} - \frac{C_{2r\pm4}}{C_{2r\pm2}}.$$

Recursive insertion yields

$$\frac{C_{2r\pm2}}{C_{2r}} = \left(\gamma_{2r\pm2} - \left(\gamma_{2r\pm4} - (\ldots)^{-1}\right)^{-1}\right)^{-1}.$$

The higher order contributions drop rapidly for increasing $|r|$ as the $|\gamma_{2r}|$ grow with $(2r)^2$. For a lowest-order approximation, we thus truncate the sums in Equation (2.6) after $C_{\pm2} \approx C_0/\gamma_{\pm2}$. In order to further evaluate the solution, we need to find β. From γ_0 for

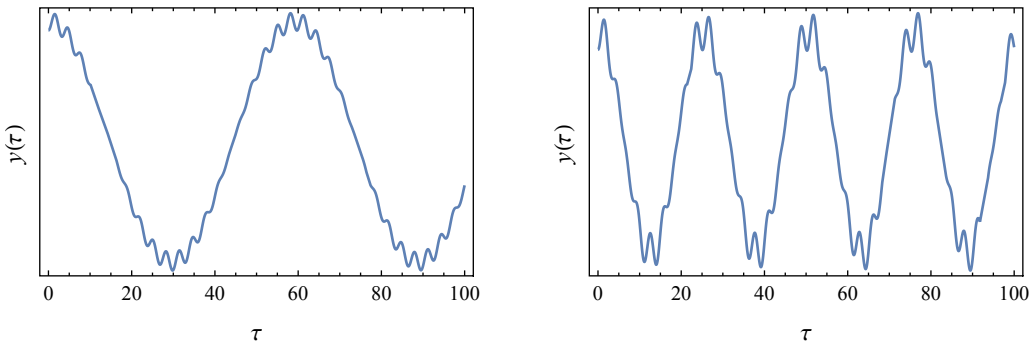

Figure 2.2: Solutions to the Mathieu equation as given by Equation (2.7) for $a = 0$ and $q = 0.15/0.35$ (left/right). One can see how the secular frequency as well as the micromotion amplitude increase with q.

$r = 0$, we have

$$\beta^2 = a - q\gamma_0 = a - q\left(\frac{C_2}{C_0} + \frac{C_{-2}}{C_0}\right) \approx a - q\left(\frac{1}{\gamma_2} + \frac{1}{\gamma_{-2}}\right),$$

which, upon using $\beta^2 \approx a$ as a first approximation to evaluate the $\gamma_{\pm 2}$, yields

$$\beta \approx \sqrt{a + q^2/2}.$$

Consequently, we get $C_{\pm 2} \approx -C_0 q/4$. Setting $A = B = 1/2$ as initial conditions, we obtain

$$y(\tau) \approx C_0 \cos(\beta\tau)\left[1 - \frac{q}{2}\cos(2\tau)\right] \tag{2.7}$$

as our relevant solution to the Mathieu equation (see Figure 2.2 for example plots). In the next subsection, we will switch back to the experimental parameters and interpret this result.

2.1.2. Physical interpretation

We have found that the equations of motion for an ion in the quadratic potential in Equation (2.1) with static and dynamic components can be decoupled under certain circumstances and then have the form of the Mathieu equation.[4] Whether they have stable solutions depends on the Mathieu parameters a_i, q_i defined in Equation (2.3), and can be read off the stability charts in Figure 2.1. They are typically small, in this dissertation $a \lesssim 0.005$ and $q \lesssim 0.15$ for the design parameters of the SET, which leads to bound solutions of the form in Equation (2.7).

[4] Note that I have assumed for the potential in Equation (2.1) that the eigenaxes of the static and dynamic potentials are aligned. If this is not the case, the equations of motion are coupled and stability criteria cannot be formulated so easily.

In the specific case of a linear Paul trap, where the oscillating potential only confines in the radial y, z-plane, implying $q_x = 0$ and $q_y = -q_z$, the ion trajectory is given by

$$x(t) \propto \cos(\omega_x t), \tag{2.8a}$$

$$y(t) \propto \cos(\omega_y t)\left[1 + \frac{q_y}{2}\cos(\omega_{\mathrm{rf}} t)\right], \tag{2.8b}$$

$$z(t) \propto \cos(\omega_z t)\left[1 + \frac{q_z}{2}\cos(\omega_{\mathrm{rf}} t)\right]. \tag{2.8c}$$

Along the trap axis, the motion is harmonic at frequency $\omega_x = \sqrt{eu_x/m}$, exclusively due to the static potential. In the radial directions, the slow *secular* harmonic oscillations at frequencies

$$\omega_i = \frac{\beta_i \omega_{\mathrm{rf}}}{2} = \sqrt{\frac{eu_i}{m} + \frac{e^2 v_i^2}{2m^2\omega_{\mathrm{rf}}^2}}$$

are superposed with fast and small driven excursions at the rf frequency, called *micromotion*. Note that there is no motion at exactly the drive frequency, so that the drive does not resonantly excite the motion.

If the ion's kinetic energy is reasonably low, micromotion can be neglected and the ion's motion be approximated by that of a three-dimensional harmonic oscillator. A full quantum mechanical treatment shows that even though the wavefunctions of an ion in a Paul trap "breath" at the rf frequency, the dynamics are still to a good approximation described by a simple harmonic oscillator [Lei03a].

Finally, we briefly examine the net effect of the rf potential. We have found that a potential

$$\Phi_{\mathrm{rf}}(\boldsymbol{r}, t) = \frac{1}{2}\sum_i v_i r_i^2 \cos(\omega_{\mathrm{rf}} t) \tag{2.9}$$

leads to the ion trajectories in Equations (2.8b) and (2.8c), with secular frequencies $\omega_i = ev_i/(\sqrt{2}m\omega_{\mathrm{rf}})$. This can also be understood in terms of a ponderomotive force. Since the electric driving field $\boldsymbol{E}_{\mathrm{rf}}(\boldsymbol{r}, t) = \boldsymbol{\nabla}\Phi_{\mathrm{rf}}(\boldsymbol{r}, t)$ is inhomogeneous, it exerts a net force [Deh68]

$$\boldsymbol{F}_{\mathrm{pm}}(\boldsymbol{r}) = -\frac{e^2}{4m\omega_{\mathrm{rf}}^2}\boldsymbol{\nabla}\boldsymbol{E}_{\mathrm{rf}}^2(\boldsymbol{r}, 0)$$

in the direction of weakest rf field amplitude when averaged over one rf period. The corresponding time-independent potential

$$\Phi_{\mathrm{ps}}(\boldsymbol{r}) = \frac{e}{4m\omega_{\mathrm{rf}}^2}\boldsymbol{E}_{\mathrm{rf}}^2(\boldsymbol{r}, 0) = \frac{e}{4m\omega_{\mathrm{rf}}^2}\left(\boldsymbol{\nabla}\Phi_{\mathrm{rf}}(\boldsymbol{r}, 0)\right)^2 \tag{2.10}$$

is called the *electric pseudopotential*. We make use of this formula in simulations of the

effective potential of a SET in the next section.

2.2. Electric potentials in SETs

There are countless experimental realizations of ion traps. The first ion traps consisted of a hyperbolically shaped ring and two hyperbolic rotationally symmetric caps, symmetrically placed above and below the ring [Pau90]. For this geometry, the trap potential between the electrodes can be analytically calculated and is exactly of the form in Equation (2.1).

In traps which are non-ideal and which do not have as much symmetry, the potential created by the electrodes cannot be determined so easily anymore, but often needs to be simulated on a computer using some form of boundary or finite element method (BEM/FEM). The electrostatic field above a planar electrode pattern, however, can be calculated analytically from a Biot-Savart-like law [Oli01], assuming an infinite grounded plane around and no gaps between the electrodes.[5]

Consider a flat area $\mathcal{A}$ in the x, y-plane that is kept at a fixed potential V, while the potential is kept at zero in the rest of the plane. Using Green's theorem for Dirichlet conditions, the electric field in the charge-free half-space $z > 0$ is given by [Oli01]

$$\boldsymbol{E}(\boldsymbol{r}) = -\boldsymbol{\nabla}\phi(\boldsymbol{r}) = \frac{V}{2\pi} \oint_{\partial\mathcal{A}} \frac{\mathrm{d}\boldsymbol{s}' \times (\boldsymbol{r}' - \boldsymbol{r})}{|\boldsymbol{r}' - \boldsymbol{r}|^3}$$

where $\mathrm{d}\boldsymbol{s}'$ is an element of length of the integration part $\partial\mathcal{A}$. Note that to calculate the total field, one just needs to integrate along the boundary of each electrode's area.

Our SET consists of two elongated "rf electrodes" parallel to the trap axis along x, to which an rf potential is applied, and 19 "Direct Current (dc) electrodes", to which static potentials can be applied (Figure 2.3). Approximately 2 mm above the SET is a conducting mesh, which is used as an additional grounded *cover plane* to shield from stray electric fields.

We use Roman Schmied's *SurfacePattern* package [Sch09; Sch10; Sch12b] for the computational software program Mathematica[6]. It applies the Biot-Savart-like law described above and thereby calculates the electric potential ϕ_i per unit voltage, as well as its spatial derivatives, above polygon-shaped surface electrodes, also taking into account the influence of the cover plane. Since the superposition principle applies, the total static potential and its derivatives are obtained by summing the contributions from the individual electrodes, multiplied by the voltages U_i applied to them,

$$\Phi_{\mathrm{dc}}(\boldsymbol{r}) = \sum_i \phi_i(\boldsymbol{r})\, U_i,$$

[5] These assumptions are usually fulfilled in SETs, in our case the ion–electrode distance ($\approx 50\,\mu\mathrm{m}$) is large compared to electrode–electrode gaps ($\approx 6\,\mu\mathrm{m}$) and much smaller than the chip's dimensions ($\approx \pm 5\,\mathrm{mm}$).

[6] Computational software program Mathematica from Wolfram Research, version 10.0.2.

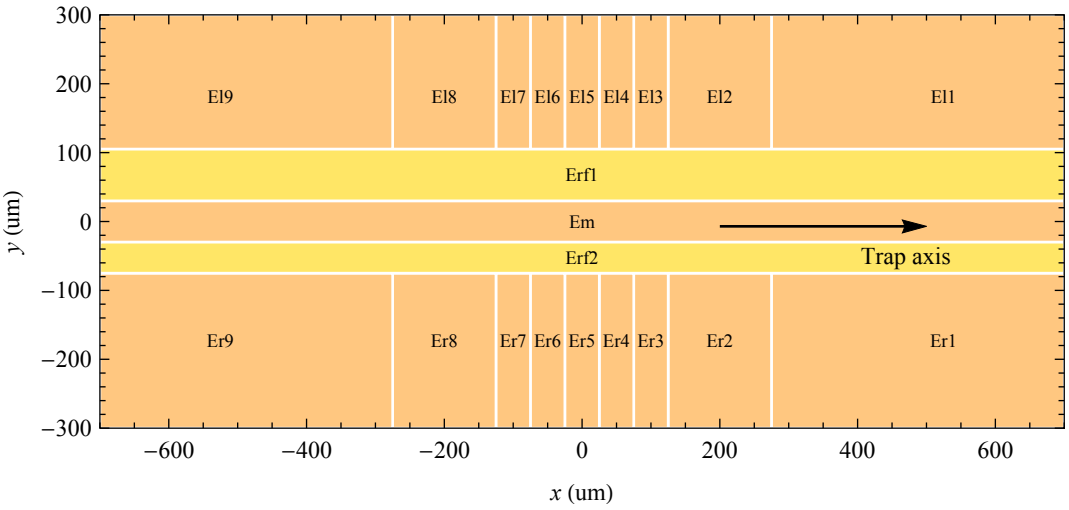

Figure 2.3: Schematic layout of the SET used in this dissertation. An rf potential applied to Erf1 and Erf2 confines radially in the y, z-plane, static potentials applied to El1..9, Em and Er1..9 allow for axial confinement at different positions along the trap axis above and parallel to Em.

where the sum extends over all dc electrodes (El1..9, Em and Er1..9).

Axial confinement of ions in the trap is realized with suitable voltages U_i. As we have seen, full radial confinement cannot be achieved with static fields only. Figure 2.4 (top) shows the electric potential $\Phi_{\mathrm{rf}}(\boldsymbol{r}, 0)$ and field lines above the SET due to the rf electrodes at an instant in time where the voltage $V_{\mathrm{rf}}(t) = V_{\mathrm{rf}} \cos(\omega_{\mathrm{rf}} t)$ has reached its maximum amplitude V_{rf}. At the marked critical point is a saddle point. Inward forces confine along y, but outward forces along z push the ion away from the trap center. Half a period later, the situation is reversed. The resulting pseudopotential $\Phi_{\mathrm{ps}}(\boldsymbol{r})$ can be calculated from Equation (2.10). It is fully confining in the radial directions at the trapping position above the central dc electrode (Figure 2.4 (bottom)).

At the trapping position $\boldsymbol{r}_{\mathrm{tr}}$, the momentary potential has a saddle point, $\boldsymbol{\nabla} \Phi_{\mathrm{rf}}(\boldsymbol{r}_{\mathrm{tr}}, t) = 0$, which implies zero force and hence minimal micromotion. Due to the nature of the pseudopotential, it is zero at that point and has a local minimum [Sch11],

$$\partial_j \Phi_{\mathrm{ps}}|_{\boldsymbol{r}_{\mathrm{tr}}} \propto \partial_j (\partial_i \Phi_{\mathrm{rf}}\, \partial_i \Phi_{\mathrm{rf}})|_{\boldsymbol{r}_{\mathrm{tr}}} = 2(\partial_j \partial_i \Phi_{\mathrm{rf}})|_{\boldsymbol{r}_{\mathrm{tr}}} \underbrace{(\partial_i \Phi_{\mathrm{rf}})|_{\boldsymbol{r}_{\mathrm{tr}}}}_{=0} = 0,$$

where Einstein notation implies summation over indices that occur twice. These criteria allow one to find $\boldsymbol{r}_{\mathrm{tr}}$ for a given pseudopotential.

Ideally, the static potential from the dc electrodes is placed such that its saddle point falls onto $\boldsymbol{r}_{\mathrm{tr}}$. Then the full potential $\Phi_{\mathrm{tot}}(\boldsymbol{r}) = \Phi_{\mathrm{dc}}(\boldsymbol{r}) + \Phi_{\mathrm{ps}}(\boldsymbol{r})$ has a local minimum at $\boldsymbol{r}_{\mathrm{tr}}$ and can trap an ion with minimal micromotion. Around that minimum, the potential is quadratic to leading order and the ion's motion is of the form in Equation (2.8). But in

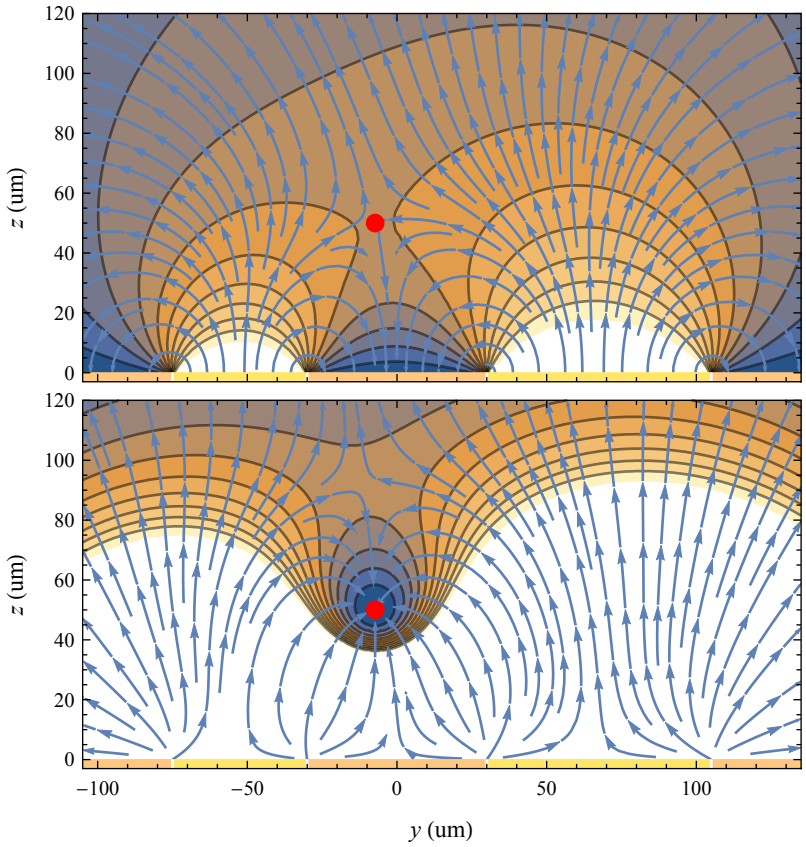

Figure 2.4: (top) Instantaneous electric potential and field in the $x = 0$ plane above the SET due to the voltage amplitude V_{rf} applied to the rf electrodes. The potential has a saddle point (red dot) where the horizontal forces are confining and the vertical anti-confining. (bottom) Pseudopotential and corresponding force field above the SET due to the oscillating voltage applied to the rf electrodes. The saddle point of the momentary potential above now becomes a local minimum (red dot). The bottom row in each plot illustrates the electrodes Er5, Erf2, Em, Erf1, El5 from left to right.

contrast to the formal potential in Equation (2.1), the real eigenmodes[7] of the motion do not necessarily align with the Cartesian axes of the SET (Figure 2.5). In fact, trap chips are often designed such that no eigenaxis aligns with the z-axis because that would prevent laser cooling (Section 3.6).

We find the eigenmodes and eigenfrequencies of the secular motion by first expanding the total potential around the ion's equilibrium position,

$$e\Phi_{\mathrm{tot}}(\boldsymbol{r}_{\mathrm{tr}} + \boldsymbol{r}) \approx e\Phi_{\mathrm{dc}}(\boldsymbol{r}_{\mathrm{tr}}) + \frac{e}{2}\left(\boldsymbol{r}\cdot\boldsymbol{\nabla}\right)^2 \Phi_{\mathrm{tot}}|_{\boldsymbol{r}_{\mathrm{tr}}} \equiv e\Phi_{\mathrm{dc}}(\boldsymbol{r}_{\mathrm{tr}}) + \frac{m}{2}\, r_i r_j \mathcal{H}_{ij}. \qquad (2.11)$$

The Hessian matrix $\mathcal{H}_{ij} = \frac{e}{m}\partial_i\partial_j\Phi_{\mathrm{tot}}|_{\boldsymbol{r}_{\mathrm{tr}}}$ of second-order partial derivatives is positive definite

[7] In an ellipsoid harmonic potential, the eigenmodes are oscillations in the directions along which the restoring force is parallel to the displacement.

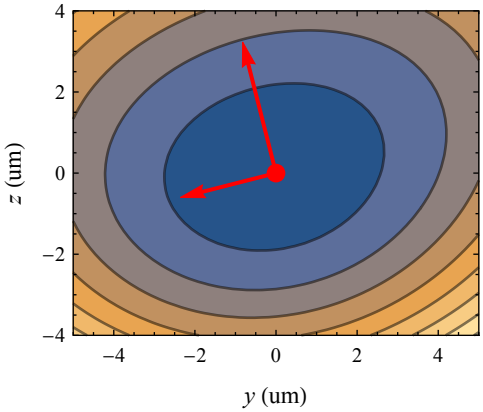

Figure 2.5: Equipotential lines of the total electric potential Φ_{tot} in the radial plane around the trapping position (red dot) for an example set of realistic parameters. Red arrows mark the directions of the eigenmodes of motions with lengths proportional to the respective oscillation frequencies.

and describes the potential's local curvature. The motional eigenmodes are oscillations along its eigenvectors at frequencies given by the square root of its eigenvalues, $\omega_i = \sqrt{\lambda_i}$.

In the case of our linear rf trap, the eigenmode along the trap axis is solely due to the static potential and the oscillation given by Equation (2.8a) has the frequency

$$\omega_x^2 = \lambda_x = \frac{eu_x}{m}.$$

The oscillation frequencies in the radial directions are given by

$$\omega_i^2 = \lambda_i = \lambda_{i,\text{dc}} + \lambda_{i,\text{ps}} = \frac{eu_i}{m} + \frac{e^2 v_i^2}{2m^2\omega_{\text{rf}}^2}, \tag{2.12}$$

where the λ_i and the $\lambda_{i,\text{ps}}$ are positive, but at least one $\lambda_{i,\text{dc}}$ is negative because of $\sum_i \lambda_{i,\text{dc}} = 0$. Note that the $\lambda_{i,\text{ps}}$ are equal because Φ_{rf} fulfills Laplace's equation at its critical point,

$$\begin{aligned}\frac{4m\omega_{\text{rf}}^2}{e}\,\partial_y\partial_y\Phi_{\text{ps}}|_{\boldsymbol{r}_{\text{tr}}} &= 2(\partial_y\partial_y\partial_i\Phi_{\text{rf}})|_{\boldsymbol{r}_{\text{tr}}}\overbrace{(\partial_i\Phi_{\text{rf}})|_{\boldsymbol{r}_{\text{tr}}}}^{=0} + 2(\partial_y\partial_i\Phi_{\text{rf}})|_{\boldsymbol{r}_{\text{tr}}}(\partial_y\partial_i\Phi_{\text{rf}})|_{\boldsymbol{r}_{\text{tr}}} \\ &= 2\Big(\underbrace{(\partial_y\partial_y\Phi_{\text{rf}})|_{\boldsymbol{r}_{\text{tr}}}}_{-(\partial_z\partial_z\Phi_{\text{rf}})|_{\boldsymbol{r}_{\text{tr}}}}\Big)^2 + 2\Big((\partial_y\partial_z\Phi_{\text{rf}})|_{\boldsymbol{r}_{\text{tr}}}\Big)^2 = \frac{4m\omega_{\text{rf}}^2}{e}\,\partial_z\partial_z\Phi_{\text{ps}}|_{\boldsymbol{r}_{\text{tr}}}.\end{aligned}$$

In other words, the pseudopotential is circular around $\boldsymbol{r}_{\text{tr}}$, even if the rf potential is of higher than quadratic order. This means that it is solely the curvatures of the static potential that lift the degeneracy of the radial eigenmodes and determine the orientation of the eigenaxes.

Note that Equation (2.12) also applies if the eigenaxes of the rf potential do not align with the ones of the rf potential, which had been presumed for Equation (2.1). In that case,

the Hessian of Φ_{rf} has non-zero entries $v_{yy} = -v_{zz}$ and $v_{yz} = v_{zy}$. But the curvature of Φ_{ps} would still be proportional to v_i^2 in all directions at its critical point as in Equation (2.12) with $v_i^2 = v_{yy}^2 + v_{yz}^2$, which follows directly from Equation (2.10).

2.3. The quantum harmonic oscillator

At sufficiently low kinetic energy, a trapped ion is a prime example of the textbook quantum harmonic oscillator. This is of course an exhaustively studied object. But for completeness' sake and later use, it is worthwhile to review relevant formulas for this thesis.

Since the harmonic oscillator eigenmodes of a trapped ion are decoupled, the Hamiltonian describing the ion's dynamics can be decomposed. For a single eigenmode, we have

$$H = \frac{P^2}{2m} + \frac{m\omega_{\mathrm{m}}^2 X^2}{2} = \hbar\omega_{\mathrm{m}}\left(\tilde{P}^2 + \tilde{X}^2\right) = \hbar\omega_{\mathrm{m}}\left(a^\dagger a + \frac{1}{2}\right), \tag{2.13}$$

where the two dimensionless quadrature operators,

$$\tilde{X} = \frac{X}{2x_0}, \qquad \tilde{P} = \frac{P}{2x_0 m\omega_{\mathrm{m}}} \qquad \text{with} \qquad x_0 = \sqrt{\frac{\hbar}{2m\omega_{\mathrm{m}}}}, \tag{2.14}$$

represent momentum and position, respectively, using the characteristic length x_0. The lowering and raising operators are defined by

$$a = \tilde{X} + \mathrm{i}\tilde{P} \qquad \Longleftrightarrow \qquad \tilde{X} = \frac{1}{2}\left(a^\dagger + a\right), \quad \tilde{P} = \frac{\mathrm{i}}{2}\left(a^\dagger - a\right) \tag{2.15}$$

and satisfy $[a, a^\dagger] = 1$.

2.3.1. Number states

The energy eigenstates are the eigenstates of the number operator $N = a^\dagger a$, hence called *number states*, and obey the ladder algebra

$$a|n\rangle = \sqrt{n}\,|n-1\rangle, \qquad a^\dagger|n\rangle = \sqrt{n+1}\,|n+1\rangle, \qquad N|n\rangle = n|n\rangle.$$

They form a complete orthonormal set of the Hilbert space, so that any state $|\psi\rangle$ can be written as a linear combination

$$|\psi\rangle = \sum_n c_n|n\rangle, \qquad c_n = \langle n\,|\,\psi\rangle.$$

From the moments for $\tilde{X}$ and $\tilde{P}$ of the number states follows

$$\left(\Delta\tilde{X}\right)_n^2 = \frac{2n+1}{4}, \qquad \left(\Delta\tilde{P}\right)_n^2 = \frac{2n+1}{4}, \qquad (\Delta X)_n(\Delta P)_n = \frac{\hbar}{2}(2n+1).$$

Hence the vacuum state $|0\rangle$ has a spatial standard deviation of x_0 and is a *minimum-uncertainty* state, saturating Heisenberg's uncertainty relation. The position representation,

$$\psi_0(x) = \langle x \,|\, 0\rangle \propto \mathrm{e}^{-x^2/(4x_0^2)},$$

is a Gaussian state, which is characteristic of minimum-uncertainty states in general [Wis10, Section A.3].

2.3.2. Coherent states

Consider the Heisenberg equation (A.2) for the lowering operator,

$$\mathrm{i}\hbar \frac{\mathrm{d}}{\mathrm{d}t} a^{\mathrm{H}}(t) = \left[a^{\mathrm{H}}(t), H^{\mathrm{H}}(t)\right] = \hbar\omega_{\mathrm{m}} a^{\mathrm{H}}(t).$$

It is equivalent to the classical equations of motion of a harmonic oscillator in terms of a classical phasor defined in analogy to Equation (2.15), see for example [Coh99a, p. 534ff]. Eigenstates of the lowering operator, $a|\alpha\rangle = \alpha|\alpha\rangle$ with α a complex number, therefore resemble classical motion and are called *coherent states*. They are generated by applying the unitary *displacement* operator

$$D(\alpha) = \mathrm{e}^{\alpha a^\dagger - \alpha^* a}$$

onto the ground state. The corresponding transformation of the lowering operator in Equation (F.4),

$$D(\alpha)\, a\, D(-\alpha) = a - \alpha = (\tilde{X} - \alpha_{\mathrm{r}}) + \mathrm{i}(\tilde{P} - \alpha_{\mathrm{i}}),$$

essentially means that $D(\alpha)$ translates the quadratures of position by $\alpha_{\mathrm{r}} = \Re[\alpha]$ and of momentum by $\alpha_{\mathrm{i}} = \Im[\alpha]$. Coherent states are, therefore, displaced ground states and hence also minimum-uncertainty states.

Using the Baker-Campbell-Hausdorff formula in Equation (F.2a), one finds an expression for the coherent states in terms of number states,

$$|\alpha\rangle = D(\alpha)|0\rangle = \mathrm{e}^{-|\alpha|^2/2} \sum_n \frac{\alpha^n}{\sqrt{n!}} |n\rangle.$$

This number-state distribution is a *Poissonian* distribution with mean and variance $|\alpha|^2$,

$$P_\alpha(n) = \left|\langle n \,|\, \alpha\rangle\right|^2 = \mathrm{e}^{-|\alpha|^2} \frac{|\alpha|^{2n}}{n!}. \tag{2.16}$$

The time-evolution of a coherent state in the Schrödinger picture reads

$$\left|\alpha(t)\right\rangle = \mathrm{e}^{-\mathrm{i}Ht/\hbar} \left|\alpha(0)\right\rangle = \left|\alpha(0)\, \mathrm{e}^{-\mathrm{i}\omega_{\mathrm{m}} t}\right\rangle.$$

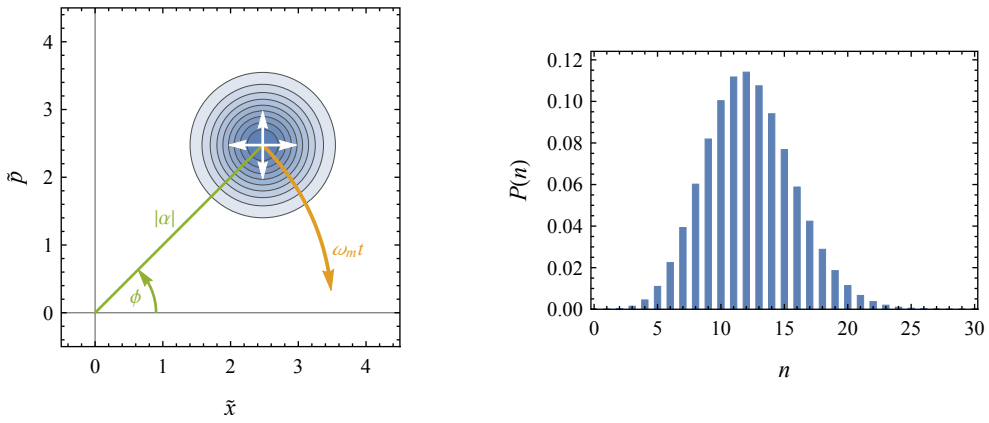

Figure 2.6: (left) Contour plot of a coherent-state Wigner function with $\alpha = 3.5\,\mathrm{e}^{\mathrm{i}\pi/4}$. It evolves along a circle with radius $|\alpha|$. The quadrature variances are 1/4 in all directions. (right) The number-state distribution of a coherent state, given by Equation (2.16), is Poissonian with mean and variance $|\alpha|^2$.

This is still a coherent state, only the phase changes at rate ω_m. Coherent states hence remain minimum-uncertainty states under harmonic-oscillator evolution, which again justifies their name.

The motion can be illustrated in phase space with the help of *Wigner functions* (see Appendix C). The Wigner function of a coherent state, given in Equation (C.2) as

$$W_\alpha(\tilde{x},\tilde{p}) = \frac{2}{\pi}\,\mathrm{e}^{-2(\tilde{x}-\alpha_\mathrm{r})^2}\,\mathrm{e}^{-2(\tilde{p}-\alpha_\mathrm{i})^2},$$

is a Gaussian in the dimensionless coordinates $\tilde{x}$ and $\tilde{p}$, normalized analogously to Equation (2.14), and evolves clockwise on a circle around the origin (Figure 2.6). The expectation value for the oscillator's position at a time t is

$$\tilde{x}(t) = \langle\alpha(t)\,|\,\tilde{X}\,|\,\alpha(t)\rangle = \frac{1}{2}\left(\alpha(0)\mathrm{e}^{-\mathrm{i}\omega_\mathrm{m}t} + \alpha^*(0)\mathrm{e}^{\mathrm{i}\omega_\mathrm{m}t}\right) = \Re\left[\alpha(0)\mathrm{e}^{-\mathrm{i}\omega_\mathrm{m}t}\right],$$

fully resembling the classical motion.

2.3.3. Squeezed states

Coherent states are only a particular class of minimum-uncertainty states, picked out by a given harmonic-oscillator Hamiltonian. All other Gaussian pure states are called *squeezed* states. Besides the complex displacement parameter α, a general squeezed state is specified by an additional complex parameter $\zeta = r\mathrm{e}^{\mathrm{i}\theta}$,

$$|\alpha,\zeta\rangle = D(\alpha)|\zeta\rangle = D(\alpha)S(\zeta)|0\rangle,$$

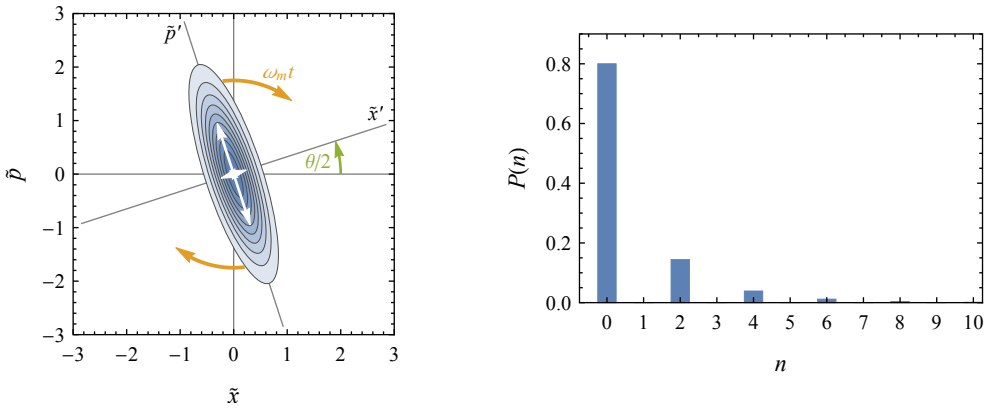

Figure 2.7: (left) Contour plot of a squeezed-state Wigner function with $r = \ln 2$, $\theta = 0.2\pi$. Each point on it evolves on a circle around the origin so that the squeezed state appears to rotate. (right) The number-state distribution of a squeezed state, Equation (2.17), shows that only even number states are populated.

where $|\zeta\rangle$ is called *squeezed vacuum* and the squeezing operator is defined as

$$S(\zeta) = \mathrm{e}^{\left(\zeta^* a^2 - \zeta a^{\dagger 2}\right)/2}.$$

In order to understand the effect of the squeezing operator, we define a rotated complex amplitude at an angle $\theta/2$ [Scu08, p. 64],

$$\tilde{X}' + \mathrm{i}\tilde{P}' = (\tilde{X} + \mathrm{i}\tilde{P})\mathrm{e}^{-\mathrm{i}\theta/2} = \left(\tilde{X}\cos\tfrac{\theta}{2} + \tilde{P}\sin\tfrac{\theta}{2}\right) + \mathrm{i}\left(-\tilde{X}\sin\tfrac{\theta}{2} + \tilde{P}\cos\tfrac{\theta}{2}\right),$$

and transform it with the squeezing operator using Equation (F.6) as

$$S(\zeta)\left(\tilde{X}' + \mathrm{i}\tilde{P}'\right) S(-\zeta) = \tilde{X}'\mathrm{e}^{r} + \mathrm{i}\tilde{P}'\mathrm{e}^{-r}.$$

With respect to rescaled rotated quadrature axes, the squeezed vacuum state is a ground state. Therefore, the variance of the squeezed state along $\tilde{X}'$ is divided by e^{2r} due to the squeezing, while the variance of $\tilde{P}'$ is divided by e^{-2r} (Figure 2.7). The reduction in the variance of one coordinate squeezes the uncertainty into the conjugate coordinate.

Due to the form of the exponent in the squeezing operator, the squeezed vacuum state is a superposition of only even phonon number states [Bar97, p. 68],

$$|\zeta\rangle = \frac{1}{\sqrt{\cosh(r)}} \sum_{n=0}^{\infty} \frac{\sqrt{(2n)!}}{n!} \left[-\frac{1}{2}\,\mathrm{e}^{\mathrm{i}\theta}\tanh(r)\right]^n |2n\rangle,$$

with the number-state distribution

$$P_\zeta(2n) = \frac{1}{\cosh(r)} \frac{(2n)!}{2^n (n!)^2}\,\tanh^{2n}(r). \tag{2.17}$$

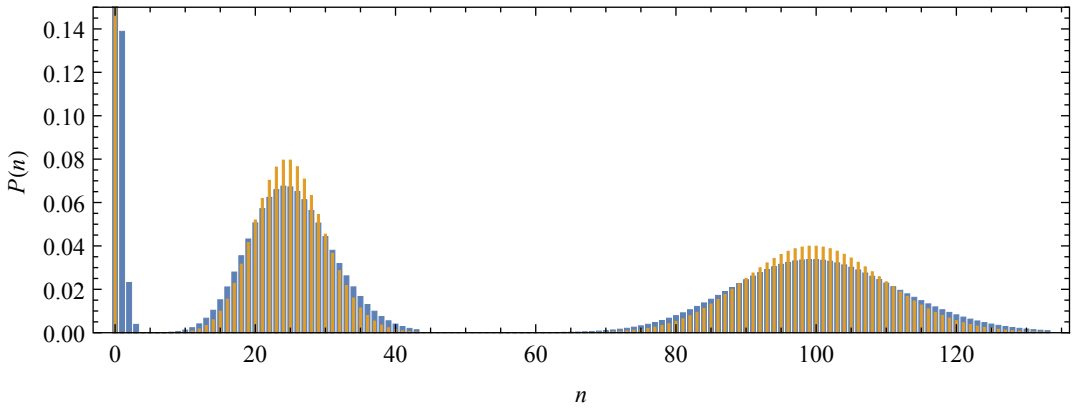

Figure 2.8: Number-state distributions of displaced thermal states with $n_{\mathrm{th}} = 0.2$ for $\alpha = 0, 5, 10$ corresponding to the peaks from left to right (blue bars). For comparison, the number-state distributions of coherent states with the same displacements are shown (orange bars).

2.3.4. Thermal states

A harmonic oscillator in thermal equilibrium with a heat bath is in a statistically mixed state with the number-state populations weighted by the Boltzmann factors $\exp[-n\hbar\omega_{\mathrm{m}}/k_{\mathrm{B}}T]$. The number-state distribution (Figure 2.8) is hence given by

$$P_{n_{\mathrm{th}}}(n) = \frac{1}{1+n_{\mathrm{th}}}\left(\frac{n_{\mathrm{th}}}{1+n_{\mathrm{th}}}\right)^n \tag{2.18}$$

with the average phonon number

$$n_{\mathrm{th}} = \langle n\rangle = \left(\mathrm{e}^{\hbar\omega_{\mathrm{m}}/k_{\mathrm{B}}T} - 1\right)^{-1}.$$

The density matrix (Appendix B) of a thermal state reads

$$\rho_{\mathrm{th}} = \frac{1}{1+n_{\mathrm{th}}}\sum_n \left(\frac{n_{\mathrm{th}}}{1+n_{\mathrm{th}}}\right)^n |n\rangle\langle n|.$$

When a thermal state is displaced, the number-state distribution is altered to

$$P_{\alpha,n_{\mathrm{th}}}(n) = \sum_m P_{n_{\mathrm{th}}}(m)\,\left|\langle n\,|\,D(\alpha)\,|\,m\rangle\right|^2, \tag{2.19}$$

where the matrix elements can be calculated as [Wün91, p. 364]

$$\langle n\,|\,D(\alpha)\,|\,m\rangle = \mathrm{e}^{-|\alpha|^2/2}\sqrt{n!m!}\sum_{j=0}^{\min\{n,m\}} \frac{\alpha^{n-j}(-\alpha^*)^{m-j}}{j!(n-j)!(m-j)!}.$$

If the cooling of the ion leaves it in a thermal state rather than in the ground state, this

is the relevant phonon distribution after diabatic displacement in our experiments. It is broader than that of a displaced ground state (Figure 2.8).

3. Laser–Ion Interactions

Lasers are indispensable tools for trapped-ion quantum information experiments. They are used for cooling, manipulating and detecting ions, as well as analyzing their internal and motional states.

This chapter starts by introducing the relevant energy levels and transitions of the $^{40}Ca^{+}$ ion (Section 3.1). Then the general Hamiltonian for coherent laser–ion interactions is derived (Section 3.2) and applied in the simplest form to a two-level system yielding Rabi oscillations (Section 3.3). To take dissipative processes into account, the evolution of the system's density matrix is described using optical Bloch equations (Section 3.4). Section 3.5 evaluates the previously found Rabi frequencies. Two forms of laser cooling, Doppler and Electromagnetically Induced Transparency (EIT) cooling, are discussed in Section 3.6. Section 3.7 presents methods for spin- and oscillator-state analysis. Finally, I introduce the concept of spin decoherence under the influence of discrete noise and how to detect it by means of Ramsey interferometry (Section 3.8).

3.1. The calcium ion

All our experiments are performed using singly charged ions of the most abundant isotope of calcium, ^{40}Ca. Having zero nuclear spin, the atomic energy levels of the single valence electron only show fine structure with LS coupling (Figure 3.1).

The levels are identified using the standard atomic level notation $n\,^{2S+1}L_J(m_J = m_J)$, where n is the principal quantum number, S the spin angular momentum, L the orbital angular momentum, J the total angular momentum and m_J its projection onto the quantization axis. For the given relevant levels (all having a spin $S = 1/2$; $n = 4$ for $L = 0, 1$ and $n = 3$ for $L = 2$), the shorthand notation L_J is unambiguous and will be used henceforth.

All of the lowest transitions in the $^{40}Ca^{+}$ ion are accessible by solid-state laser sources. The near-UV transitions $S \leftrightarrow P$ are dipole allowed and have sufficiently short lifetimes to permit cooling and detection. The near-IR transitions $D \leftrightarrow P$ are also dipole allowed and are used to repump population from the D-levels to the ground state. The visible transitions $S \leftrightarrow D$ are only quadrupole allowed with lifetimes of roughly 1 s. This is long compared to timescales of our experiments such that the D-states can be considered metastable. Two states from the $S_{1/2}$- and $D_{5/2}$-manifolds are chosen as pseudo-spin or *qubit* states for coherent manipulation (Section 3.5.3).

A magnetic field lifts the degeneracy of the fine structure levels and shifts their eigenen-

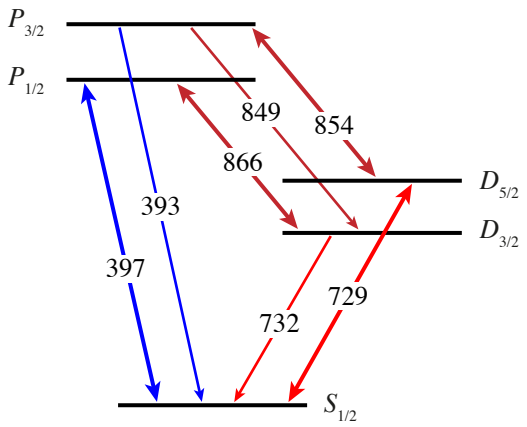

Table 3.1: Natural lifetimes and spontaneous emission rates in $^{40}Ca^{+}$ [Jam98].

λ (nm)	τ (ns)	Γ (2π MHz)
397	7.7	20.7
729	1.05×10^{9}	1.52×10^{-7}
866	94.3	1.69
854	101	1.58
393	7.4	21.5
732	1.08×10^{9}	1.47×10^{-7}
849	901	0.18

Figure 3.1: Level diagram of the $^{40}Ca^{+}$ ion and possible transitions. The numbers give the approximate wavelengths of the transitions in nm. Thick double-ended arrows mark transitions driven by lasers in our experiments.

ergies due to the Zeeman effect by

$$\Delta\omega = g_J \mu_B B m_j/\hbar, \qquad g_J = \frac{3}{2} - \frac{L(L+1) - S(S+1)}{2J(J+1)}$$

in terms of angular frequency, where μ_B is Bohr's magneton and g_J the Landé factor. The frequency splittings (Table 3.2) broaden the dipole transitions and allow for resolving the individual quadrupole transitions.

Table 3.2: Landé factors and Zeeman splittings per unit magnetic field for relevant levels.

	$S_{1/2}$	$P_{1/2}$	$P_{3/2}$	$D_{3/2}$	$D_{5/2}$
g_J	2	2/3	4/3	4/5	6/5
$\Delta\omega/(2\pi B m_J)$ (MHz/G)	2.7993	0.9331	1.8662	1.1197	1.6796

3.2. Coherent interaction

The free Hamiltonian for a single trapped ion consists of terms for the internal atomic states $|i\rangle$ with eigenenergies $\hbar\omega_{a,i}$ and the three harmonic oscillator modes at frequencies $\omega_{m,j}$,

$$H_0 = \sum_i \hbar\omega_{a,i} |i\rangle\langle i| + \sum_j \hbar\omega_{m,j} \left(a_j^\dagger a_j + \frac{1}{2}\right).$$

In the following, I examine the interaction of the ion with a monochromatic laser field of

frequency ω_l described by

$$\boldsymbol{E}(t,\boldsymbol{r}) = \frac{E_0}{2}\Big[\boldsymbol{\epsilon}\,\mathrm{e}^{-\mathrm{i}(\omega_\mathrm{l} t-\boldsymbol{k}\cdot\boldsymbol{r}+\phi)} + \boldsymbol{\epsilon}^*\,\mathrm{e}^{\mathrm{i}(\omega_\mathrm{l} t-\boldsymbol{k}\cdot\boldsymbol{r}+\phi)}\Big],$$

where E_0 is the positive field amplitude, $\boldsymbol{\epsilon}$ the (potentially complex) polarization vector, $\boldsymbol{k} = \boldsymbol{\kappa}k$ the wave-vector with $k = \omega_\mathrm{l}/c$, and ϕ the phase. If the laser is only resonant with the transition between two atomic states, $|g\rangle$ (lower) and $|e\rangle$ (upper), that is $\omega_\mathrm{l} \approx \omega_\mathrm{a} = \omega_{\mathrm{a},e} - \omega_{\mathrm{a},g}$, and spontaneous emission to other levels can be neglected, it is justified to treat the atom as a two-level or *pseudo-spin* system. Omitting constant terms, the free Hamiltonian reduces to

$$H_0 = \frac{\hbar\omega_\mathrm{a}}{2}\,\sigma_z + \sum_j \hbar\omega_{\mathrm{m},j}\,a_j^\dagger a_j \tag{3.1}$$

with the Pauli matrix $\sigma_z = |e\rangle\langle e| - |g\rangle\langle g|$.

The coupling Hamiltonian for the interaction with laser light (assuming a hydrogen-like atomic configuration) expanded to second order (neglecting magnetic interaction) only contains terms for electric dipole and quadrupole coupling [Šaš02; Jac62, p. 101],

$$H_1(t) = \frac{eE_0}{2}\left[(\boldsymbol{r}\cdot\boldsymbol{\epsilon}) + \frac{(\boldsymbol{r}\cdot\boldsymbol{k})(\boldsymbol{r}\cdot\boldsymbol{\epsilon})}{2}\right]\mathrm{e}^{-\mathrm{i}(\omega_\mathrm{l} t-\boldsymbol{k}\cdot\boldsymbol{R}+\phi)} + \mathrm{H.c.},$$

where e is the elementary charge of the valence electron, $\boldsymbol{r}$ its internal position operator, and $\boldsymbol{R}$ the external position operator of the ion in the trap. From the matrix elements of $H_1(t)$, the coupling constants

$$\tilde{\Omega}_{eg}^{\mathrm{DP}} = \frac{eE_0}{\hbar}\,\langle e\,|\,\boldsymbol{r}\cdot\boldsymbol{\epsilon}\,|\,g\rangle, \qquad \tilde{\Omega}_{eg}^{\mathrm{QP}} = \frac{eE_0 k}{2\hbar}\,\langle e\,|\,(\boldsymbol{r}\cdot\boldsymbol{\kappa})(\boldsymbol{r}\cdot\boldsymbol{\epsilon})\,|\,g\rangle,$$

and in analogy $\tilde{\Omega}_{ge}^{\mathrm{DP}}$ and $\tilde{\Omega}_{ge}^{\mathrm{QP}}$ can be defined for the dipole and quadrupole terms, respectively.[1] If the transition is dipole allowed, the dipole terms dominate, otherwise they vanish and the weaker quadrupole terms play the key role. I henceforth write $\tilde{\Omega}_{eg}$ and $\tilde{\Omega}_{ge}$ for the relevant coupling constants.

Introducing the *Lamb-Dicke parameters* η_j via

$$\boldsymbol{k}\cdot\boldsymbol{R} = \sum_j \eta_j(a_j^\dagger + a_j), \qquad \eta_j = k\kappa_j\sqrt{\frac{\hbar}{2m\omega_{\mathrm{m},j}}} \tag{3.2}$$

for the three oscillator modes and the operators $\sigma_{eg} = |e\rangle\langle g|$ and $\sigma_{ge} = |g\rangle\langle e|$, the coupling

[1] Diagonal matrix elements of the quadrupole terms do actually not vanish. They would, however, drop out in the rotating wave approximation below.

Hamiltonian can be written

$$\begin{aligned} H_1(t) &= \frac{\hbar}{2}\left(\tilde{\Omega}_{eg}\sigma_{eg} + \tilde{\Omega}_{ge}\sigma_{ge}\right) \mathrm{e}^{-\mathrm{i}(\omega_\mathrm{l}t+\phi)} \prod_j \mathrm{e}^{\mathrm{i}\eta_j\left(a_j^\dagger + a_j\right)} + \mathrm{H.c.} \\ &= \frac{\hbar}{2}\left(\tilde{\Omega}_{eg}\sigma_{eg} + \tilde{\Omega}_{ge}\sigma_{ge}\right) \mathrm{e}^{-\mathrm{i}(\omega_\mathrm{l}t+\phi)} \prod_j \sum_{s_j=-\infty}^{\infty} \sum_{n_j=I_j}^{\infty} |n_j + s_j\rangle\langle n_j|\, g_{s_j,n_j}(\eta_j) + \mathrm{H.c.} \end{aligned} \tag{3.3}$$

with $I_j = \max[0, -s_j]$. The *Franck-Condon coefficients* $g_{s,n}$ [Esc03] can be calculated using the Baker-Campbell-Hausdorff formula in Equation (F.2a) to be

$$g_{s,n}(\eta) = \left\langle n+s \,\middle|\, \mathrm{e}^{\mathrm{i}\eta(a^\dagger + a)} \,\middle|\, n \right\rangle = \mathrm{e}^{-\eta^2/2}\,(\mathrm{i}\eta)^{|s|} \sqrt{\frac{n_<!}{n_>!}}\, L_{n_<}^{|s|}\left(\eta^2\right) \tag{3.4}$$

with $n_<$ ($n_>$) the lesser (greater) of $n+s$ and n, and the generalized Laguerre polynomials given in Equation (F.13). It is useful to transform this to the interaction picture (Section A.3) with respect to H_0 in Equation (3.1) to determine resonances. Using the transformation in Equation (F.8) and neglecting terms rapidly oscillating at the frequency $\omega_\mathrm{l} + \omega_\mathrm{a}$, which is called the *Rotating Wave Approximation* (RWA), one finds

$$H_1^\mathrm{I}(t) = \frac{\hbar\Omega}{2}\,\sigma_{eg}\,\mathrm{e}^{-\mathrm{i}(\delta t+\phi)} \prod_j \sum_{s_j=-\infty}^{\infty} \sum_{n_j=I_j}^{\infty} |n_j + s_j\rangle\langle n_j|\, g_{s_j,n_j}(\eta_j)\,\mathrm{e}^{\mathrm{i}s_j\omega_{\mathrm{m},j}t} + \mathrm{H.c.} \tag{3.5}$$

where $\delta = \omega_\mathrm{l} - \omega_\mathrm{a}$ is the detuning of the laser from the transition frequency. Furthermore, I have set $\Omega = |\tilde{\Omega}_{eg}|$ to represent the relevant of the *on-resonance Rabi frequencies*

$$\Omega^\mathrm{DP} = \frac{eE_0}{\hbar}\,|\langle e|\,\boldsymbol{r}\cdot\boldsymbol{\epsilon}\,|g\rangle|, \qquad \Omega^\mathrm{QP} = \frac{eE_0 k}{2\hbar}\,|\langle e|\,(\boldsymbol{r}\cdot\boldsymbol{\kappa})(\boldsymbol{r}\cdot\boldsymbol{\epsilon})\,|g\rangle| \tag{3.6}$$

for the dipole and quadrupole terms, respectively. They will be examined in detail in Section 3.5. The additional phase from the coupling, $\arg(\tilde{\Omega}_{eg})$, was lumped into the global laser phase ϕ.

According to the Hamiltonian in Equation (3.5), resonances occur for $\delta = \sum_j s_j\omega_{\mathrm{m},j}$ and induce transitions that create and/or annihilate phonons in the motional modes, including mode-mode couplings. Two more approximations can be made to limit the derivation to the axial motional mode. First, I assume that the laser is tuned close to a resonance involving only axial motion ($s_j = 0$ for the radial modes) and that other possible resonances are far away compared to Ω, such that no significant excitations on off-resonant transitions occur (*weak coupling regime*). Second, motional excitations in the radial modes are assumed to be low such that

$$\eta_j \sqrt{\left\langle \left(a_j + a_j^\dagger\right)^2 \right\rangle} \ll 1$$

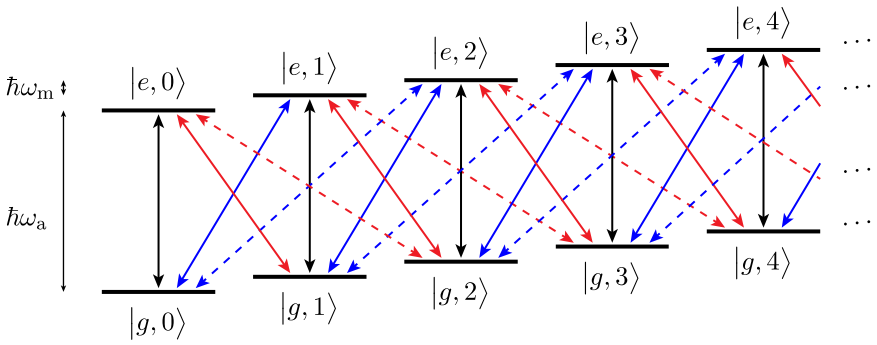

Figure 3.2: Energy levels and transitions of the spin-oscillator system. At a detuning $\delta \approx s\omega_\mathrm{m}$, the laser drives the transitions $|g,n\rangle \leftrightarrow |e,n+s\rangle$ with Rabi frequencies $\Omega_{s,n}$. Black arrows represent carrier transitions (s =0), red arrows red-sideband transitions ($s<0$), and blue arrows blue-sideband transitions ($s>0$). Solid arrows mark transitions for $s=0,\pm1$, dashed arrows transitions for $s=\pm2$. Note that $\Omega_{s,n}=\Omega_{-s,n+s}$, which means that the transitions $|g,n\rangle \leftrightarrow |e,n+s\rangle$ and $|g,n+s\rangle \leftrightarrow |e,n\rangle$ are driven at the same rates.

holds at all times, which is called *Lamb-Dicke regime* of the respective mode [Lei03a, p. 292]. Making these approximations and henceforth omitting the index j for the axial mode, the coupling Hamiltonian finally simplifies to

$$H_1^\mathrm{I}(t) = \frac{\hbar}{2}\,\mathrm{e}^{-\mathrm{i}(\delta t - s\omega_\mathrm{m} t+\phi)} \sum_{n=I}^{\infty} \Omega_{s,n}\,|e,n+s\rangle\langle g,n|\,\mathrm{e}^{-\mathrm{i}\phi_{s,n}} + \mathrm{H.c.} \tag{3.7}$$

for $\delta \approx s\omega_\mathrm{m}$ with $s\in\mathbb{Z}$. The laser hence couples the manifolds of states $|g,n\rangle$ and $|e,n+s\rangle$ (Figure 3.2) with coupling strengths

$$\Omega_{s,n} = \Omega\,|g_{s,n}(\eta)| = \Omega\,\mathrm{e}^{-\eta^2/2}\,(\eta)^{|s|}\sqrt{\frac{n_<!}{n_>!}}\left|L_{n_<}^{|s|}\left(\eta^2\right)\right|. \tag{3.8}$$

The relative Rabi frequencies of the *carrier* ($s=0$) and the first five *blue sidebands* ($s>0$; transitions with $s<0$ are called *red sidebands*) are plotted versus n in Figure 3.3 and will become important in the experiments in Chapter 6. The additional phases $\phi_{s,n} = -\arg(g_{s,n}(\eta))$ can at this stage not be pulled into the laser phase, but they will drop out later and not affect the measurements.

If additionally the axial mode is in the Lamb-Dicke regime, the coupling Hamiltonian for laser frequencies close to resonance with the carrier transition reduces to

$$H_\mathrm{car}^\mathrm{I}(t) = \frac{\hbar\Omega}{2}\left(\sigma_{eg}\mathrm{e}^{-\mathrm{i}(\delta t+\phi)} + \sigma_{ge}\mathrm{e}^{+\mathrm{i}(\delta t+\phi)}\right). \tag{3.9}$$

It induces flops exclusively between the two spin states, called *Rabi oscillations*, which are studied in the next section.

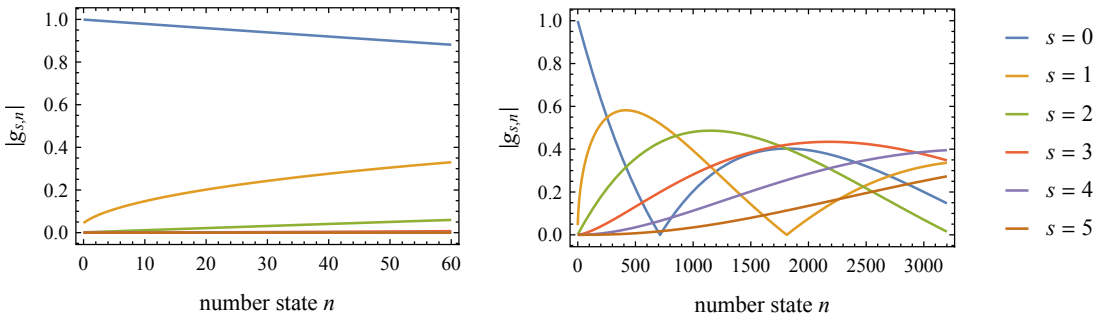

Figure 3.3: Franck-Condon coefficients $|g_{s,n}(\eta)| = \Omega_{s,n}/\Omega$ from Equation (3.8) as functions of Fock-state number n for $\eta = 0.045$. For low n, the coefficient for the carrier decreases linearly while the one for the first blue sideband increases with $\sqrt{n+1}$. Higher sidebands become increasingly significant for higher n.

3.3. Rabi oscillations

When a two-level system is driven by an oscillating field, it is cyclically excited and de-excited, a process called *Rabi oscillations*. This can for example be observed by driving the carrier transition of a trapped ion in the Lamb-Dicke regime, described by Equation (3.9). In order to make the Hamiltonian time independent, I start from the corresponding Schrödinger-picture Hamiltonian (with shifted zero-point energy for convenience)

$$H(t) = -\hbar\omega_{\mathrm{a}}\sigma_{gg} + \frac{\hbar\Omega}{2}\left(\sigma_{eg}\mathrm{e}^{-\mathrm{i}(\omega_{\mathrm{l}}t+\phi)} + \sigma_{ge}\mathrm{e}^{+\mathrm{i}(\omega_{\mathrm{l}}t+\phi)}\right)$$

Transforming to the rotating frame of the laser according to Equation (A.5) with the unitary matrix $T(t) = \sigma_{ee} + \sigma_{gg}\mathrm{e}^{-\mathrm{i}\omega_{\mathrm{l}}t}$ yields the time-independent Hamiltonian

$$H^{\mathrm{T}} = \hbar\delta\,\sigma_{gg} + \frac{\hbar\Omega}{2}\left(\sigma_{eg}\mathrm{e}^{-\mathrm{i}\phi} + \sigma_{ge}\mathrm{e}^{\mathrm{i}\phi}\right). \tag{3.10}$$

The corresponding time-evolution operator can be found analytically and is given by

$$U^{\mathrm{T}}(t) = \mathrm{e}^{-\mathrm{i}\delta t/2}\begin{pmatrix} \cos\left(\frac{\Omega_\delta t}{2}\right) + \frac{\mathrm{i}\delta}{\Omega_\delta}\sin\left(\frac{\Omega_\delta t}{2}\right) & -\frac{\mathrm{i}\Omega}{\Omega_\delta}\sin\left(\frac{\Omega_\delta t}{2}\right)\mathrm{e}^{-\mathrm{i}\phi} \\ -\frac{\mathrm{i}\Omega}{\Omega_\delta}\sin\left(\frac{\Omega_\delta t}{2}\right)\mathrm{e}^{\mathrm{i}\phi} & \cos\left(\frac{\Omega_\delta t}{2}\right) - \frac{\mathrm{i}\delta}{\Omega_\delta}\sin\left(\frac{\Omega_\delta t}{2}\right) \end{pmatrix} \tag{3.11}$$

with the effective Rabi frequency $\Omega_\delta = \left(\Omega^2 + \delta^2\right)^{1/2}$. If the qubit is initially in one of the basis states, the interaction with the laser makes the populations ρ_{ee} and ρ_{gg} oscillate at Ω_δ with a peak-to-peak amplitude $(\Omega/\Omega_\delta)^2$. Larger detuning leads to faster oscillations with smaller amplitude.

The dynamics of the driven pseudo-spin become particularly illustrative on the *Bloch sphere*. Like any 2×2-matrix, the density matrix of a spin-1/2 system can be decomposed

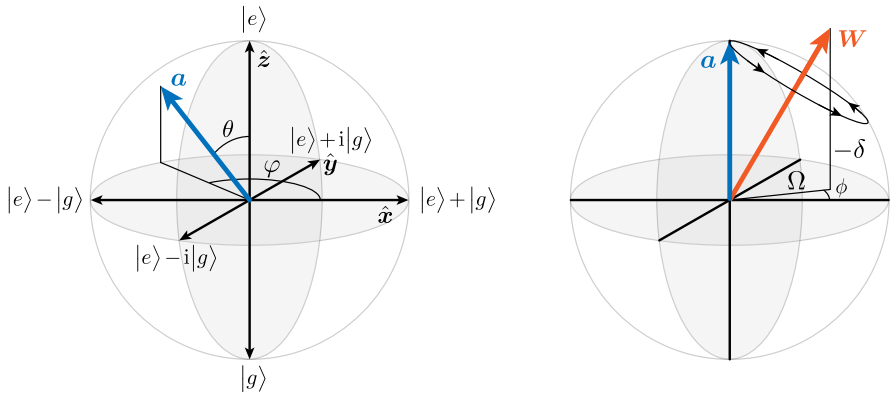

Figure 3.4: (left) The Bloch sphere with eigenstates of σ_z at the poles and equal superpositions of them on the equator. The Bloch vector of a pure state points onto the surface and is characterized by polar angles θ and φ. (right) The Rabi oscillations due to the Hamiltonian in Equation (3.10) can be pictured as rotations around the vector $\boldsymbol{W} = (\Omega\cos\phi, \Omega\sin\phi, -\delta)$.

into a linear combination of the identity and the three Pauli matrices (Equations (F.7)),

$$\rho = \frac{1}{2}\left(\mathbb{1} + \boldsymbol{a}\cdot\boldsymbol{\sigma}\right),$$

where the constraint of unity trace leaves only three degrees of freedom. The vector

$$\boldsymbol{a} = \langle\boldsymbol{\sigma}\rangle = \mathrm{Tr}[\rho\boldsymbol{\sigma}] = \Big(\rho_{eg} + \rho_{ge}, \mathrm{i}(\rho_{eg} - \rho_{ge}), \rho_{ee} - \rho_{gg}\Big)$$

is considered the *Bloch vector* and is pictured to extend from the center of a unit sphere to its inside volume or surface (Figure 3.4). The radius $|\boldsymbol{a}|$ is a measure of the purity of a state; the state is pure if $|\boldsymbol{a}| = 1$, and totally mixed if $|\boldsymbol{a}| = 0$, see Appendix B.

The two pure spin states that are aligned and anti-aligned with an arbitrary Bloch vector $\boldsymbol{a} = (\sin\theta\,\cos\varphi, \sin\theta\,\sin\varphi, \cos\theta)$ are the positive and negative eigenstates of $\boldsymbol{a}\cdot\boldsymbol{\sigma}$ given by

$$|\boldsymbol{a}_+\rangle = \cos\tfrac{\theta}{2}\,|e\rangle + \sin\tfrac{\theta}{2}\,e^{+\mathrm{i}\varphi}\,|g\rangle, \qquad |\boldsymbol{a}_-\rangle = -\sin\tfrac{\theta}{2}\,e^{-\mathrm{i}\varphi}\,|e\rangle + \cos\tfrac{\theta}{2}\,|g\rangle. \tag{3.12}$$

The evolution of the density matrix under the influence of the Hamiltonian in Equation (3.10) is given by the von Neumann Equation (B.1) and reduces to

$$\dot{\boldsymbol{a}}\cdot\boldsymbol{\sigma} = \frac{1}{\mathrm{i}\hbar}\left[H^{\mathrm{T}}, \rho\right] = (\boldsymbol{W}\times\boldsymbol{a})\cdot\boldsymbol{\sigma}.$$

The Bloch vector therefore rotates around the vector $\boldsymbol{W} = (\Omega\cos\phi, \Omega\sin\phi, -\delta)$ with magnitude $W = \Omega_\delta$ (Figure 3.4). This allows for simple visualization of the dynamics, taking all relevant parameters into account.

Full spin-flip operations require resonant driving, i.e. $\delta = 0$. In this case, the evolution operator in Equation (3.11) simplifies to a rotation by $\theta = \Omega t$ around an axis in the

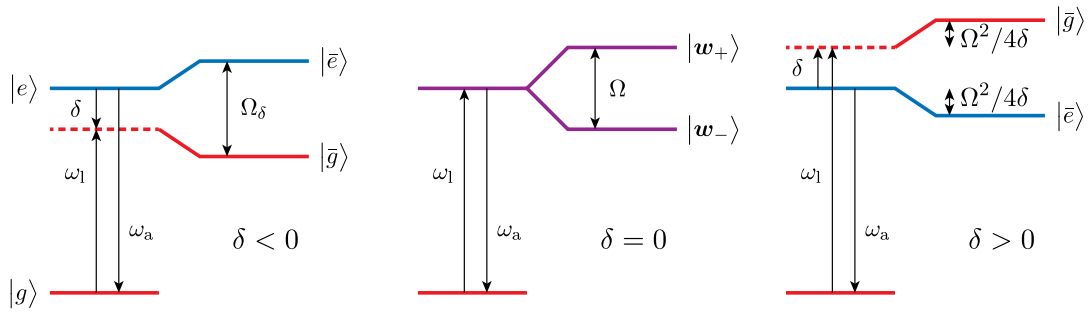

Figure 3.5: Energy diagrams for a driven two-level system for different laser detunings (energies given in units of $\hbar$). The bare energy levels (solid lines on left-hand sides) are shifted due to the interaction with the laser (perturbed dressed states on the right-hand sides). For large detunings, $|\delta| \gg \Omega$, the dressed states approach the original states but with energy levels shifted by the AC Stark shifts $\pm\hbar\Omega^2/4\delta$.

x, y-plane fixed by ϕ, which is described by

$$R(\theta, \phi) = \begin{pmatrix} \cos(\theta/2) & -\mathrm{i}\sin(\theta/2)\,\mathrm{e}^{-\mathrm{i}\phi} \\ -\mathrm{i}\sin(\theta/2)\,\mathrm{e}^{\mathrm{i}\phi} & \cos(\theta/2) \end{pmatrix}. \tag{3.13}$$

Starting at one of the poles, a "π-pulse" over a duration $t = \pi/\Omega$ flips the spin entirely, and a "$\pi/2$-pulse" for $t = \pi/(2\Omega)$ rotates it onto the equator.

Note that the two eigenstates of $\boldsymbol{w} \cdot \boldsymbol{\sigma}$ with $\boldsymbol{w} = \boldsymbol{W}/W$, given by Equations (3.12) for $\cos\theta = -\delta/\Omega_\delta$, $\sin\theta = \Omega/\Omega_\delta$ and $\varphi = \phi$, are unaffected by the interaction. They are the eigenstates of the Hamiltonian in Equation (3.10) with eigenvalues

$$E_\pm = \frac{\hbar\delta}{2} \pm \frac{\hbar\Omega_\delta}{2} \xrightarrow{|\delta|\gg\Omega} \frac{\hbar\delta}{2} \pm \frac{\hbar|\delta|}{2} \pm \frac{\hbar\Omega^2}{4|\delta|}, \tag{3.14}$$

and are often called *dressed states*. For zero detuning, the eigenlevels are split by $\hbar\Omega$. For large detunings, the eigenstates approximate the unperturbed dressed states ("atom + photons"), $|\bar{g}\rangle$ and $|\bar{e}\rangle$, and the corresponding eigenenergies

$$E_{\bar{g}}^{|\delta|\gg\Omega} = \hbar\delta + \frac{\hbar\Omega^2}{4\delta}, \qquad E_{\bar{e}}^{|\delta|\gg\Omega} = -\frac{\hbar\Omega^2}{4\delta},$$

show energy shifts known as *AC Stark shifts* (Figure 3.5).

3.4. Optical Bloch equations

In the previous two sections, I have only treated the coherent part of laser–ion interactions by considering the ion as a closed system. This is a good approximation when dissipative effects can be neglected. In order to account for dissipative dynamics due to spontaneous emission of photons from excited states, the evolution of the density matrix of the ion as

an open system (Section B.3) can be described by the master equation in Lindblad form (writing ρ instead of ρ_S for simplicity)

$$\partial_t \rho = \frac{1}{\mathrm{i}\hbar}\,[H,\rho] + \sum_k \gamma_k \Big(L_k \rho L_k^\dagger - \frac{1}{2}\, L_k^\dagger L_k \rho - \frac{1}{2}\, \rho L_k^\dagger L_k \Big).$$

The corresponding coupled differential equations for the components of the density matrix are called *optical Bloch equations*.

3.4.1. The two-level system

Suppose the two-level system from Section 3.3 with the Hamiltonian in Equation (3.10) couples to the environment in the form of all possible vacuum modes of the light field. Then the excited state with lifetime τ decays at a rate $\Gamma = 1/\tau$ (measured in radians per second) by spontaneously emitting a photon. In this case, there is only one Lindblad operator, namely $L_1 = \sqrt{\Gamma}\sigma_{ge}$, see for example ref. [Bre02, p. 148]. The optical Bloch equations then read

$$\begin{aligned}
\partial_t \rho_{ee} &= -\partial_t \rho_{gg} = -\Gamma \rho_{ee} + \frac{\mathrm{i}\Omega}{2}\Big(\rho_{eg} - \rho_{ge}\Big), \\
\partial_t \rho_{eg} &= \partial_t \rho_{ge}^* = -\mathrm{i}\Big(\frac{\Gamma}{2} - \mathrm{i}\delta\Big)\rho_{eg} + \frac{\mathrm{i}\Omega}{2}\Big(\rho_{eg} - \rho_{ge}\Big).
\end{aligned}$$

Due to dissipation they have a steady-state solution with $\partial_t \rho = 0$, which can analytically be found by replacing one of the first two (linearly dependent) equations by the normalization condition $\rho_{ee} + \rho_{gg} = 1$. Usually one is most interested in the excited-state population

$$\rho_{ee} = \frac{\Omega^2}{\Gamma^2 + 2\Omega^2 + 4\delta^2} = \frac{1}{2}\frac{S}{1+S} = \frac{1}{2}\frac{S_0}{1+S_0}\frac{(\Gamma_\mathrm{s}/2)^2}{\delta^2 + (\Gamma_\mathrm{s}/2)^2} \tag{3.16}$$

because $\Gamma\rho_{ee}$ is the rate at which the atom scatters photons from the laser. I have introduced the saturation parameter

$$S = \frac{\Omega^2/2}{\delta^2 + (\Gamma/2)^2} = S_0\,\frac{(\Gamma/2)^2}{\delta^2 + (\Gamma/2)^2} \qquad \text{with} \qquad S_0 = \frac{2\Omega^2}{\Gamma^2} = \frac{I}{I_\mathrm{s}},$$

where I is the laser intensity and I_s the transition's saturation intensity, and the power-broadened linewidth $\Gamma_\mathrm{s} = \Gamma\sqrt{1+S_0}$ (FWHM). So the result is an absorption profile in the form of a Lorentzian function of the detuning whose amplitude and width depend on the laser intensity. For $\delta = 0$, the steady-state population of the excited state is $1/4$ for $I = I_\mathrm{s}$ ("saturation") and approaches $1/2$ for $I \gg I_\mathrm{s}$.

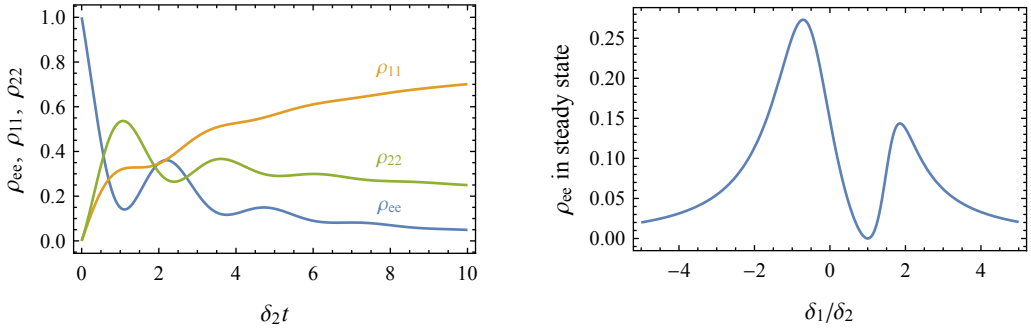

Figure 3.6: Solutions to the optical Bloch equations for the three-level system. (left) Time evolution of the diagonal elements of the density matrix for parameters $\delta_1 = \delta_2 = \Omega_1 = \Omega_2/2 = 2\Gamma_1 = 2\Gamma_2$. After an onset of coherent oscillations, the population is coherently trapped in the dark state given by Equation (3.17) and the excited-state population drops to zero. (right) Excitation spectrum as a function of laser detuning δ_1, all other parameters as before. The positions of the peaks depend on $\delta_2, \Omega_1, \Omega_2$.

3.4.2. The three-level Λ-system

One more level of complexity is added for a three-level Λ-system, consisting of an excited state and two ground states, $|g_1\rangle$ and $|g_2\rangle$. Two lasers with Rabi frequencies $\Omega_{1/2}$ and detunings $\delta_{1/2}$ couple them with $|e\rangle$, respectively. Example situations in our experiments are Doppler cooling and readout sequences (neglecting Zeeman sublevels; Sections 3.6.1 and 3.7), where the $S_{1/2} \leftrightarrow P_{1/2}$ and $D_{3/2} \leftrightarrow P_{1/2}$ transitions are driven, or EIT cooling (see Section 3.6.2), where two transitions in $S_{1/2} \leftrightarrow P_{1/2}$ are driven.

The Hamiltonian in the frame of the lasers reads (ignoring laser phases)

$$H^{\mathrm{T}} = \hbar\delta_1\,\sigma_{g_1g_1} + \hbar\delta_2\,\sigma_{g_2g_2} + \frac{\hbar\Omega_1}{2}\,(\sigma_{eg_1} + \sigma_{g_1e}) + \frac{\hbar\Omega_2}{2}\,(\sigma_{eg_2} + \sigma_{g_2e}).$$

The Lindblad operators for spontaneous emission are $L_1 = \sqrt{\Gamma_1}\sigma_{g_1e}$ and $L_2 = \sqrt{\Gamma_2}\sigma_{g_2e}$. The optical Bloch equations for this system can again be solved analytically for the steady state. Figure 3.6 shows the steady-state solution for ρ_{ee} and the time evolution of the diagonal density matrix elements for a given parameter set.

At $\delta_1 = \delta_2$, a *dark resonance* occurs where the population is coherently trapped in the dark state

$$|\Psi_{\mathrm{D}}\rangle = \left(\Omega_1^2 + \Omega_2^2\right)^{-1/2}\left(\Omega_2|g_1\rangle + \Omega_1|g_2\rangle\right), \tag{3.17}$$

which is an eigenstate of the Hamiltonian with eigenvalue $\hbar\delta_2$ [Mor03]. Since it is orthogonal to $|e\rangle$, the atom does not scatter any photons anymore.

Modeling the expected excitation spectrum for given experimental parameters helps understanding the ion's behavior and finding the right settings. While the detunings are simple to measure and the decay rates can be found in the literature, the Rabi frequencies

still need to be related to experimentally available parameters. I will do this in the next section.

3.5. Evaluation of Rabi frequencies

The Rabi frequencies defined in Equation (3.6) depend on the electric field amplitude and the matrix elements of the dipole and quadrupole moments. The first can be calculated from the average laser intensity $I = c\epsilon_0 E_0^2/2$ at the ion's position. If the ion is placed at the center of the waist of a Gaussian laser beam, the electric field amplitude follows from Equation (D.2), and only depends on the total power P in the beam and the waist spot size w_0,

$$E_0 = \sqrt{\frac{4P}{\pi c \epsilon_0 w_0^2}}.$$

The matrix elements are not directly accessible but they can be linked to the decay rate

$$\Gamma_{e\bar{g}} = \sum_{m_g} \Gamma_{eg}$$

from the excited state to all Zeeman sub-levels of the ground-state manifold. Those can be found experimentally and are tabulated in the literature (Table 3.1). As a precursor, I start by expressing the components r_i of the the position vector $\boldsymbol{r}$ in terms of *regular solid harmonics*,

$$R_l^m(\boldsymbol{r}) = \sqrt{\frac{4\pi}{2l+1}}\, r^l\, Y_l^m(\theta, \varphi),$$

which are rescaled spherical harmonics that satisfy Laplace's equation in spherical polar coordinates. Their matrix elements with respect to angular-momentum states can be directly evaluated. From the explicit form of the spherical harmonics Y_1^m follows

$$R_1^{+1} = -\frac{1}{\sqrt{2}}\,(x + \mathrm{i}y), \qquad R_1^0 = z, \qquad R_1^{-1} = \frac{1}{\sqrt{2}}\,(x - \mathrm{i}y)$$

and hence (summations are always over the allowed range of the summation index)

$$r_i = \sum_m c_i^{(m)} R_1^m \qquad \text{with} \qquad \boldsymbol{c}^{(1)} = \frac{1}{\sqrt{2}}\begin{pmatrix} -1 \\ \mathrm{i} \\ 0 \end{pmatrix},\ \boldsymbol{c}^{(0)} = \begin{pmatrix} 0 \\ 0 \\ 1 \end{pmatrix},\ \boldsymbol{c}^{(-1)} = \frac{1}{\sqrt{2}}\begin{pmatrix} 1 \\ \mathrm{i} \\ 0 \end{pmatrix}. \quad (3.18)$$

These normalized spherical-basis vectors have the properties

$$\boldsymbol{c}^{(m)} = (-1)^m \boldsymbol{c}^{(-m)*}, \qquad \boldsymbol{c}^{(m)} \cdot \boldsymbol{c}^{(m')*} = \delta_{mm'}, \qquad \sum_m c_i^{(m)} c_j^{(m)*} = \delta_{ij}.$$

Using these, the product formula for spherical harmonics in Equation (F.11), the properties of the Wigner 3-j symbols next to Equation (F.9), and $R_0^0 = 1$, one can find

$$r_i r_j = \frac{1}{3} r^2 \delta_{ij} + \sum_m c_{ij}^{(m)} R_2^m, \qquad c_{ij}^{(m)} = (-1)^m \sqrt{\frac{10}{3}} \sum_{q,q'} c_i^{(q)} c_i^{(q')} \begin{pmatrix} 1 & 1 & 2 \\ q & q' & -m \end{pmatrix}. \quad (3.19)$$

These coefficient matrices are easily calculated but can also be found in the appendix of [Jam98]. With these tools, the Rabi frequencies can be evaluated, first for the dipole moment and then for the quadrupole moment.

3.5.1. Rabi frequency for dipole transitions

Spontaneous emission of a photon via a dipole-allowed transition due to coupling to all empty light modes of the free-space environment happens at a rate [Lou01, Section 4.10; Cow81, Section 14-3; Bre02, Section 3.4.1][2]

$$\Gamma_{eg}^{\mathrm{DP}} = \frac{e^2 \omega_{\mathrm{a}}^3}{3\pi\epsilon_0 \hbar c^3} \left|\langle e \,|\, \boldsymbol{r} \,|\, g \rangle\right|^2 = \frac{4c\alpha k^3}{3} \sum_m \left|\langle e \,|\, R_1^m \,|\, g \rangle\right|^2,$$

where $\alpha = e^2/(4\pi\epsilon_0\hbar c)$ is the fine-structure constant and Equation (3.18) was used. With the help of the Wigner-Eckart theorem in Equation (F.12), the matrix elements in the last term can be split as

$$\langle n_e, j_e, m_e \,|\, R_1^m \,|\, n_g, j_g, m_g \rangle = (-1)^{j_e - m_e} \begin{pmatrix} j_e & 1 & j_g \\ -m_e & m & m_g \end{pmatrix} \langle n_e, j_e \,||\, R_1 \,||\, n_g, j_g \rangle$$

into parts that only depend on angular momentum and the *reduced matrix element*, which is real[3] and independent of the magnetic quantum number. The sum rule for Wigner 3-j symbols in Equation (F.10) then allows us to write

$$\Gamma_{e\bar{g}}^{\mathrm{DP}} = \sum_{m_g} \Gamma_{eg}^{\mathrm{DP}} = \frac{4c\alpha k^3}{3(2j_e+1)} |\langle e \,||\, R_1 \,||\, g \rangle|^2,$$

[2] Note that the formulas in [Lou01; Cow81] are given in Gaussian units with $\alpha = e/(\hbar c)$.

[3] The reduced matrix element boils down to a product of a Clebsch-Gordan coefficent and the integral of R_1 over the radial parts of the atomic wave functions [Coh99b, p. 252].

with which the modulus of the reduced matrix element can be calculated from the tabulated decay rate $\Gamma^{\mathrm{DP}}_{e\bar{g}}$. To calculate the Rabi frequency in Equation (3.6),

$$\Omega^{\mathrm{DP}} = \frac{eE_0}{\hbar} \left|\langle e \,|\, \boldsymbol{r}\cdot\boldsymbol{\epsilon} \,|\, g\rangle\right| = \frac{eE_0}{\hbar} \left|\sum_m \langle e \,|\, R_1^m \,|\, g\rangle \, \boldsymbol{c}^{(m)}\cdot\boldsymbol{\epsilon}\right|,$$

one can apply the Wigner-Eckart theorem again and insert the reduced matrix element from above, resulting in

$$\Omega^{\mathrm{DP}} = \frac{eE_0}{\hbar}\left(\frac{3(2j_e+1)\Gamma^{\mathrm{DP}}_{e\bar{g}}}{4c\alpha k^3}\right)^{1/2} \left|\sum_m \begin{pmatrix} j_e & 1 & j_g \\ -m_e & m & m_g \end{pmatrix} \boldsymbol{c}^{(m)}\cdot\boldsymbol{\epsilon}\right|.$$

The last factor gives the selection rule $\Delta m = m_e - m_g = m$ and determines the required laser polarization for driving a certain transition (Table 3.3).

Table 3.3: Laser polarization for dipole-allowed transitions.

Δm	Polarization
0	π (linear), parallel to quantization axis
± 1	$\sigma^{\pm}$ (circular), perpendicular to quantization axis

3.5.2. Rabi frequency for quadrupole transitions

All derivations for the quadrupole transition can be carried out in full analogy to the preceding section with only slightly different coefficients. I start from the decay rate of a quadrupole-allowed transition [Cow81, Section 15-2],

$$\Gamma^{\mathrm{QP}}_{e\bar{g}} = \frac{c\alpha k^5}{15} \sum_{m_g,m} \left|\langle e \,|\, R_2^m \,|\, g\rangle\right|^2 = \frac{c\alpha k^5}{15(2j_e+1)} \left|\langle e \,||\, R_2 \,||\, g\rangle\right|^2.$$

Inserting Equation (3.19) into the Rabi frequency in Equation (3.6) and proceeding as before, one finds

$$\Omega^{\mathrm{QP}} = \frac{eE_0}{\hbar}\left(\frac{15(2j_e+1)\Gamma^{\mathrm{QP}}_{e\bar{g}}}{4c\alpha k^3}\right)^{1/2} \left|\sum_m \begin{pmatrix} j_e & 2 & j_g \\ -m_e & m & m_g \end{pmatrix} \sum_{i,j} c_{ij}^{(m)} \kappa_i \epsilon_j\right|. \tag{3.20}$$

Note that the diagonal terms in the quadrupole moments in Equation (3.19) vanished because $\boldsymbol{\kappa}$ and $\boldsymbol{\epsilon}$ are orthogonal. If the laser is linearly polarized, the polarization and wave vector can be parametrized by the angle ϕ between the laser beam and the magnetic field $\boldsymbol{B} = (0, 0, B)$, and the angle γ between the polarization vector and the projection of $\boldsymbol{B}$ into the plane of incidence. Due to cylindrical symmetry, one can fix $\boldsymbol{\kappa} = (\sin\phi, 0, \cos\phi)$ and obtain $\epsilon = (-\cos\gamma\cos\phi, \sin\gamma, \cos\gamma\sin\phi)$. The polarization- and geometry-dependent part

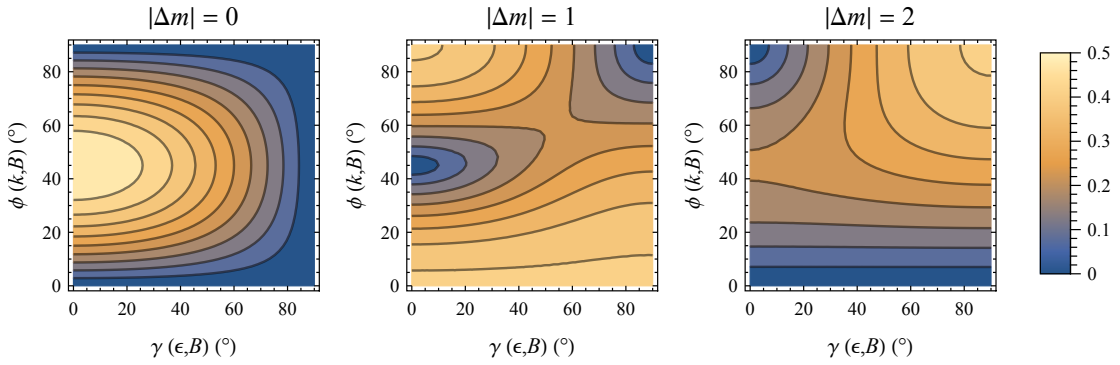

Figure 3.7: Geometry-dependent coupling strength $g^{(m)}(\gamma, \phi)$ of a quadrupole transition for $|\Delta m| = 0, 1, 2$, where ϕ is the angle between laser beam and magnetic field, and γ the angle between linear polarization and projection of the magnetic field into the plane of incidence.

in Equation (3.20) is then contained in the quadratic form [Roo00a, p. 30]

$$g^{(m)}(\gamma, \phi) = \left| \sum_{i,j} c_{ij}^{(m)} \kappa_i \epsilon_j \right| = \begin{cases} \frac{1}{2} \left| \cos\gamma \sin(2\phi) \right| & m = 0 \\ \frac{1}{\sqrt{6}} \left| \cos\gamma \cos(2\phi) + \mathrm{i} \sin\gamma \cos\phi \right| & m = \pm 1 \\ \frac{1}{\sqrt{6}} \left| \frac{1}{2} \cos\gamma \sin(2\phi) + \mathrm{i} \sin\gamma \sin\phi \right| & m = \pm 2 \end{cases} .$$

One can utilize this dependency of the coupling strength on the geometry to suppress excitation of unwanted transitions in order to approximate a two-level atom. Three configurations are particularly useful: for $\phi = 90°, \gamma = 0°$ and for $\phi = 0°$ only $|\Delta m| = 1$ transitions can be driven; for $\phi = 90°, \gamma = 90°$ only $|\Delta m| = 2$ can be driven (Figure 3.7). Note that even for elliptical polarization, parametrized by α in $\epsilon = (-\cos\gamma\cos\phi, \mathrm{e}^{\mathrm{i}\alpha}\sin\gamma, \cos\gamma\sin\phi)$, the coupling strength in these cases, and indeed for all cases with $\gamma = 0°, 90°$, remains unaffected.

3.5.3. Choice of qubit

In principle, any Zeeman transition in $S_{1/2} \leftrightarrow D_{5/2}$ could be used for coherent manipulation of the ion's quantum state. Besides the geometric factor $g^{(m)}(\gamma, \phi)$, however, the sensitivity of the qubit transition to magnetic field fluctuations can be considered, which influences coherence times and overall coupling strength.

From the Zeeman shifts in Table 3.2 follow the frequency shifts of the spectral lines from the unperturbed resonance. The coupling strength is proportional to the Wigner 3-j symbol in Equation (3.20). Both dependencies are depicted in Figure 3.8. Since our experiments do not require maximum coherence times of the internal atomic state and a higher Rabi frequency is desirable, we have chosen the

$$|S_{1/2}(m_J = -1/2)\rangle \leftrightarrow |D_{5/2}(m_J = -5/2)\rangle$$

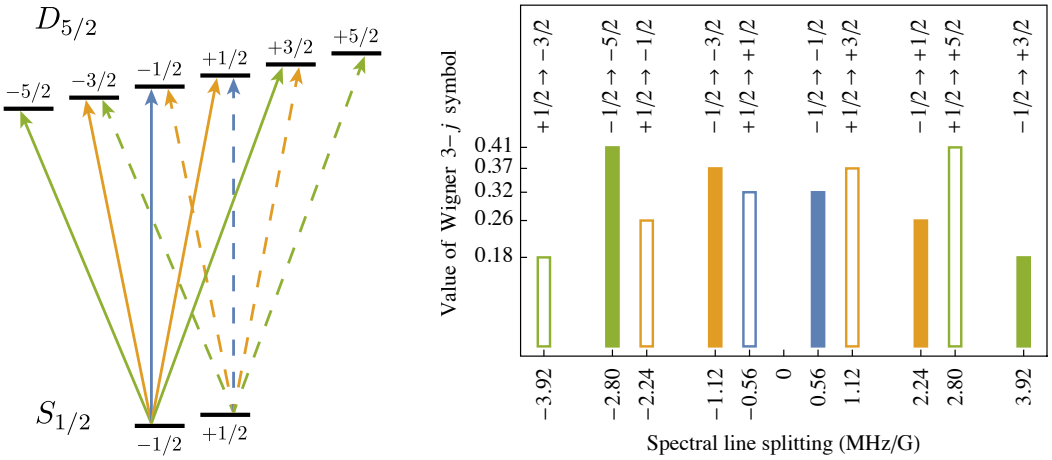

Figure 3.8: Spectral lines on the $S_{1/2} \leftrightarrow D_{5/2}$ quadrupole transition in a magnetic field (blue/orange/green arrows and bars for $|\Delta m| = 0/1/2$). The frequencies are Zeeman shifted (Table 3.2) by the given values in MHz/G. The Rabi frequencies of the lines are proportional to the Wigner 3-j symbol in Equation (3.20). The full/empty bars correspond to the solid/dashed arrows on the left.

transition for coherent manipulations. From a quantum information perspective, these states are also called *qubit states*. I henceforth denote them as $|S\rangle$ and $|D\rangle$.

3.6. Laser cooling

Laser cooling of atoms and ions has become a routine tool in the past three decades and provides the basis for many modern experiments in the fields of atomic physics and quantum optics. It was first experimentally observed in 1978 by Wineland, Drullinger, and Walls with trapped Mg^+ ions [Win78]. In 1989, cooling to the motional ground state of a single trapped ion was achieved for the first time [Die89].

All types of laser cooling rely on light pressure, that is momentum transfer from photons onto the ion. Consider the laser–atom interaction Hamiltonian in Equation (3.3). After applying the RWA and neglecting the laser phase, it reads

$$H_1(t) = \frac{\hbar\Omega}{2}\,\sigma_{eg}\,\mathrm{e}^{-\mathrm{i}\omega_1 t}\,\mathrm{e}^{\mathrm{i}\boldsymbol{k}\cdot\boldsymbol{R}} + \text{H.c.}. \tag{3.21}$$

The exponential $\mathrm{e}^{\mathrm{i}\boldsymbol{k}\cdot\boldsymbol{R}}$ causes a shift in a free atom's momentum eigenfunction by $\hbar\boldsymbol{k}$ upon absorption of a photon from the laser and vice versa. If an atom at rest is continuously driven on a cycling transition, that is the excited state always decays back to the ground state, with an excitation profile given by Equation (3.16), it experiences such momentum kicks at a rate $\Gamma\rho_{ee}$. Since they are all in the direction of the laser beam and the momentum kicks due to spontaneous emission are randomly distributed, the atom experiences a net

force

$$\boldsymbol{F}(\delta) = \Gamma\hbar\boldsymbol{k}\,\frac{\Omega^2}{\Gamma^2 + 2\Omega^2 + 4\delta^2},$$

called *radiation pressure force*. If the atom, on the other hand, moves at a velocity $\boldsymbol{v}$, the laser frequency is shifted by $\delta_\mathrm{D} = -\boldsymbol{k}\cdot\boldsymbol{v}$ in the rest frame of the atom due to the Doppler effect. For a red-detuned laser (that is below resonance, $\delta < 0$), the atom preferably scatters photons moving towards the laser and is hence decelerated.

The same picture applies to a trapped ion in the *weak confinement regime* where $\omega_\mathrm{m} \ll \Gamma$ and therefore photons are scattered on shorter timescales than the ion changes its velocity due to the oscillation in the trap [Ste86, p. 722]. Repeated momentum transfers when the ion moves against the direction of a red-detuned laser damp the oscillation amplitude and cool the ion in the sense that the mean phonon number is reduced.

We apply two stages of laser cooling in our experiments. Doppler cooling reduces the ion's kinetic energy to the quantum regime, and *Electromagnetically Induced Transparency* (EIT) cooling cools to near the motional ground state.

3.6.1. Doppler cooling

A possible Doppler cooling transition in $^{40}\mathrm{Ca}^+$ is $S_{1/2} \leftrightarrow P_{1/2}$ as it decays fast (Table 3.1) and is almost closed. It is driven by the laser at 397 nm, to which the detuning δ and real Rabi frequency Ω correspond in this section. Population transferred to the $D_{3/2}$-state is repumped with the laser at 866 nm. Most photons are, however, scattered on the 397 nm transitions because of the splitting ratio of $(P_{1/2} \leftrightarrow S_{1/2})/(P_{1/2} \leftrightarrow D_{3/2}) = 12.2 : 1$ for spontaneous decay from $P_{1/2}$.

Disregarding Zeeman splittings, the excitation spectrum qualitatively looks like the one in Figure 3.6. I approximate the left-hand shoulder of the left-hand peak, which is the relevant region for Doppler cooling, by the two-level low-saturation excitation probability

$$W(\delta) = W_0\left(\frac{\Omega}{\Gamma}\right)^2 \frac{(\Gamma_W/2)^2}{\delta^2 + (\Gamma_W/2)^2},$$

similar to Equation (3.16) with heuristic approximation parameters W_0 and Γ_W for peak height and FWHM, respectively (Figure 3.9).

Since the weak binding limit applies for a typical axial frequency $\omega_\mathrm{m} \approx 2\,\mathrm{MHz}$, Doppler cooling can be understood in the framework of an oscillating particle that is radiatively decelerated when moving towards the red-detuned laser. For estimates of optimal cooling parameters and final vibrational excitation, it is, however, instructive to apply the framework from Section 3.2. In terms of Fock states, the Hamiltonian in Equation (3.21) can be written

$$H_1(t) = \frac{\hbar\Omega}{2}\,\sigma_{eg}\,\mathrm{e}^{-\mathrm{i}\omega_\mathrm{l} t} \sum_{s=-\infty}^{\infty}\sum_{n=I}^{\infty} |n+s\rangle\langle n|\, g_{s,n}(\eta) + \mathrm{H.c.}.$$

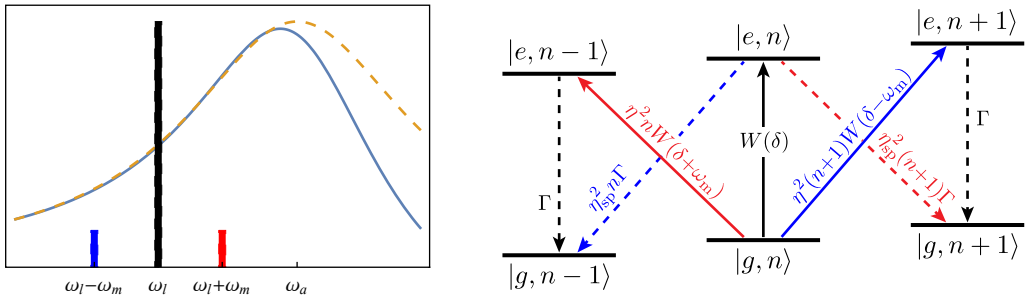

Figure 3.9: (left) The Lorentzian (orange, dashed line) is the approximated atomic resonance for the example excitation profile (blue, solid line) from Figure 3.6. It has a FWHM Γ_W and its peak position defines ω_a for the derivation in the text. The laser spectrum (vertical bars) is displayed in the reference frame of the ion, with a laser detuning $\delta = \Gamma_W/2$. The red and blue sidebands are at frequencies $\omega_\mathrm{l} + \omega_\mathrm{m}$ and $\omega_\mathrm{l} - \omega_\mathrm{m}$, and have an absorption rate proportional to their Franck-Condon factors. (right) Cooling and heating transitions starting from $|g, n\rangle$ with relative probabilities for absorption (solid lines) and transition rates for spontaneous emission (dashed lines) processes. Adapted from [Esc03].

The Franck-Condon factor (evaluated in Equation (3.4)) gives the overlap between $|n + s\rangle$ and the momentum-shifted $|n\rangle$, and determines the coupling strength. Note that one cannot limit the treatment here to a certain sideband as in Equation (3.7) because the sidebands are not resolved in the weak binding regime. At low vibrational excitation (approaching the Lamb-Dicke regime) near the end of cooling, however, the couplings are dominated by the carrier and first sidebands[4] (Figure 3.3). In the interaction picture, the coupling Hamiltonian reads to lowest order in η

$$H_1^\mathrm{I}(t) = \frac{\hbar\Omega}{2}\,\sigma_{eg} \sum_{s=-\infty}^{\infty} \sum_{n=I}^{\infty} (\mathrm{i}\eta\sqrt{n_>})^{|s|}\, |n+s\rangle\langle n|\, \mathrm{e}^{-\mathrm{i}(\delta - s\omega_\mathrm{m})t} + \mathrm{H.c.}.$$

Solving the full master equation for the density matrix is difficult because of the high dimensionality of the Hilbert space. But since the processes are dominated by dissipation ($\Gamma \sim \Omega \gg \omega_\mathrm{l}$), it suffices to solve rate equations for its diagonal elements involving $|g\rangle$. The spontaneous Raman transitions coupling the state $|g, n\rangle$ to $|g, n + 1\rangle$ and $|g, n - 1\rangle$ happen at rates $(n + 1)A_+$ and nA_-, respectively (Figure 3.9), where the rate coefficients are given by [Esc03]

$$A_\pm = \Gamma\left[\eta^2 W(\delta \mp \omega_\mathrm{m}) + \eta_\mathrm{sp}^2 W(\delta)\right], \tag{3.22}$$

and the Lamb-Dicke parameter for spontaneous emission, $\eta_\mathrm{sp}^2 = \alpha(kx_0)^2$, includes the factor

[4] The overlap of a momentum-shifted low number state $|n\rangle$ with $|n \pm s\rangle$ rapidly decreases with increasing s. A pictorial interpretation of this is that transitions between number states are only likely when peaks of the probability distributions in momentum space, $\varphi_n(p)$, which look exactly like those in position representation, have maximum overlap. For low n, this is the case for small s [Ste86, p. 723f].

α describing the average recoil component on the motional axis.[5] The transition rates lead to changing number state probabilities given by a *Pauli master equation*,

$$\dot{P}(n) = nA_+P(n-1) + (n+1)A_-P(n+1) - \Big[nA_- + (n+1)A_+\Big]\,P(n). \quad (3.23)$$

Consequently, the average vibrational number evolves as

$$\dot{\langle n\rangle} = -(A_- - A_+)\langle n\rangle + A_+,$$

and cooling occurs when $A_- < A_+$, that is when the red sideband is favored over the blue sideband, which is the case for a negative detuning δ (Figure 3.9). Then the mean $\langle n\rangle$ exponentially approaches the steady-state excitation number $\bar{n} = A_+/(A_- - A_+)$ at a rate $A_- - A_+$. Maximizing A_-/A_+ in the weak confinement regime, a minimal vibrational excitation of

$$\bar{n}_{\min} = \frac{\Gamma_W}{\omega_\mathrm{m}}\frac{\eta^2+\eta_\mathrm{sp}^2}{4\eta^2} = \frac{\Gamma_W}{\omega_\mathrm{m}}\frac{\cos^2\vartheta+\alpha}{4\cos^2\vartheta} \approx \frac{\Gamma_W}{2\omega_\mathrm{m}} \qquad \text{for} \quad \delta = -\frac{\Gamma_W}{2},\ \vartheta = \frac{\pi}{4} \quad (3.24)$$

is achieved, where ϑ is the angle between the laser wave vector and the oscillation axis as in Equation (3.2). This cooling occurs because motion-reducing transitions are favored over motion-adding ones. But the still relatively high scattering rates on carrier and blue sideband compared with the red sideband prevent Doppler cooling beyond this limit. Higher cooling rates can be realized by higher laser intensities, leading to a larger absolute difference between the red and blue sideband absorption. But for Doppler cooling, this translates into a broadened linewidth Γ_W at the expense of higher final vibrational excitation.

Note that the cooling laser's wave vector must have sufficient overlap with all oscillator modes that need to be cooled. In our experiments, the 397 nm laser makes an angle of 45° with the trap axis. For the axial oscillator mode at ≈ 2 MHz, the minimum excitation is hence expected to be $\langle n\rangle \approx 5$, which could be experimentally verified (Section 5.6).

3.6.2. EIT cooling

Ground-state cooling of the ion can be achieved using EIT to tailor the absorption profile such that carrier excitations are suppressed and blue sideband excitations reduced by coherent population trapping (Section 3.4.2). The method requires a three-level Λ-system, which we approximately implement in a similar way to Roos et al. in ref. [Roo00b] on the $P_{1/2} \leftrightarrow S_{1/2}$ transition by applying two laser beams at 397 nm with π- and σ^--polarization (Figure 3.10). I neglect in this theoretical treatment the presence of the $P_{1/2}(m_J = 1/2)$-state and the effect of repumping on the $P_{1/2} \leftrightarrow D_{3/2}$ transition.

The blue-detuned, strong, σ^--polarized laser beam dresses the atom. The absorption

[5] The factor α depends on the orientation of the emitting dipole pattern with respect to the oscillation axis (2/5 for parallel alignment, see for example [Ste86, p. 711]), but is often approximated by 1/3 for isotropic spontaneous emission.

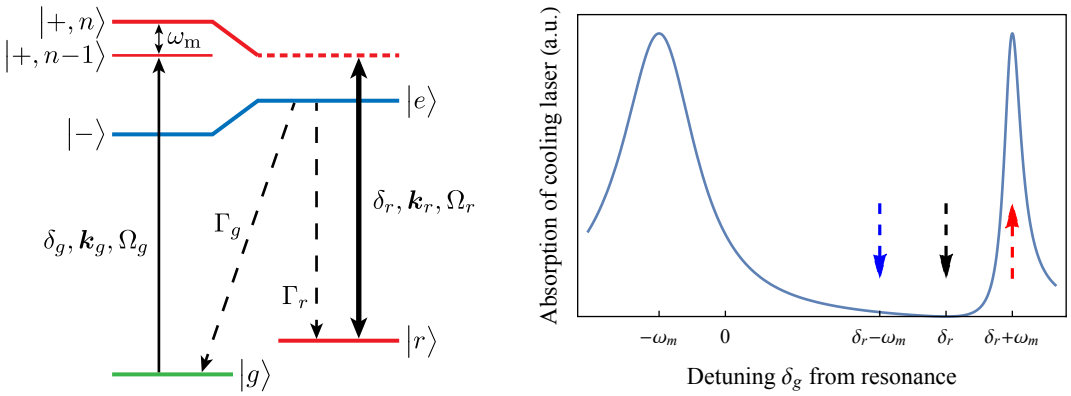

Figure 3.10: (left) Three-level Λ-system for EIT cooling consisting of the states $|g\rangle = |S_{1/2}(m_J = -1/2)\rangle$, $|r\rangle = |S_{1/2}(m_J = +1/2)\rangle$ and $|e\rangle = |P_{1/2}(m_J = -1/2)\rangle$. The strong, σ^--polarized laser beam with detuning $\delta_r > 0$ from the $|r\rangle \leftrightarrow |e\rangle$ resonance, wave vector $\boldsymbol{k}_r$, and Rabi frequency Ω_r induces the dressed states $|+\rangle$ and $|-\rangle$ with energy eigenvalues given by Equation (3.14). The weaker, π-polarized laser beam with detuning δ_g from the $|g\rangle \leftrightarrow |e\rangle$ resonance experiences the absorption profile on the right-hand side. (right) When the detunings are equal, $\delta_g = \delta_r$, a dark resonance forms on the carrier transition. If the AC Stark shift is made equal to the ion's motional frequency, the weaker laser is resonant with the motion-reducing transition $|g,n\rangle \leftrightarrow |+,n-1\rangle$.

profile for the weaker, π-polarized laser beam can be calculated analytically from optical Bloch equations (Section 3.4.2) and simplified for $\Omega_g \ll \Omega_r$ to

$$W(\Delta) = \frac{3\Delta^2\Omega_g^2}{\Delta^2\Gamma^2 + 4(\Omega_r^2/4 - \Delta\delta_g)^2}$$

with $\Delta = \delta_g - \delta_r$, $\Gamma_g = \Gamma/3$ and $\Gamma_r = 2\Gamma/3$, where Γ is the decay rate on the $P_{1/2} \leftrightarrow S_{1/2}$ transition (Section 3.5.1). Absorption vanishes for $\Delta = 0$ and peaks at

$$\Delta_\pm = \frac{\pm\sqrt{\delta_r^2 + \Omega_r^2} - \delta_r}{2},$$

showing resonances with transitions to the dressed states at eigenenergies given by Equation (3.14). Experimentally setting $\Delta = 0$ and $\Delta_+ = \omega_\mathrm{m}$, the narrow bright resonance coincides with the red sideband, greatly enhancing absorption on the red sideband ($W(+\omega_\mathrm{m})$) over the blue sideband ($W(-\omega_\mathrm{m})$) and carrier ($W(0)$). The rate equation treatment from the preceding section then leads to a cooling limit of (cf. [Lei03a, p. 302])

$$\bar{n} = \frac{W(-\omega_\mathrm{m})}{W(+\omega_\mathrm{m}) - W(-\omega_\mathrm{m})} = \left(\frac{\Gamma}{4\delta_r}\right)^2.$$

In order to cool the ion well into the motional ground state, $\bar{n} \ll 1$, one chooses large detunings, $\delta_g = \delta_r \gg \Gamma$, and fulfills the condition $\omega_\mathrm{m} = (\sqrt{\delta_r^2 + \Omega_r^2} - \delta_r)/2$ by setting the appropriate laser power of the stronger beam.

Note that even though η from Equation (3.22) does not occur in the cooling limit, it is a necessary condition that $\eta \neq 0$. In the case of EIT cooling, motion-reducing events mainly consist of a stimulated Raman process bringing the atom from $|g\rangle$ to $|r\rangle$ (absorption of ω_g and stimulated emission of w_r photons) followed by a spontaneous Raman process bringing the atom back from $|r\rangle$ to $|g\rangle$ [Lou92, p. 590]. Therefore, the Lamb-Dicke parameter for cooling is $\eta = \Delta\boldsymbol{k} \cdot \boldsymbol{R}$ with $\Delta\boldsymbol{k} = \boldsymbol{k}_g - \boldsymbol{k}_r$, which must have a non-vanishing overlap with the motional mode to be cooled.

3.6.3. Final state after cooling

The time evolution of the motional-state populations during Doppler and EIT cooling is governed by the Pauli master equation in Equation (3.23). As a consequence, the motional quantum state at the end of a cooling process is a thermal state. In order to show this, assume that the system has reached the steady state in which the occupation probabilities $P(n)$ remain constant. Using mathematical induction starting with the immediate result $A_- P(1) = A_+ P(0)$, one can prove that

$$A_- P(n+1) = A_+ P(n) \qquad \forall n.$$

The normalized solution hence is

$$P(n) = \left(1 - \frac{A_+}{A_-}\right)\left(\frac{A_+}{A_-}\right)^n = \frac{1}{1+n_{\mathrm{th}}}\left(\frac{n_{\mathrm{th}}}{1+n_{\mathrm{th}}}\right)^n,$$

which is the number-state distribution of a thermal state with $n_{\mathrm{th}} = A_+/(A_- - A_+)$ already found in Section 2.3.4.

3.7. State analysis

Fluorescence photons at 397 nm from the nearly cycling transition $S_{1/2} \leftrightarrow P_{1/2}$ are detected with a CCD camera or photomultiplier tube (PMT) to verify the presence of single ions in the trap. When the ion is strongly excited on that transition, it emits tens of millions of photons per second, of which our imaging optics collect up to 0.7 % (Section 5.7), typically on the order of 10^5 cts/s. Accordingly, the ion can be detected within tens of microseconds. By scattering photons on the same transition, the ion's internal and external state can be analyzed, which is described in the following sections.

3.7.1. Spin-state analysis

The qubit states $|S\rangle$ and $|D\rangle$ (Section 3.5.3) can be discriminated by illuminating the ion with the detection laser at 397 nm. This projects the qubit state either to $|D\rangle$ or its orthogonal subspace because no fluorescence is observed when the ion is in the $|D\rangle$-state and, otherwise, photons are scattered on the $S_{1/2} \leftrightarrow P_{1/2}$ transition. Recording the number of detected

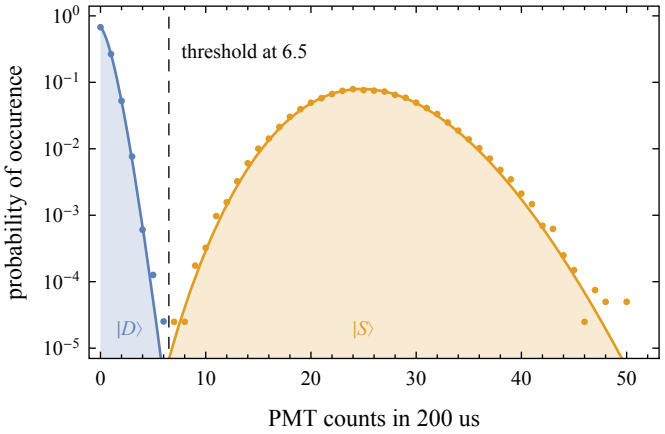

Figure 3.11: Photon count probabilities within a detection window of 200 µs for both qubit states from a total of 80 000 shots. Dots represent experimental data, lines fitted Poisson distributions with mean values of 0.4 and 25.4. Thresholding single-shot counts at 6.5 cts allows distinguishing between $|S\rangle$ and $|D\rangle$ at every projective measurement with an uncertainty below $1 : 10^{-5}$.

photons N times for a qubit state always prepared in the same way yields Poissonian photon count statistics for both the dark $|D\rangle$ and the bright $|S\rangle$-state (Figure 3.11). For sufficiently long detection times (200 to 500 µs in our case), these peaks can be well distinguished and the spin state identified for every single measurement, depending on whether the photon counts were above ($|S\rangle$) or below ($|D\rangle$) a certain threshold.

If the $|S\rangle$-state was found n out of N times, the $|S\rangle$-state population before the measurements is given by $P_S = n/N$. Without significant noise from other sources, the uncertainty of this value is governed by *quantum projection noise*,

$$\Delta P_S = \max\left\{\sqrt{\frac{P_S(1-P_S)}{N}}, \frac{1}{N+2}\right\},$$

where the first term derives from the variance of the binomial distribution and the second term is given by Laplace's rule of succession for N trials and 2 possible results ($|S\rangle$ and $|D\rangle$). The latter is only relevant in the extreme cases, $P_S = \{0, 1\}$, and accounts for the probability that the $(N+1)_{\text{th}}$ trial yields a different outcome [Hem14, p. 51].

3.7.2. Oscillator-state analysis

In general, a direct measurement of the motional state of a trapped ion is not possible. But $|S\rangle \leftrightarrow |D\rangle$ transitions depend on the motional state via the Rabi frequency given by Equation (3.8). Therefore, at least the population distribution of the motional state can be mapped onto the internal state in the following way. Consider the ion to initially be in $|S\rangle$

and an arbitrary motional state,

$$\rho(0) = |S\rangle\langle S| \otimes \rho_{\mathrm{m}}.$$

The time evolution operator for resonant driving can be calculated from Equation (3.7) for a given s to be

$$\begin{aligned} U^{\mathrm{I}}(t) = &\sum_{n=I}^{\infty} \cos\!\left(\frac{\Omega_{s,n}t}{2}\right)\Big(|D,n+s\rangle\langle D,n+s| + |S,n\rangle\langle S,n|\Big) \\ &- \mathrm{i}\sum_{n=I}^{\infty} \sin\!\left(\frac{\Omega_{s,n}t}{2}\right)\Big(|D,n+s\rangle\langle S,n|\,\mathrm{e}^{-\mathrm{i}\phi_{s,n}} + |S,n\rangle\langle D,n+s|\,\mathrm{e}^{\mathrm{i}\phi_{s,n}}\Big) \\ &+ \sum_{n=0}^{s-1}|D,n\rangle\langle D,n| + \sum_{n=0}^{-s-1}|S,n\rangle\langle S,n|, \end{aligned}$$

where $I = \max[0,-s]$ and sums evaluate to zero if the upper limit is lower than the starting value. The probability for detecting the ion in the internal state $|S\rangle$ after a time t is

$$\begin{aligned} P_S^{(s)}(t) &= \sum_{n=0}^{\infty}\langle S,n\,|\,U^{\mathrm{I}}(t)\rho(0)U^{\mathrm{I}\dagger}(t)\,|\,S,n\rangle \\ &= \frac{1}{2}\sum_{n=I}^{\infty}P(n)\Big(1+\cos(\Omega_{s,n}t)\Big) + \sum_{n=0}^{-s-1}P(n) \end{aligned} \tag{3.25}$$

with $P(n) = \langle n\,|\,\rho_{\mathrm{m}}\,|\,n\rangle$. For low number states, the most interesting transitions are the first red ($s=-1$) and blue ($s=1$) sidebands because the $\Omega_{\pm1,n} \approx \Omega\eta\sqrt{n_>}$ are distinct frequencies (Figure 3.3) and hence the number-state population $P(n)$ can be extracted from the Fourier transform of $P_S^{(s)}(t)$. Alternatively, if the supposed type of motional state (coherent, squeezed, thermal; see Section 2.3) is known, the theoretical model in Equation (3.25) can be fitted to the data to find unknown parameters. This is the main tool for evaluating highly excited coherent states in Chapter 6.

If the ground state is substantially populated and one assumes that the final motional state has a thermal distribution, the mean excitation number can also be obtained more directly. From the above, Equation (2.18), and $\Omega_{-s,n} = \Omega_{s,n-s}$ follows for driving on the sth red and blue sidebands (here with $s>0$) that

$$\begin{aligned} P_D^{(-s)}(t) &= \sum_{n=s}^{\infty}P_{\mathrm{th}}(n)\,\sin^2\!\left(\frac{\Omega_{-s,n}t}{2}\right) = \left(\frac{n_{\mathrm{th}}}{n_{\mathrm{th}}+1}\right)^s\sum_{n=0}^{\infty}P_{\mathrm{th}}(n)\,\sin^2\!\left(\frac{\Omega_{+s,n}t}{2}\right) \\ &= \left(\frac{n_{\mathrm{th}}}{n_{\mathrm{th}}+1}\right)^s P_D^{(+s)}(t). \end{aligned}$$

The ratio of the probabilities $R_s = P_D^{(-s)}(t)/P_D^{(+s)}(t)$ is therefore independent of drive time

and gives

$$n_{\mathrm{th}} = \frac{(R_s)^{1/s}}{1-(R_s)^{1/s}} \tag{3.26}$$

for the mean occupation number. In principle, s should be chosen to be the positive integer nearest to the expected n_{th} in order to maximize sensitivity [Tur00].

3.8. Spin coherence and Ramsey interferometry

A qubit in one of its basis states, $|S\rangle$ or $|D\rangle$, is well isolated from its environment. The radiative lifetime of $|D\rangle$ is long ($\approx 1\,\mathrm{s}$, Table 3.1) compared to typical experimental sequences, and coupling to background radiation is negligible provided that the laser beams are sufficiently extinguished. For superposition states such as $|\psi(\phi)\rangle = (|D\rangle + \mathrm{e}^{\mathrm{i}\phi}|S\rangle)/\sqrt{2}$, however, the situation is different because the phase ϕ between the basis states is, for example, susceptible to magnetic-field fluctuations and laser-phase noise. Both affect the instantaneous detuning $\delta = \omega_{\mathrm{l}} - \omega_{\mathrm{a}}$ of the qubit from the laser and hence cause decoherence [Win98]. A useful method to quantify the qubit's phase stability is *Ramsey interferometry*, originally invented to measure transition frequencies of atoms [Foo05, p. 132ff].

3.8.1. Ramsey interferometry

In Ramsey interferometry, a first $\pi/2$-pulse, described by the matrix $R(\pi/2, \phi_1)$ in Equation (3.13), rotates the initialized qubit state $|S\rangle$ to $|\psi(\phi_1 + \pi/2)\rangle$ on the equator of the Bloch sphere (Figure 3.12).[6] Since this is the first coherent-manipulation pulse in the sequence, its phase can be treated as zero. Subsequently, the qubit evolves freely for a time τ under the influence of the Hamiltonian $H^{\mathrm{T}} = \hbar\delta(t)\sigma_{SS}$ in the rotating frame of the laser (cf. Equation (3.10)). The corresponding evolution operator (Section A.1) causes a rotation of the qubit state on the Bloch sphere around the z-axis to

$$|\psi(\tau)\rangle = \frac{1}{\sqrt{2}}\left(|D\rangle + \mathrm{i}\mathrm{e}^{-\mathrm{i}\Phi(\tau)}|S\rangle\right) \qquad \text{with} \qquad \Phi(\tau) = \int_0^\tau \mathrm{d}t\,\delta(t).$$

Finally, a second $\pi/2$-pulse is applied and the $|S\rangle$-state population

$$P_S = \left\langle S \,\middle|\, R(\pi/2,\phi_2)\,\rho(\tau)\,R^\dagger(\pi/2,\phi_2) \,\middle|\, S\right\rangle$$

inferred from many experimental repetitions. For a detuning $\delta(t)$ that is identical in all

[6] Note that I ignore a possible detuning during laser pulses. Since Ramsey interferometry is usually applied when $\delta \ll \Omega$, this is justified because the Rabi flop amplitude and period are only affected to second order in δ/Ω.

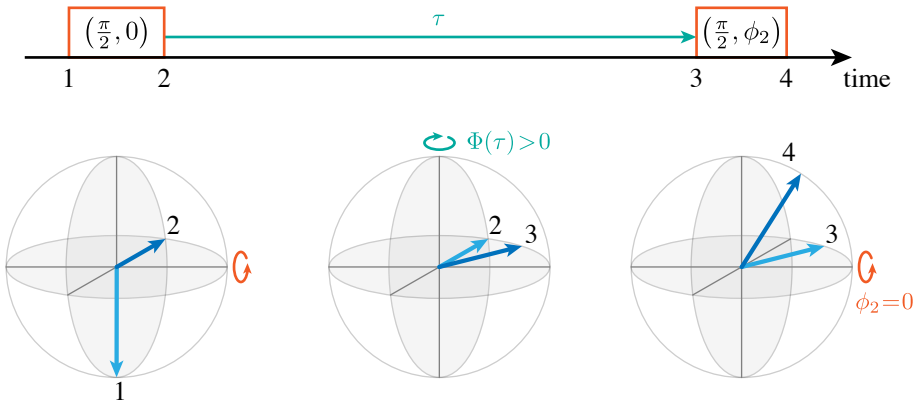

Figure 3.12: Pulse sequence (top) and corresponding spin evolution on the Bloch sphere (bottom) in Ramsey interferometry. The pulse angles indicate the corresponding rotations $R(\theta, \phi)$ on the Bloch sphere. First, the initialized qubit state is rotated to $(|D\rangle + \mathrm{i}|S\rangle)/\sqrt{2}$. During the waiting time τ (long compared to the pulse durations), it irregularly precesses around the z-axis under the influence of fluctuating detuning with respect to the laser (depicted for $\Phi(\tau) > 0$). A second $\pi/2$-pulse at phase ϕ_2 (here zero) is followed by spin state detection. Multiple measurements with varying ϕ_2 allow the detection of a constant detuning offset and/or a loss in fringe contrast.

experimental runs, the probability to find the qubit in the $|S\rangle$-state is

$$P_S = \frac{1}{2}\Big(1 - \cos\big(\Phi(\tau) + \phi_2\big)\Big). \tag{3.27}$$

A constant detuning $\delta(t) = \delta_0$, for example, leads to a linear phase shift $\Phi(\tau) = \delta_0\tau$ of these so-called *Ramsey fringes* (Figure 3.13 (left)). By increasing τ, the sensitivity to small detunings of the laser from the atomic transition is enhanced (Figure 3.13 (right)). On the other hand, a variant of Ramsey experiments with an additional *spin-echo* pulse that performs a rotation $R(\pi, 0)$ at time $\tau/2$ allows canceling the effect of (slowly varying) detunings.

3.8.2. Discrete noise

In case of noise, $\delta(t) = \delta_0 + N(t)$ varies over experimental realizations. Phase coherence between the qubit states, given by the off-diagonal terms in the corresponding density matrix

$$\rho(\tau) = \frac{1}{2}\begin{pmatrix} 1 & -\mathrm{i}\mathrm{e}^{+\mathrm{i}\Phi(\tau)} \\ +\mathrm{i}\mathrm{e}^{-\mathrm{i}\Phi(\tau)} & 1 \end{pmatrix},$$

consequently diminishes due to statistical averaging over noise realizations. In anticipation of the experimental results in Section 5.9, I shall be interested here in noise dominated by

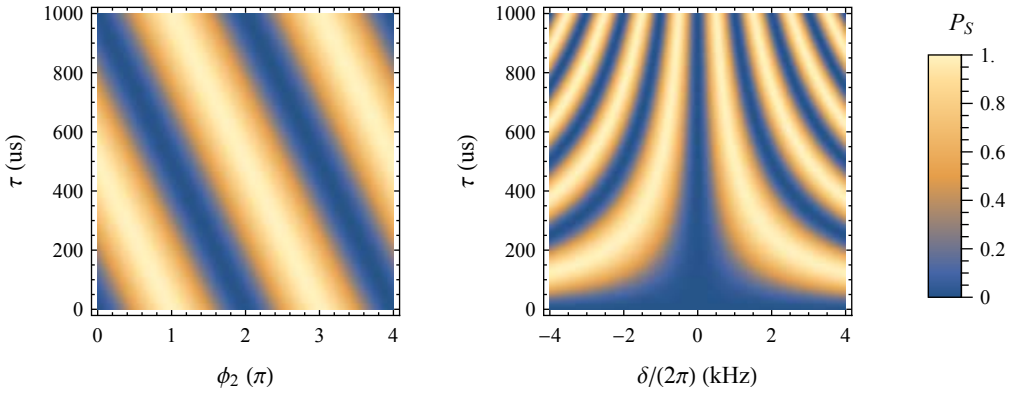

Figure 3.13: Ramsey fringes according to Equation (3.27) for constant detuning and typical experimental parameters. (left) Sinusoidal fringes can be observed by scanning the phase ϕ_2 of the second laser pulse. At non-zero detuning, here $\delta_0 = (2\pi)1\,\mathrm{kHz}$, the fringes are linearly displaced with the waiting time τ between the two pulses. (right) Scanning the laser frequency over the atomic transition for different waiting times results in the depicted pattern. Longer τ leads to narrower peak width, which is utilized for precision measurements of atomic frequencies. Furthermore, obtaining such a pattern in experiments is useful to identify the fringe peak corresponding to zero detuning.

discrete, sinusoidal components,

$$N(t) = \sum_k N_k \cos(\omega_k t + \alpha_k),$$

with amplitudes $N_k > 0$, frequencies ω_k and phases α_k. In order to evaluate $\left\langle \mathrm{e}^{+\mathrm{i}\Phi(\tau)} \right\rangle$, averaged over the randomly distributed α_k, I follow the derivations presented in [Kot11; Kot13]. I start by rewriting the phase accumulated during a single experimental realization as

$$\Phi(\tau) = \int_0^\tau \mathrm{d}t\, [\delta_0 + N(t)]\, F(t) \equiv \Phi_0(\tau) + \frac{1}{2\pi} \int_{-\infty}^{\infty} \mathrm{d}\omega\, \hat{N}^*(\omega)\, \hat{F}_\tau(\omega), \tag{3.28}$$

where $F(t) = 1$ for a Ramsey sequence without and $F(t) = \mathrm{sgn}(\tau/2 - t)$ for a sequence with a spin-echo pulse [Kot11, Supplementary Information]. The phase offset $\Phi_0(\tau)$ results from δ_0 and the two Fourier transforms (cf. Equations (F.14)) are given by

$$\hat{N}^*(\omega) = \int_{-\infty}^{\infty} \mathrm{d}t\, N(t)\, \mathrm{e}^{+\mathrm{i}\omega t}, \qquad \hat{F}_\tau(\omega) = \int_0^\tau \mathrm{d}t\, F(t)\, \mathrm{e}^{-\mathrm{i}\omega t}.$$

Making use of Equation (F.15), the expression for the accumulated phase due to the noise simplifies to

$$\Phi_N(\tau) = \Phi(\tau) - \Phi_0(\tau) = \int_0^\tau \mathrm{d}t\, \delta_0\, F(t) + \sum_k N_k \left|\hat{F}_\tau(\omega_k)\right| \cos(\alpha_k - \varphi_k)$$

with $\varphi_k = \arg\big(\hat{F}_\tau(\omega_k)\big)$. Finally, averaging the coherence term $A(\tau) = \left\langle \mathrm{e}^{+\mathrm{i}\Phi_N(\tau)} \right\rangle$ uniformly over the phases of the noise components yields

$$A(\tau) = \frac{1}{2\pi} \prod_k \int_0^{2\pi} \mathrm{d}\alpha_k\, \exp\Big[\mathrm{i}N_k \left|\hat{F}_\tau(\omega_k)\right| \cos(\alpha_k - \varphi_k)\Big] = \prod_k J_0\Big(N_k \big|\hat{F}_\tau(\omega_k)\big|\Big). \quad (3.29)$$

The second equality stems from the integral representation of the Bessel function in Equation (F.17). Note that the form of $F(t)$ and hence $\hat{F}_\tau(\omega_k)$ depends on whether a spin-echo pulse is performed or not. The resulting Ramsey fringes, given by

$$P_S = \frac{1}{2}\Big(1 - A(\tau)\, \cos\Big(\Phi_0(\tau) + \phi_2\Big)\Big), \quad (3.30)$$

have a reduced contrast[7] of $|A(\tau)|$ and are shifted by $\Phi_0(\tau)$ (or by $\Phi_0(\tau) + \pi$ if $A(\tau)$ is negative).

We use this expression to analyze noise affecting the spin coherence in Section 5.9.

[7] Fringe visibility or contrast is commonly defined as the ratio of the amplitude to the average of fringe oscillations, that is $(\max - \min)/(\max + \min)$.

4. Experimental Apparatus

The experiments described in this thesis are performed with calcium ions spatially confined above a Surface-Electrode ion Trap (SET) chip, which is placed inside Ultra-High Vacuum (UHV)[1] and cooled to liquid helium temperature. Working at cryogenic temperatures offers some advantages compared to room-temperature ion-trap systems [Ant09]: cryopumping produces UHV and thereby reduces the collision rate with background gas; low temperatures reduce electrical (Johnson) noise and the anomalous heating rate of trapped ions; and materials normally not UHV compatible can be used due to suppressed outgassing. The latter allows us to place conventional active electronics for fast switching of trap electrode potentials close to the trap chip, whereas it poses a considerable technical effort to prepare UHV-compatible electronics for operation at room temperature [Gui14]. On the downside of a cryogenic setup are possible vibrations of the cryocooler, that not all vacuum technologies and electrical circuits are directly transferable to low-temperature systems, and that care must be taken of thermal loads.

The main building blocks of the experimental apparatus (Figures 4.1 and 4.2), the ion trap apparatus and the laser, imaging and control systems, are briefly introduced here and discussed in detail in the ensuing sections of this chapter.

The ion trap apparatus includes the SET placed inside a UHV chamber, which is mounted on the cold plate of a liquid-helium bath cryostat of a recondensing pulse-tube refrigerator [Wan10]. It was designed for quantum control experiments with beryllium and calcium ions. Even though experiments have thus far only been performed with calcium, the design considerations were important for the SET layout, rf drive (the lighter beryllium ions require a higher drive frequency), and imaging setup (the two species absorb and emit light at different wavelengths). The UHV chamber around the SET was designed to be hermetically sealed from the isolation vacuum in the cryostat and care was taken to use only materials with the lowest possible magnetizability close to the trap. Section 4.1 describes the SET, Cryo-Electronics Board (CEB), rf resonator, atom source, UHV chamber, and cryostat in detail.

The light for ion creation and manipulation is produced by multiple lasers at wavelengths of 375, 397, 423, 729, 854 and 866 nm. All lasers except for the ionization lasers at 375 and 423 nm require frequency stabilization, frequency shifting, and switching during experimental sequences. Laser light is delivered to the trap region via fibers and focusing optics. These

[1] Ultra-high vacuum refers to pressures between 10^{-9} and 10^{-12} mbar. I use this term due to its ubiquity in the community despite the fact that we expect the pressure in our system to be $< 10^{-12}$ mbar, which would normally be called extremely high vacuum.

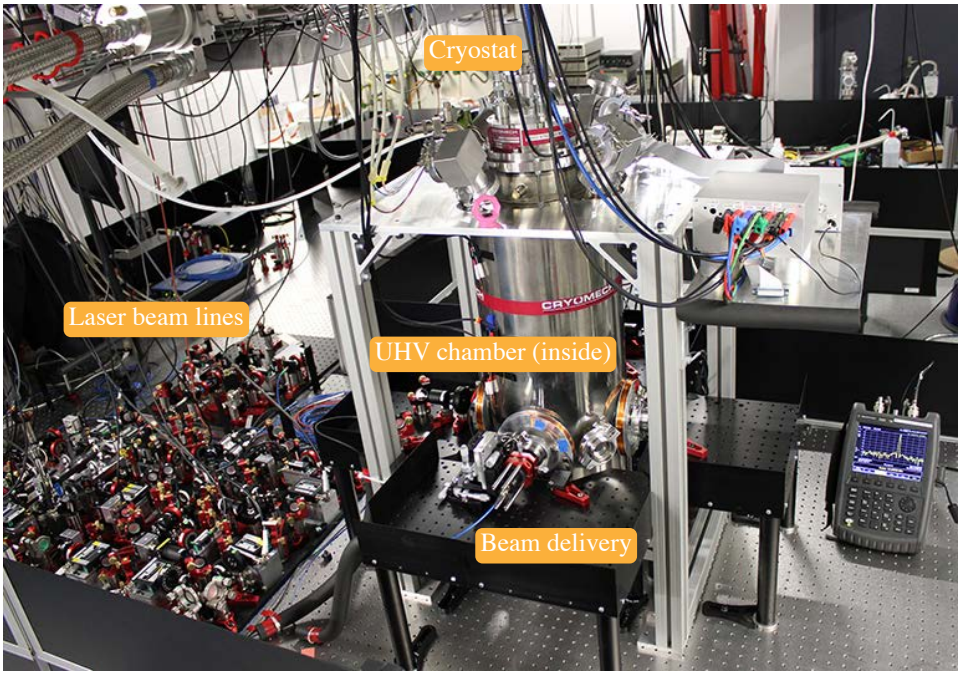

Figure 4.1: Overview of the experimental setup in the laboratory. The cryostat houses the UHV chamber with the SET and keeps them at a temperature of 4 K. On the same optical table, laser light coming from the neighboring lab is prepared and delivered to the trapped ions.

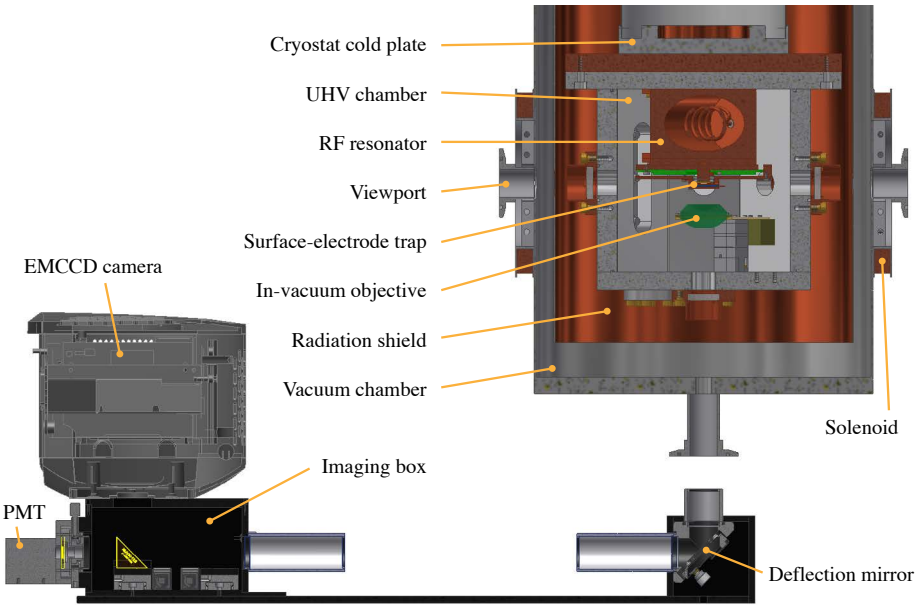

Figure 4.2: The SET is mounted on the rf resonator inside the UHV chamber. The latter is attached to the cryostat cooling station inside the isolation vacuum of the cryostat. An additional radiation shield anchored to the first stage of the cryocooler reduces thermal radiation on the cryogenic parts. The ion's fluorescence is captured by an EMCCD camera and/or a PMT via an in-vacuum objective.

aspects are expounded in Section 4.2.

Fluorescence light from ions is captured and focused by a single-component reflective objective onto an EMCCD camera and/or a PMT. The objective is mounted on a three-axes nanopositioner stack inside the UHV chamber (Figure 4.2). Section 4.3 elucidates design considerations, implementation and performance of the imaging system.

The computer-control system mainly controls the laser pulses and electrode voltages during experiments, and registers photon counts from the PMT to detect an ion and its internal state. Section 4.4 presents an overview of its components and functioning.

4.1. Ion-trap apparatus

4.1.1. Surface-electrode ion trap

The electrode layout of our SET (Figures 2.3 and 4.3) is adapted from the asymmetric 5-wire design by Chiaverini et al. [Chi05]. The center and outer electrodes (along the y-direction) are maintained at rf ground, with the rf potential applied to the ones in between. The resulting pseudopotential creates a trap axis $\approx 50\,\mu\text{m}$ above the center electrode. The two outer electrodes are segmented for axial confinement and control. Because of the asymmetry in the rf electrodes' widths (Erf1 is 75 µm, Erf2 45 µm wide), the principal axes of the total potential are tilted against the z-axis (Figure 2.5), which allows for laser cooling of all motional modes (Section 3.6).

According to simulations (Section 2.2), the electrode layout allows for trapping of $^{9}\text{Be}^{+}$ and $^{40}\text{Ca}^{+}$ with an rf drive amplitude of 100 V at 130 MHz. However, we have thus far used it for $^{40}\text{Ca}^{+}$ exclusively. We typically drive the rf at 93.4 MHz (see Section 4.1.3 for the rf resonator) and apply control voltages between -10 and 10 V to obtain an axial trap frequency $\omega_\text{m} \approx 2.3\,\text{MHz}$ and radial trap frequencies of $\sim 6\,\text{MHz}$. With these settings, the simulated overall trap depth is 15 meV, limited by a saddle point of the potential diagonally above the trap axis (at higher y and z coordinate values). Higher trap depths can be achieved by increasing the rf drive amplitude.

The SET consists of gold electrodes on a crystalline quartz[2] substrate, similar to the ones in refs. [Sei06; Bro11]. The photolithographic fabrication process [Hug11] is described in the next section.

Trap-chip fabrication

Our trap chip was fabricated by Joseba Alonso[3] in the technology and cleanroom facility for micro- and nano-technology "FIRST" at ETH Zurich. Using photolithographic techniques, an array of trap chips was produced simultaneously on a 0.5 mm thick 2 inch quartz wafer[4],

[2] Crystalline quartz is a material with low rf loss, comparatively high breakdown voltage, and, most importantly, high thermal conductivity [Sim94].

[3] The information in this section is based on private communication with him.

[4] Quartz wafer from The Roditi International Corporation

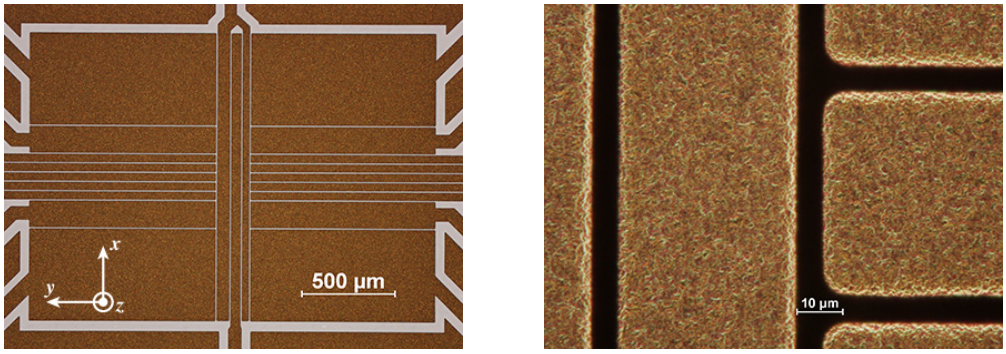

Figure 4.3: Microscope images of the SET chip after etching, showing the wider trapping region (left) and a close-up of the central electrodes (right). The trap electrodes are plated to a thickness of 8 µm with an inter-electrode spacing of 6 µm.

which was X-cut to avoid piezo-electric expansion and saw polished on the side where electrodes were subsequently grown.

Prior to fabrication, the substrate was cleaned in ultrasonic baths with acetone, isopropanol and deionized water, followed by oxygen-plasma ashing and baking at 180 °C for water removal. Then, a 10 nm adhesion layer of titanium and a 100 nm seed layer of gold were evaporated. After spin-coating with HexaMethylDiSilazane (HMDS) adhesion promoter, the wafer was pre-baked at 110 °C for a few minutes. This reduced the number of defects in the 10 µm layer of spin-coated positive photoresist[5]. The photoresist was baked again at 110 °C for a few minutes and then left cooling for at least 10 min for fixation.

After exposure through a printed photomask[6] with UltraViolet (UV) light, the photo-resist was developed in a 1:4 solution of AZ-400-K[7] in deionized water. In the exposed seed layer areas, an 8 µm thick gold layer was grown by electroplating in a sulphite-based gold bath[8] with a neutral pH-value. This layer contains all the electrodes, ground plane, pads and any other conducting features on the chip. The separation was provided by the remaining photo-resist, which was then removed in a hot ultrasonic bath of N-Methyl-2-Pyrrolidone (NMP) or DiMethyl Sulfoxide (DMS).

The seed and adhesion layers were at this point still electrically shorting the electroplated gold. The former was wet-etched away with soft aqua regia (70 ml of deionized water, 30 ml of HCl 32 %, 9 ml of HNO_3 65 %), and the latter removed with HCl 32 %. A few drops of Triton X-100 surfactant were added to both etching solutions in order to enable etching in the ≈ 6 µm thick trenches between the electrodes close to the trap center.

Finally, the wafer was cleaned again and diced into individual $10 \times 10\,\mathrm{mm}^2$ chips. The best chip, as judged by visual inspection for surface defects and shortcuts, was selected for use.

[5] Photoresist AZ9260 from MicroChemicals
[6] Chrome Soda Lime (Clearfield, 128k) from JD Photo-Tools
[7] Developer AZ-400-K from MicroChemicals
[8] Gold-SF from METAKEM

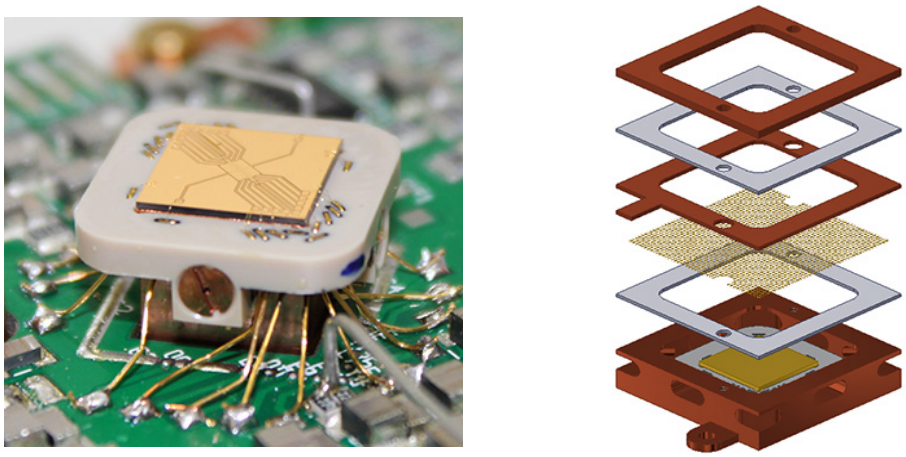

Figure 4.4: (left) SET chip epoxied to a copper pedestal elevated above the CEB. The electrodes are wire bonded to gold wires, which are fixed in a PEEK connector piece and soldered to pads on the CEB. (right) Faraday cage around the mounted SET. The cover mesh is electrically isolated from the cage by alumina spacers and connected to the CEB separately.

Trap-chip mounting

The finished trap chip was epoxied[9] to a mounting pedestal. The pedestal is made from Oxygen-Free High-Conductivity (OFHC) copper and thermally anchored to the 4 K stage of the cryostat.

On the trap chip, the surface electrodes are routed to bonding pads close to its edges but away from desired laser beam directions. Electrical connections to the CEB, see next section, were made by wire bonding with 25 µm gold wires to flat-polished gold wires[10] in a PolyEther Ether Ketone (PEEK) connector (Figure 4.4 (left)), which were previously soldered to pads on the CEB.

In the final assembly, a Faraday cage around the trap chip shields it from electric noise (Figure 4.4 (right)). The cage walls have openings for optical access. A cover mesh[11], approximately 2 mm above the SET, provides an additional rf ground. Being electrically isolated by alumina spacers from the cage ground, it is connected to the CEB and can be used as an additional control electrode. Applying a positive voltage of 10 V to it during ion loading was simulated to increase the trap depth to 94 meV with all other parameters as given above.

[9] STYCAST 2850 FT with curing agent CATALYST 24 LV from Emerson and Cuming, now Henkel LOCTITE. It is low-temperature compatible, provides high thermal conductivity and has a low coefficient of thermal expansion.

[10] Gold wires in the connector from MaTecK; diameter 0.3 mm

[11] Electroformed gold mesh MG-17 from Precision Eforming; 19 µm wire diameter, 90 % transmission

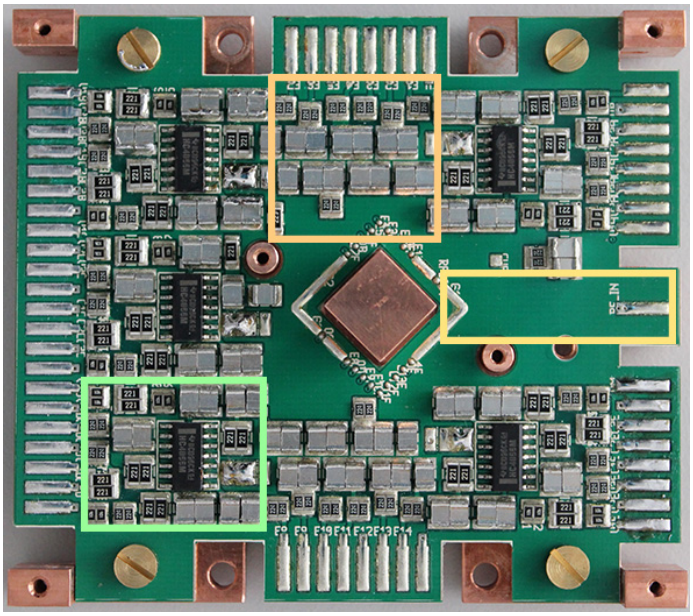

Figure 4.5: CEB mounted on the OFHC carrier before fixing the trap chip on the square pedestal in the center. The colored rectangles mark the rf track (yellow), RC-filtered lines for regular control electrodes (orange), and one of five circuitries for fast switching (green).

4.1.2. Cryo-electronics board and fast switches

The CEB is the last interface between the voltage and signal sources outside vacuum and the SET chip. It is mounted on an OFHC carrier below the trap chip (Figure 4.4) and thereby thermally anchored to the 4 K stage. The low temperature allows us to use conventional Printed Circuit Board (PCB) and soldering technology. Three types of connections run through the PCB: a direct connection for the rf drive signal, RC-filtered lines for regular control electrodes, and lines for switchable control electrodes (Figure 4.5).

Regular control electrodes are supplied with DC voltages from outside the cryostat (Section 4.4). RC-filters[12] with cutoff frequencies of 14 Hz mitigate electrical pickup and noise at the supply lines (Figure 4.6). The filter capacitors also provide a low-impedance path from the control electrodes to ground to avoid voltage buildup due to capacitive coupling to the rf electrodes [Ami11, p. 404].

The voltages on five electrodes (El2, El8, Em, Er2, Er8) can be switched on timescales of few nanoseconds using Complementary Metal–Oxide–Semiconductor (CMOS) ICs. Three bilateral SPST switches inside a single IC[13] are combined to a Single-Pole-Triple-Throw (SPTT) to switch an electrode voltage between three preset and filtered input voltages (Figure 4.6). At any given time, only one SPST per control electrode is closed by setting

[12] To ensure low-temperature compatibility, all resistors are thin film and capacitors are from the ECHU(X) series from Panasonic.
[13] CD74HC4066M from Texas Instruments

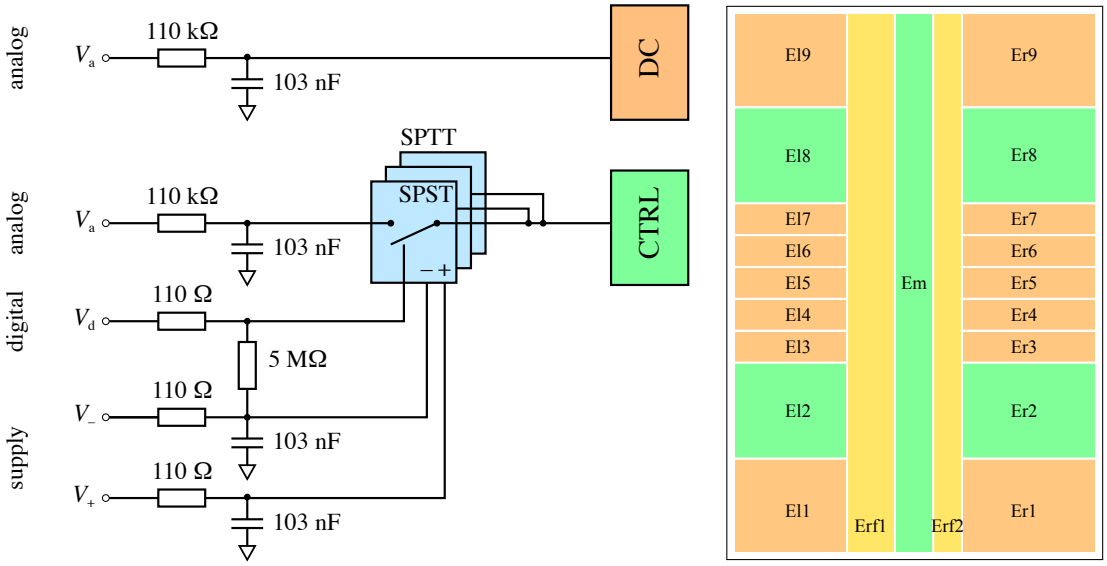

Figure 4.6: (left) Schematics of filtered and switched voltage lines to the control electrodes. The analog input voltages V_a are passed through RC filters with cutoff frequencies of 14 Hz before the regular control electrodes (orange) or the SPST switches for switchable control electrodes (green). The SPST switches require supply voltages $V_+ = 8\,\mathrm{V}$ and $V_- = -1\,\mathrm{V}$, which are filtered with cutoff frequencies of 14 kHz. Digital signals V_d control the closing of the switches. Two resistors are added for protection and pull-down of the control line. All resistors are doubled, that is two resistors with twice the given values, in order to protect from possible solder-point damage. The capacitances consist of two capacitors at 100 nF and 3 nF with different internal inductances for faithful filtering above the cutoff frequency. (right) Schematic electrode layout with electrode labels and color codes for rf (yellow), switchable (green) and regular (orange) control electrodes.

Table 4.1: Performance data of the CD74HC4066M switching IC at room and cryogenic temperature. The power consumption was measured at a switching rate of 1 MHz. Crosstalk suppression gives the fraction of noise at 1.5 MHz that passes from the control line to the output. Rise and fall times were measured for 10 % to 90 % transitions of a 9 V step. [Fad13]

	300 K	4 K
Off resistance (MΩ)	> 10	> 10
On resistance (Ω)	12	3.5
Power consumption (mW)	8	10
Crosstalk suppression (dB)	-50	-50
Rise/fall time (ns)	13	< 5

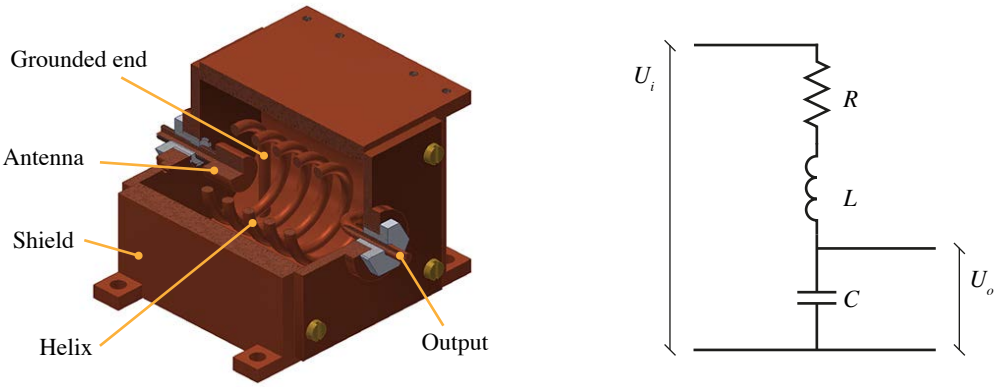

Figure 4.7: (left) CAD drawing of the helical resonator. The rf signal is coupled in from the left. A load is connected directly to the outcoming end of the helix on the right. The copper is OFHC, insulators are from PTFE, and brass screws are used for fixing the side lids as well as for mounting the resonator on the UHV chamber and the CEB on top of the resonator. (right) Resonant series-LCR circuit, shown explicitly as a voltage divider. The SET is modeled as a capacitance in parallel with the circuit's capacitance, and hence increases C.

the digital control voltage V_d to "HI" (7 V versus 0 V for "LO"). With supply voltages[14] $V_+ = 8\,\mathrm{V}$ and $V_- = -1\,\mathrm{V}$, faithful switching between input voltages is possible in the range from -0.5 to 7.5 V.

The particular switching IC was chosen after extensive testing of a range of possible alternatives by submersion in liquid helium, performed by Roland Hablützel [Hab12]. Among the tested GaAs and CMOS switches, the chosen switch proved to feature reliable operation and fast switching times when cold-started at 4 K. Further characterization of the switch IC was done by Matteo Fadel, documented in [Fad13]. Table 4.1 summarizes the most relevant results.

4.1.3. Resonator

The rf voltage is applied to the trap through a cryogenic, in-vacuum quarter-wave helical resonator, which provides low-noise voltage amplification and impedance matching to the SET. It consists of a coil inside a cylindric shield, both fabricated from OFHC copper, with one end of the coil solidly connected to the shield. On that side, the signal from an rf amplifier is coupled inductively into the resonator via an antenna (Figure 4.7). The other end of the helix extends outside the shield and is coupled via a short copper braid to the rf electrodes. The resonator is mounted on the top lid of the UHV chamber, directly below the CEB and trap chip (Figure 4.2), which yields an increased voltage step up due to the low temperature (see below).

The resonance frequency and quality factor of a helical resonator made from copper follow from its geometry and were semi-empirically calculated in [Mac59]. The shield has a

[14] The supply voltages can have a maximum difference of 9 V.

length $B \approx 60\,\mathrm{mm}$ and an inner diameter $D \approx 45\,\mathrm{mm}$. The helix has 4.9 turns at a winding diameter $d \approx 25\,\mathrm{mm}$, a winding height $b \approx 37\,\mathrm{mm}$, a winding pitch $\tau \approx 7.6\,\mathrm{mm}$, and a wire diameter $d_0 = 3.2\,\mathrm{mm}$. For these parameters, the unloaded resonator (open-ended output) was expected to have a quality factor $Q \approx 1300$ at a resonance frequency of 220 MHz. Loaded with an estimated trap capacitance of 4 pF, the resonance was planned to drop to 130 MHz [Roh09, Section 4.1.5], which was the design parameter for the SET.

To gain a qualitative understanding of why and how the resonance frequency drops when the resonator is loaded, a helical resonator can to a good extent be modeled by a series-LCR circuit [Sta03, Chapter 5]. The quality factor of such a resonance circuit (Figure 4.7), generally defined as $Q = \omega_0(\text{energy stored})/(\text{power loss})$ with ω_0 the resonance frequency, is given by

$$Q = \frac{\omega_0 L}{R} = \frac{1}{\omega_0 RC},$$

where $\omega_0 = 1/\sqrt{LC}$. The voltage gain, as given by the absolute of the transfer function, can then be written

$$G(\omega) = \left|\frac{U_o(\omega)}{U_i(\omega)}\right| = \left|\frac{1/(\mathrm{i}\omega C)}{R + \mathrm{i}\omega L + 1/(\mathrm{i}\omega C)}\right| = \frac{\omega_0^2}{\sqrt{(\omega^2 - \omega_0^2)^2 + (\omega\omega_0/Q)^2}}.$$

A series-LCR circuit of high quality ($Q \gg 1$), which essentially means a low resistance, therefore provides a voltage step up $G(\omega_0) = Q$ on resonance. The quality factor can also be directly calculated from the Full Width at Half Maximum (FWHM) $\Delta\omega$ of the resonance power curve as $Q = \omega_0/\Delta\omega$. In conclusion, one expects the resonance frequency and quality factor of the resonator to drop as $\propto 1/\sqrt{C}$ when C is increased by a (parallel) capacitive load.

This effect of loading on the resonator's performance was tested and confirmed by Matteo Fadel as documented in [Fad13]. Using a network analyzer[15], the reflected-power spectrum from incoupling into the resonator was measured at 300 K and 4 K for different load capacitances. The impedence matching of the incoupling was optimized by moving the coupling antenna in and out of the resonator such that the on-resonance reflection was minimal. After cleaning the resonator by sanding the inside surfaces, the unloaded resonance frequency was 162 MHz with Q values of 450 at 300 K and 1800 at 4 K. Cleaning was found to triple the Q value at low temperatures, which we attribute to a reduced skin depth[16] of 500 nm, on the order of surface contaminant layer thickness. The design resonance frequency might not have been met because of the open end of the helix extending to outside the shield in contrast to the design in [Mac59], where the helix is cut in the

[15] Network analyzer FieldFox N9912A from Agilent Technologies

[16] Due to the skin effect, an alternating electric current flows mainly at the "skin" of the conductor. The skin depth is given by $\delta = (2\rho/\omega\mu)^{1/2}$ where ρ and μ are the resistivity and magnetic permeability of the conductor, and ω is the angular frequency of the current [Jac62, Section 7.8]. The resistivity of OFHC copper drops from $1.7 \times 10^{-8}\,\Omega\,\mathrm{m}$ at 295 K to $1.5 \times 10^{-10}\,\Omega\,\mathrm{m}$ at 10 K [Eki06, Appendix 6.5a].

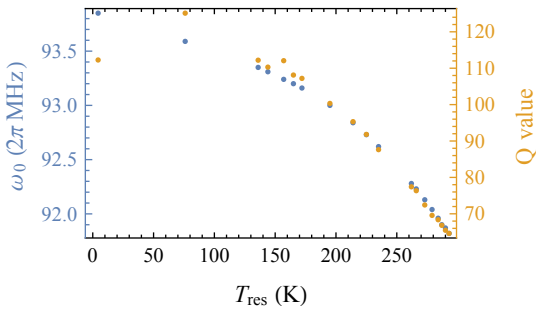

Figure 4.8: Measured resonance frequency and Q value of the resonator versus its temperature.

winding part. With a capacitive load of 6 pF, which was later found to be the capacitance of CEB plus SET, the resonance frequency shifted to 105 MHz with a reduced Q value of 300 at 300 K and 400 at 4 K.

Loading the resonator with CEB and SET via a bare copper braid, the resonance frequency shifted down to 92 MHz and the Q value to 65. The fact that the Q factor was affected less dramatically by loading with the test capacitor than with CEB and SET hints at the latter not being purely capacitive but could at that point not be altered anymore. Furthermore, the tuning range of the cylindrically shaped incoupling antenna did not suffice anymore and was replaced by a wire loop [Siv12]. During cooling of the cryostat to 4 K, the resonance frequency and Q value increased again (Figure 4.8), but not to the previous values. We always observe a drop in the Q value at the lowest temperature, probably due to the skin effect as discussed above. Another possibility would be that this is due to changing impedance matching at the incoupling because of thermal contraction.

While the output peak voltage from the resonator cannot be measured directly in our current setup, it can be predicted given an input power P and assuming the model in Figure 4.7. A desired peak voltage U_0 across the capacitor requires a peak current $I_0 = U_0\omega_0 C$, which leads to an average dissipated power of

$$P = \frac{I_0^2 R}{2} = \frac{(U_0\omega_0 C)^2 R}{2} = \frac{U_0^2}{2\omega_0 Q L}$$

in the resistor. The resonator's inductance can be estimated to $L = 220\,\mathrm{nH}$ from the resonance frequency measurements with and without capacitive load. A peak voltage $U_0 = 100\,\mathrm{V}$ would therefore require an input power of 340 mW. This estimate is higher than our usual input power of 21 dBm (126 mW), which yields a voltage amplitude of $\approx 140\,\mathrm{V}$ as estimated from the secular frequencies (Section 5.3), but gives an idea of the required range. The input power is generated from a stable frequency source[17] and amplified[18] before being

[17] Signal generator SMC100A from Rohde & Schwarz
[18] Amplifier TIA-1000-1R8-2 from Mini-Circuits; gain 38 dB, maximum output power 35 dBm

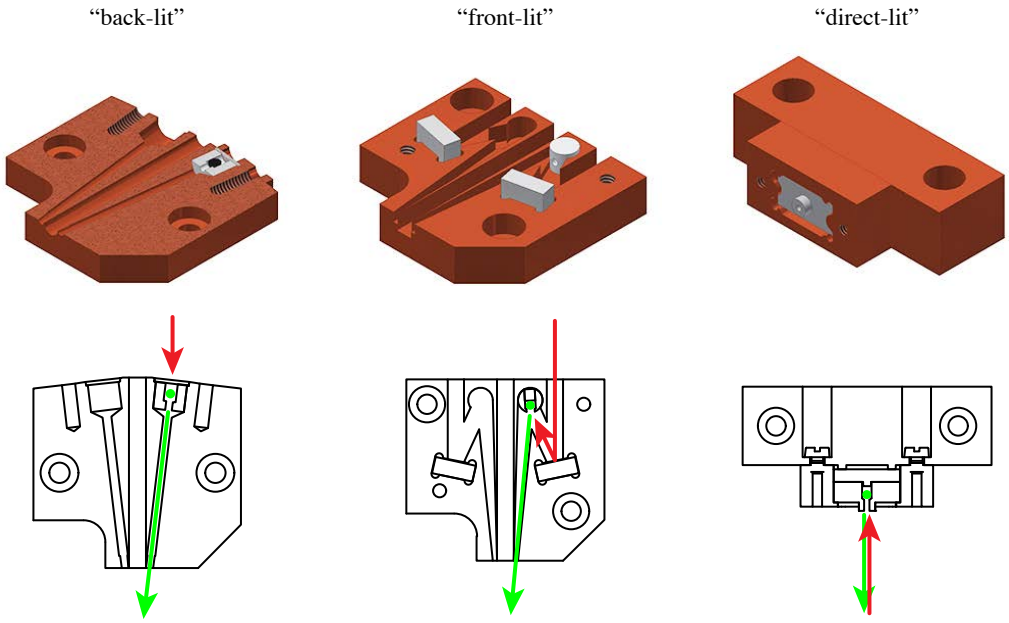

Figure 4.9: Atom oven designs for laser desorption in the “back-lit”, “front-lit”, and “direct-lit” configurations. In the first two configurations, the illuminating laser beams (red arrows) does not cross the trapping region, where desorbed atoms (green arrows) are supposed to fly; in the third configuration it does.

passed through a bi-directional coupler[19], which allows for monitoring the reflected power during operation.

4.1.4. Atom source

The neutral atoms that are subsequently photoionized and loaded into the trap are produced in an atom oven adjacent to the Faraday cage in the trap assembly (Figure 4.4). Two techniques for generating atoms in the gas phase from bulk material are common: laser ablation and resistive heating. The first has the advantage of a low heat load and was successfully tested for loading $^{88}Sr^{+}$ ions into a SET in a cryogenic environment using a pulsed Neodymium-Doped Yttrium Aluminium Garnet (Nd:YAG) laser [Ant09]. Without such a device at hand, we have attempted laser desorption with Continuous-Wave (CW) lasers. Based on the encouraging result that calcium atoms could be desorbed with laser powers of as little as 300 mW at 1050 nm [Hab12], three different atom oven designs were designed, built and tested (Figures 4.9 and 4.10).

In the “back-lit” configuration, a calcium granule[20] was placed inside a hollow cylindric holder (from Macor[21] and later a calcium silicate compound[22]), mounted in a copper housing

[19] Bi-directional coupler ZFBDC20-62HP+ from Mini-Circuits
[20] Calcium granules (42917) from Alfa Aesar; 16 mesh
[21] Macor is a machineable glass-ceramic developed and sold by Corning
[22] DURATEC-1000 from Promat

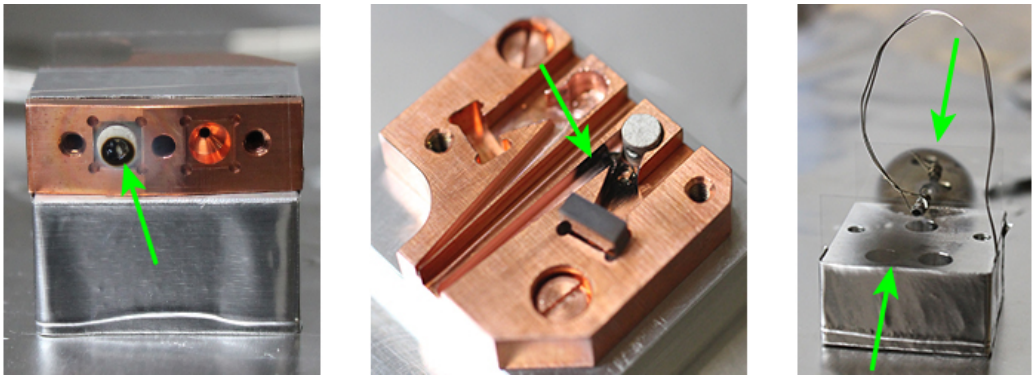

Figure 4.10: Images of tested atom ovens. (left) Calcium depositions (marked by the green arrow) on a glass slide in the direction of the illuminating laser beam for the back-lit configuration. (middle) Visible depositions in the vicinity of the calcium granule in the front-lit design. (right) Proof-of-principle test of laser desorption with a calcium granule inside a stainless steel tube. At sufficiently high laser intensity, depositions on glass slides at both ends of the tube emerge, the stronger one being on the far slide, through which the laser passed.

such that its rotational axis crosses the trapping region. The laser beam was directed onto the granule from the far side of the trap. Atoms emitted from the back side of the granule (as seen by the laser) were spatially filtered by the copper housing. Under the assumption that the exact InfraRed (IR) wavelength should be irrelevant, the oven was tested with fiber-coupled laser light at 940 nm. In multiple test runs, the granule was visibly heated up with laser powers up to 400 mW for up to 2 h. While a lot of calcium atoms were deposited on a glass slide on the front (Figure 4.10), no depositions could be detected on a glass slide at the output end of the oven.

The "front-lit" configuration differed from the back-lit configuration in that atoms desorbed from the front side (as seen by the laser) of the granule were to be directed towards the trapping region. A protected-silver mirror reflected the laser from the same direction as before onto the granule. The test results were that the vicinity of the granule became coated with calcium, sometimes not isotropically but in a seemingly directed way. This might be explained by the fact that the plume from laser ablation always comes out perpendicular to the surface [Bak06, Section 4.3.3]. However, atom deposition in the direction of the trap could not be observed for a flat-polished calcium granule either. Another issue with this design was the laser burning of the mirror surface after it had been coated with calcium and exposed to air.

In the "direct-lit" configuration, thermal insulation of the granule was increased by placing it in a larger Macor housing with reduced contact to copper parts. The desorption laser illuminated the granule from the direction of the trap. Due to unknown reasons, calcium depositions on a glass slide in front of the granule could not be produced by laser powers of up to 1.4 W. Possibly, thermal dissipation through the Macor was too high.

The proof-of-principle experiment in [Hab12] was then meant to be repeated (Figure 4.10).

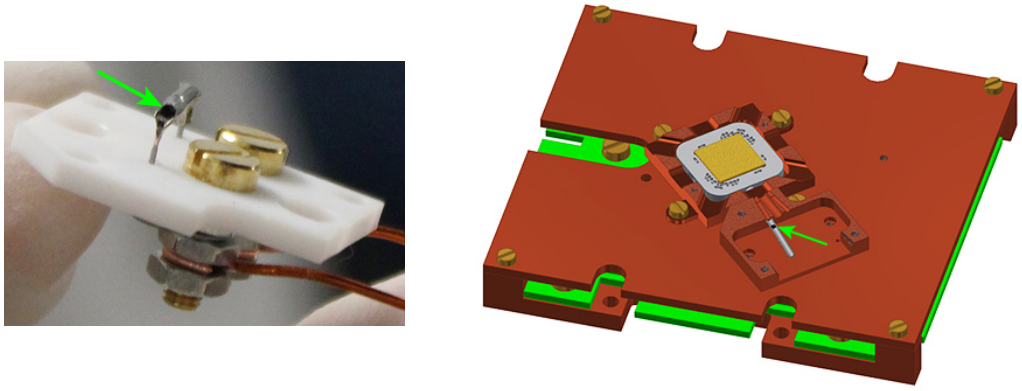

Figure 4.11: (left) Image of the resistively heated oven. A thin-walled stainless steel tube houses calcium granules (green arrow) and is fixed by wires spot-welded to its ends. The wires extend through an insulating PTFE mount and are clamped to screws by nuts. Current-supplying wires are connected to the screws in the same way. (right) CAD model of the trap assembly including CEB (green), cage around the trap (yellow), and the oven mounted next to it.

but it was found that to produce visible calcium depositions required a laser power of 800 mW at 1051 nm, substantially higher than reported for the previous experiments. Irreproducible beam pointing and the granule surface quality might have been the problems here and in the cases described above.

Since reliable creation of an atom beam in the direction of the trapping region was not achieved with the laser-heated ovens, we have built a resistively heated oven, which introduces a large heat load (on the order of 3.5 W) during loading but performs reliably. Tantalum wires[23] were spot-welded to two ends of a steel tube[24] with an inner diameter of 1 mm and anchored with nuts on screws fixed in a PTFE lid on the oven housing (Figure 4.11). The open end of the steel tube containing the calcium granule is oriented toward the trapping region. With the electric resistance of the thin-walled steel tube being the highest in the supply circuit, the tube can be resistively heated. We typically operate the oven at a current of 3.5 A and a voltage of 1 V. Evaporated calcium atoms are spatially filtered by a 0.8 mm diameter aperture in the oven's copper housing before flying through the trapping region.

4.1.5. Ultra-high-vacuum chamber

The UHV chamber houses the heart of the experimental setup, the SET assembly, as well as the rf resonator, and the imaging objective (Figure 4.12). It is made from OFHC copper[25], a material with high thermal conductivity and low magnetizability [Eki06; Fic92]. It was

[23] Tantalum wire (10349) from Alfa Aesar; 0.5 mm diameter
[24] Precision miniature tubing (89935K228) from McMaster-Carr; stainless steel 316, 1 mm inner diameter, 100 µm wall thickness
[25] OFHC copper from Montanwerke Brixlegg, annealed at Härterei Arbon

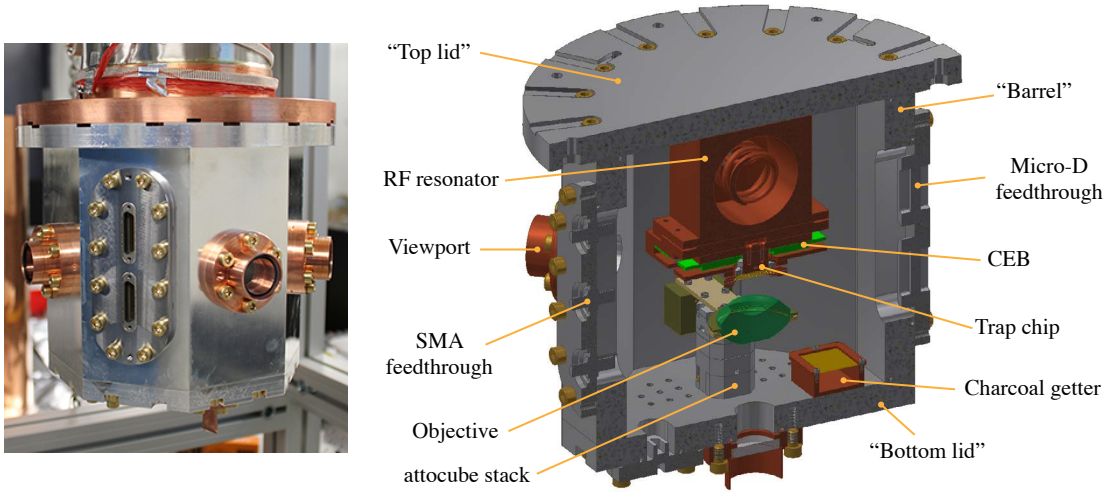

Figure 4.12: (left) UHV chamber mounted on the cryostat cold plate. (right) The UHV chamber houses the SET, CEB, and rf resonator, as well as the imaging objective on an attocube stack and a charcoal getter for increased cryopumping. SMA and Micro-D feedthroughs provide electrical access, viewports on the barrel and bottom lid optical access for laser beams and imaging.

designed as a hermetically sealed pillbox, to be evacuated and sealed before cooling in the cryostat, which promises extremely high vacuum, on the order of 10^{-16} mbar as reported in [Gab90].

Hermetic sealing of a low-temperature vacuum vessel is not trivial. The seals must compensate differences in thermal contraction coefficients. A common technique of sealing uses indium O-rings compressed between the sealing parts [Lim86; Rot97; Ste10]. Rectangular grooves around every opening in the barrel are filled with indium wire[26] matched by lips on the opposite flanges and lids (Figure 4.13). Brass M5 screws lubricated with grease[27] were used to tighten the sealing parts,[28] whereby the indium is compressed into the remaining volume in the grooves and forms a vacuum tight, low-temperature compatible seal. In a test run, we evacuated the UHV chamber outside the cryostat and sealed it by pinching off the copper tube connected to a flange on the bottom lid (not visible in Figure 4.12). With the chamber mounted inside, the cryostat was then pumped and cooled. Unexpectedly, the viewport windows on the UHV chamber did not withstand the full temperature cycle down to 4 K (Section "Optical access" below).

As a result of this, we relaxed the criterion of hermetic sealing. The UHV chamber is now pumped together with the isolation vacuum in the cryostat through the hole formerly covered by the pinch-off flange before every cool down. At low temperature, cryopumping decreases the pressure inside the UHV chamber sufficiently to prevent collisions of background-gas

[26] Indium wire, 2 mm diameter (43265) from Alfa Aesar
[27] Cryogenic high vacuum grease Apiezon N from Apiezon
[28] Brass screws are used everywhere out- and inside the UHV chamber where strong tightening is required because brass has a similar thermal contraction coefficient as copper but does not contact weld to it.

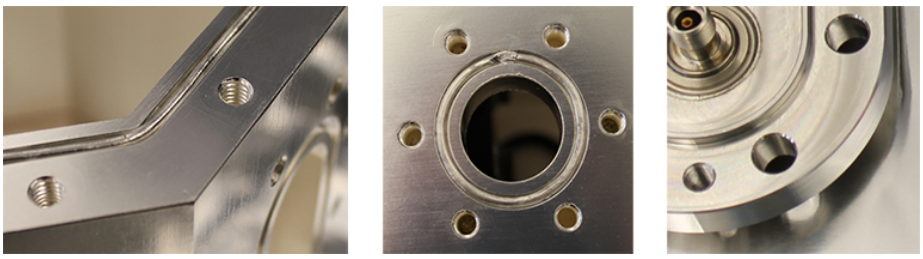

Figure 4.13: Cryogenic vacuum sealing with indium O-rings. Indium wire is placed in groves in the barrel around all openings for lids (left) and flanges (middle), which have matching lips (right) to compress the indium and form a vacuum tight seal.

molecules with trapped ions from being the limiting factor for ion storage time. We were able to keep an ion trapped for 2 days with the cooling lasers on (with the cooling lasers off, we typically lose ions within 1 min).[29] Cryopumping is further aided by a charcoal[30] getter, which increases the cryosorption area [Ant09; Day06]. The surface of the OFHC vacuum vessel consisting of barrel, top and bottom lids was silver plated[31] to reduce oxidization and emissivity, which reduces heating due to thermal radiation.[32]

Optical access

Viewports on the octagonal UHV chamber barrel and bottom lid allow for optical access to the ion while blocking any line of sight for gas particles from the isolation vacuum. Two distinct types of viewports were built. After the vacuum-tight version was found to malfunction, a second generation of viewports was implemented that does not seal the UHV chamber hermetically.

The two main problems with low-temperature compatible vacuum windows are the glass-to-metal seals and strain-induced birefringence in the otherwise isotropic glass due to nonuniform clamping forces. A solution are the custom low-stress vacuum windows reported in [McM04]. Adapted from that design, glass windows[33] were epoxied[34] on the thin tubes (100 µm wall thickness) of copper flanges with a robust base for indium-O-ring sealing (Figure 4.14 (left)). The viewports were successfully tested for vacuum tightness at room and liquid nitrogen temperature. However, after the first temperature cycle down to 4 K, some of the viewport windows had fallen off and others had started cracking. The difference to the original design was that we had epoxied the windows onto the tubes instead

[29] Antohi et al. also found that not hermetically sealing the innermost vacuum chamber did not adversely affect ion lifetime [Ant09].
[30] Charcoal activated, granuled (22631.293) from VWR
[31] Silver plating done by RERO AG
[32] In hindsight, the emissivity could have been reduced further by polishing the surfaces before and after silver plating.
[33] Laser Grade Windows PW1-1012-UV from Melles Griot
[34] STYCAST 2850 FT with curing agent CATALYST 24 LV from Emerson and Cuming, now Henkel LOCTITE

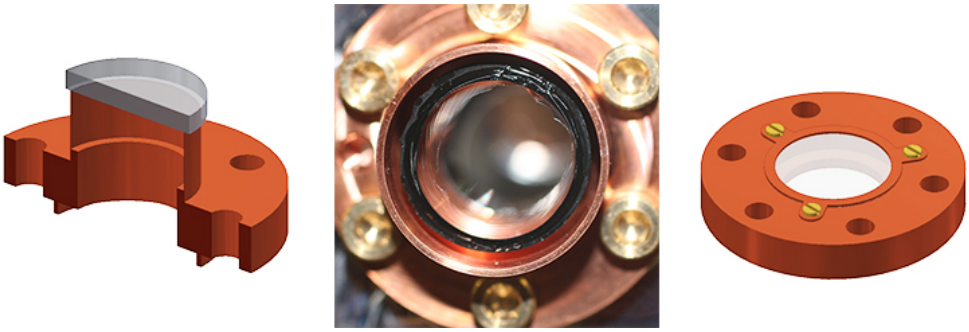

Figure 4.14: (left) Low-stress vacuum viewport design adapted from [McM04]. The copper flange has a thin-walled tube to hold the window and a lip at the bottom for sealing with an indium O-ring. (middle) Broken viewport after first full temperature cycle. The window has fallen off while some glass shards still stick to the epoxy. (right) Current viewport design, in which the window is loosely mounted into the copper flange and fixed by a thin copper clamp.

of into them, so that the contracting copper tubes must have exerted a too strong shear force on the glass surfaces.

With the requirement of vacuum tightness lifted, the viewport windows[35] did not need to be epoxied or compressed to the flange anymore. In the current design, the windows are loosely placed inside a copper flange and held in place by thin copper clamping rings (Figure 4.14 (right)). Six viewports on the barrel enable irradiation of trapped ions along three axes at angles of 0, 45 and 135° with respect to the trap axis. A viewport on the bottom lid is used for imaging the ions.

An ongoing problem we have with the viewports on the UHV chamber are white, semi-transparent coatings that occur on the side of the isolation vacuum. They build up over time of operation and become grave after two to eight months. The strong 729 nm laser keeps an aperture clear where it passes the window, but the other lasers are increasingly diffused by the coatings. The windows can be cleaned by heating the cryostat to room temperature; the coatings vanish mostly at a temperature of $\approx 250\,\mathrm{K}$ and entirely at $\approx 300\,\mathrm{K}$. I discuss possible reasons for the fogging of the cold windows at the end of Section 4.1.6, after introducing the cryostat.

Electrical access

Electrical connections to the devices inside the UHV chamber are facilitated by electrical feedthroughs, which were laser-welded into stainless-steel flanges with lips for indium O-ring compression (Figure 4.15).

The analog and digital lines to the CEB run through two 51-pin micro-D type connectors[36]. On the inside, Kapton-insulated copper wires[37] are directly soldered into the female pins

[35] UV fused silica uncoated optical windows (1-OS-2-0254-5) from Altechna
[36] Micro-D type connector (23053-01-W) from CeramTec
[37] Kapton-insulated copper wire (311-KAP-025) from allectra

Figure 4.15: Micro-D type (left and right) and SMA (middle) connectors laser-welded into stainless steel flanges with lips for compression sealing with indium O-rings.

(cryo-compatible male plugs do not seem to be purchasable). At the other ends, the wires are soldered to card-edge connectors[38] with gold-coated beryllium copper contacts in a PolyButylene Terephthalate (PBT) housing for plugging onto the CEB.

The attocubes (Section 4.3.1) require 15 lines, 5 lines per axis for closed-loop positioning, which run through a single 15-pin micro-D type connector[39] welded into a flange that is mounted on the bottom lid. The provided wires were also directly soldered into the female receptacles of the feedthrough.

The rf drive signal is fed through one of three SMA connectors[40] welded into a single flange. The ends of a cryo-compatible coaxial cable[41] are soldered to the feedthrough pin and the input of the rf resonator. Leaks in the welding seam were sealed with epoxy[42].

The atom oven is the only device requiring a higher current, typically 3.5 A. The enameled copper wires (0.7 mm diameter) are routed through the hole in the bottom lid that was previously used for pre-pumping through the copper pinch-off flange.

4.1.6. Cryostat

The UHV chamber is bolted[43] to the cold plate of a cryostat cooled by liquid helium and a 4 K pulse tube cryocooler[44] with a specified cooling capacity of 0.9 W at 4.2 K (2nd stage) combined with 31.5 W at 45 K (1st stage). The cryostat design features cooling with no mechanical contact between the 4 K heat exchanger and the cryogenic device. Instead, the heat transfer is achieved by helium in the liquid or gas phase contained inside a gas-tight chamber and cooled by the 1st and 2nd stage heat exchangers of the cryocooler (Figure 4.16).

[38] Female card edge connectors (HCC08DREN, HCC20DREN) from Sullins
[39] Micro-D type connector (23051-01-W) from CeramTec
[40] Coaxial 50 Ω SMA connector (15263-03-W) from CeramTec
[41] Coaxial single wire, double strand GVLZ034 from GVL Cryoengineering Dr. George V. Lecomte GmbH
[42] STYCAST 2850 FT with curing agent CATALYST 24 LV from Emerson and Cuming, now Henkel LOCTITE
[43] We apply Apiezon N high vacuum grease between bolted copper parts inside and on the UHV chamber to increase heat conductivity.
[44] Cryocooler PT410-RM with compressor CP289C from Cryomech

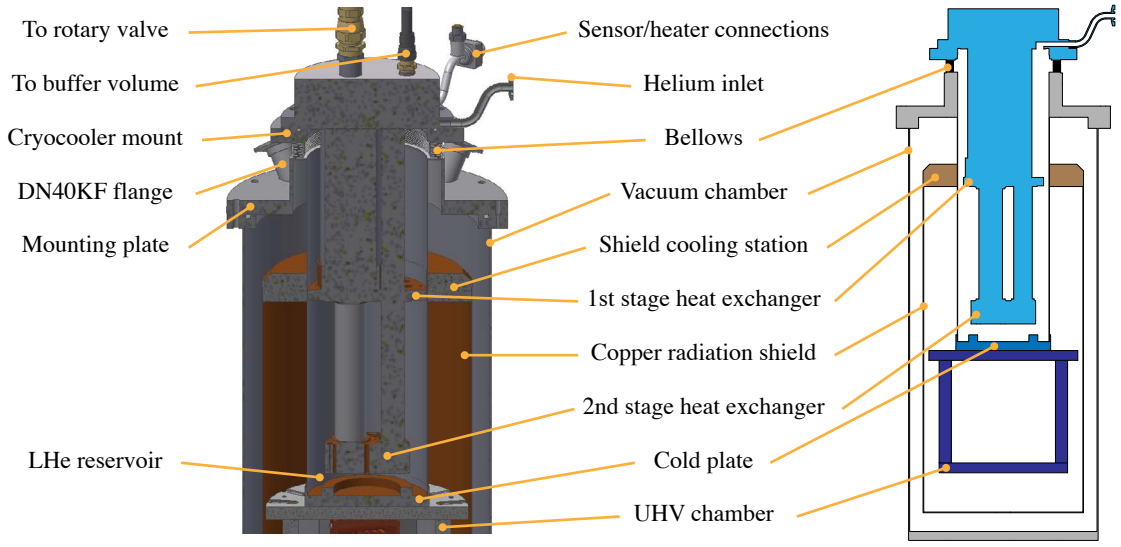

Figure 4.16: Cross-section view and schematic of the cryostat. The UHV chamber is attached to the cold plate of the liquid helium reservoir, into which the cold parts of the pulse tube cold head extend. The latter is mechanically isolated from the rest by a bellows. The radiation shield in the isolation vacuum and around the UHV chamber is convection cooled by the 1st stage heat exchanger. The entire apparatus is bolted via the mounting plate to a stand on the optical table. The schematic on the right-hand side clarifies the connections and gaps between the parts.

A bellows mechanically isolates the cryocooler mount from the cryostat mounting plate, so that vibrations generated by the remote motor and rotary valve are not transmitted to the vacuum chamber and cold plate [Wan10].

In order to reduce radiation losses, the lower part of the liquid helium reservoir and the UHV chamber are surrounded by a copper radiation shield. It is anchored to the shield cooling station, to which cooling capacity is transferred from the 1st stage heat exchanger by convection heat transfer of gas via the narrow gap between the two. Holes in the shield align with the UHV chamber viewports and DN40KF viewport flanges in the cryostat vacuum chamber, which are sealed with fused silica viewports[45] using Viton[46] O-rings.

Electric feedthroughs and cabling

The electrical feedthroughs on the UHV chamber are mirrored by feedthroughs in DN40KF flanges[47], sealing the flanges on the cryostat mounting plate. Inside the isolation vacuum, connections to all micro-D type feedthroughs are made with cryo-compatible vacuum-side plugs[48]. The wires inside the isolation vacuum were chosen to be as thin as possible for the respective applications and wrapped around the helium dewar a few times to reduce

[45] Fused silica viewports KVPZ40/32Q-NM from MDC Vacuum Ltd
[46] Viton is the registered trade mark of DuPont for fluoroelastomers.
[47] Micro-D type (23057-01-KF and 23055-01-KF) and SMA (21233-01-KF) connectors from CeramTec
[48] Micro-D type vacuum-side plugs (23111-01-A and 23109-01-A) from CeramTec

the heat load on the cryogenic parts. The analog voltage lines are PerFluoroalkoxy Alkane (PFA) insulated, 70 µm diameter constantan wires[49] with a measured resistance on the order of 220 Ω. For the high-frequency digital control signals to the electrode voltage switches, 100 µm constantan twisted pair wires in a cryogenic ribbon cable loom[50] were used. The rf signal runs through the same type of coaxial cable as inside the UHV chamber. The wires from the atom oven are soldered to a 9-pin D-sub connector[51], which is specified for currents of up to 5 A per pin.

Magnetic field

A pair of magnetic-field coils is attached to viewport flanges on opposite sides of the cryostat vacuum chamber (Figure 4.2). They consist of 930 loops of enameled 0.5 mm copper wire on an aluminum drum, which shapes the solenoid to an inner diameter of 10 cm, an outer diameter of 15 cm and a width of 13 mm. The distance between the coils is 28.5 cm. Operated in series at a voltage of 21.44 V and a current of 310 mA, they produce a magnetic field of 3.85 G at the position of the ion. Two additional coils are mounted similarly for potentially compensating the earth's magnetic and stray fields but were not required so far.

Mounting and moving the cryostat

The cryostat mounting plate is bolted to a 12 mm thick rectangular aluminum plate with a centered hole (Figure 4.17). That plate in turn is supported by a stand with four aluminum profile rods[52] in its corners. The remote rotary valve and buffer volumes, which are connected to the cold head via flexible lines, are mounted to an equipment sledge on a rail system above the cryostat.

In order to open the cryostat, it needs to be placed on a trolley besides the optical table with a suitable hole underneath the cryostat. We move the cryostat between optical table and trolley by lifting it with ratchet hoists hooked into eye bolts on the equipment sledge and top plate of the cryostat stand, and translating the sledge along the rail system (Figure 4.17).

Operation

Before the cryostat can be operated, the helium reservoir and the vacuum chamber must be evacuated. First, with both mechanical valves in the helium supply assembly (Figure 4.18 (left)) open, the dewar and hoses are evacuated with a TurboMolecular Pump (TMP)[53] to a pressure below 1×10^{-5} mbar. With valve 2 closed, the TMP is disconnected and used for pumping the isolation vacuum of the cryostat (Figure 4.18 (right)). After the

[49] Constantan wire (TFCI-003) from Omega Engineering
[50] Cryogenic ribbon cable loom (A8-312) from Oxford Instruments
[51] D-sub connector (KF40-SUBD-9-DE-CE-SSG) from VACOM
[52] Aluminum extrusion (Base 50) from Kanya
[53] TMP HiPace 80 from Pfeiffer Vacuum

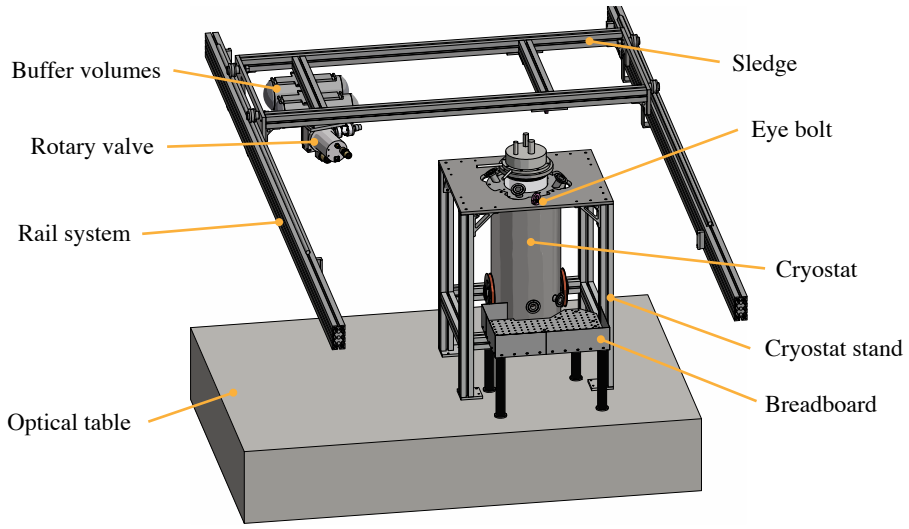

Figure 4.17: Cryostat stand and equipment sledge. The sledge holds the rotary valve and buffer mounts (hoses between those and the cryostat are not shown), and is used for moving the cryostat off and onto the optical table for opening.

vacuum chamber reaches a pressure of 1×10^{-3} mbar, valve 4 is closed, and the TMP can be removed from the assembly.

The pulse tube compressor can then be switched on. When the cooling starts, the helium bottle outlet is opened and the reducing valve set to an inlet pressure of 1 atm. The pressure inside the helium dewar is then stabilized to between the variable inlet pressure and the release pressure of the check valve[54] of 0.5 psig. The 2nd stage heat exchanger reaches a temperature of 4.2 K after 16 to 20 h of cooling, at which point liquefaction of helium starts and a dynamic equilibrium of helium in the gas and fluid phase is reached. We monitor the temperatures at the 2nd stage heat exchanger, the resonator near the CEB, and the shield cooling station with silicon diode temperature sensors[55] (Figure 4.19).

For heating of the cryostat back to room temperature, the helium bottle outlet is closed and the compressor switched off. After re-thermalization of the apparatus, which takes up to two days, the ball valve on the vacuum chamber can slowly be opened to flood the vacuum chamber with air. When the pressure inside has reached ambient pressure, the chamber can be opened.

Performance

During regular experimentation with trapped ions, the cryostat maintains an equilibrium temperatures of 4.5 K at the resonator, 4.2 K at the 2nd stage heat exchanger, and 48 K at

[54] Check valve 559B-2MP-.5 from Circle Valve Technologies
[55] Silicon diode temperature sensors Model Si-410 attached to temperature instruments Model 9700 and Model 9302 from Scientific Instruments

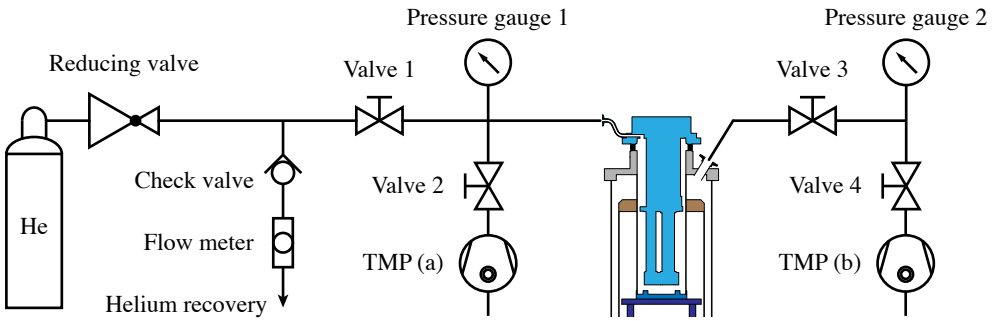

Figure 4.18: Assemblies for helium supply (to the left of the cryostat) and isolation vacuum (to the right). (left) The dewar and hoses are pumped with valves 1 and 2 open. After closing valve 2, the TMP can be removed from position (a) in this assembly. With the helium bottle outlet open, the pressure inside the dewar is kept between the inlet pressure of the reducing valve and the release pressure of the check valve. Released helium is fed into a helium-recovery facility. (right) For evacuating the cryostat, the TMP is mounted in position (b) behind valve 4. Pressure gauge 2 is left in place during operation to monitor the isolation vacuum pressure.

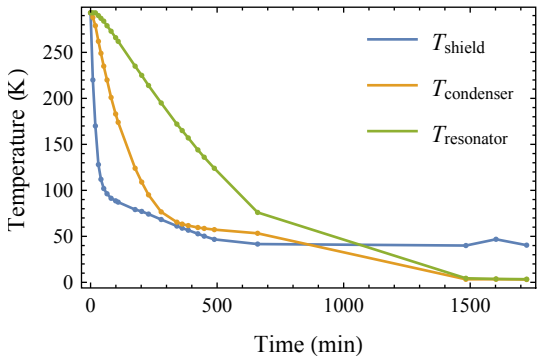

Figure 4.19: Temperature curves during the cooling process. The sensors are placed on the 2nd stage heat exchanger, the resonator near the CEB, and the shield cooling station.

the shield cooling station. While loading an ion, the resonator reaches a peak temperature around 5 K; afterwards the system takes half an hour to settle.

One issue with our setup are vibrations. The system in [Wan10] was reported to be "vibration-free" but we have had it slightly modified. In the original design, the pulse tube cold head was mounted on a stand, with the vacuum system, dewar, and cryogenic device being suspended by the flexible bellows. Since we need the UHV chamber to be stably referenced to the laser beams on the optical table, our vacuum chamber is mounted on the cryostat stand while the pulse tube cold head is floating on the bellows. We have thus far not managed to fix it in a position where the 1st stage heat exchanger does not touch the helium dewar wall (Figure 4.16). We could reduce lateral oscillations at the rotary valve frequency of 1.4 Hz by bypassing the bellows with steel bolts, but not fully mitigating them.

Another problem is the fogging of the cold windows on the UHV chamber (Section 4.1.5),

which hints at the adsorption of residual gas. We did, however, not find any leaks in the cryostat, and the pressure inside the isolation vacuum remains on the order of 10^{-7} mbar during operation. Possibly, residual gas enters the cryostat through the Viton O-rings sealing the room-temperature viewports [Thi14], or volatiles in the Viton itself outgas. In both cases, cryo-pumping of gaseous particles in the isolation vacuum via adsorption on cold surfaces would explain the non-increase in pressure.

4.2. Lasers

We utilize laser beams for PhotoIonization (PI) of neutral calcium atoms and for manipulating $^{40}Ca^{+}$ ions at frequencies given in Table 4.2. The (master) lasers are extended-cavity diode lasers, except for the diode laser at 375 nm. The light from the master laser at 729 nm is amplified with a Tapered Amplifier (TA). Light at 397 nm is produced by frequency doubling TA-amplified light at 794 nm in a bow-tie cavity with a nonlinear Lithium triBOrate (LBO) crystal. Light at 423 nm is generated from 846 nm by Second-Harmonic Generation (SHG) in a fiber-based Periodically Poled potassium Titanyl Phosphate (PPKTP) waveguide chip[56].

Table 4.2: List of the laser sources used. Given are the desired wavelengths, the frequencies of the master lasers as measured with our wavelength meter, the driven transitions (or use for PI), the source systems from Toptica, and the specified laser linewidths within 5 µs.

Wavelength	Frequency	Transition	Source	Linewidth (5 µs)
397 nm	377.6114 THz	$S_{1/2} \leftrightarrow P_{1/2}$	TA-SHG pro	< 1 MHz
729 nm	411.0422 THz	$S_{1/2} \leftrightarrow D_{5/2}$	BoosTA pro	< 0.5 MHz
854 nm	350.8625 THz	$D_{5/2} \leftrightarrow P_{3/2}$	DL pro	< 1 MHz
866 nm	346.0002 THz	$D_{3/2} \leftrightarrow P_{1/2}$	DL pro	< 1 MHz
375 nm	–	PI	iBeam smart	–
423 nm	354.5392 THz	PI	DL 100 (846 nm)	< 1 MHz

Some light from the (master) lasers at 729, 794, 846, 854 and 866 nm is fed into a wavelength meter[57] for coarse frequency tuning and monitoring, as well as into Fabry-Pérot cavities for frequency stabilization (Section 4.2.1).

All laser sources are located in a lab adjacent to the one with our ion-trap apparatus. The light is brought to our optical table using optical fibers[58]. There, the beams are further prepared for the experiments. The PI beams can be switched on and off using an electronic shutter[59]. The dipole and quadrupole beams are frequency-shifted and

[56] Fiber module including PPKTP SHG waveguide chip from ADVR
[57] Wavelength meter WS6-200 from HighFinesse/Ångström
[58] Fibers PMC-400Si-2.3-NA012-3-APC-2000-P for 397 nm, and PMC-360Si-2.3-NA012-3-APC-2000-P for 375 and 423 nm from Schäfter + Kirchhoff; and PMJ-3A3A-850-5/125-1-20-1 for 854 and 866 nm from OZ Optics
[59] C-mount Electrical Shutter (87-208) from Edmund Optics

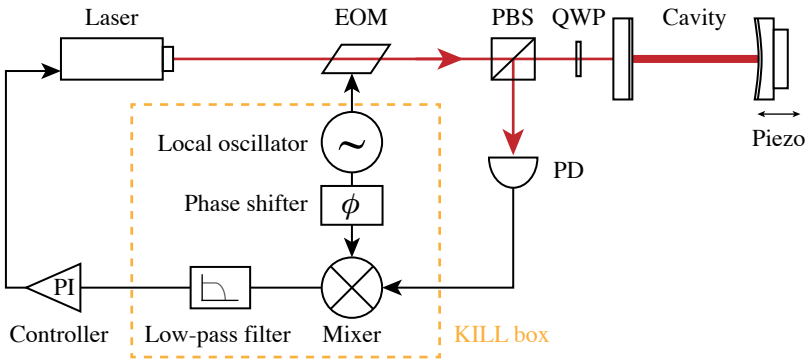

Figure 4.20: Schematic of a PDH locking setup. The signal from the local oscillator is used to modulate sidebands on the laser and to mix the PD signal from the cavity-reflected beam. The low-pass-filtered error signal is fed into a PIC, which then feeds back on the laser. The marked (dashed orange line) components are integrated in a KILL box. The length of the cavity can be adjusted with a piezo for coarse detuning of the locked laser. Adapted from [Bla01].

switched on microsecond timescales using Acousto-Optic Modulators (AOMs) driven by computer-controlled Direct Digital Synthesizer (DDS) boards (Section 4.2.2).

Finally, the laser beams are coupled into optical fibers for mode cleaning and guiding them onto the optical breadboards around the cryostat, where the light is appropriately expanded and focused on the trapped ions (Section 4.2.3). Besides Polarization-Maintaining (PM) Single-Mode (SM) fibers, we use a Photonic-Crystal Fiber (PCF), in which we combine the light beams at 375, 423, 397, 854 and 866 nm.

4.2.1. Frequency stabilization

All our lasers for manipulating $^{40}Ca^{+}$ ions are frequency stabilized by locking them to optical resonators using the *Pound-Drever-Hall* (PDH) technique [Dre83]. The dipole lasers are referenced to "low-finesse" cavities with a finesse[60] of 36 against slow drifts. These cavities are passively temperature stabilized and drift by less than 10 MHz in 12 h. One mirror of each cavity is mounted on a piezo, which allows for coarse tuning of the laser frequencies. The quadrupole laser is locked to a "high-finesse" cavity with a finesse of 270 000, whereby the linewidth is narrowed to below 10 Hz[61]. I discuss the PDH locking scheme by the example of the 866 nm laser.

The low-finesse cavities were designed and built by Frieder Lindenfelser and are described in detail in [Lin11]. They consist of two mirrors with a reflectance $r^2 = 0.92$, one flat and the other concave with a radius of curvature of 100 mm, at a distance $L = 99$ mm. From Equation (D.1) follows that a Gaussian beam with a beam waist of radius 54 µm at the position of the flat mirror is reflected by the concave mirror onto itself, which makes it

[60] The finesse of a cavity only depends on the coefficient of reflectance r of the two mirrors and is given by $\mathcal{F} = \pi r/(1 - r^2)$ [Hec02, Chapter 9.6].
[61] Private communication with Christa Flühmann.

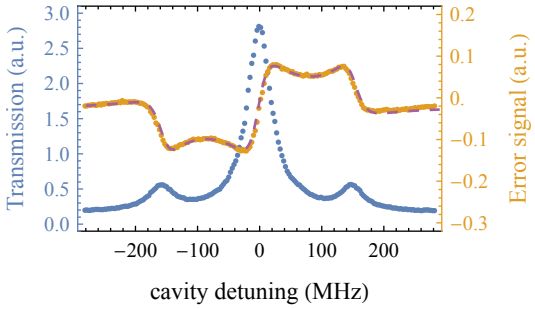

Figure 4.21: Example data of a transmission (blue) and PDH error (orange) signal from a low-finesse cavity versus cavity detuning, and a fitted error signal function (purple) according to Equation (4.2). The scaling of the abscissa was calculated from the sidebands at modulation frequencies of 154 MHz. The transmission curve has a FWHM ≈ 47 MHz, which corresponds to a cavity finesse $\mathcal{F} \approx 31$ at the free spectral range $\Delta\nu_{\mathrm{fsr}} \approx 1490$ MHz. The dispersive part of the error signal around its center can be used for laser-frequency stabilization.

the fundamental resonator mode. Assuming that the cavity is lossless, a laser beam with frequency ω_l and incoming electric field amplitude $E_i = E_0 \mathrm{e}^{-\mathrm{i}\omega_\mathrm{l} t}$ at the flat mirror that is perfectly overlapped[62] with the Gaussian resonator mode will be reflected with an amplitude reflection coefficient of [Hec02, Chapter 9.6]

$$F(\omega_\mathrm{l}) = \frac{E_r}{E_i} = -\frac{r(1 - \mathrm{e}^{\mathrm{i}\omega_\mathrm{l}/\Delta\nu_{\mathrm{fsr}}})}{1 - r^2\,\mathrm{e}^{\mathrm{i}\omega_\mathrm{l}/\Delta\nu_{\mathrm{fsr}}}},$$

where $\Delta\nu_{\mathrm{fsr}} = c/2L$ is the *free spectral range* of the cavity. At resonance, that is at $\omega_\mathrm{l}/2\pi = n\Delta\nu_{\mathrm{fsr}}$ with $n \in \mathbb{N}$, the entire laser power is transmitted through the cavity. Around these resonances, the imaginary part of $F(\omega_\mathrm{l})$ is dispersive and can be used for stabilizing the laser frequency to the cavity's resonance. In the PDH scheme (Figure 4.20), this works as follows.

The 866 nm laser light is phase-modulated using a fiber-based Electro-Optic Modulator (EOM)[63] at frequency $\Omega \approx (2\pi)\,150$ MHz and modulation strength $\beta \ll 1$ to generate frequency sidebands,

$$\begin{aligned} E_i &= E_0\,\mathrm{e}^{-\mathrm{i}(\omega_\mathrm{l} t - \beta \sin\Omega t)} = E_0\,\mathrm{e}^{-\mathrm{i}\omega_\mathrm{l} t} \sum_{j=-\infty}^{\infty} J_j(\beta)\,\mathrm{e}^{\mathrm{i}j\Omega t} \\ &\approx E_0\Big[J_0(\beta)\,\mathrm{e}^{-\mathrm{i}\omega_\mathrm{l} t} + J_1(\beta)\,\mathrm{e}^{-\mathrm{i}(\omega_\mathrm{l}+\Omega)t} - J_1(\beta)\,\mathrm{e}^{-\mathrm{i}(\omega_\mathrm{l}-\Omega)t}\Big], \end{aligned} \tag{4.1}$$

where J_j are Bessel functions of the first kind. The reflected beam from the cavity is

[62] Note that higher-order rectangular transverse modes are excited when the beam is not aligned with the optical axis of the cavity. Higher-order cylindrical transverse modes are excited when the waist spot size is not matched to the fundamental resonator mode.

[63] Integrated optical phase modulator PM830 from JENOPTIK

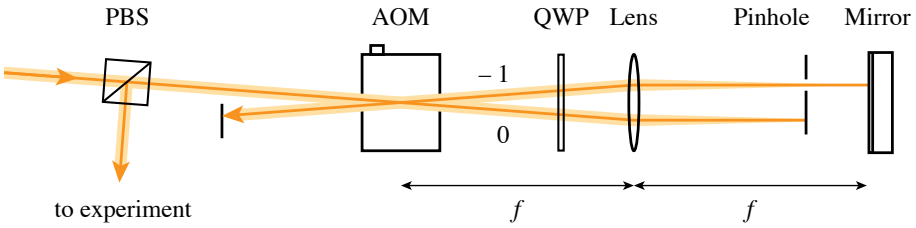

Figure 4.22: AOM double pass setup with changing beam polarization. The incoming, horizontally polarized beam passes the AOM and is partially diffracted. The deflected beam (here in -1st order) is retroreflected using a lens and a mirror, while the 0th-order beam is blocked. The lens makes the beam parallel to the optical axis, regardless of the deflection angle. It, furthermore, focuses the beam onto the mirror and thereby ensures that it is collimated after the second pass. The beam then crosses the AOM at the same angle as before and is deflected a second time. Having passed the QWP twice, the outgoing beam is vertically polarized and hence reflected by the PBS, which separates it from the incoming beam.

separated from the incoming beam using a Polarizing Beam Splitter (PBS) in combination with a Quarter-Wave Plate (QWP), and guided onto a high-frequency PD. Its output signal is mixed with the driving signal at frequency Ω and passed through a low-pass filter, which yields a near-DC error signal of the form [Bla01]

$$\epsilon(\omega_\text{l}) \propto \Im\Big[\Big(F(\omega_\text{l})\,F^*(\omega_\text{l}+\Omega) - F^*(\omega_\text{l})\,F(\omega_\text{l}+\Omega)\Big)\,\mathrm{e}^{\mathrm{i}\phi}\Big], \tag{4.2}$$

depending on the signal phase ϕ introduced between local oscillator and mixer (Figure 4.21). All electronic components mentioned so far are combined in the home-built *Keitch Integrated Laser Lock* (KILL) system [Kei07]. The error signal is fed into a home-built Field-Programmable Gate Array (FPGA)-based[64] *Electronically Variable Interactive Lockbox* (EVIL) [dCle15], which is programed as a PIC and stabilizes the laser frequency by feeding back on the laser's grating piezo.

4.2.2. Acousto-optic modulation

In an AOM, light is scattered off a traveling sound wave inside a crystal. The sound wave is generated by a piezoelectric transducer attached to the crystal and driven at rf frequency ω_rf. When the periodic planes of expansion and compression that change the index of refraction locally are sufficiently wide, diffraction occurs upon fulfillment of the $\pm1^{\text{st}}$-order Bragg condition. This is equivalent to the absorption ($\omega_\text{l}' = \omega_\text{l} + \omega_\text{rf}$) or emission ($\omega_\text{l}' = \omega_\text{l} - \omega_\text{rf}$) of a phonon [Sla58]. We use AOMs to switch and shift the frequency of laser beams.

The diffraction efficiency into the desired order typically ranges from 50 to 80 % over an rf range of ±20 MHz, depending on the AOM model[65]. The tuning range can be doubled

[64] Papilio One board with Xilinx Spartan XC3S500E from Gadget Factory

[65] Some manufacturers distinguish between acousto-optic deflectors and modulators. The modulators have a peak deflection efficiency around the design frequency. Deflectors, on the other hand, are normally

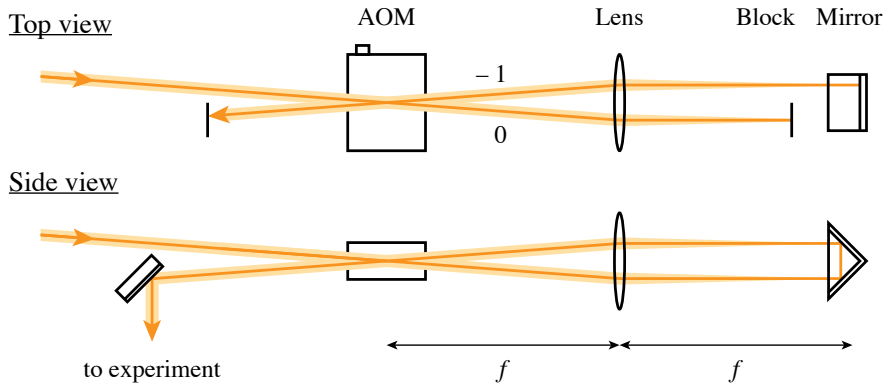

Figure 4.23: AOM double pass setup with constant beam polarization. Viewed from the top, the setup is analogous to the scheme in Figure 4.22. But the outgoing beam is separated from the incoming by a vertical tilt. The tilt of the incoming beam is reversed by a right-angle prism, which offsets the beams vertically behind the lens. The outgoing beam is then picked off with a mirror in a clear-edge mirror mount.

by retroreflecting the diffracted beam and passing it through the AOM a second time. In such a double-pass scheme, the effective deflection angle ideally reduces to zero, which is advantageous for subsequent fiber coupling or beam pointing. If the AOM model is able to diffract both horizontally and vertically polarized light, the frequency-shifted beam can be separated from the incoming beam using a PBS in combination with a QWP (Figure 4.22). If the AOM model requires the incoming light to be vertically polarized, the outgoing beam can be spatially separated using a right-angle prism for retroreflection (Figure 4.23). In both cases, a focusing lens is placed between the AOM and the retroreflector in f-f-configuration. This guarantees that the beam after the first pass is always perpendicular to the mirror, independent of the deflection angle, and that it is collimated again after the second pass through the lens.

All dipole and quadrupole laser beam lines contain AOMs (Figure 4.24). Some AOMs (marked a and b) correct for differences in the required frequencies between the three experiments that share the same laser sources. The last AOM in every beam line (marked c) both shifts the frequency as desired and switches the beam on and off during experimental sequences.

The AOMs are driven with rf signals generated by fixed-frequency sources[66] or by computer-controllable DDS[67] (Section 4.4), and are subsequently amplified, some with an additional pre-amplifier[68]. The maximum output power of 2 W is sufficient for current experiments, but reaching the specified maximum diffraction efficiency of most models

used for deflecting a beam over a certain range of angles, and hence frequencies. They thus usually have a flatter efficiency curve over the specified frequency range.

[66] Novasource M2 and G6 from AtlanTecRF

[67] Milldown DDS1 ChannelCard from Enterpoint

[68] High power amplifier (ZHL-1-2W-S+) and low noise pre-amplifier (ZX60-33LN+) from Mini-Circuits

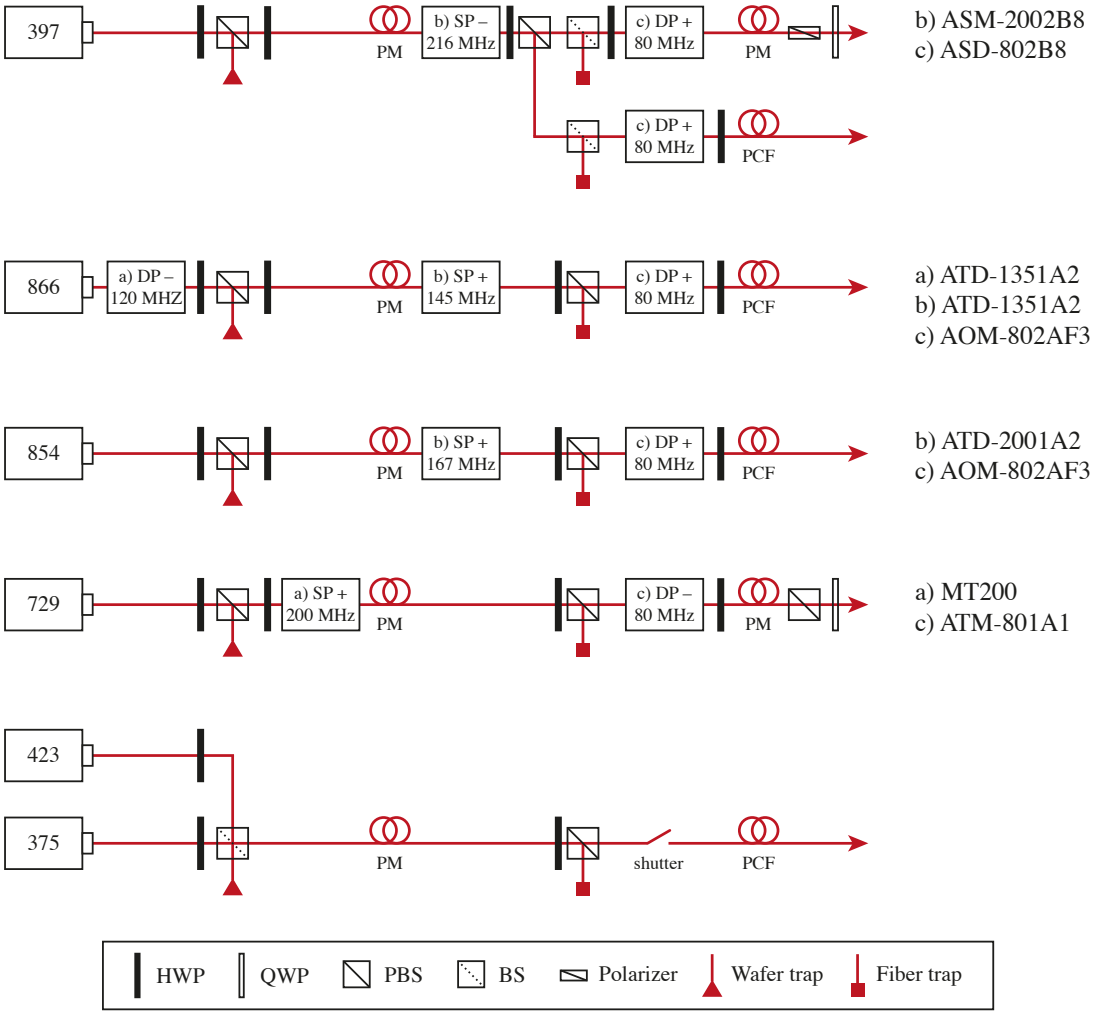

Figure 4.24: AOM and fiber setup of all laser-beam lines. The left-hand fibers transport light between laboratories, the right-hand fibers deliver the laser light to the breadboards around the cryostat (Figure 4.1). The AOMs are operated at or around the given frequencies in either single-pass (SP) or double-pass (DP) mode, with the sign differentiating between -1st and $+1^{\text{st}}$ diffraction order. The DP setups follow the scheme in Figure 4.22, expect for the ones for 397 nm, which use right-angle prisms (Figure 4.23). The AOM model MT200 is from AA OPTO-ELECTRONIC, all others are from IntraAction. The PI beams are switched by a mechanical shutter. Laser light for the other two experiments with $^{40}Ca^{+}$ ions (in a wafer and a fiber-based trap) is split off in the marked places, mostly using a combination of a HWP and a PBS to balance powers.

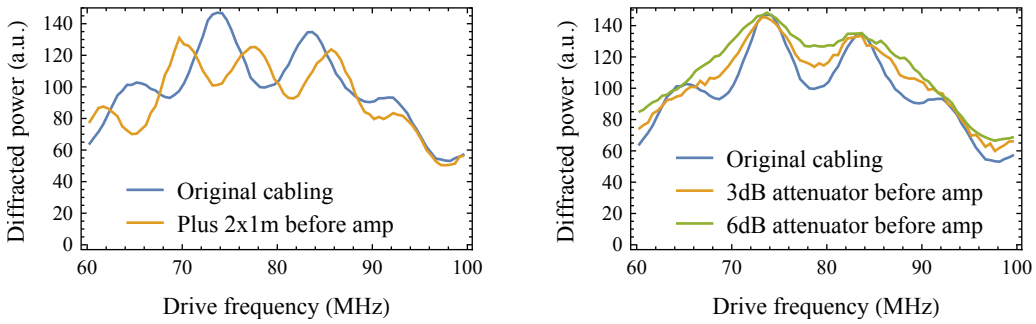

Figure 4.25: Diffraction power spectra for the DDS-driven 397 nm AOM. (left) With the original cabling, resonance peaks occur, which can be shifted by extending the cable between DDS and amplifier. (right) This effect can be mitigated by inserting attenuators before the amplifier, yielding a flatter diffraction curve. The DDS output power was increased accordingly for comparison.

would require a higher power.[69]

The diffraction efficiency is usually maximal for the specified center frequency of an AOM model and decreases below saturation for increasing frequency deviation. However, some beam lines show a resonance-like diffraction efficiency spectrum (Figure 4.25). The free spectral range (distance between two adjacent peaks) corresponds to coaxial resonators formed by the 10 m-long BNC cables (with a internal signal propagation speed of 2×10^8 m/s) between DDSs and amplifiers. The resonance peaks shift when the cable lengths are changed. This effect can be mitigated by inserting an attenuator before the amplifiers, which effectively introduces losses in the resonator and reduces its quality factor. Alternatively, but more involved, one could move the DDSs closer to the amplifiers and use short cables.

4.2.3. Beam delivery

After the AOMs, the laser beams are coupled to optical fibers and delivered to breadboards around the cryostat (Figure 4.1), where they are focused into the trapping region. We use standard PM fibers for the 729 nm beam and the 397 nm beam parallel to the magnetic field axis; and a PCF[70] for the beams at 375, 397, 423, 854 and 866 nm. The four beams are combined using dichroic beam splitters and a bandpass filter (Figure 4.26), and then coupled into the PCF via a plan-achromatic objective[71].

The beams are injected into the vacuum system in such a way that the quadrupole laser is perpendicular to the magnetic field, the single 397 nm beam is parallel to the magnetic field to exclusively drive σ-transitions (Table 3.3), and the beams from the PCF are parallel to the magnetic field and perpendicular to the neutral-atom beam (Figure 4.26). The latter is relevant for addressing the neutral atoms during PI without Doppler shifts. The square

[69] The required rf input power for optimum diffraction in an AOM scales quadratically with the wavelength used.
[70] PCF aeroGUIDE-5-PM (based on fiber LMA-PM-5) from NKT Photonics
[71] Plan achromatic objective PLN 20X from Olympus

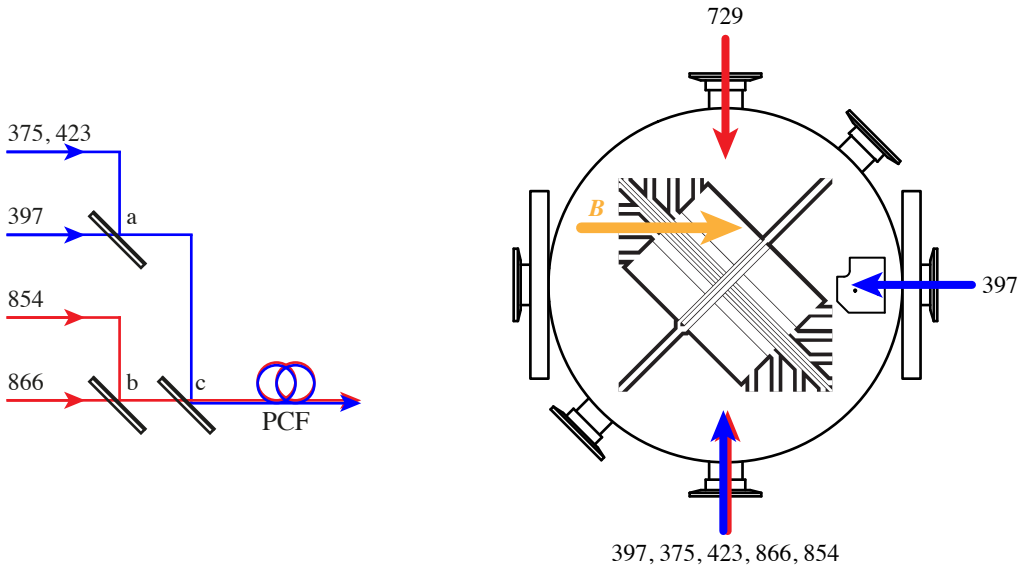

Figure 4.26: (left) Combination of all beams going into the PCF using a bandpass filter (a, FF01-390/18-25 from Semrock) and dichroic beam splitters (b, ZT860lpxr from Chroma Technology, and c, Di02-R442-25x36 from Semrock). (right) Laser beam delivery to the ion trap as seen when looking at the mounted SET chip from below. Depicted are also the cryostat viewports, the magnetic-field coils and the atom oven.

trap chip is positioned such that the beams are perpendicular to its edges and the trap axis is at 45° with respect to all laser beams. In order to scatter the least amount of light, the beams are made nearly parallel to the chip surface, particularly the ones at 397 nm, from which scattered photons would be registered in the imaging system. At a focal-spot height of 50 µm above the trap chip and a distance of 5 mm from its edges, this poses constraints on the minimal spot sizes. For minimal beam clipping at the edges, the near-UV beams should have a spot size (radius) between 20 and 30 µm, and the near-IR beams a spot size between 30 and 45 µm, which can be calculated from Equation (D.1).

The beam at 729 nm is focused to a beam waist diameter of 49 µm. After collimation at the fiber output,[72] the beam is expanded to a spot diameter of 5 mm, transmitted through a PBS and a HWP to clean and rotate its polarization, and finally focused using a 250 mm plano-convex lens[73].

The circularly polarized beam at 397 nm parallel to the magnetic field is focused to a spot diameter of 55 µm using only two lenses. Instead of collimating, the multi-element fiber-output lens[74] is adjusted such that the beam still expands and is focused into the trap region by a 175 mm plano-convex lens[75]. Before the second lens, the beam polarization

[72] Fixed focus collimation package F240APC-780 from Thorlabs
[73] Plano-convex lens LA1461-B from Thorlabs
[74] Collimating lens for diode lasers GLC-8.0-8.0-405 from CVI Laser Optic
[75] Plano-convex lens LA1229-A from Thorlabs

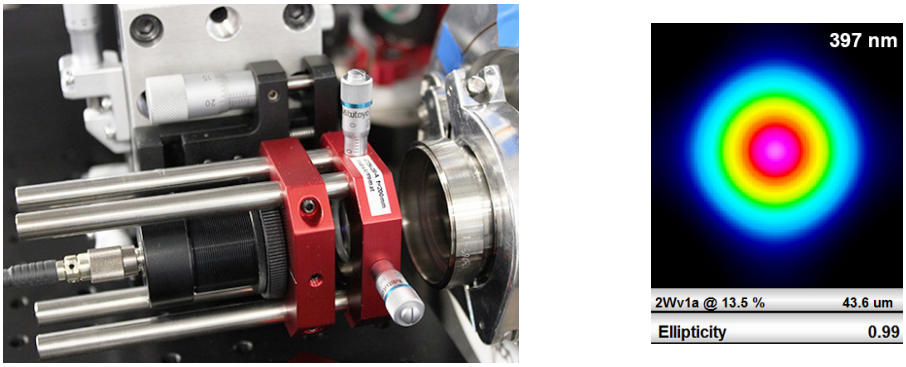

Figure 4.27: (left) Outcoupling setup for the PCF beams. The focusing lens can be translated transversely to the optical axis for tilting the beam, while the whole optical assembly is mounted on a translation stage to move the beam without tilting. (right) Beam-waist spot of the focused 397 nm beam at the same image distance as the ion trap would be. A Gaussian-beam spot diameter of 44 µm is reached with an ellipticity close to 1.

is cleaned by a Glan-Taylor polarizer[76] with an extinction ratio of $< 5 \times 10^{-6}$ and made σ^--circularly polarized by a QWP. A good extinction of σ^+-polarization is necessary for faithful spin polarization (Section 5.2.1).

The beams from the PCF are collimated using a plan-achromatic objective[77] and are focused by a 200 mm achromatic doublet[78]. The near-UV beams reach a Gaussian-waist spot diameter of 44 µm (Figure 4.27 (right)). The near-IR beam waist with a spot diameter of 64 µm is located 4 mm closer to the lens, but this only leads to a slightly reduced laser power at the ion's position. We have placed the focusing lens in an x-y-translation mount and mounted the whole optics assembly on a x-y-z-translation stage (Figure 4.27 (left)). This decouples tilting and translation of the beam, which allows for accurate beam steering through the trap region at 50 µm above the trap chip.

4.3. Imaging system

Trapped $^{40}Ca^+$ ions are detected and their internal state read out by capturing fluorescence light at 397 nm with a high-Numerical Aperture (NA) in-vacuum objective and focusing it on an EMCCD and/or a PMT attached to an optically sealed imaging box (Figure 4.2). The objective is mounted on a three-axes positioner stack for in-situ positioning.

4.3.1. Schwarzschild-type objective

The objective is the centerpiece of the imaging system. Our performance criteria were operation inside the UHV chamber for high light-collection efficiency and hence at cryogenic

[76] Glan-Taylor polarizer 2-GT-3522-1 from Altechna
[77] Plan achromatic objective PLN 10X from Olympus
[78] Achromatic doublet AC254-200-A from Thorlabs

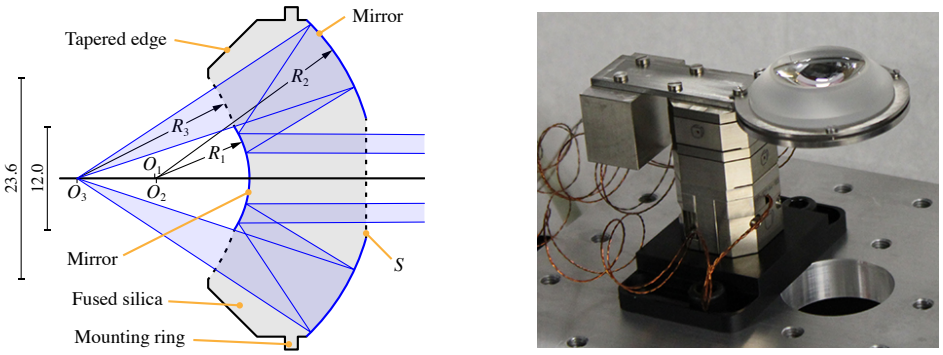

Figure 4.28: (left) Cross section of the custom-made single-component SO. It consists of a cylindrically symmetric fused-silica substrate with three spherical surfaces (radii R_{1-3} and centers of curvature O_{1-3}) and a flat surface S. Light from a point source at O_3 is focused at a distance of 800 mm. A glass ring around the objective's circumference allows for stress-free mounting, and the tapered edge for ion illumination with lasers at 45° with respect to the optical axis. (right) SO mounted on a three-axes piezo-driven positioner stack in a testing assembly. The titanium block to the left of the stack balances the objective's weight to reduce the torque on the positioners.

temperatures, and to allow for simultaneous imaging of $^{40}Ca^+$ and $^{9}Be^+$ ions without further active optics. Imaging at low temperature, however, often suffers from chromatic aberration because chromatically corrected multicomponent objectives typically cannot withstand cooling to liquid-helium temperature. Another approach to mitigate chromatic aberration is using reflecting optics.

The Ion Storage Group at NIST, Boulder, successfully designed and tested a fully reflective Schwarzschild-type Objective (SO). Such an objective consists of two concentric mirrors, a smaller convex (radius of curvature R_1) and a bigger concave (R_2) mirror, facing each other (Figure 4.28), and is equivalent to a thin lens with focal length $f = R_1R_2/(2(R_2 - R_1))$ located at the mirrors' center of curvature [Art00]. A difficulty in the NIST design, however, was to precisely position and fix the smaller mirror above the larger mirror.[79]

In order to meet our unique performance criteria but avoid difficult assembly, we decided to design a single-component imaging objective based on the design reported in [Fuj07]. The authors have constructed a SO from a single piece of fused silica, reflectively coated with aluminum, to maintain a rigid alignment of the mirrors at low temperature. Despite the light passing through a dispersive medium, achromaticity could be preserved by shaping the refracting surfaces (R_3 and S) such that rays cross them perpendicularly. The ratio between R_1, R_2, and f was set to $\sqrt{5}-1 : \sqrt{5}+1 : 1$ to nullify lowest-order spherical aberrations when light from an object at the focal point, a distance f from the center of curvatures, is collimated, which left f and NA the only free parameters. In general, the imaging properties at low temperature were found to be similar to those at room temperature [Fuj07]. Between two objectives with different focal lengths (2 and 4 mm) and hence sizes, the smaller one

[79] Private communication with members of the Trapped-Ion Quantum Information and Simulation group at the Leibniz University of Hannover who have assembled one such objective.

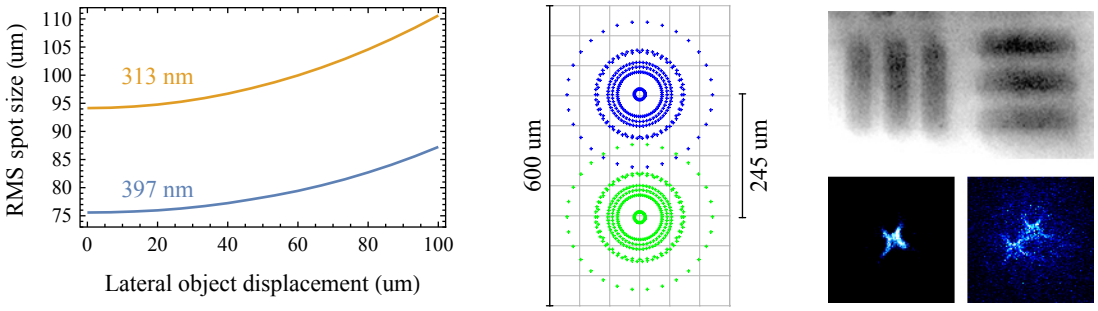

Figure 4.29: (left) Simulated RMS spot size versus lateral displacement of the point source. (middle) Simulated spot diagram for two point-like objects separated by 3 µm and a radiation wavelength of 397 nm. The images have a center distance of 245 µm and an RMS spot radius of ≈ 75 µm. (right) Resolution test of the SO. At room temperature, the finest features in a USF1951 target with a line width of 2.2 µm can be resolved even when illuminated with white light (top). At cryogenic temperature, one and two ions are imaged at 397 nm (bottom).

showed less spherical aberrations [Fuj09]. Further simulations by the same authors revealed that an NA of 0.55 optimally balances spherical aberration and brightness of an image at a wavelength of 400 nm [Fuj11].

We have modified the original design for refocusing the annular output light from ions at O_3 at a total distance of 800 mm, after passing through the two viewport windows of the vacuum enclosure without requiring any further optics. Our SO has an NA of 0.55 and an effective focal length of 9.5 mm, which yields a working distance of 18 mm. It was optimized for minimal Peak-To-Valley (PTV) spot size in the image plane for 313 and 397 nm using the *Hammer Optimization* in ZEMAX[80]. The floated parameters were the radii of curvature R_1 and R_2 of the mirrors, and the axial distance between them (see Table 4.3 for simulation steps and data). In the simulation, the point-light source was placed at a lateral distance of 100 µm to achieve similar performance over an extended lateral distance (Figure 4.29 (left)). Diffraction-limited performance could not be achieved for a single-component SO at that high an NA using only spherical surfaces. With a simulated RMS spot size below 90 µm (110 µm) at 397 nm (313 nm) for lateral displacements up to 100 µm and a magnification factor of 81, two ions separated by 3 µm were, however, expected to be resolvable. This was confirmed experimentally (Figure 4.29 (right)).

The objective was custom made by the lens-making company Asphericon. The High-Reflection (HR) surfaces were coated with aluminum with an average reflectivity of over 85 % at the near-UV wavelengths (where silver mirrors would be worse). The transparent surfaces have a magnesium fluoride Anti-Reflection (AR) coating with a specified reflectivity below 0.6 % at room temperature, potentially different at cryogenic temperature. The light-collection efficiency is reduced by the smaller mirror blocking light at an NA of 0.31, so that the objective effectively covers 5.7 % of the full solid angle. Taking into account specified losses of all optical elements in the imaging system, the overall detection efficiency

[80] Optical system design software ZEMAX-SE (version 31409) from Radiant Zemax

Table 4.3: Surface parameters from ZEMAX for the three design steps of the SO. R gives the radii of curvature of the surfaces (negative when it lies to the left), d the surface thickness, that is the distance to the next surface. Rows are labeled by surface number; surfaces 2-5 describe the SO, 6-7 the first and 8-9 the second viewport window (C79-80 and LITHOSIL-Q are fused silica from Corning and Schott, respectively). The optimization started from the original design constraints in [Fuj07]. The radii of curvature of the mirrors as well as their distance were then floated to minimize the PTV spot size in the imaging plane using the Hammer Optimization method in ZEMAX. In the last step, the transparent SO surfaces were adjusted to form a physically manufacturable object. Colored values changed with respect to the previous step; red values according to simulation or manual adjustment, blue values to maintain constraints or optical performance.

		original		optimized		adjusted	
#	Glass	R (mm)	d (mm)	R (mm)	d (mm)	R (mm)	d (mm)
0		Infinity	9.000	Infinity	9.0000	Infinity	9.000
1		Infinity	11.125	Infinity	11.125	Infinity	10.344
2	C79-80	−20.125	18.000	−20.125	14.613	−19.344	15.415
3	MIRROR	−29.125	−18.000	−25.491	−14.613	−25.491	−14.605
4	MIRROR	−11.125	18.000	−11.086	14.613	−11.086	13.625
5		Infinity	65.875	Infinity	69.262	Infinity	70.221
6	LITHOSIL-Q	Infinity	3.000	Infinity	3.000	Infinity	3.000
7		Infinity	93.000	Infinity	93.000	Infinity	93.000
8	LITHOSIL-Q	Infinity	3.000	Infinity	3.000	Infinity	3.000
9		Infinity	597.000	Infinity	597.000	Infinity	597.000

is expected to be 0.9 % (Table 4.4). Experimentally, the single photon detection efficiency was determined to be 0.7 % (Section 5.7).

Inside the UHV chamber, the SO is mounted in a titanium clasp, which gently compresses the glass ring around the objective's circumference (Figure 4.28). The clasp is screwed onto a three-axes piezo-driven positioner stack[81], with a counterweight to balance the center of mass of the load above the stack and thereby reduce the torque on the slip-sticks inside the positioners. This assembly allows for in-situ closed-loop positioning of the SO with respect to the SET on the micrometer level.

An open question concerning the performance of the objective is the star-shaped form of ion images, which is presumably not caused by diffraction from the cover-electrode mesh as that is oriented at 45° with respect to the arms of the stars. In astronomy, such patterns are, however, known to originate from astigmatism when a point source is laterally displaced from the optical axis of the objective. In our setup this could arise from a tilted position of the SO, possibly due to incorrect balancing on top of the attocube stack. It is unlikely that errors in the fabrication process cause the astigmatism as the images were not affected by rotating the SO in its mount before the latest cool down. Translating the SO horizontally in order to place the ion on its potentially tilted optical axis is limited by the size of the

[81] Piezo-based nano drives (two ANPx101/RES/LT/UHV and one ANPz101/RES/LT/UHV) and motion controller (ANC350/3/RES) from attocube

Table 4.4: Expected SO detection efficiency.

Cover mesh	90 %
Solid angle coverage of SO	5.7 %
HR coatings of SO	72 %
AR coatings of SO	99 %
UHV chamber viewport	93 %
Cryostat viewport	93 %
Deflection mirror	99 %
Quantum efficiency of PMT	30 %
Expected detection efficiency	0.9 %

viewports which the imaging beams must pass. Therefore this hypothesis could not be confirmed yet.

4.3.2. Imaging system outside the cryostat

The output light from the SO passes the bottom viewports of the UHV chamber and the cryostat, and enters the part of the imaging system that is placed on the optical table below. An elliptic mirror in a kinematic mirror mount[82] deflects the light by 90° into the imaging box. The mirror mount is fixed inside a black-anodized aluminum housing with a hole in its bottom plate to embrace a pin on the optical table centered under the SET, which allows for rotating the mirror around the vertical optical axis. The bottom plate also features a guide rail, on which the imaging box can be translated along the horizontal optical axis for focusing (Figure 4.30).

Inside the imaging box made from black-anodized aluminum, the fluorescence light passes an optical bandpass filter[83] for 397 nm and is guided onto an EMCCD[84] and/or a PMT[85]. Where it is guided can be chosen by either moving a beam splitter, a mirror[86], or neither into the optical path. Both components are fixed on a slide[87], which is moved by a linear actuator[88]. The actuator position is controlled by the pulse-width-modulated signal generated from a micro controller board[89]. The bandpass filter is also mounted on a slide and its position can be computer controlled via a Transistor-Transistor Logic (TTL) signal.

Both imaging system boxes are made light tight by design. Lens tubes in between them and a light absorbing sticky tape, which gaps the distance from the mirror box to the cryostat viewport, protect from stray light. Optical access to the PMT is further narrowed

[82] Dielectric elliptical mirror (BBE1E02) in right-angle kinematic mount (KCB1E) Thorlabs
[83] Bandpass filter FF01-390/18-25 from Semrock
[84] EMCCD iXon DU-897D-CSO-UVB from Andor
[85] PMT H10682-210 from Hamamatsu
[86] Non-polarizing beamsplitter cube 50:50 (BS013) and right-angle prism (MRA25-E02) from Thorlabs
[87] Stainless slide (122-2115) from OptoSigma
[88] Linear actuator L12-R from Firgelli
[89] Micro-controller board Arduino Uno from Arduino

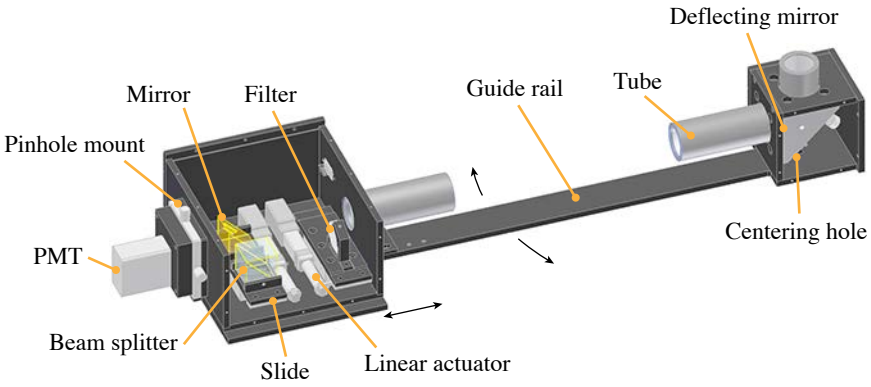

Figure 4.30: Imaging system outside the cryostat. A mirror under the cryostat bottom viewport (to the right) guides the fluorescence light coming from the SO into the imaging box (on the left). After passing a bandpass filter, the light is directed to a PMT and/or EMCCD (on top of the imaging box, not displayed) by a beam splitter and a mirror, which sit on a horizontal slide. Linear actuators move this slide and the slide carrying the filter. The imaging system can be rotated around the vertical optical axis, and the imaging box be translated along the horizontal axis for focusing.

by a 1.7 mm pinhole mounted in a x-y-translation stage in front of it. Measured stray light counts are below 6 cts/s under normal laboratory conditions.

4.4. Control system

The trapped-ion quantum control experiments described in this thesis require synchronous control over laser pulses and trap-electrode voltages, as well as readout of the ion's internal state. This is facilitated by a computer-based control system using an FPGA for real-time input and output operations. The Graphical User Interface (GUI) *Ionizer* running on a PC allows for inputting parameters and starting experiments, and displays experimental results.

The centerpiece of our control system (Figure 4.31) is a ZedBoard[90] built around a Zynq-7000 All Programmable System-on-Chip, which integrates a dual-core ARM Cortex-A9 based Processing System (PS) and PL on an FPGA in a single device. The PS handles the communication with the GUI running on the control PC and manages the experiments, while the PL takes care of real-time inputs and outputs. Three code components are employed: the PL is specified in a hardware description language, the PS and the GUI are programmed in C/C++. They were inherited from the NIST Ion Storage Group and further developed by Ben Keitch, Vlad Negnevitsky, and Matteo Marinelli.

Laser pulses in experimental sequences are parametrized by frequency, amplitude, phase, and duration. The PS feeds these parameters via the PL communications module and a bi-directional differential serial backplane connection to the respective DDS board. Each

[90] Evaluation board ZedBoard from Digilent

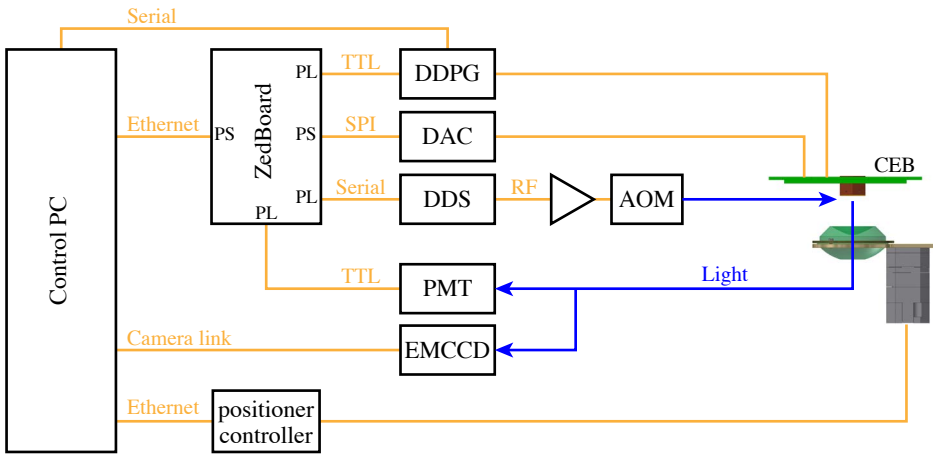

Figure 4.31: Overview of the computer-control system. Laser pulses (via AOMs driven by DDS outputs) and electrode voltages (analog supply voltages from a DAC and switches driven by a DDPG) are controlled in real time by Programmable Logic (PL) on a ZedBoard. Fluorescence light from the ion is detected by a PMT (single-photon counting in PL) and/or an EMCCD. GUIs on the control PC are used to input parameters to and display results from the Zedboard via its Processing System (PS), program the DDPG, control the nanopositioners and read out the EMCCD.

DDS board features four rf output channels with a shared clock for phase coherence. The rf signals are amplified and sent to the switching AOMs (Section 4.2). When the PL triggers an experimental run, the DDS cards autonomously run the programmed pulse sequences. During pulses marked as detection time windows, the PL counts PMT output pulses as single fluorescence photon events and returns the results via the PS to the GUI.

The electrode voltages are generated by a 14-bit, $\pm 10\,\mathrm{V}$ DAC[91] and fed to the CEB via vacuum feedthroughs (Section 4.1). The DAC is programmed via a Serial Peripheral Interface (SPI) bus with voltage settings computed in the PS according to parameter settings in the GUI (Section 5.3). The three SPST switches per controllable electrode (Section 4.1.2) are connected to outputs A, B and C of a DDPG[92] with a specified resolution of 1 ps. The outputs are always in one of two states, either HI (7 V) or LO (0 V). Due to an inverting buffer after the P400, the switches close when the P400 output is LO. In order to apply well-defined voltages to the electrode, exactly one of the three SPST switches should be closed at any given time.

The P400 can be programed to execute a pulse sequence upon a TTL trigger signal. Every output starts in its default state given by the assigned polarity and inverts its state first at the "leading edge" and subsequently at the "trailing edge". Afterwards, the state stays in the default state. The times between start and leading edge, and between leading and trailing edge can be pre-programed via the GUI. Essentially, this means that we can apply three different voltage profiles per sequence to the switchable electrodes, which we

[91] DAC AD5371 on an evaluation board EVAL-AD5371EBZ from Analog Devices
[92] DDPG P400 from Highland Technology

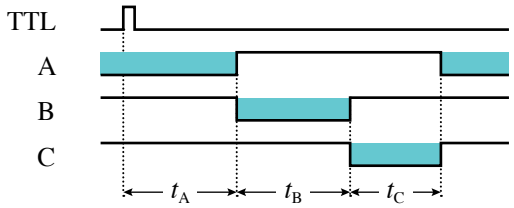

	polarity	leading	trailing
A	−	t_A	$t_B + t_C$
B	+	t_A	t_B
C	+	$t_A + t_B$	t_C

Figure 4.32: Pulse sequence for switching the electrode voltages. Starting in the default state given by the polarity, the output of each channel is inverted twice, at a leading and a trailing edge. The times for the edges are programed such that only one switch per electrode is closed at any given moment in time. A sequence runs through the profiles A → B → C → A, named according to the output channel set to LO, and is fully characterized by the profile duration times t_A, t_B and t_C.

label A, B and C according to the output channels that are LO during the profile durations t_A, t_B and t_C (Figure 4.32).

The EMCCD for ion imaging and the controller for the nanopositioners carrying the SO, which is connected via ethernet, are controlled directly from the PC using their proprietary software.

5. Calibration Experiments and Techniques

There are a number of routine calibration experiments and preparatory steps that need to be performed as precursors to the quantum control experiments described in Chapter 6. Here, I give a brief overview of these experimental techniques as a practical guideline in the context of our setup, assuming that the whole experimental apparatus described in Chapter 4 is basically functional.

Section 5.1 describes the first steps from beam alignment to ion loading and calibration of the dipole lasers. Section 5.2 introduces spin-state polarization and coherent qubit manipulations. Section 5.3 illustrates how we control the Direct Current (dc) potential and calculate the required voltages to move a trapped ion. Section 5.4 covers micromotion, its symptoms and how to compensate for it. Sections 5.5 and 5.6 discuss ground-state cooling using Electromagnetically Induced Transparency (EIT) and heating of motional states. Section 5.7 details how we measure the detection efficiency of our imaging system using the ion as a single-photon source. Section 5.8 presents a method for determining the state-initialization fidelity by driving two $S_{1/2} \leftrightarrow D_{5/2}$ transitions. Section 5.9 provides data obtained from Ramsey interferometry and an analysis of the noise leading to spin decoherence.

5.1. First steps

The initial steps for trapping and detecting ions are adjusting the imaging system, aligning the laser beams into the trapping region, and observing fluorescence from the neutral atomic beam. Ions can then be loaded and the dipole lasers calibrated for optimized cooling and detection.

5.1.1. Imaging system

Imaging of the trapping region above the Surface-Electrode ion Trap (SET) requires positioning of the Schwarzschild-type Objective (SO) (Section 4.3). At an optical magnification factor of 81 and an Electron-Multiplying Charge-Coupled Device (EMCCD) image area of $(8.2\,\mathrm{mm})^2$, the area imaged by the system covers $100 \times 100\,\mu\mathrm{m}^2$. Without lasers directly pointed at the trap chip, white light from an electrical lamp shone into the Ultra-High Vacuum (UHV) chamber suffices for first orientation. When the imaging box is placed

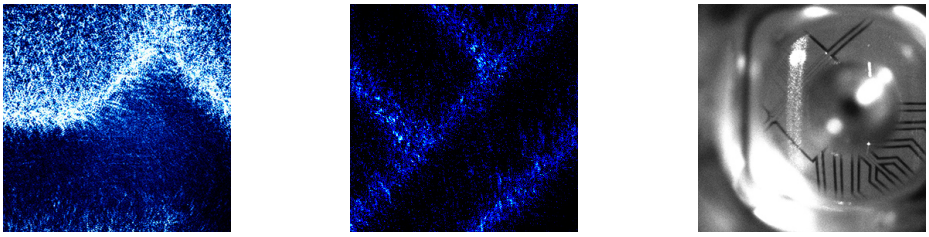

Figure 5.1: Images of the SET using the imaging system. (left) The SO is placed such that features on the SET, illuminated by an unfocused laser, can be resolved. Within the covered area of $100 \times 100\,\mu m^2$, reflections from the trenches around the rf electrode allow for orientation. (middle) Three control electrodes, an rf electrode, and the middle electrode underneath the trapping zone are illuminated by a laser from the inside of the quartz crystal. (right) Putting an additional converging lens in front of the EMCCD, the imaged area is widened to a diameter of $\approx 3.5\,mm$. This is helpful for aligning laser beams with respect to the SET. Besides reflections of white light used to illuminate the surroundings, light of the 397 nm laser beam from the PCF scattered from the surface of the SET can be seen (bright vertical line).

330 mm away from the mirror box (distance between facing surfaces), the total imaging path length is 80 cm, for which the SO was designed. Setting the z-positioner of the attocube stack to 1400 µm, features of the SET can be resolved on the EMCCD (Figure 5.1). The SO can then be moved horizontally by the x, y-positioners for orientation and placement below the expected trapping zone. For ion imaging, the SO is lowered by the ion–surface distance of 50 µm.

5.1.2. Beam pointing

With the SO in place, the imaging system can be used to align all laser beams into the trap region. As a precursor, coarse alignment of the laser beams through the holes in the trap cage can be monitored with a Charge-Coupled Device (CCD) camera behind the respective opposing viewport. After that is done, it is helpful to mount a 150 mm lens in front of the lens tube on the imaging box (Figure 4.2), move the imaging box close to the mirror box, and the SO up to a z-position in the range of 3000 to 3200 µm to focus on the SET. This allows imaging a bigger area on the chip of $\approx 3.5\,mm$ in diameter while coarsely steering the laser beams onto the center of the SET (Figure 5.1 (right)). Fine beam pointing and tilting can, finally, be done when the imaging system is reset to normal working conditions.

The beams from the PCF include the detection beam at 397 nm and the PhotoIonization (PI) beams. Scattering of the UltraViolet (UV) beams from the electrode surfaces can cause two undesirable effects. First, it might charge the SET locally, which affects the trap potential. Second, scatter from the detection beam decreases the Signal-to-Noise Ratio (SNR). Therefore, the PCF beams should pass the SET as horizontally as possible. The position and tilt of the beams (Figure 4.27) can be iteratively adjusted to minimize scattered light. For each iteration, the beam is first tilted to point directly on the trap, which maximizes the scatter as detected by the PhotoMultiplier Tube (PMT). Second,

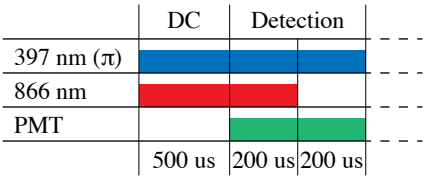

Figure 5.2: Laser pulse and PMT detection sequence for ion loading. It includes stages for DC and differential fluorescence detection with typical duration times given. Not shown are the PI and 0-0-order 397 nm beams, which are continuously on (see text).

after translating the beam by 50 µm away from the SET, the scattering rate is noted down. These steps are repeated for different tilt angles of the beam. Finally, the tilt and position are adjusted to the parameters which yielded the minimum scatter.

5.1.3. Neutral atom fluorescence

The functioning of the atom oven can be checked and the frequency of the 423 nm for resonantly driving on the $4s\,^1S_0 \leftrightarrow 4p\,^1S_1$ dipole transition be found by observing fluorescence from the neutral atomic beam. To that end, the oven is operated at around 3.5 A, the SO placed to focus on the trap region, and the filter, beam splitter and mirror in the imaging box are moved out of the beam path. Then the 846 nm master-laser frequency is scanned by ±0.1 GHz around 354.5392 THz (cf. Table 4.2) via its extended-cavity grating piezo. After the oven has heated up, which takes about 2 min, an oscillating fluorescence signal is seen. For ion loading, the 846 nm laser frequency is set for maximum fluorescence.

5.1.4. Ion loading

We load ions into the Paul trap by ionizing neutral calcium atoms in a two-step PI process, similar to [Gul01]. The laser at 423 nm excites atoms to the $4p\,^1S_1$ excited state, from where the 375 nm laser can remove the outer electron. Since the second step couples to the continuum, that diode laser does not require careful tuning or stabilization, and can be left free running.

At this stage, the rf and dc voltages, as well as the lasers at 397 and 866 nm need to be operational. If working conditions for trapping are not known, these are the main parameters to vary. Reference settings that have allowed for initial trapping in the past are a reflected rf power of −10 to 0 dBm, dc voltage settings for a trap potential with an axial frequency of 2 MHz (cf. Section 5.3), and laser powers of 5 to 20 µW. In addition to the main 397 nm frequency, which is generated by double-passing the switching Acousto-Optic Modulator (AOM) at around 80 MHz (Section 4.2.2), we open the laser beam shutter after that AOM (Figures 4.23 and 4.24) for loading to add the 0-0-order frequency component to the beam. At a higher power of around 100 µW and a red detuning of −160 MHz, this beam increases the cooling rate of highly excited ions.

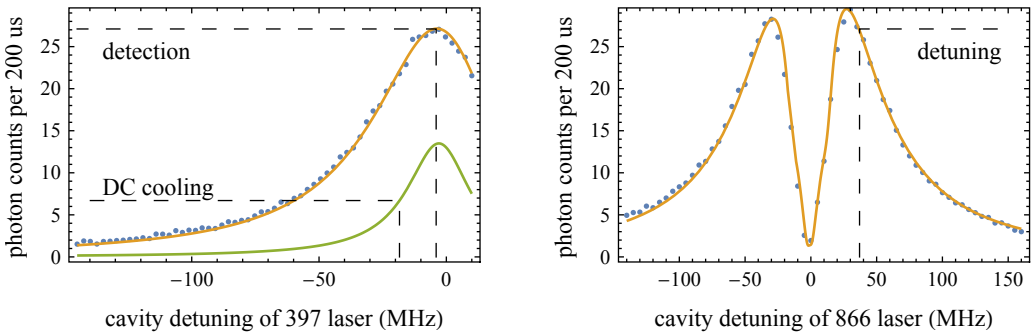

Figure 5.3: Spectral profiles of the driven $S_{1/2} \leftrightarrow P_{1/2} \leftrightarrow D_{3/2}$ system versus detuning of each of the driving lasers. Experimental data (blue dots) is fitted with the steady-state solution of OBE by manually varying relevant parameters (orange lines). Reducing the 397 nm laser power to 10 % would half the fluorescence signal (green line), which corresponds to driving at saturation intensity (Section 3.4.1). Optimum DC would be achieved at this intensity and a red detuning of 14 MHz from the resonance peak.

The computer-controlled experimental sequence (Figure 5.2) consists of the 397 nm and 866 nm laser pulses for DC and time windows for differential fluorescence detection. In the first detection window, the ion fluorescence including background is recorded. In the second, the 866 nm repump light is switched off, due to which the ion is pumped and remains in the dark $D_{3/2}$-state. The photon counts from the second window are subtracted from the ones from the first to give the background-corrected signal. The signal from 200 such sequences is averaged, displayed, and saved as a single data point.

When the signature of a loaded ion occurs, that is a clearly positive background-corrected count rate, the oven and the PI beams can be turned off and the 0-0-order beam shutter be closed.

5.1.5. Calibrating the dipole lasers

Once an ion is loaded, the frequencies and powers of the dipole lasers can be adjusted. The experimental sequence is the same as for ion loading (Figure 5.2). The fluorescence signal is measured versus laser frequency, which is scanned by varying the reference cavity length via the piezo-mounted mirror. An example is shown in Figure 5.3, similar to those of a three-level Λ-system discussed in Section 3.4.2. The number, shape and width of dark resonances can, however, differ from that simplified case due to the total of eight Zeeman-shifted levels involved in the $S_{1/2} \leftrightarrow P_{1/2} \leftrightarrow D_{3/2}$ system. The fitted curves are from simulating the OBE of the eight-level system, in analogy to [Obe99], with manually fitted parameters for the Rabi frequencies, detunings and polarization of the two lasers in a magnetic field of 4 G.

Typically, we set the repumper frequency 10 to 30 MHz blue detuned from the right-hand resonance peak and the 397 nm laser frequency to resonance for detection and red detuned

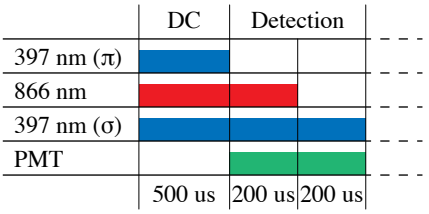

Figure 5.4: Experimental sequence for rough calibration of the SP laser. The QWP in the beam line of the 397 nm beam parallel to the magnetic field is rotated such that the background-corrected fluorescence is minimal.

by 10 to 20 MHz for DC. The power of the repumper can then be reduced as long as the fluorescence is not significantly affected. The power of the fluorescence laser can be adjusted depending on the purpose. A higher power during DC yields a higher cooling rate, while a power corresponding to the saturation intensity or lower yields lower final mean phonon numbers in the motional modes (Section 3.6.1). During detection, one can increase the power for maximum fluorescence (SNR of 64 within a detection window of 200 µs for the experimental data shown) or reduce it for higher SNR (up to 290 according to simulation based on the fitting parameters).

Before, after, or ideally interleaved with tweaking the frequency and amplitude of the dipole laser, the PCF beam alignment can be optimized for highest SNR.

5.2. Coherent manipulation of the qubit

For Coherent Manipulation (CM) of the qubit, three more laser beams are required. The 397 nm beam parallel to the magnetic field (Figure 4.26) is used for initializing the $|S\rangle$-state, the 729 nm beam drives the qubit transition, and the 854 nm beam repumps population from the $|D\rangle$-state to the $S_{1/2}$-states. The following sections describe the experimental calibration procedures.

5.2.1. Spin polarization

Initialization of the qubit ground state $|S\rangle$, called *Spin Polarization* (SP), requires transferring all population into the $S_{1/2}(m_J = -1/2)$-state. This can be achieved by pumping with a σ^--polarized beam at 397 nm, which does not couple to the target $|S\rangle$-state (Table 3.3).

The beam frequency is set to the same frequency as the fluorescence detection beam, with power between 1 and 10 µW. It can be aligned on the ion by running the sequence in Figure 5.4 and maximizing the fluorescence signal with the QWP removed from the beam path. Next, the QWP is inserted again and rotated such that the fluorescence signal is minimal, which is the case when the beam polarization is either σ^- or σ^+. Once Rabi oscillations (see below) can be driven, the two circular polarization directions can be distinguished by driving the according quadrupole transitions.

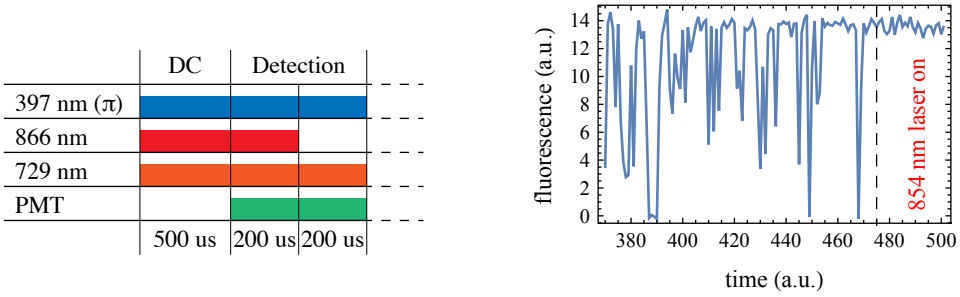

Figure 5.5: Experimental sequence for observing and signature of quantum jumps. During the cooling and detection cycles, the 729 nm laser is continuously on. When the valence electron probabilistically "jumps" to the dark $D_{5/2}$-states, fluorescence drops and only recovers when the electron jumps back to $S_{1/2}$. Intermediate count rates result from quantum jumps during a detection window. The jumps vanish when the 854 nm laser is switched on additionally, which happened after the last dip, because the $D_{5/2}$-states get immediately emptied via the $P_{3/2}$-states.

With typical settings (Section 5.2.4), we achieve $|S\rangle$-state initialization with a fidelity of 98.96(5) % (Section 5.8).

5.2.2. Quantum jumps

If the 729 nm quadrupole laser is used for the first time or with unknown parameters, it is essential to make sure the beam hits the ion. Running the sequence in Figure 5.5 with the 854 nm repumper beam off, quantum jumps occur when the 729 nm beam illuminates the ion [Ber86]. At times where the ion is in the $|D\rangle$-state, the fluorescence drops and only recovers when the electron jumps back to the $|S\rangle$-state. The quadrupole laser does not need to be precisely resonant with the qubit transition at this stage because its linewidth is broadened to the order of the $S_{1/2} \leftrightarrow P_{1/2}$ transition due to the coupling with the detection beam.[1]

The 854 nm will already be aligned on the ion together with the other beams from the PCF. One can check whether it is roughly on resonance by switching it on during the sequence above and observing that the quantum jumps stop. Finer tuning of the frequency is done once Rabi oscillations can be driven (see below).

5.2.3. Rabi spectroscopy and Rabi oscillations

With the quadrupole laser aligned on the ion, one can perform spectroscopy around the $S_{1/2} \leftrightarrow D_{5/2}$ center frequency to find allowed transitions. – At perpendicular polarization of the laser with respect to the magnetic field, only transitions with $|\Delta m| = 2$ can be driven (Figure 3.7). After DC and SP by a 2 to 10 µs pulse of the $\sigma^{\pm}$-polarized beam at

[1] This can be qualitatively checked by analytically solving the Optical Bloch equations (Section 3.4) for a three-level "V"-system consisting of the states $S_{1/2}$, $P_{1/2}$, and $D_{5/2}$ in the limit of no decay on the quadrupole transition.

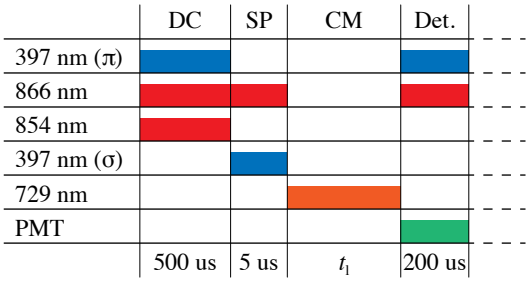

Figure 5.6: Laser-pulse sequence for Rabi spectroscopy (where the 729 nm laser detuning δ is varied) and driving Rabi oscillations (t_l is varied). Differential signal detection is not necessary anymore because the photon counts are binned for bright and dark qubit state.

397 nm, the quadrupole laser is switched on for a duration t_l at a detuning δ, followed by a spin-detection pulse (Figure 5.6). The spin-state population P_S is inferred from repeated photon counting measurements (Section 3.7.1). Dips in the spectrum of P_S versus δ reveal resonances (Figure 5.7).

The main resonances are found at detunings from the center frequency of -16.3, -11.5, 11.5 and 16.3 MHz and correspond to the four possible $|\Delta m| = 2$ transitions from the two states $S_{1/2}(m_J = \pm 1/2)$. Based on the theoretical spectral line splittings in Figure 3.8, one can deduce a magnetic field strength $B = 4.1$ G. Furthermore, one can infer the states involved in the driven transitions and whether the spin was polarized to $S_{1/2}(m_J = -1/2)$ or $S_{1/2}(m_J = +1/2)$.

Symmetric around the main resonances are sidebands at the motional frequencies and their higher harmonics, as well as servo bumps at ≈ 1 MHz from the laser feedback stabilization [Kie15a, p. 67].

Rabi spectroscopy is performed frequently to calibrate the carrier and sideband frequency settings of the 729 nm laser, which can vary due to drifts of the magnetic field or the reference cavity. Note that the shape and width of a resonance peak depend on the pulse duration (Figure 5.8 (left)). As one would expect in Fourier-limited spectroscopy, longer interrogation times lead to a narrower peak in frequency space. The model for fitting a spectral scan for a fixed pulse time (Figure 5.8 (right)) can be derived from the evolution operator for Rabi oscillations in Equation (3.11),

$$P_S(t_l) = 1 - \frac{\Omega^2}{2\Omega_\delta^2}\left(1 - \mathrm{e}^{-\gamma t}\cos(\Omega_\delta t_l)\right) \tag{5.1}$$

with $\Omega_\delta^2 = \Omega^2 + \delta^2$ and a heuristic exponential factor to account for spin and motional decoherence at rate γ [Mee96].

Setting the quadrupole laser to resonance on the carrier transition, Rabi oscillations can be observed by recording P_S for different laser pulse durations t_l (Figure 5.8 (left)). The time t_l at which the first minimum is reached is called "π-time", denoted as t_π, because it

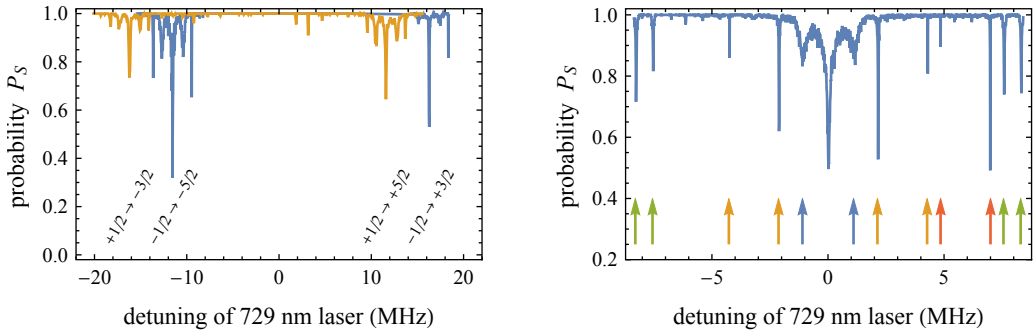

Figure 5.7: Rabi spectroscopy on the quadrupole transition, where the $|S\rangle$-state population is plotted versus laser frequency detuning for $t_\mathrm{l} = 200\,\mu\mathrm{s}$. (left) The blue (orange) lines correspond to $\sigma^-(\sigma^+)$-polarization of the SP laser, which was inferred from the spectral lines, with the given m_J for the states involved in the transitions. (right) A finer scan around the qubit transition reveals axial (orange arrows) and radial (green arrows) sidebands, as well as servo bumps (blue arrows), and carrier and first red sideband (red arrows) of the $S_{1/2}(m_J = -1/2) \leftrightarrow D_{5/2}(m_J = -3/2)$ transition, which implies weakly driving a $|\Delta m| = 1$ transition due to imperfect polarization of the quadrupole laser (Figure 3.7).

corresponds to a π-pulse on the Bloch sphere, fully inverting the spin (Section 3.3). The signal from Rabi oscillations is useful for further calibrations.

5.2.4. Calibrations based on Rabi oscillations

As soon as Rabi oscillations can be driven, further laser parameters can be fine-tuned. For the first calibration routines, the experimental sequence in Figure 5.6 is run in continuous mode with the 729 nm laser frequency on resonance with the carrier transition.

At $t_\mathrm{l} = t_\pi/2$, the beam pointing of the 729 nm laser is improved by bringing the signal P_S down, which corresponds to faster Rabi flopping. If the beam pointing was bad at the beginning, this might take a few iterations, between which t_π is measured and t_l adjusted.

In order to optimize the polarization of the 397 nm laser beam for SP, the probe-pulse duration is set to $t_\mathrm{l} = t_\pi$. The QWP in the beam is then rotated such that the probability P_S is minimal, which maximizes the contrast of the Rabi oscillations. A value close to zero should be reached if SP pumps the entire population to $|S\rangle$ (see also Section 5.8).

The SP pulse duration can be scanned for $t_\mathrm{l} = t_\pi$ to measure the time the SP takes. Furthermore, the beam pointing of the circularly polarized 397 nm beam can be optimized by setting the pumping pulse duration to a value where $P_S \approx 0.5$ and subsequently minimizing the signal.

The frequency of the 854 nm repump laser has so far only been determined roughly. Applying the experimental sequence in Figure 5.9, in which the π-pulse is followed by a $\approx 5\,\mu\mathrm{s}$ long repump pulse prior to spin-state detection, the reference cavity of the repump laser can be scanned. As the 854 nm laser repumps population from the $D_{5/2}$-manifold via $P_{3/2}$ to the ground-state manifold, the signal P_S peaks when the repump laser reaches

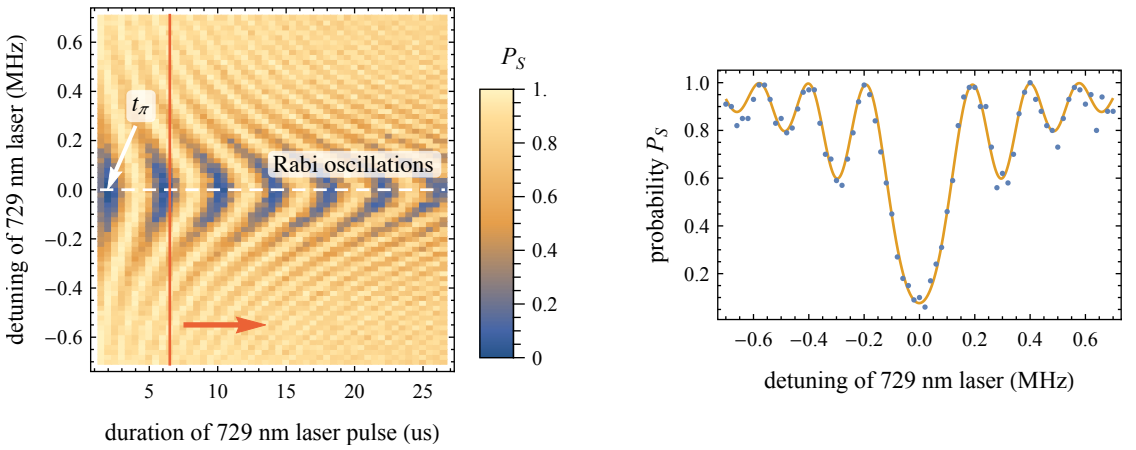

Figure 5.8: (left) Chevron-like curve of probability oscillations versus duration and detuning of the 729 nm laser pulse. Horizontal lines show Rabi oscillations, with the π-time" t_π for the first full spin inversion marked in green. Vertical lines Fourier-limited Rabi spectroscopy around the qubit carrier transition. (right) Rabi spectroscopy data corresponding to the red line in the previous plot. The orange graph is a fit of Equation (5.1) to the data with parameters of interest $\Omega = (2\pi)\,0.25\,\text{MHz}$ and $\gamma = 4\,\text{kHz}$.

resonance. For repumping in regular experimental sequences, the laser power is increased sufficiently for full population transfer.

5.3. Control over trap potential

The total electric potential created by the SET consists of the pseudopotential due to the oscillating rf drive and the static dc potential. The experimental controls are hence the amplitude of the rf potential (its frequency is fixed to the resonance of the rf resonator) and the dc voltages applied to the 19 dc electrodes. A suitable set of dc voltages for a given position of the static potential's saddle point and a desired axial oscillation frequency can be numerically calculated (Section 2.2). We do this by minimizing the modulus of the electrode voltages under the constraints of a zero potential gradient and the required curvature at the chosen position.

In a first iteration of our computer-control system, such a set of calculated voltages could be entered into the GUI and then be sent to the DACs via the Processing System (PS) (Section 4.4). Making changes to single electrode voltages in order to adjust or move the potential, however, was impractical. Therefore, a more operation-oriented and reproducible solution was implemented, in which the experimenter can set the Cartesian coordinates for the saddle point of the dc potential as well as its axial frequency. The required voltages are then calculated by the PS on the fly for the given parameters.

This is realized by first computing voltage sets for the saddle point positions (x_s, y_s, z_s) on a Cartesian cuboidal grid spanning the region of interest (Section 2.2) relative to the

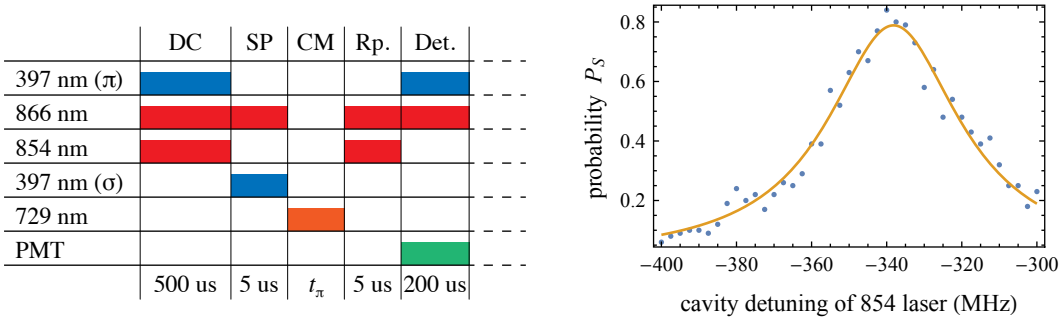

Figure 5.9: Experimental sequence and signal for scanning the 854 nm repump laser. The signal P_S corresponds to the population that has been repumped from the $D_{5/2}$-manifold.

pseudopotential minimum. The voltage setting for each electrode as a function of position is then approximated by polynomials in (x_s, y_s, z_s). The coefficients of those are saved and included in the source code of the PS. Finally, the PS is programed to calculate the required electrode voltages from the given parameters and set them. Changing the axial frequency by a factor F is accomplished by scaling the whole voltage set by $\sqrt{F}$. Note that this only works assuming that the ion is placed on the trap axis and zero electric stray fields. In the experiments performed thus far, however, changing the axial frequency was not necessary. Voltages for switchable electrodes to create a desired relative potential offset are calculated in the same fashion with all other voltages fixed.

5.3.1. Understanding the trapping potential

Based on the method for determining the voltage settings for the dc electrodes from only a few experimental parameters, we can simulate the full electric trapping potential. This allows us to get a qualitative and somewhat quantitative understanding of the effects of the experimental parameters. Figure 5.10 shows how the position of the potential minimum, the orientation of the oscillator eigenmodes, and their eigenfrequencies, which correspond to the expected secular frequencies, are affected by changes in the saddle point position and the rf voltage amplitude.

If the saddle point is shifted vertically (along the z-direction), the ion position only follows to some extent and also moves horizontally, which one might not expect at first glance. If the saddle point, on the other hand, is shifted horizontally, the ion moves in the opposite direction due to the anti-confining curvature of the dc potential in that direction. Furthermore, the secular frequencies as well as the orientation of the eigenmodes are affected by shifts of the saddle point, especially for horizontal shifts. The latter can be of concern for laser cooling (Section 3.6) and optically addressing motional modes (Section 3.2). Since the axial frequency also depends on the saddle-point position, a mismatch of expected and measured axial frequency hints at an incorrectly placed dc potential with respect to the pseudopotential null.

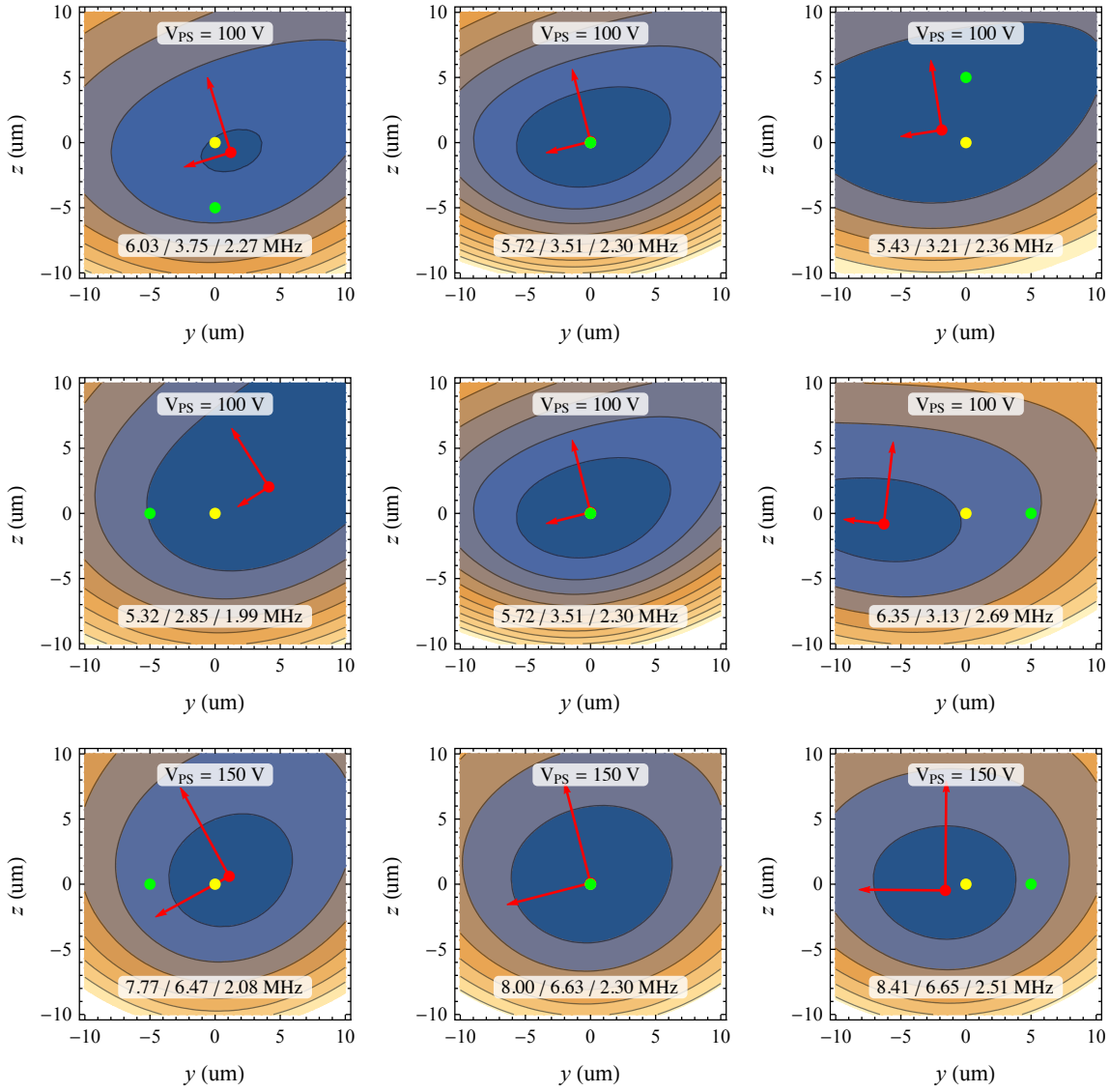

Figure 5.10: Illustrations of the trap potential for different experimental parameters. The yellow points indicate the position of the pseudopotential null, the green points the position of the saddle point of the dc potential with a nominal axial frequency of 2.3 MHz, and the red points the local minimum of the total potential, where the ion is expected. The red arrows give the directions of the eigenmodes of the total potential and are scaled by the corresponding eigenfrequencies, which are given in the lower texts together with the axial frequency (third value). Excursions of the ion position do not directly follow the shifts of the saddle point (first two rows) and are reduced when the rf voltage amplitude is increased (bottom row). Contour lines and coloring are not consistent between plots.

5.3.2. Determining the rf voltage amplitude

Often the actual rf amplitude voltage is not known a priori and can only be estimated from the rf power input to the resonator (Section 4.1.3). Assuming that the ion is trapped at the node of the pseudopotential, one can apply the following method to experimentally extract the eigenmode frequency solely due to the pseudopotential and hence rf amplitude voltage for a fixed rf frequency. First, the radial secular frequencies ω_y and ω_z (the index only distinguishes the two eigenfrequencies and does not imply orientation of the eigenmodes along the Cartesian axes) are measured for two different rf amplitudes and corresponding eigenvalues $\lambda_{\mathrm{ps,I}}$ and $\lambda_{\mathrm{ps,II}}$ of the pseudopotential Hessian defined by Equation (2.11). Then the latter and the two eigenvalues of the dc potential $\lambda_{y,\mathrm{dc}}$ and $\lambda_{z,\mathrm{dc}}$ can be calculated from Equation (2.12) by solving the four equations

$$\omega_{y,\mathrm{I}}^2 = \lambda_{y,\mathrm{dc}} + \lambda_{\mathrm{ps,I}}, \quad \omega_{z,\mathrm{I}}^2 = \lambda_{z,\mathrm{dc}} + \lambda_{\mathrm{ps,I}}, \quad \omega_{y,\mathrm{II}}^2 = \lambda_{y,\mathrm{dc}} + \lambda_{\mathrm{ps,II}}, \quad \sum_i \lambda_{i,\mathrm{dc}} = 0.$$

The fourth permutation was replaced by Laplace's equation in order to maintain solvability in case of numerical errors, that is if only $\omega_{z,\mathrm{II}}^2 \approx \lambda_{z,\mathrm{dc}} + \lambda_{\mathrm{ps,II}}$ is fulfilled.

While this method works for simulated cases depicted in the center column of Figure 5.10, it does not for the other columns. The reason for that is of fundamental nature and applies whenever the rf potential contains terms of higher than quadratic order. The eigenfrequencies of the pseudopotential are then not equal anymore at places other than its critical point, as can be seen from Equation 2.2.

5.4. Micromotion

Besides secular motion, the trajectory of an ion trapped in a Paul trap inevitably has a micromotion component. It arises as fast oscillations from a classical treatment in Equation (2.8) or as breathing of the wave function in a quantum mechanical treatment [Lei03a]. Under ideal conditions, micromotion is small to the extent that it can be neglected. If the minimum of the effective static potential does not coincide with the rf potential node, however, which can occur either due to deliberate or unintentional misplacement of the static potential, or due to stray electric fields, the ion has excess micromotion. Intuitively, micromotion can be understood as fast modulation of the secular motion by the force of the oscillating rf potential. The amplitude of the excess micromotion hence increases with the strength of that force and its direction is aligned with the rf field lines (Figure 5.11).

Consider an ion with excess micromotion amplitude $\boldsymbol{a}$ being illuminated by a laser with wave vector $\boldsymbol{k}$. In the rest frame of the ion, the laser beam appears phase modulated at the rf drive frequency, expressed in the coupling Hamiltonian as (analogous to Equation (4.1))

$$\mathrm{e}^{-\mathrm{i}\omega_\mathrm{l} t} \to \mathrm{e}^{-\mathrm{i}(\omega_\mathrm{l} t + \boldsymbol{k}\cdot\boldsymbol{a}\sin(\omega_\mathrm{rf} t))} = \mathrm{e}^{-\mathrm{i}\omega_\mathrm{l} t} \sum_{j=-\infty}^{\infty} J_j(\beta)\, \mathrm{e}^{\mathrm{i}j\omega_\mathrm{rf} t}$$

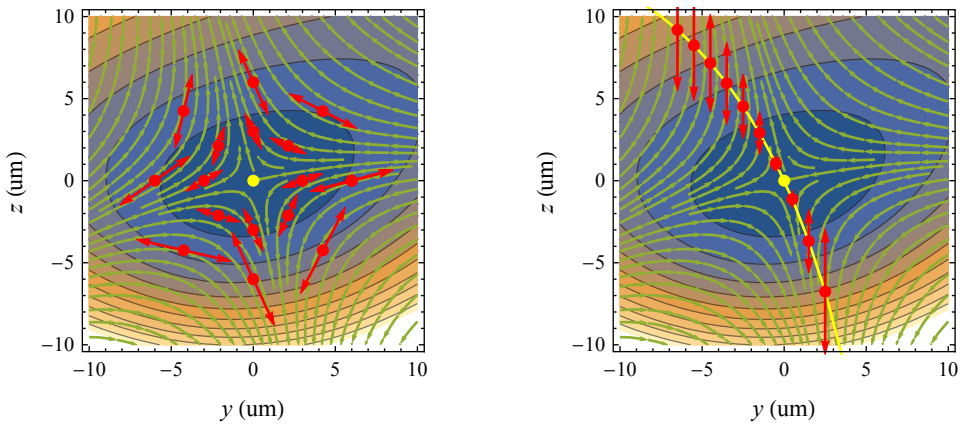

Figure 5.11: Simulated micromotion for different ion positions in the radial plane. (left) Excess micromotion vanishes at the pseudopotential null (yellow point) and increases for larger displacements from it. The strength and orientation of the driven micromotion (red arrows, arbitrary scaling) are determined by the electric field lines of the rf drive potential. (right) At certain positions (yellow line), micromotion is exclusively oriented perpendicular to the SET chip, which makes the interaction with all lasers in the plane of the chip insensitive to it.

with modulation index $\beta = \boldsymbol{k} \cdot \boldsymbol{a}$. For small but increasing β, sideband transitions at $j\omega_{\mathrm{rf}}$ with $j \neq 1$ become stronger at the expense of the carrier transition. This can be observed in the detected ion fluorescence while scanning the position of the static potential's saddle point as well as in the fluorescence spectrum of the 397 nm detection laser (Figure 5.12).

Besides laser frequency modulation, which affects DC and ion fluorescence, excess micromotion is undesirable as it allows noise on the rf supply to couple to the ion and can cause heating [Win98]. There are several experimental approaches to detecting and minimizing excess micromotion, for example in [Ber98; All10; Roo00a, p. 59]. Along directions in the plane of the trap chip, one can maximize fluorescence from appropriately chosen laser beams (Figure 5.12). Most of these methods, however, rely on shining laser beams with nonzero projections along all oscillation directions, such that the modulation index β does not vanish, or the ability to accurately measure the ion position with a camera. Without these in place, a relatively simple technique is to detect excess micromotion by modulating the rf trapping voltage [Iba11].

5.4.1. Parametric driving

At positions where the ion experiences spatially varying micromotion, it is susceptible to resonant parametric driving of the secular motion by sinusoidally modulating the pseudopotential. The modulation is achieved using the circuitry depicted in Figure 5.13. Half of the power from the rf source at ω_{rf} is mixed[2] with a signal at the parametric drive frequency ω_h and subsequently recombined with the other half. The resulting signal is fed into the

[2] Frequency mixers ZLW-3+ and power splitters/combiners ZMSC-2-1+ from Mini-Circuits

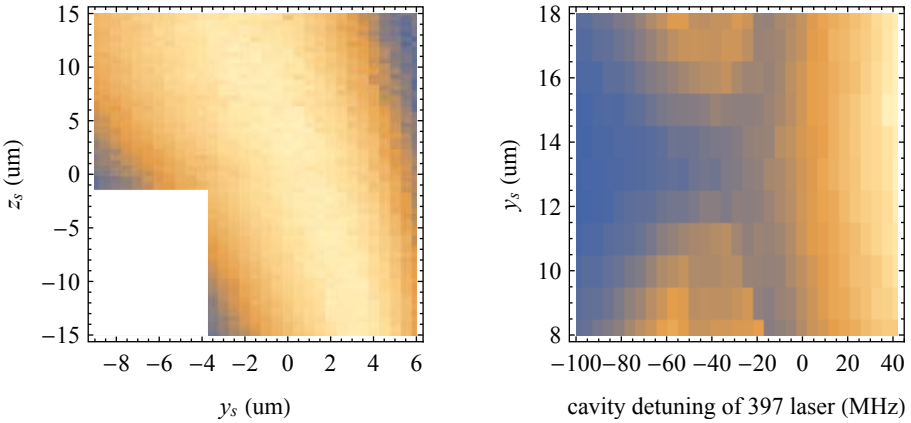

Figure 5.12: Effect of micromotion on ion fluorescence, which is color-coded in arbitrary units (blue means low, yellow high). (left) When the saddle point of the static potential is shifted in the radial plane, fluorescence is maximal where micromotion is perpendicular to the laser beam, cf. Figure 5.11. The white rectangle marks an area where the ion would escape and no data was taken. (right) The same can be observed when the frequency of the detection laser is scanned. The carrier is strongest when the sideband, red shifted by ω_{rf}, vanishes. Note that the data sets were taken on different days with different stray fields, which is why the scan ranges do not match.

resonator to create the modulated rf potential

$$\Phi_{\mathrm{rf}}^{(h)} = \Phi_{\mathrm{rf}} \Big(1 - h\cos(\omega_h t)\Big),$$

where Φ_{rf} is the original potential in Equation (2.9) and h the amplitude-modulation index. The modulation index is made small, $h \lll 1$, such that the modulation of the pseudopotential from Equation (2.10) can be approximated as

$$\Phi_{\mathrm{ps}}^{(h)} = \Phi_{\mathrm{ps}} \Big(1 - h\cos(\omega_h t)\Big)^2 \approx \Phi_{\mathrm{ps}} \Big(1 - 2h\cos(\omega_h t)\Big).$$

The secular motion in the trapping potential, which is purely harmonic in the pseudopotential approximation, then obeys the parametric equation

$$\ddot{r}_i + \omega_i^2 \Big(1 - 2h\cos(\omega_h t)\Big)\, r_i = 0.$$

Note that ideally this would only apply along the two radial directions. But given a finite pseudopotential gradient along the trap axis, also the axial mode can be parametrically driven. Brought into the form of a Mathieu equation, cf. Equation (2.4), with $a = 4\omega_i^2/\omega_h^2$ and $q = ha$, one can deduce that unstable solutions should occur for [Iba11; Tan11]

$$\omega_h = 2\omega_i/n \qquad \text{with} \qquad n = 1, 2, 3, \ldots \tag{5.2}$$

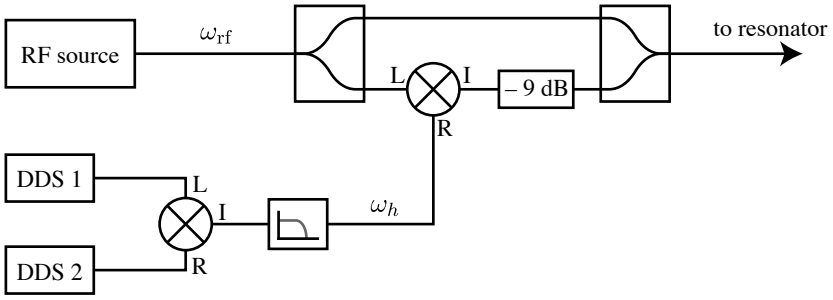

Figure 5.13: Circuitry for generating a modulated rf signal for parametric driving. The signal at the modulation frequency ω_h is created by mixing and low-pass filtering the output from two DDS channels with a frequency difference of ω_h, which standalone do not provide signals at a few MHz. It is mixed with one half of the rf drive signal output and after an attenuator subsequently combined with the other half. The frequency spectrum of the signal sent to the resonator hence consists of a carrier at ω_{rf} and sidebands at $\omega_{\mathrm{rf}} \pm \omega_h$.

which is where the instability regions in Figure 2.1 touch the ordinate. At these resonances, the ion is heated and its fluorescence reduced (Figure 5.14).

The observed parametric resonances match the pattern in Equation (5.2) and at first sight suggest secular frequencies of 1.13, 3.43 and 3.97 MHz (for $n' = 2$). These are, however, only half the values of the frequencies independently determined from a sideband spectrum with the quadrupole laser (Figure 5.7). The correct values, on the other hand, would be inferred if one assumes that heating of the ion only occurred at fractional frequencies with even n.

Similar observations were already made in the past for $H_2{}^+$ molecules in a Paul trap [Raz98] and electrons in a Penning trap [Tom04]. In both experiments, the minimum values of the excitation amplitude (corresponding to the modulation index h here) necessary to make the subharmonics visible were determined. The first main result was that the threshold amplitudes increase with n, that means higher drive amplitudes are required to visibly excite motion at higher-order subharmonics. This was attributed to a finite damping of the oscillators, which reduces the instable areas in such a way that instabilities only occur at certain thresholds of the parameter q. The second main result was an even-odd staggering of the threshold amplitudes. Subharmonics with odd n showed higher threshold amplitudes than with even n. Tommaseo et al. could reproduce this staggering in numerical simulations of the instability regions for small values of the damping constant [Tom04].

In our system, weak but finite damping of the ion oscillation is conceivable due to collisions with background gas molecules and electromagnetic coupling to the metallic surface of the SET. In this sense, the series of fractional frequencies in Figure 5.14 is compatible with an even-odd staggering of driving amplitude thresholds. With this in mind, we purposely searched for and found the subharmonics with odd n at the expected frequencies by moving the ion farther away from the trap axis and increasing the modulation index.

Regardless of and unimpeded by the even-odd staggering, parametric driving, most

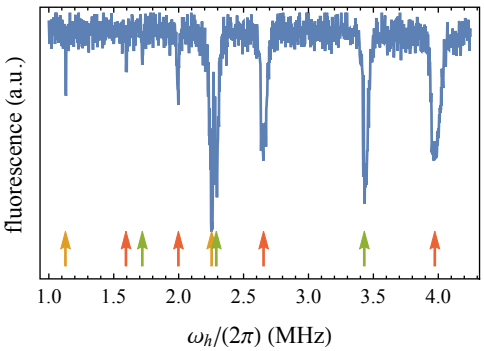

n'	Axial	Radial	Radial	n
1	2.26	6.86	7.94	2
2	1.13	3.43	3.97	4
3	0.75	2.29	2.65	6
4		1.72	1.98	8
5			1.60	10

Figure 5.14: Parametric resonance spectrum. Ion fluorescence is measured over a range of modulation frequencies ω_h applying the experimental sequence in Figure 5.15. Resonances occur in sets (listed on the right-hand side in MHz) for the axial and the two radial modes given by Equation (5.2). Values listed but not visible in the spectrum required different modulation indexes and were measured separately. The assigned values n and n' follow from the assumptions that either only even-order or all subharmonics were excited, respectively. The first assumption proved to be true as the frequencies for $n = 2$ agree with the Rabi spectrum and the subharmonics for odd n were independently found at the expected frequencies.

frequently done on resonance for $n = 2$, is a useful tool for micromotion compensation.

5.4.2. Micromotion compensation

Parametric resonance is only observed if the modulation index h exceeds a certain critical value. For a given subharmonic, that value depends on the displacement from the ideal trapping position [Iba11]. The farther the ion is away from it, the lower the critical modulation index. Therefore one can iteratively compensate micromotion and place the ion at the trap center by minimizing its response to parametric driving.

Applying the experimental sequence depicted in Figure 5.15, ion fluorescence is recorded for modulation frequencies around the secular frequency of interest and different positions of the static potential saddle point. At a suitable modulation index, that is neither too low (nothing would be observed) nor too high (the ion would escape), a parametric resonance occurs and ideally shows a gap, in which the modulation is too weak to cause heating, for certain saddle-point coordinates (Figure 5.15). Note that the driving frequency range should not be chosen too narrow as the resonance is shifted for varying trapping positions (Figure 5.11).

One can subsequently check the response to driving on the other motional modes or at saddle-point positions along another spatial axis. Doing this, one should approach the ideal trapping position at the pseudopotential node. Increasing the modulation index or the parametric driving duration can help narrowing the optimum position down as the ion becomes less susceptible to the driving.

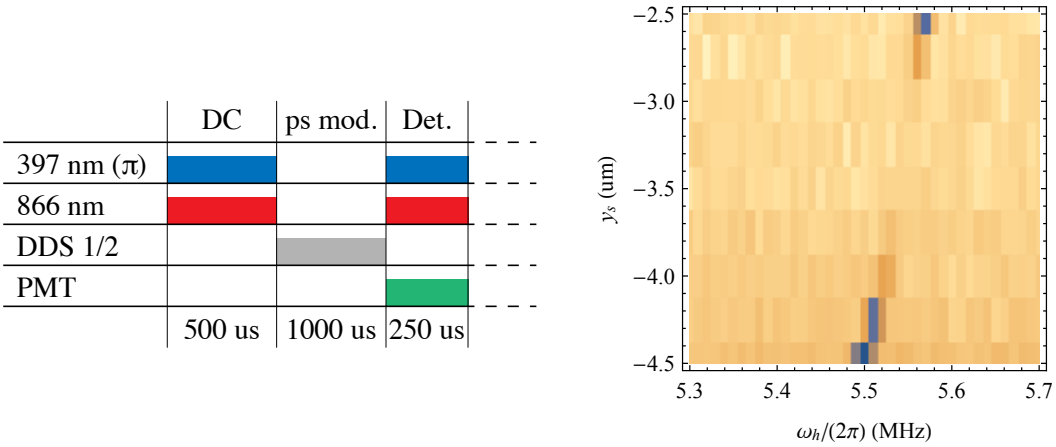

Figure 5.15: Micromotion compensation via detection of parametric resonance. (left) Between cooling and fluorescence detection, the pseudopotential is amplitude modulated ("ps mod.") by the signal from two DDS channels. (right) If the modulation frequency hits a parametric resonance, the ion is heated, which manifests in reduced fluorescence (color coded; blue means low, yellow high fluorescence). Close to the trap center, the response to parametric driving is reduced. In order to heat the ion there, the modulation index or the drive duration need to be increased.

5.5. EIT cooling

With the dipole lasers calibrated (Section 5.1.5), DC reduces the mean excitation number in the axial oscillator mode to a mean phonon number $n_{\mathrm{th}} \approx 5$. This can be estimated from red or blue sideband flopping curves (Section 3.7.2) and is compatible with the theoretical minimum in Equation (3.24).

Ground-state cooling of the ion can subsequently be achieved by exploiting quantum interference in a three-level Λ-system in the $S_{1/2}$ and $P_{1/2}$ manifolds driven by two laser beams at 397 nm (Section 3.6.2). The stronger beam is σ^--polarized and parallel to the magnetic field, the weaker beam π-polarized and perpendicular to it. Their difference in $\boldsymbol{k}$-vectors is parallel to the trap axis such that axial motion can be cooled (Figure 4.26). The frequency detunings δ_r (δ_g) and Rabi frequencies Ω_r (Ω_g) of the stronger (weaker) lasers, can be optimized by minimizing the excitation probability on the red sideband in the following way.

After the EIT cooling pulse, the qubit is initialized and coherently driven on the red sideband for a time t_{l}. The probability of detecting it in the $|S\rangle$-state, given by Equation (3.25), depends on the mean thermal state excitation n_{th} and the drive time. The higher the population of the motional ground state, which means lower n_{th}, the less spin population gets transfered to the $|D\rangle$-state (Figure 5.16). For experimental parameters $\Omega \approx \pi/(2\,\mu\mathrm{s})$ and $\omega_{\mathrm{m}} \approx (2\pi)\,2.7\,\mathrm{MHz}$, one could for example set t_{l} to between 20 and 50 µs and get a practically monotonic measure of n_{th} via a single measurement of P_S. For optimal cooling, P_S is maximized within the parameter ranges of δ_g, Ω_r and Ω_g.

Two possible ways of estimating the thermal state occupation number at the end of

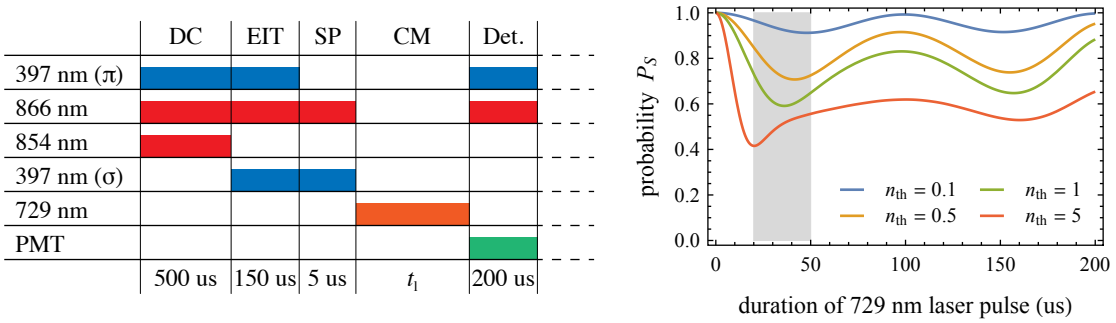

Figure 5.16: (left) Pulse sequence for optimizing EIT cooling. The EIT pulse is followed by SP, coherent manipulation on the red sideband, and thresholded spin-state detection. (right) Simulated curves of the probability P_S versus red-sideband-pulse duration for thermal states with different n_{th} according to Equation (3.25) with parameters $\Omega_0 = \pi/(2\,\mu\mathrm{s})$, $\eta = 0.04$, and $\omega_{\mathrm{m}} = 2.7\,\mathrm{MHz}$. For pulse durations in the range of 20 to 50 µs, the probability P_S can be used as a monotonic measure of n_{th}.

cooling were described in Section 3.7.2. Figure 5.17 shows example data for both. Driving the red and blue sidebands on resonance, respectively, and at constant laser power for a fixed duration t_l, one can infer n_{th} from the dips in P_S according to Equation (3.26). From the displayed data, which was recorded for $t_l = 50\,\mu\mathrm{s}$, one finds $n_{\mathrm{th}} = 0.33(7)$ after EIT cooling. Alternatively, one can measure the time evolution of P_S while driving the blue sideband and fit the data to the model function (cf. Equation (3.25))

$$P_S(t_l) = \frac{1}{2}\sum_{n=0}^{\infty} P_{n_{\mathrm{th}}}(n)\left(1 + \mathrm{e}^{-\gamma t_l}\cos(\Omega_{1,n} t_l)\right) \tag{5.3}$$

with $P_{n_{\mathrm{th}}}(n)$ from Equation (2.18) and the exponential term to account for decoherence at rate γ [Mee96]. The fit gives $n_{\mathrm{th}} = 0.27(2)$, which corresponds to a ground-state population of 0.79(2).

We have thus far not been able to cool an ion to the motional ground state with substantially lower n_{th} (the lowest was $n_{\mathrm{th}} = 0.13(6)$, Section 6.3). Resolved-sideband cooling on the qubit transition [Mar94; Roo99], for example, yielded similar results. We think that our comparatively high heating rate (discussed below) limits our cooling.

5.6. Heating rate

Despite all efforts in trapped-ion physics to isolate the ion from the environment, uncontrolled heating of the motion cannot be fully suppressed. It occurs when noisy electric fields at the position of the ion couple to its charge and the spectrum of the resulting fluctuating forces overlaps the secular motion frequencies. The origins of the noisy fields are part of ongoing investigations in the ion-trap community; a comprehensive review of the topic was recently published in [Bro15].

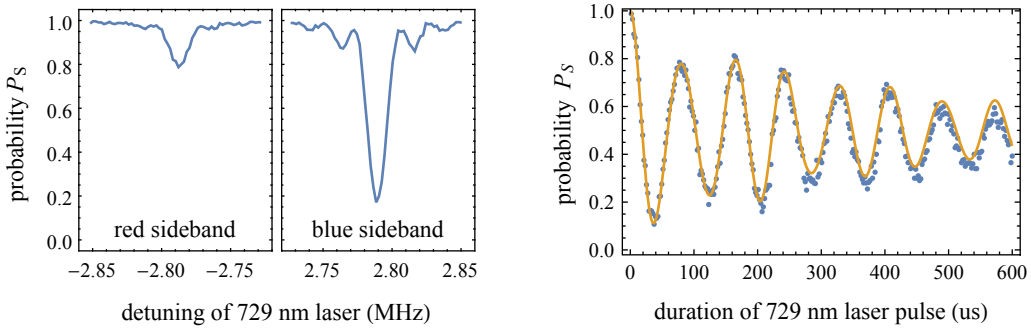

Figure 5.17: Two methods for thermal-state estimation after EIT cooling. (left) The frequency spectra around the red and blue sidebands were obtained for a driving time of 50 µs. Inserting the peak values into Equation (3.26) gives a thermal state excitation $n_{\mathrm{th}} = 0.33(7)$. (right) The time evolution data for driving on the blue sideband can be fitted (orange line) using the model in Equation (5.3), which results in $n_{\mathrm{th}} = 0.27(2)$.

Systematic studies of the dependence of the heating rate on trap properties such as ion-to-surface distance or trap temperature are difficult because they can generally not be changed at will or with all other parameters held constant. Furthermore, the mechanisms generating the noise are to-date poorly understood; possible sources under consideration include thermal electronic noise (Johnson noise) in the trap electrodes or external circuitry, fluctuating patch potentials, and ambient electric fields from injected electronic noise [Tur00].

From a phenomenological point of view, heating of a trapped ion can be described by a single parameter, the heating rate Γ_{h}, measured in 1/s. It is defined as the rate at which an ion in the motional ground state is excited to the first vibrational state and can be linked to the spectral density of electric-field fluctuations $E(t)$ [Tur00],

$$S_E(\omega) = 2 \int_{-\infty}^{\infty} \mathrm{d}\tau \, \langle E(t)E(t+\tau)\rangle_t \, \mathrm{e}^{\mathrm{i}\omega\tau}$$

in units of $\mathrm{V}^2/(\mathrm{cm}^2\,\mathrm{Hz})$ as

$$\Gamma_{\mathrm{h}} = \frac{e^2}{4m\hbar\omega_{\mathrm{m}}} S_E(\omega_{\mathrm{m}}).$$

The heating rate as a characteristic parameter of an ion trap apparatus can be measured by repeatedly determining the mean phonon number after different waiting times, during which the cooling lasers are switched off. The data points obtained by fitting blue-sideband-driving curves to the model in Equation (5.3) are fitted with a linear function (Figure 5.18). Its slope gives the heating rate, in this case $\Gamma_{\mathrm{h}} = 1.09(2)/\mathrm{ms}$. The resulting spectral noise density $S_E(\omega_{\mathrm{m}}) = 2 \times 10^{-11}\,\mathrm{V}^2/(\mathrm{cm}^2\,\mathrm{Hz})$ at $\omega_{\mathrm{m}} = 2.73\,\mathrm{MHz}$ is rather high compared to other modern cryogenic SET with an ion-electrode distance of 50 µm [Bro15, Figure 12].

We believe that it is not technical noise that leads to our high heating rate. When we

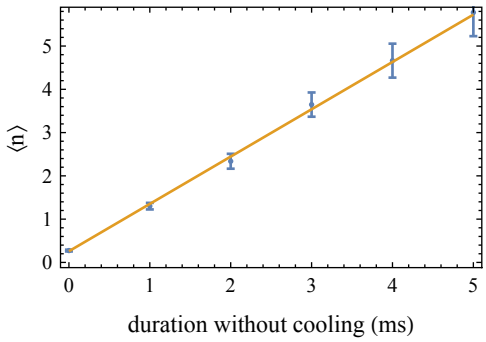

Figure 5.18: Heating-rate measurement data. After EIT cooling, the ion was not cooled for varying time intervals, after which the mean phonon number was determined from blue-sideband flopping curves. The slope of the linear fit (orange line) yields a heating rate $\Gamma_\mathrm{h} = 1.09(2)/\mathrm{ms}$.

first put our apparatus into operation and performed ion-trapping experiments, we had bypassed the active switches on the CEB to exclude possible sources of error. The heating rate we measured then was the same as we measure now. Additionally, the control voltage lines are heavily filtered on the CEB with cutoff frequencies of 14 Hz. In fact, the filtering works so well that we were not able to artificially heat the ion by applying rf signals at the secular frequencies to the control electrodes. Therefore, we currently suspect that the high heating rate in our trap is caused by a polluted or rough SET chip surface. Whether surface contaminants or technical noise cause the heating could potentially be found out by measuring the noise polarization as demonstrated in [Sch15].

5.7. Detection efficiency

An interesting figure of merit from an experimenter's or optics designer's point of view is the overall detection efficiency of the imaging system based on our custom-designed objective (Section 4.3.1). A crude estimate can be gained from ion fluorescence as displayed in Figure 5.3 (left). At the top of the peak, 27 cts were registered in 200 µs. The corresponding population of the $P_{1/2}$ found from the fit was 0.2. Since the lifetime of that state is $\tau = 7.7$ ns (Table 3.1), one can estimate that 2600 photons were scattered within the detection window, yielding a detection efficiency on the order of 1 %.

A more refined technique for determining the detection efficiency that does not rely on knowing the induced scattering rate uses the ion as sub-Poissonian single-photon source [Alm09]. After DC, the repump beam is switched off such that the 397 nm beam pumps the electronic state into the $D_{3/2}$-manifold (Figure 5.19, part (I)). During the subsequent detection window, the pump beam is off and the repump laser switched on again. This transfers the electronic population back to the $S_{1/2}$-manifold and releases a single 397 nm photon with no background since the 397 nm beam is off and light at 866 nm is blocked by the bandpass filter in the imaging system. The measured detection probability per

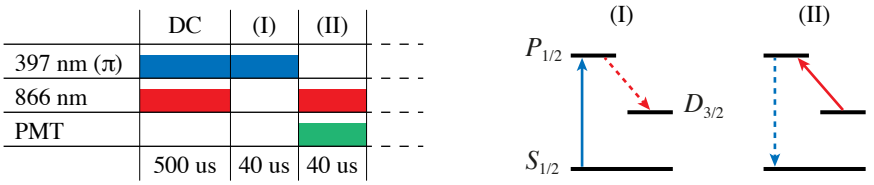

Figure 5.19: Laser-pulse and detection sequence for measuring the detection efficiency of the imaging system. Pumping to the $D_{3/2}$-manifold (I) followed by repumping (II) releases a single photon from the ion per cycle.

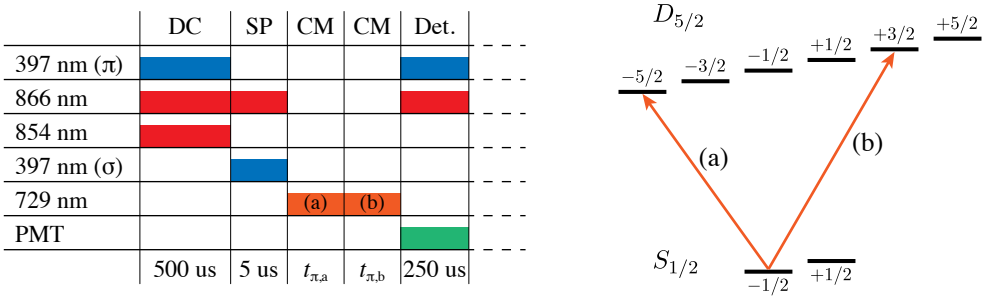

Figure 5.20: Pulse sequence and transitions for measuring the SP fidelity. The SP pulse is followed by π-transitions on (a), (b), or both, before the ground-state population is read out.

excitation and repumping cycle from over a million shots is 0.699(9) %. This is in the region of the expected detection efficiency of 0.9 % based on specifications of the imaging system components but hints at losses, which are currently not well understood. A possible source for losses are the anti-reflection and reflective coatings of the SO, which were explicitly specified only for ambient but not cryogenic temperatures.

5.8. Fidelity of spin polarization

SP into the $|S\rangle$-state was optimized coarsely by observing fluorescence (Section 5.2.1) and more refined via Rabi flops (Section 5.2.4). Quantifying the state-initialization fidelity $\mathcal{F}$ (as defined in Section B.1), however, requires a more elaborate technique.

We measure the ground-state population P_S (which always includes the population in the $S_{1/2}(m_J = +1/2)$-state) after three different pulse sequences, making use of the fact that we can address different transitions between the $S_{1/2}$- and $D_{5/2}$-manifolds by exclusively shifting the frequency of the quadrupole laser: Following the SP pulse, we either apply a π-pulse on the $S_{1/2}(m_J = -1/2) \leftrightarrow D_{5/2}(m_J = -5/2)$ transition (marked (a) in Figure 5.20), a π-pulse on the $S_{1/2}(m_J = -1/2) \leftrightarrow D_{5/2}(m_J = 3/2)$ transition (marked (b)), or both. In an exemplary measurement, we have found the populations $P_S^{(\mathrm{a})} = 2.03(7)\,\%$, $P_S^{(\mathrm{b})} = 1.49(6)\,\%$, and $P_S^{(\mathrm{a,b})} = 1.04(5)\,\%$.

Consider that the two pulses have spin-flip probabilities p_a and p_b, respectively. The

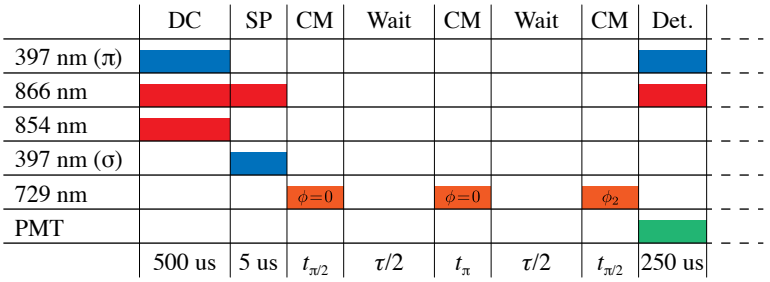

Figure 5.21: Pulse sequences for Ramsey experiments. For Ramsey interferometry without spin echo, the CM pulse sandwiched between the wait times is left out. The phase ϕ_2 of the second $\pi/2$-pulse is varied to obtain Ramsey fringes.

expected ground-state populations can then be expressed as

$$\begin{aligned} P_S^{(\mathrm{a})} &= 1 - \mathcal{F}\, p_\mathrm{a}, \\ P_S^{(\mathrm{b})} &= 1 - \mathcal{F}\, p_\mathrm{b}, \\ P_S^{(\mathrm{a,b})} &= 1 - \mathcal{F}\, p_\mathrm{a} - \mathcal{F}\,(1 - p_\mathrm{a})\, p_\mathrm{b}, \end{aligned}$$

from where one can find a formula for the fidelity

$$\mathcal{F} = 1 - \frac{P_S^{(\mathrm{a,b})} - P_S^{(\mathrm{a})}\, P_S^{(\mathrm{b})}}{1 + P_S^{(\mathrm{a,b})} - P_S^{(\mathrm{a})} - P_S^{(\mathrm{b})}}.$$

Inserting the measured values yields a SP fidelity $\mathcal{F} = 98.96(5)\,\%$.

Since this was sufficient for the experiments in this thesis, we did not put more effort into improving the fidelity. In principle, one way to do so would be to clean the polarization of the corresponding 397 nm laser beam and ensure parallelism between that beam and the magnetic field. An alternative and potentially more promising approach would be frequency-resolved optical pumping on the quadrupole transition after the original SP pulse [Roo06].

5.9. Spin-coherence measurement

Coherent manipulation of any quantum system is ultimately limited by decoherence caused by its interaction with the environment. We perform Ramsey interferometry (Section 5.9) to measure how long coherence between the qubit states and the driving laser prevails, and to identify and eliminate possible noise sources.

After cooling and SP, the first $\pi/2$-pulse on the carrier (Figure 5.21) creates an equal superposition of the qubit states and defines the phase (set to zero). After a wait time τ, the second $\pi/2$-pulse is applied and subsequently the $|S\rangle$-state population P_S measured. Optionally, a spin-echo π-pulse after half the wait time can be applied to suppress the effect

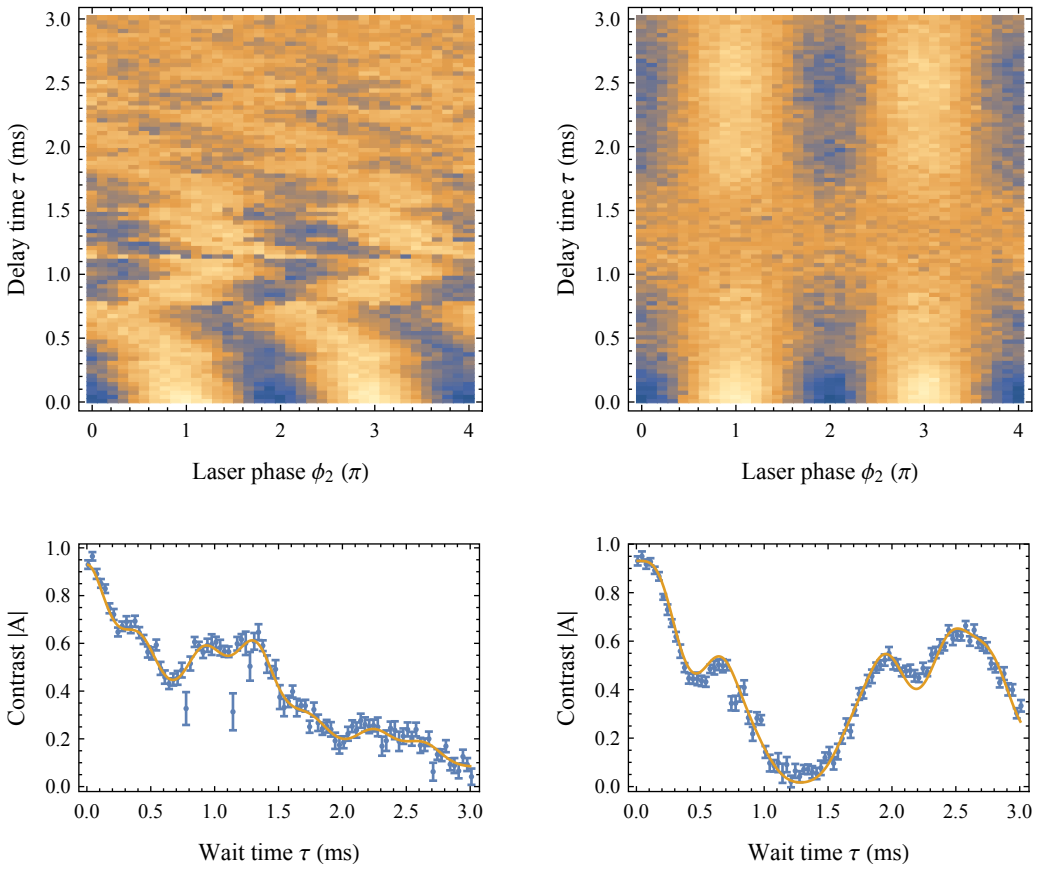

Figure 5.22: Experimental and evaluated data from Ramsey experiments (left) without and (right) with a spin-echo pulse (Figure 5.21). The 2D plots give P_S for varying laser phase ϕ_2 and wait time τ (color coded; blue means 0, yellow 1). The phase offsets in the Ramsey fringes without spin echo are caused by a slowly drifting detuning. The contrast of the fringes generally decreases for longer wait times, but not monotonously. By fitting the model in Equation (5.4) to the contrast data at the bottom, one obtains the noise components listed in Table 5.1.

Table 5.1: Fitted noise components for Ramsey experiments without and with spin-echo pulse.

Without spin echo		With spin echo	
$\omega_k/(2\pi)$ (kHz)	$N_k/(2\pi)$ (kHz)	$\omega_k/(2\pi)$ (kHz)	$N_k/(2\pi)$ (kHz)
0.143(8)	0.156(4)	0.20(6)	0.11(2)
0.79(1)	0.501(15)	0.784(5)	0.459(5)
2.24(3)	0.92(6)	2.28(1)	0.805(15)

of slowly varying or constant detuning of the laser from the atomic transition. The spin dynamics throughout the sequence is described in Section 5.9.

We vary the phase ϕ_2 of the second $\pi/2$-pulse from 0 to 4π and the wait time from 0 to 3 ms and record $P_S(\phi_2, \tau)$ (Figure 5.22). The contrast $\big|A(\tau)\big|$ of the Ramsey fringes at time τ is obtained by fitting the function in Equation(3.30) to the corresponding dataset. The phase offsets $\Phi_0(\tau)$ from Equation (3.28) due to a nearly constant but drifting detuning δ_0 are not of interest at this point, but one can see that they are canceled in the Ramsey sequences with spin-echo pulse.

The contrast curves versus wait time τ (Figure 5.22) can be fitted well using the model in Equation (3.29) with three frequency components,

$$A(\tau) = A_0 \prod_{k=1}^{3} J_0\Big(N_k \big|\hat{F}_\tau(\omega_k)\big|\Big), \tag{5.4}$$

where the initial value A_0 is fixed to the first data point. The results are listed in Table 5.1.

Both variants of Ramsey experiments hint at the same discrete noise components.[3] But it shall be noted that the data presented here are not sufficient to discriminate between low-frequency discrete and white noise. Instead of the lowest-frequency components, one could have equally well fitted a Gaussian decay envelope $\mathrm{e}^{-(\tau/T)^2}$ with dephasing time T [Lan06, p. 149; Kie01, p. 129] to the data.

[3] In experiments performed during the revision of this thesis, it turned out that the noise component at 0.8 kHz had vanished due to unknown reasons, and the one at 2.3 kHz was caused by the GHz-source clocking the DDS boards which create the AOM signals.

6. Quantum Control

published in: *Nat. Commun.* **7** (2016)
arXiv:1509.06157 [quant-ph]

The active electronic switches we have put close the ion trap in our apparatus (Section 4.1.2) allow us to switch between sets of control voltages (Section 4.4). Since the voltage supply lines are filtered before but not after the switches, we can realize changes to the electric trapping potential on the order of nanoseconds, much faster than the ion oscillation period. Of particular interest in this chapter are displacements of the trapping potential along the trap axis without changing its curvature. We use such nonadiabatic shifts of the trap center to create coherent states of the ion motion.

Section 6.1 starts with the mathematical description of the evolution of a wave function in a moving harmonic potential, which is narrowed down to quasi-instantaneous displacements in Section 6.2. Section 6.3 presents the creation of coherent states in the axial motional mode of a single ion and the tracking of its oscillation trajectory by a combination of two potential-well displacements. Section 6.4 examines the quality of our control over the timing of the potential displacements. A large coherent state is de-excited to the ground state by a well-timed second well displacement. Section 6.5 details how we create coherent states of sizes up to $\alpha \approx 100$ and utilize these to map out the laser–ion interaction matrix elements, the Franck-Condon coefficients in Equation (3.8), for blue sidebands up to fifth order.

6.1. Oscillator in a moving potential

Consider an ion trapped in a linear Paul trap at the pseudopotential null line. Disregarding radial motion, it oscillates in a harmonic well along the axial x-direction at frequency ω_m created by the confining electrostatic potential. The dynamics of the oscillating ion are then described by the Hamiltonian in Equation (2.13),

$$H_0 = \frac{1}{2m}\,P^2 + \frac{m\omega_\mathrm{m}^2}{2}\,X^2 = \hbar\omega_\mathrm{m}\left(a^\dagger a + \frac{1}{2}\right).$$

In our experiments, we intend to shift the harmonic potential well along the trap axis while keeping its curvature constant. The Hamiltonian governing the system is now time-dependent and given by

$$H(t) = \frac{1}{2m}\,P^2 + \frac{m\omega_\mathrm{m}^2}{2}\left(X - d(t)\right)^2 = D\big(\tilde{d}(t)\big)\,H_0\,D^\dagger\big(\tilde{d}(t)\big)$$

where $d(t)$ is the position of the well minimum, D the displacement operator defined in Equation (F.4), and $\tilde{d}(t) = d(t)/(2x_0)$ the normalized displacement with $x_0 = \sqrt{\hbar/(2m\omega_\mathrm{m})}$ from Equation (2.14). I will derive how the wave function $|\psi(t)\rangle$ of the ion subject to $H(t)$ evolves in time, based on [Lau11] but seeking to correct mistakes therein.[1]

We start by transforming the wave function to the rest frame of the potential well as $|\chi(t)\rangle = D^\dagger(\tilde{d}(t))\,|\psi(t)\rangle$ such that it oscillates around its center according to the Schrödinger equation

$$\mathrm{i}\hbar\partial_t\,|\chi(t)\rangle = \Big(H_0 - \dot{d}(t)\,P\Big)\,|\chi(t)\rangle.$$

In the interaction picture (Section A.3) with respect to H_0, we have

$$|\chi^\mathrm{I}(t)\rangle = \mathrm{e}^{\mathrm{i}H_0 t/\hbar}\,|\chi(t)\rangle \qquad \Rightarrow \qquad \partial_t\,|\chi^\mathrm{I}(t)\rangle = \mathcal{H}(t)\,|\chi^\mathrm{I}(t)\rangle,$$

where Equation (F.3) can be used to find

$$\mathcal{H}(t) = -\dot{\tilde{d}}(t)\Big(a^\dagger\,\mathrm{e}^{\mathrm{i}\omega_\mathrm{m}t} - a\,\mathrm{e}^{-\mathrm{i}\omega_\mathrm{m}t}\Big) = \dot{\tilde{u}}(t)\,a^\dagger - \dot{\tilde{u}}^*(t)\,a$$

with the complex phase-space distance $\tilde{u}(t)$

$$\tilde{u}(t) = -\int_0^t \mathrm{d}t_1\,\dot{\tilde{d}}(t_1)\,\mathrm{e}^{\mathrm{i}\omega_\mathrm{m}t_1}.$$

The corresponding unitary evolution operator for $|\chi^\mathrm{I}(t)\rangle$ can be computed using the Magnus expansion (Appendix A) as

$$\tilde{U}(t) = \exp\left\{\int_0^t \mathrm{d}t_1\,\mathcal{H}(t_1) + \frac{1}{2}\int_0^t \mathrm{d}t_1 \int_0^{t_1} \mathrm{d}t_2\,[\mathcal{H}(t_1), \mathcal{H}(t_2)]\right\} = D\big(\tilde{u}(t)\big)\,\mathrm{e}^{\mathrm{i}\phi(t)}$$

with the real overall phase $\phi(t)$ defined as

$$\phi(t) = \Im\left[\int_0^t \mathrm{d}t_1 \tilde{u}^*(t_1)\dot{\tilde{u}}(t_1)\right].$$

Higher-order terms in the Magnus expansion vanish because the commutator $[\mathcal{H}(t_1), \mathcal{H}(t_2)]$ is a scalar. Combining these results, the wave function of the ion is given by

$$|\psi(t)\rangle = \mathrm{e}^{\mathrm{i}\phi(t)}\,D\big(\tilde{d}(t)\big)\,\mathrm{e}^{-\mathrm{i}H_0 t/\hbar}\,D\big(\tilde{u}(t)\big)\,D^\dagger\big(\tilde{d}(0)\big)\,|\psi(0)\rangle.$$

[1] The errors in [Lau11] are: "$+\dot{s}(t)$" in Equation (4) should read "$-\dot{s}(t)$"; the operators $\hat{a}$ and $\hat{a}^\dagger$ in Equation (5) should be swapped; the right-hand side of Equation (8) should be multiplied by -1. The result in Equation (9) is correct.

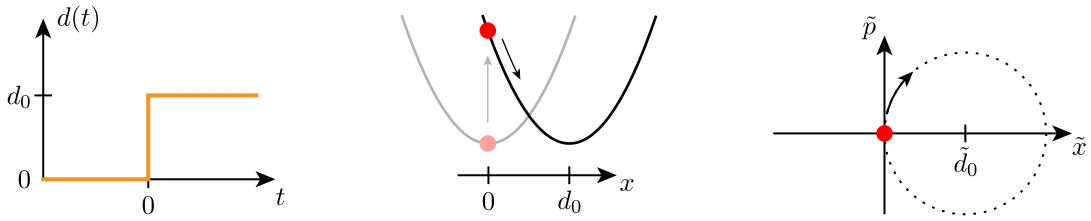

Figure 6.1: Evolution after a quasi-instantaneous harmonic-well displacement. When the well minimum is displaced from $d(t \leq 0) = 0$ to $d(t > 0) = d_0$ (left), an ion initially in the motional ground state is excited and starts oscillating (middle). In normalized phase space, the coherent-state Wigner function (cf. Figure 2.6), depicted as a red dot, simply rotates around the well minimum (right).

If we assume the initial state of the ion is the motional ground state of the harmonic oscillator, then the motional state of the ion remains in a coherent state throughout the whole process, i.e. $|\psi(t)\rangle = |\alpha(t)\rangle$ with coherent state amplitude

$$\alpha(t) = \tilde{d}(t) - \tilde{d}(0) - \mathrm{e}^{-\mathrm{i}\omega_\mathrm{m} t} \int_0^t \mathrm{d}t_1 \, \dot{\tilde{d}}(t_1) \, \mathrm{e}^{\mathrm{i}\omega_\mathrm{m} t_1}. \tag{6.1}$$

6.2. Quasi-instantaneous displacements

The switches we have placed close to the Surface-Electrode ion Trap (SET) (Section 4.1.2) allow us to make changes to the trapping potential within a few nanoseconds, two orders of magnitude shorter than the axial oscillation period of an ion. We hence describe a switching event at time $t = 0$ from a well position at $d(t \leq 0) = 0$ to $d(t > 0) = d_0$ as

$$d(t) = d_0 \, \Theta(t),$$

where $\Theta(t)$ is the Heaviside function defined in Equation (F.16). An ion that was at rest in the well at $d = 0$, that is in the motional ground state, finds itself still at rest in the displaced well but in an excited state, and subsequently oscillates in the new potential (Figure 6.1). The coherent state amplitude follows from Equation (6.1) and is given by

$$\alpha(t > 0) = \tilde{d}_0 \left(1 - \mathrm{e}^{-\mathrm{i}\omega_\mathrm{m} t}\right). \tag{6.2}$$

Note that this type of classical behavior in phase space is not restricted to coherent states. Any point of a Wigner function follows a classical trajectory in phase space as long as the potential is not of higher than quadratic order in position (Appendix C). In normalized phase space, spanned by the quadratures $\tilde{x}$ and $\tilde{p}$, the trajectory is therefore a circle around the center of a momentarily stationary potential well. Consequently, any Wigner function

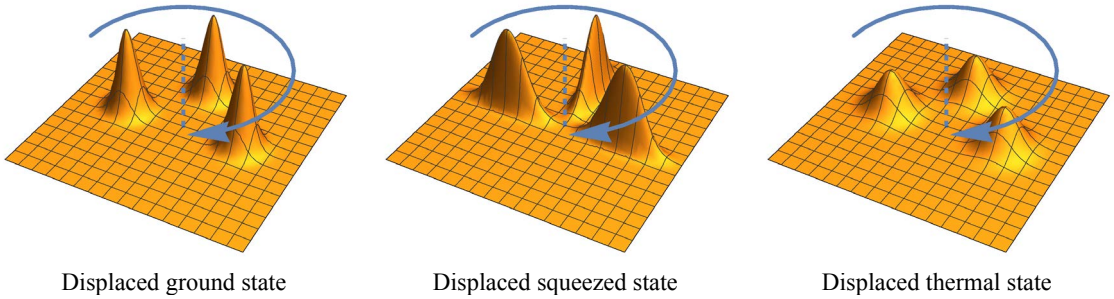

Figure 6.2: Evolution of displaced Wigner functions in phase space. Any Wigner function rotates clockwise around the position of the harmonic-well minimum, shown for displaced ground, squeezed and thermal states at three different moments in time, $t = 0, \pi/(2\omega_\mathrm{m}), \pi/\omega_\mathrm{m}$.

$W(\tilde{x}, \tilde{p})$ rotates around the well center at $\tilde{x} = \tilde{d}_0$ as

$$W(\tilde{x}, \tilde{p}, t) = W\Big(\tilde{d}_0 + \Big(\tilde{x} - \tilde{d}_0\Big)\cos(\omega_\mathrm{m} t) - \tilde{p}\sin(\omega_\mathrm{m} t), \tilde{p}\cos(\omega_\mathrm{m} t) + (\tilde{x} - \tilde{d}_0)\sin(\omega_\mathrm{m} t), 0\Big),$$

see Figure 6.2. It periodically returns to its initial state,

$$W(\tilde{x}, \tilde{p}, t + 2\pi/\omega_\mathrm{m}) = W(\tilde{x}, \tilde{p}, t).$$

For this reason, it is valid to describe the dynamics in terms of coherent state displacements, even if the initial state is a thermal and not a pure ground state.

6.3. Tracking oscillations

In a first set of experiments using the active switches, we tracked the oscillation trajectory of a single ion described by Equation (6.2) throughout multiple oscillation cycles. At a time interval T after displacing the potential from $d(t \leq 0) = 0$ to d_0, we reversed the displacement back to $d(t > T) = 0$, which can be written mathematically as $d(t) = d_0(\Theta(t) - \Theta(t - T))$ (Figure 6.3). Subsequently, the coherent state evolved as

$$\alpha(t > T) = \tilde{d}_0 \left(1 - \mathrm{e}^{-\mathrm{i}\omega_\mathrm{m} T}\right) \mathrm{e}^{-\mathrm{i}\omega_\mathrm{m}(t-T)}. \tag{6.3}$$

This protocol maps the complex coherent state amplitude of the ion in the well around d_0 onto the coherent-state size in the final potential,

$$|\alpha(T)| = \tilde{d}_0 \sqrt{2 - 2\cos(\omega_\mathrm{m} T)}, \tag{6.4}$$

which can be determined from sideband-flopping curves (Section 3.7).

An experimental sequence (Figure 6.4) began by cooling a trapped ion to near the ground

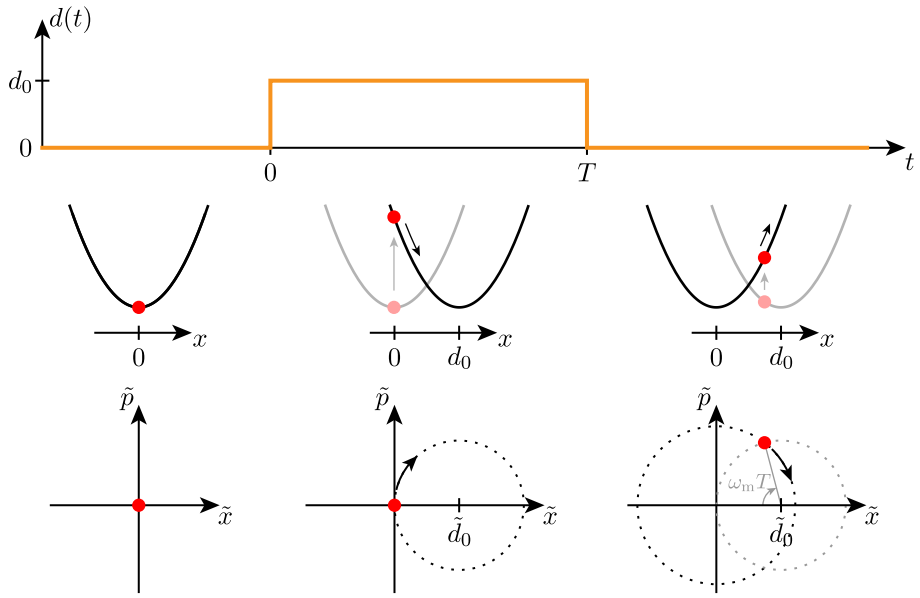

Figure 6.3: Protocol for tracking the coherent state evolution in a displaced potential. The position of the axial potential minimum (top graph) is shifted quasi-instantaneously between positions 0 and d_0 and back at times $t = 0$ and T, respectively. The potential energy-versus-position diagram (middle row) and the phase-space diagram (bottom row) depict the oscillator dynamics. Prior to the first displacement, the ion is cooled to near the motional ground state. The first displacement excites the ion at rest, whereupon it starts oscillating at frequency ω_m. The coherent-state size in the potential after the second displacement depends on T and is given by Equation (6.4).

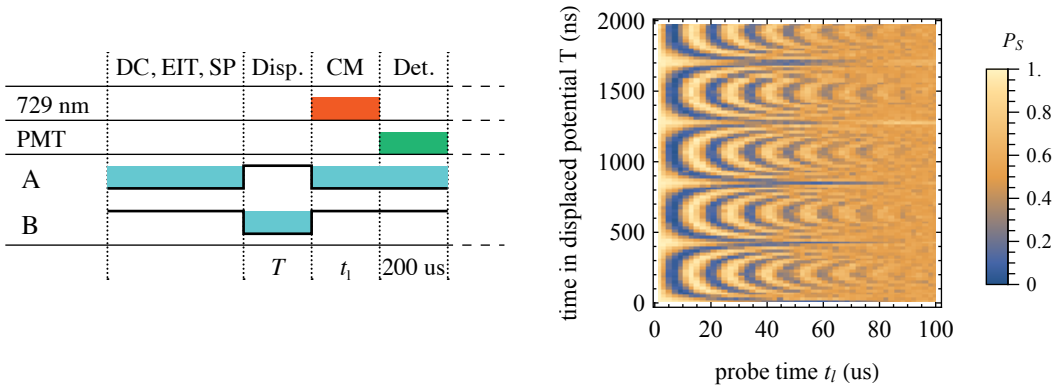

Figure 6.4: Experimental sequence and data of the coherent-state-tracking experiment. (left) After ground-state cooling and SP (the pulses of all other lasers equal those in Figure 5.16), the pulse generator switches from profile A to B for a time T and back, which displaces the trapping potential. Subsequently, the ion is coherently driven on the first blue sideband for a duration t_1 and the spin state is read out. (right) The probability for finding the spin in state $|S\rangle$ was measured versus T and t_1, where every data point for P_S was obtained from 200 experimental shots.

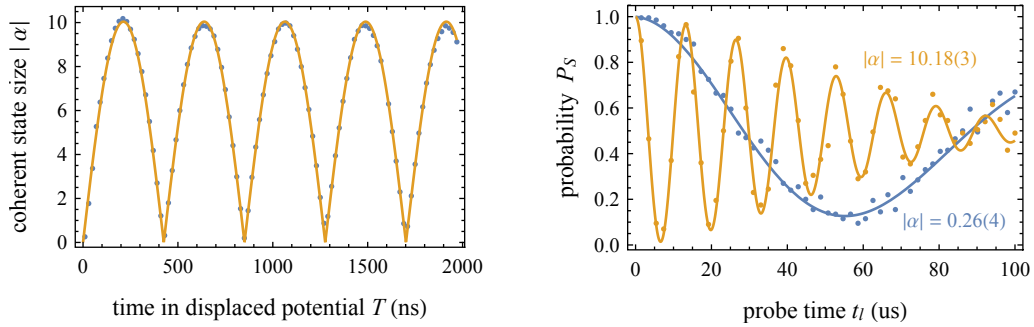

Figure 6.5: Coherent state evolution in the displaced potential. (left) The coherent-state size of the ion in the final potential in- and decreases periodically with T, corresponding to the evolution in the displaced potential (Figure 6.3) predicted by Equation (6.4). The fit (orange line) allows for precise determination of the motional frequency to be $\omega_\mathrm{m} = (2\pi)\,2.3506(6)\,\mathrm{MHz}$. (right) Comparison of the flopping curves of two states with different excitations, $|\alpha| = 0.26(4)$ at $T = 10\,\mathrm{ns}$ and $|\alpha| = 10.18(3)$ at $T = 210\,\mathrm{ns}$. The increase in flopping frequency for the more excited state is due to the number-state dependence of the Franck-Condon factor (Equation (3.8) and Figure 3.3).

state (Section 5.5) of the axial oscillator mode, and spin-state initialization (Section 5.2.1). Then the Digital Delay and Pulse Generator (DDPG) was triggered to switch from profile A to profile B and back after the time interval T (Section 4.4). The control voltages for the electrodes had previously been programed such that profile B created a potential in the SET that was displaced by d_0 along the trap axis with respect to the one for profile A. After the second displacement, the quadrupole laser was switched on for a duration t_l with the frequency set to the first blue sideband and a Lamb-Dicke parameter $\eta \approx 0.045$. Finally, the spin state was read out with binned fluorescence detection (Section 3.7.1). This sequence was repeated 200 times to estimate the probability P_S of the spin to be in the $|S\rangle$-state, for every combination of probe time t_l in the range from 0 to 100 µs and time T in the displaced potential in the range from 0 to 1970 ns (Figure 6.4).

The acquired experimental data agrees well with the functional form (cf. Section 3.7.1)

$$P_S(t_\mathrm{l}) = \frac{1}{2}\sum_n P_{\alpha,n_\mathrm{th}}(n)\left(1 + \mathrm{e}^{-\gamma t_\mathrm{l}}\cos(\Omega_{s,n} t_\mathrm{l})\right), \tag{6.5}$$

where $P_{\alpha,n_\mathrm{th}}(n)$ is the number-state distribution of a thermal state displaced by the phase-space distance α (Equation (2.19)) and the exponential decay at rate γ accounts for spin and motional decoherence during the probe pulse.

The flopping curve for a single T did not allow the extraction of all parameters ($|\alpha|$, n_th, Ω, γ) independently because they are too correlated in the fitting model. Therefore, we first probed a non-displaced state directly after cooling ($\alpha = 0$) and find $n_\mathrm{th} = 0.13(6)$, $\Omega = (2\pi)\,183(3)\,\mathrm{kHz}$, $\gamma = 3.0(8)\,\mathrm{kHz}$. Then we fixed these parameters and fitted the model with floating $\alpha(T)$ to the flopping curves for all T (Figure 6.5 (left)). The resulting values match well the model of the coherent state evolution in Equation (6.4) with a maximum coherent-state size of $2\tilde{d}_0 = 10.04(2)$ and allowed us to accurately determine the motional

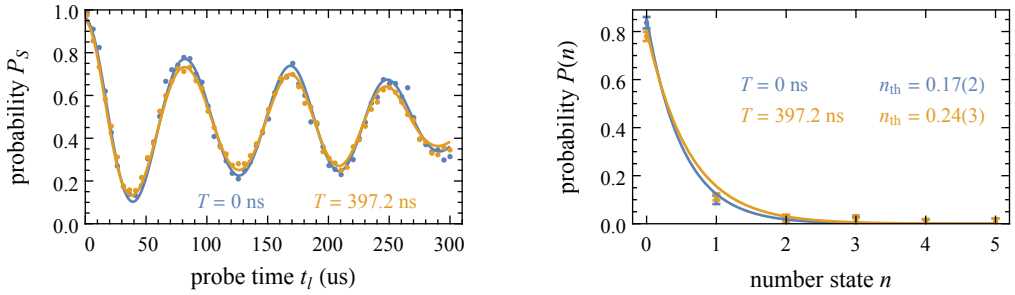

Figure 6.6: Comparison of ground and returned state. (left) The flopping curves for the initial (blue) and the returned (orange) states were analyzed using the model in Equation (6.6). (right) The number-state population probabilities (same coloring) from fits to the model in Equation (6.6) are matched by thermal-state distributions (Equation (2.18)) with the mean phonon numbers given.

frequency $\omega_m = (2\pi)\,2.3506(6)\,\mathrm{MHz}$ in the displaced potential.

While we have reliable sub-nanosecond control over T (see also Section 6.4), control over the potential displacement distance is reproducible but not accurate. The control voltages were calculated for a nominal displacement of 10 nm. However, the phase-space distance $\tilde{d}_0$ determined from the data corresponds to a displacement $d_0 = 73.6(2)\,\mathrm{nm}$. The reason for this is that such small displacements only require changes of the supply voltages on the order of or below 10 mV, which is below the calibration precision and accuracy among the DAC channels that supply the trap electrodes. This was not a limitation for this experiment because it primarily depended on reproducible timing.

6.4. Catching in the ground state

In order to characterize the timing control of the switches, we applied the same experimental sequence as in Figure 6.4 and returned the ion to the ground state after one oscillation in the displaced potential.[2] To increase sensitivity, we used a large displacement distance $d_0 \approx 1.2\,\mu\mathrm{m}$, which corresponds to a phase-space distance $\tilde{d}_0 \approx 85$ in the axial harmonic potential with an oscillator frequency $\omega_m \approx (2\pi)\,2.52\,\mathrm{MHz}$. After experimentally determining the time $T = 397.2\,\mathrm{ns}$ in the displaced potential to yield the lowest final motional excitation, we measured the probability P_S of finding the spin in the $|S\rangle$-state after probe pulse durations t_l between 0 and 300 µs. The resulting flopping curve is similar to the one for a non-displaced ion directly after ground-state cooling (Figure 6.6 (left)).

For a quantitative comparison of the initial and returned stated, we first fitted the model in Equation (6.5) to the flopping curves assuming $|\alpha| = 0$ (Table 6.1). To check whether

[2] The only difference here is that we need to trigger the experimental sequence from the phase of the Radio Frequency (rf) trap drive for minimal final motional excitation. We attribute this to a residual pseudopotential gradient along the trap axis.

the states indeed are thermal states, we furthermore fitted the model

$$P_S(t_\mathrm{l}) = \frac{1}{2}\sum_n P(n)\left(1 + \mathrm{e}^{-\gamma t_\mathrm{l}}\cos(\Omega_{s,n} t_\mathrm{l})\right), \tag{6.6}$$

in which all $P(n)$ were individually floating and no particular number-state distribution was assumed a priori. In both cases, the resulting $P(n)$ agree well with a thermal-state distribution (Figure 6.6 (right)) with fit parameters given in Table 6.1. This confirms that the axial oscillator excitation due to the first displacement was removed by the second displacement. Compared to the initial state, however, the returned state had a higher mean phonon number.

Table 6.1: Best fit values for the data in Figure 6.6.

	Initial ground state		Returned state	
Model in →	Equation (6.5)	Equation (6.6)	Equation (6.5)	Equation (6.6)
$\Omega/(2\pi)$ (kHz)	276.9(7)	276.8(6)	277.3(8)	277.2(6)
γ (kHz)	3.4(2)	3.2(2)	4.0(3)	3.7(2)
n_th	0.15(3)	0.17(2)	0.21(3)	0.24(3)

A possible source for an increase in the mean phonon number is timing jitter in T. In a single experimental realization, the final state after the second displacement with a small mis-timing $\delta T = T - 2\pi/\omega_\mathrm{m}$ is a coherent state with amplitude (cf. Equation (6.3))

$$\alpha(\delta T) = \tilde{d}_0\left(1 - \mathrm{e}^{-\mathrm{i}\omega_\mathrm{m}\delta T}\right) \approx \mathrm{i}\tilde{d}_0\omega_\mathrm{m}\delta T.$$

If the δT are statistically distributed, the final state becomes a statistical mixture of displaced thermal states. Assume that the distribution of δT is Gaussian with a standard deviation σ. In terms of Wigner functions (Appendix C), the final state is then given by

$$W_\sigma(\tilde{x},\tilde{p}) = \frac{1}{\sqrt{2\pi}\,\sigma}\int \mathrm{d}(\delta T)\,\mathrm{e}^{-\delta T^2/(2\sigma^2)}\,W_{n_\mathrm{th}}(\tilde{x},\tilde{p} + \tilde{d}_0\omega_\mathrm{m}\delta T)$$

with the Wigner function W_{n_th} from Equation (C.3) for the initial thermal state. Using Equation (C.1), the number-state distribution of W_σ can be calculated as

$$P(n) = \pi\iint \mathrm{d}\tilde{x}\,\mathrm{d}\tilde{p}\,W_n(\tilde{x},\tilde{p})\,W_\sigma(\tilde{x},\tilde{p}).$$

This distribution is not strictly but nearly thermal and can be fitted with $P_\mathrm{th}(n)$ to find the mean phonon number n_th. Applying this method, we find that the jitter would need to be on the order of $\sigma \approx 200\,\mathrm{ps}$ to increase the mean phonon number from ≈ 0.16 to ≈ 0.22. Compared to previously performed characterization experiments with the switches, where we had measured the purely electronic jitter to be below 45 ps [Fad13], this estimate of σ

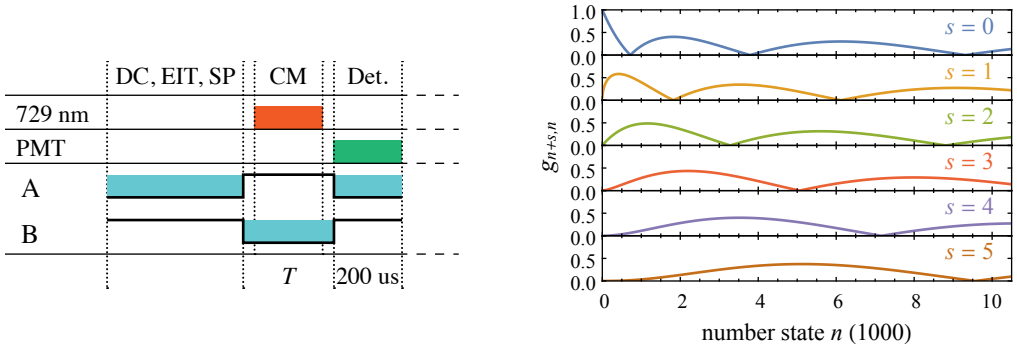

Figure 6.7: (left) Experimental sequence for creating large coherent states (the pulses of all other lasers equal those in Figure 5.16). After the first displacement by d_0 (from profile A to B), the coherent state of the ion is probed by a pulse of duration t_1. Subsequently, the motion is de-excited by shifting the potential well back to the initial position after a time $T = j2\pi/\omega_\mathrm{m}$ with j an integer. Finally, the spin state is detected. (right) Plots of the Franck-Condon coefficients in Equation (3.8) for $0 \leq s \leq 5$ and $\eta = 0.045$. Driving of higher-order sidebands only becomes accessible for states far outside the Lamb-Dicke regime.

seems too high. Nonetheless, even though we have timing control on the order of 100 ps as observed when scanning T, we cannot rule out a timing jitter on the same order of magnitude for the full SET setup.

6.5. Large coherent states and laser–ion interaction

In a second set of experiments, we created coherent states of sizes up to $\alpha \approx 100$, which involve number states with more than 10 000 quanta of energy. We used these states to verify the form of the laser–ion interaction given by the Franck-Condon coefficients (Figure 6.7 (right)) for sidebands up to $s = 5$ far outside the usual regime of operation.

The highly excited coherent states were created by quasi-instantaneously displacing the trapping potential by varying distances d_0 (Figure 6.1). This excites an ion initially at rest ($n_\mathrm{th} \approx 0.2$, $\alpha = 0$) to a coherent state of size $|\alpha| = \tilde{d}_0$ in the potential well centered around d_0. In contrast to the experiments described in Section 6.3, here we probed the coherent states with the quadrupole laser in the displaced potential (Figure 6.7). Doing this, we could directly control the coherent-state size by the displaced distance. We found that the high oscillator state excitation adversely affected the scattering rate during the detection pulse and hence the spin-state detection. To counter this, we applied a second displacement back to the original position after a multiple of the ion's oscillation period, $T = j2\pi/\omega_\mathrm{m}$ with j an integer, to de-excite the motional state. For displacements d_0 up to $\approx 1.5\,\mu\mathrm{m}$, we measured the probability P_S for probe pulse durations between 0 and 80 µs for sidebands up to $s = 5$ (Figure 6.8, top row).

For the analysis of these measurements we found it necessary to include a laser detuning due to AC Stark shifts (Section 3.3) in the model. If the laser is detuned from resonance, the

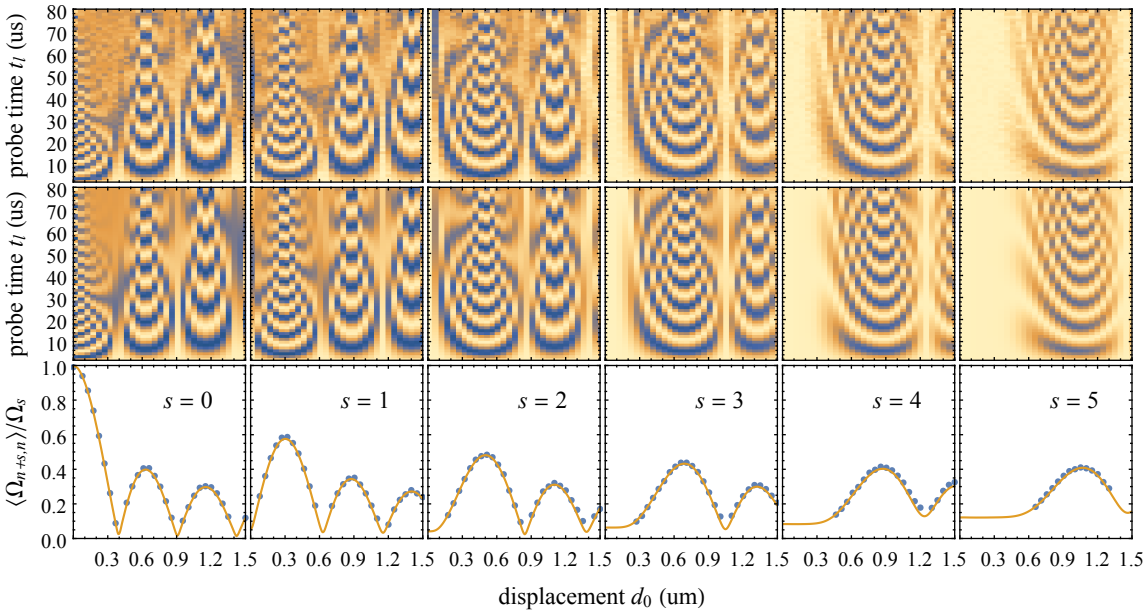

Figure 6.8: Experimental and simulated data for the laser–ion interaction. (top) Measurement of the probability P_S versus probe times t_l and displacement distances d_0 for the carrier and first five blue-sideband transitions. The color scaling is the same as in Figure 6.4. (middle) Simulated data from the model in Equation (6.7) with fitted parameters. (bottom) Plot of the mean Rabi frequencies $\langle\Omega_{s,n}\rangle$ versus displacement distance. The frequencies were obtained from the peaks in the Fourier spectra of the flopping curves (blue dots) and from averaging the simulated Rabi frequencies based on Franck-Condon factors and laser detunings over the number-state distribution (orange line, Equation (6.10)). See text for details.

frequency of Rabi oscillations is increased while their peak-to-peak amplitude is decreased (Section 3.3). The combination of Equations (3.11) and (3.25) yields the model

$$P_S^{(s\geq 0)}(t_\mathrm{l}) = 1 - \sum_{n=0}^{\infty} P_{\alpha,n_\mathrm{th}}(n)\,\frac{\Omega_{s,n}^2}{\Omega_{s,n}^2+\delta_{s,n}^2}\,\sin^2\!\left(\sqrt{\Omega_{s,n}^2+\delta_{s,n}^2}\,\frac{t_\mathrm{l}}{2}\right) \tag{6.7}$$

for the probability of detecting the spin in the $|S\rangle$-state after a probe pulse of duration t_l. The laser detuning $\delta_{s,n} = \omega_{\mathrm{l},s} - \omega_{\mathrm{a},s,n}$ as the difference between the laser frequency $\omega_{\mathrm{l},s}$ for each sideband and the atomic frequency $\omega_{\mathrm{a},s,n}$ depends on the motional state of the ion. The reason for that is that the atomic frequency, $\omega_{\mathrm{a},s,n} = \omega_\mathrm{a} + \delta_{s,n}^{(\mathrm{AC})}$, is shifted by AC Stark shifts due to off-resonant coupling to other possible transitions and the coupling constants are proportional to the number-state dependent Franck-Condon factors. We took into account the AC Stark shifts from coupling to the other sidebands of the qubit transition as well as to the sidebands of the other possible quadrupole transition for $|\Delta m| = 2$ between the $|S\rangle$ and $D_{5/2}(m_J = 3/2)$-states. The Rabi frequency for this transition is a factor $\sqrt{5}$ smaller and the transition frequency is $\approx 25.74\,\mathrm{MHz}$ higher in a magnetic field $B \approx 3.83\,\mathrm{G}$ (Figure 3.8). This frequency difference is close to $11\,\omega_\mathrm{m}$ at a motional frequency $\omega_\mathrm{m} \approx (2\pi)\,2.338\,\mathrm{MHz}$,

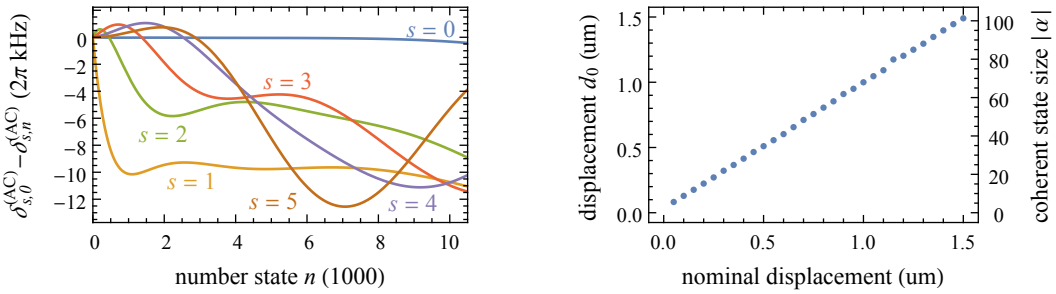

Figure 6.9: (left) Laser detunings due to AC Stark shifts versus number state calculated from Equations (6.8) and (6.9), assuming that the laser was on resonance before any potential displacements. (right) Displacement distances d_0 for the nominal displacements set in the GUI of the computer-control system. The d_0 result from fitting the model in Equation (6.7) to the flopping curves for the carrier transition. The outlier point corresponds to a displacement of $\approx 1.15\,\mu\text{m}$, which produces a coherent state of size ≈ 78 centered around the number state $n = 6110$, where $g_{n,n}$ has a local maximum, which made the fitting ambiguous.

such that the sth sideband of the qubit transition is only 14 kHz below the $(s-11)^{\text{th}}$ sideband of the secondary transition and therefore causes a considerable AC Stark shift. The total AC Stark shifts are given by

$$\delta_{s,n}^{(\text{AC})} = -\sum_{s' \neq s} \frac{\Omega_{s',n}^2}{2\omega_{\text{m}}(s-s')} - \sum_{s'} \frac{\Omega_{s',n}^2/5}{4\left(\omega_{\text{m}}(s-s') - (2\pi)\,25.74\,\text{MHz}\right)}. \tag{6.8}$$

We had set the laser frequency to resonance with the respective sideband transition while the ion was in the motional ground state, that means $\omega_{\text{l},s} = \omega_{\text{a}} + \delta_{s,0}^{(\text{AC})} + \delta_s^{(\text{off})}$. The additional offset term accounts for mis-set laser detunings in the experiment relevant for the higher sidebands, where spectroscopy in the motional ground state is impossible. The total laser detuning is finally given by

$$\delta_{s,n} = \delta_{s,0}^{(\text{AC})} - \delta_{s,n}^{(\text{AC})} + \delta_s^{(\text{off})}. \tag{6.9}$$

and is plotted in Figure 6.9 (left) for zero offset $\delta_s^{(\text{off})}$, which was later determined from the experimental data.

In order to analyze the experimental data, we started by calibrating the displacement distances using the data for the carrier transition. First, the model in Equation (6.7) was fitted with $\delta_s^{(\text{off})} = 0$ to the flopping curve for zero displacement (and hence $\alpha = 0$) to extract the coupling constant $\Omega_0 \approx (2\pi)\,205\,\text{kHz}$. Then the model was fitted to the flopping curves for all other nominal displacements with floated parameter α. The resulting α were converted to distances $d_0 = 2x_0\alpha$ with $x_0 \approx 7.35\,\text{nm}$ from Equation (2.14). The d_0 were found to depend linearly on the nominal displacements (Figure 6.9 (right)), with larger than nominal displacements for small displacements as discussed in Section 6.3.

In a next step, the coupling constants Ω_s in $\Omega_{s,n} = \Omega_s g_{n+s,n}$ and the laser detuning

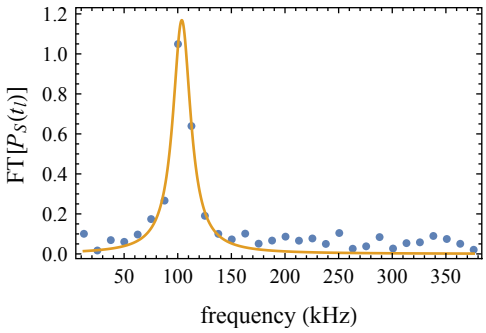

Figure 6.10: Fourier spectrum of the measured probability $P_S(t_l)$ for the first blue sideband and a displacement of 416 nm. A Lorentzian fit function was used to determine the mean Rabi frequency $\langle \Omega_{s,n} \rangle = (2\pi)\, 103.8(7)$ kHz.

offsets $\delta_s^{(\mathrm{off})}$ were determined from fitting the model (6.7) to the full data sets of the remaining sidebands. The results are summarized in Table 6.2. With these, we computed simulated data using Equation (6.7) and observed good reproduction of the experimental data (Figure 6.8).

Table 6.2: Best fit values for the coupling constants Ω_s and detuning offsets $\delta_s^{(\mathrm{off})}$.

s	$\Omega_s/(2\pi)$ (kHz)	$\delta_s^{(\mathrm{off})}/(2\pi)$ (kHz)
0	205	0
1	211	4
2	218	−4
3	224	−12
4	226	−23
5	226	−32

The model in Equation (6.7) already contains the mathematical description of the Franck-Condon factors in Equation (3.8). But we verified the dependency of the Rabi frequency on the coherent-state size independently. First note that the number-state distribution of a displaced thermal state, $P_{\alpha,n_{\mathrm{th}}}(n)$, with mean around $|\alpha|^2$ and width on the order of $|\alpha|$ for small n_{th} is narrow compared to the features in $g_{n+s,n}$. This means that the frequency spectra of the flopping curves $P_S(t_l)$ for a given sideband and displacement feature a single peak at the mean Rabi frequency $\langle \Omega_{s,n} \rangle$ (Figure 6.10). We determined these frequencies by fitting Lorentzian profiles to the discrete Fourier transform of the measured $P_S(t_l)$ for all displacement distances d_0 and sidebands. The expected mean Rabi frequencies were calculated as

$$\langle \Omega_{s,n} \rangle(\alpha) = \sum_{n=0}^{\infty} P_{\alpha,n_{\mathrm{th}}}(n) \sqrt{\Omega_{s,n}^2 + \delta_{s,n}^2}. \tag{6.10}$$

and compare well with the fitted values (Figure 6.8).

6.6. Conclusion

We have demonstrated quasi-instantaneous control over the trapping potential for a single ion using active electronic switches placed close to the ion trap. In first experiments, we excited the ion's motional state to a coherent state and tracked the oscillation by shifting the potential well forth and back. We confirmed that the timing resolution of our switching scheme should be sufficient to return such excited states to the initial state with only small additional heating. Finally, we created coherent states involving number states up to and beyond 10 000 quanta and applied them to map the number-state dependence of the Franck-Condon factors for sidebands up to fifth order.

7. Fast Ion Transport

published in: *New J. Phys.* **15** (2013)
arXiv:1208.3986 [quant-ph]

Manipulating the motional states of trapped ions on fast timescales is desirable for a number of reasons. The primary application of current interest is quantum information processing, where transport of information is necessary for scaling to large numbers of ions, and has been predicted to be one of the most time-consuming operations in a large-scale processor [Sch06]. One promising approach to scaling is the architecture of a "quantum charge-coupled device", in which the ions themselves are transported through an array of microtraps [Kie02]. The transport is controlled by time-varying potentials applied to a number of trap electrodes. These have traditionally been generated by voltage supplies placed outside the vacuum system and connected to the trap via vacuum feedthroughs. The feasibility of this approach has been demonstrated in a number of experiments, including linear transport of multiple ions [Row02; Bow12; Wal12], as well as 2-dimensional transport through T, X and Y junctions [Hen06; Ami10; Moe11; Bla09; Bla11]. The important figures of merit in these experiments were the operation time and the amount of motional excitation which persists after the transport has taken place. The latter is important because errors in multi-qubit quantum logic gates increase for higher motional excitation. Though this can be mitigated by sympathetic cooling [Bar03; Hom09a; Hom09b], it takes time and thus reduces the computing speed of the processor [Han10]. As a result of these considerations, initial experiments on transport operated in the adiabatic regime, maintaining the ion close to the ground state of motion of the co-moving time-dependent potential well throughout the transport. The adiabatic constraint limits transport to timescales slow compared to the motional period of oscillation of the ion in the trap.

The use of low-noise, high-speed Digital-to-Analog Converters (DACs) has recently enabled diabatic transport of ions over distances of $\sim 300\,\mu m$ in 5 to 16 oscillation cycles [Bow12; Wal12]. Despite being transiently excited during transport, the ions were returned to the ground state of the potential well at the end of the transport . With these techniques, the limit to the control rate is set by the finite capacitances present in the lines going to the electrodes.

In the wiring scheme we have implemented (Section 4.1.2), electronic switches are placed inside the vacuum system, directly adjacent to the Surface-Electrode ion Trap (SET) chip. The control for the switches is digital, allowing trap electrodes to be switched between two potentials supplied by standard analog supplies. Since the electronic switches can change

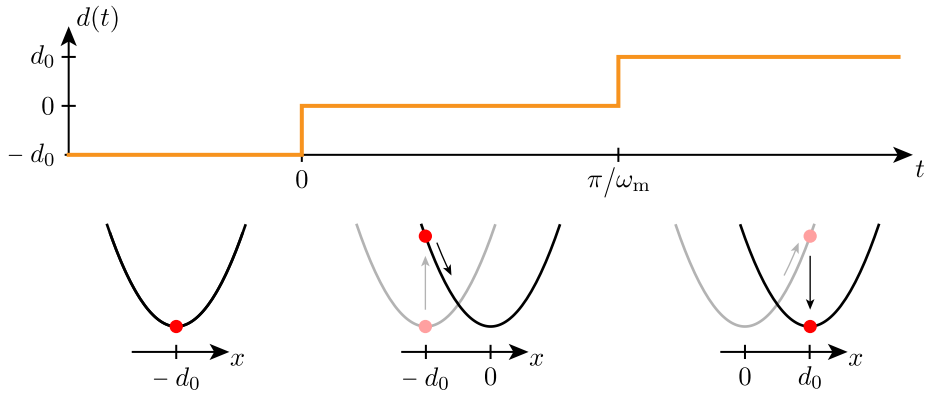

Figure 7.1: Sketch of the fast "throw-catch" transport routine. At the beginning, $t < 0$, the ion is in the motional ground state of a potential well displaced from the trap center by an offset voltage on an external electrode. At $t = 0$, the offset voltage is "instantaneously" switched off so that the potential is centered in the trap and the ion starts its coherent oscillation. After half an oscillation cycle, at $t = \pi/\omega_\mathrm{m}$, the offset is switched onto a symmetric external electrode and the ion is caught at the instant when it has no kinetic energy.

their output by up to $\approx 9\,\mathrm{V}$ on nanosecond timescales, this method facilitates changes to the trapping potentials 100 times faster than the period of oscillation of the secular motion, which is typically between 200 and 1000 ns. This would enable ion transport in times shorter than a single cycle of oscillation in the trap.

7.1. Transport protocol

The basic principle of fast transport using sudden switching of potentials is illustrated in Figure 7.1 for an ion considered a 1-dimensional harmonic oscillator. The ion starts in the ground state of an initial potential well situated at $x = -d_0$ given by

$$V(x) = \frac{m\omega_\mathrm{m}^2}{2}\,(x + d_0)^2.$$

At time $t = 0$, the potential is suddenly displaced to the transport well, which has the same curvature but is centered at $x = 0$. Consequently, the ion is in a coherent state of the transport well (Section 6.2), with coherent-state parameter $\alpha = -\tilde{d}_0 = -d_0/(2x_0)$, where $x_0 = \sqrt{\hbar/(2m\omega_\mathrm{m})}$ is the Root-mean-square (RMS) extent of the ground-state wave function. Under free evolution, this coherent state will gain and lose momentum, returning to rest periodically at times $t = j\pi/\omega_\mathrm{m}$ where j is an integer. For $j = 1$, the wave packet is positioned at $x = d_0$. If at this time the potential is suddenly displaced again to a final potential well centered at $x = d_0$ and with the same curvature as the transport well, the ion will end up in the ground state of the final potential, having been transported over a distance of $2d_0$.

Such a "throw-catch" transport routine can be carried out in trap geometries similar to

our own depicted in Figure 2.3. One possibility is to start with a potential well centered above the pair of electrodes El6/Er6 and end above the pair El4/Er4. The full transport distance would then be 100 µm. At a frequency of 1 MHz, this gives a mean velocity of 200 m/s and $\tilde{d}_0 \approx 2200$ for a $^{40}Ca^+$ ion.

There are a number of experimental challenges behind this conceptually simple transport routine, which we outline below.

7.2. Effect of trap anharmonicity

For macroscopic transport distances (100 µm in the example considered), the anharmonicities seen by the ion during its coherent oscillation might not be negligible. The transport potential can be Taylor-expanded as

$$V(x) \approx \frac{m\omega_{\mathrm{m}}^2}{2}\left(x^2 + \frac{x^3}{L_3} + \mathrm{sgn}(L_4)\,\frac{x^4}{L_4^2}\right)^2, \tag{7.1}$$

where L_3 and L_4 are the length scales at which the effects of the cubic and quartic terms of the potential are of the same size as the quadratic term. The principal anharmonicity relevant in the dynamics described above is a quartic term which causes a variation of the curvature of the potential along the transport distance (the odd term in the expansion in Equation (7.1) is negligible due to symmetry). The effect of L_4 on the local angular frequency can be evaluated by taking the second spatial derivative of the potential in Equation (7.1),

$$\omega_{\mathrm{m}}^2(x) = \omega_{\mathrm{m}}^2\left(1 + 6\,\mathrm{sgn}(L_4)\,\frac{x^2}{L_4^2}\right). \tag{7.2}$$

The consequences of Equation (7.2) were simulated numerically using a Suzuki-Trotter expansion [Suz93] of the full Hamiltonian (split-operator method). Due to the size of the coherent state under consideration, the simulation required a time resolution of 360 ps (1400 time steps) and a position resolution of ~ 8 pm to describe the wave packet with RMS extent $x_0 \approx 11$ nm.

Figure 7.2 (left) shows the effect of the quartic anharmonicity on the probability of overlap of the final state with the lowest oscillator number states in the final well. All three potential wells were taken to have the same curvature at their respective centers, leading to an axial frequency of 1 MHz. For negative values of L_4, the curvature of the transport potential becomes negative at $|x| \geq |L_4|/\sqrt{6}$ and the potential becomes anti-confining at $|x| \geq |L_4|/\sqrt{2}$. In general, the final state is no longer a minimum uncertainty state, since the variance in momentum increases. At $1/L_4 = -9/\mathrm{mm}$ for example, the probability of overlap of the state in the catch potential with the corresponding ground state is reduced to 90 %, and with the $n = 2$-state increased to 10 %.

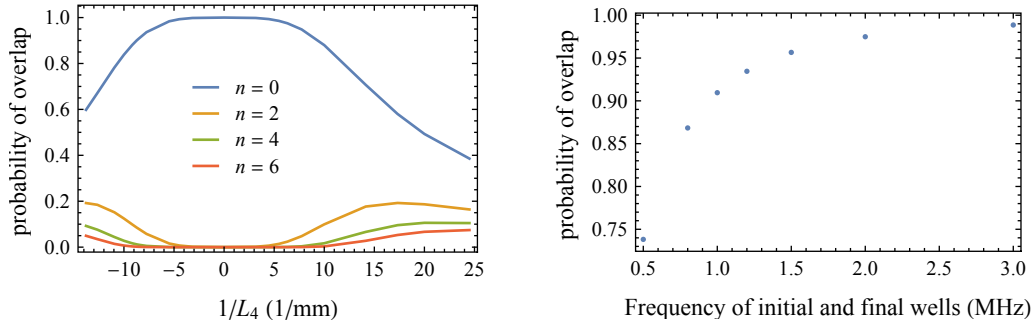

Figure 7.2: (left) Probability of overlap of the final state with the number states $n = 0, 2, 4, 6$ of the final potential as a function of the strength of the quartic anharmonic term during transport. The data points have been simulated for a $^{40}Ca^{+}$ ion at an axial frequency of 1 MHz which undergoes a transport of 100 µm ($d_0 = 50$ µm). For $1/L_4 < -14/\text{mm}$, the potential becomes anti-confining at the edges of the transport region. The transport time T was optimized for minimal excitations after transport, starting from the classical travel time. (right) Probability of overlap with the ground state of the final potential as a function of the frequency of the initial and final potentials. The transport potential is fixed to example values $\omega_m = (2\pi)\,1\,\text{MHz}$ and $L_4 = -120\,\mu\text{m}$.

One possibility to minimize this effect is to design the transport well such that the quartic term in the potential is reduced, either using the trap geometry or suitably chosen electrode potentials [Hom06]. For our SET, we find a combination of voltages from simulations for which all contributions up to 10th order are canceled, leading to frequency shifts below 3 % between $x = -d_0$ and $x = +d_0$. However, it would require applying potentials spanning ~ 80 V, which is currently not possible due to technical limitations of the switches.

We also investigated having a larger curvature in the initial and final wells than in the transport well. In that case, the ground state of the initial well projects onto a squeezed (rather than coherent) state of the transport well. The probability of overlap with the ground state of the final well is shown in Figure 7.2 (right) as a function of the frequency of the initial and final potentials, given a fixed transport potential. The highest frequency simulated was 3.0 MHz due to computational limitations. Until that value, the probability of overlap increases because the effect of the anharmonicity of the transport potential is smaller across the squeezed wave function. It might come as a surprise that the curve seems to asymptotically approach a probability of overlap of 1. Indeed, we expect that it will reach a maximum. The reason is that, close to the trap center, the wave function of the squeezed state broadens. Above a certain frequency, the effect of the anharmonicity on the broadened wave function will be large enough to reduce the probability of overlap with the final potential well.

7.3. Switch timing

Since the timing of the switching to the final potential well is a critical part of the transport protocol, it is worthwhile examining the tolerance of the scheme to timing imprecision. We

can make an estimate by considering the coherent-state size $\alpha(T)$ in the final potential. From Equation (6.1) follows, with $\tilde{d}(t) = \tilde{d}(0) = 0$ in order to describe the wave function with respect to the momentary well minimum position,

$$\alpha(t) = -\mathrm{e}^{-\mathrm{i}\omega_\mathrm{m} t} \int_0^t \mathrm{d}t_1 \, \dot{\tilde{d}}(t_1) \, \mathrm{e}^{\mathrm{i}\omega_\mathrm{m} t_1}. \tag{7.3}$$

If we describe the transport protocol mathematically as $d(t) = d_0[-1 + \Theta(t) + \Theta(t-T)]$ and assume that the catch potential is switched on at $T = \pi/\omega_\mathrm{m} + \delta T$ (rather than at $T = \pi/\omega_\mathrm{m}$) with $\omega_\mathrm{m}\delta T \ll 1$, we find

$$\alpha(T) = -\tilde{d}_0 \left(1 + \mathrm{e}^{-\mathrm{i}\omega_\mathrm{m} T}\right) \approx -\mathrm{i}\tilde{d}_0 \omega_\mathrm{m} \delta T.$$

The probability of overlap between the state after transport and the ground state in the final potential follows from Equation (F.5) and is given by

$$P_0 = \left| \langle 0 \,|\, -\mathrm{i}\tilde{d}_0 \omega_\mathrm{m} \delta T \rangle \right|^2 = \mathrm{e}^{-(\tilde{d}_0 \omega_\mathrm{m} \delta T)^2}.$$

The constraint on δT for achieving a certain overlap of P_0 is

$$\delta T = \frac{\sqrt{-\ln P_0}}{\tilde{d}_0 \omega_\mathrm{m}}.$$

For a $^{40}\mathrm{Ca}^+$ ion at $\omega_\mathrm{m} = (2\pi)\,1\,\mathrm{MHz}$ and $d_0 = 50\,\mu\mathrm{m}$, the initial coherent-state size is $\tilde{d}_0 \approx 2200$ and the timing resolution required is $\delta T \leq 24\,\mathrm{ps}$ for $P_0 \geq 0.9$. This also poses a demanding constraint on the trapping potential, which should be stable to $\approx 5 \times 10^{-5}$ throughout a measurement to avoid recalibration of the digital delays within an experiment. Timing resolutions of this order are achievable with commercially available digital delay generators. The jitter in our switching electronics has an estimated upper bound of 45 ps [Fad13].

7.4. Finite switching time

Until now, we have assumed that the voltage switching is instantaneous. Finite switching times of electrode potentials will mean that the potential minimum takes a certain time τ_1 to move from the initial position, $d(0) = -d_0$, to the transport well centered at $d(\tau_1) = 0$. The same applies to the catch procedure, which will start at $d(T) = 0$ and will end at $d(T + \tau_2) = d_0$ (Figure 7.3). Note that τ_1 and τ_2 are related to the switching times of the electrode potentials, but may slightly differ from each other if more than one electrode is switched.

If the ion is initially in the ground state of motion in the starting potential at $d(0)$,

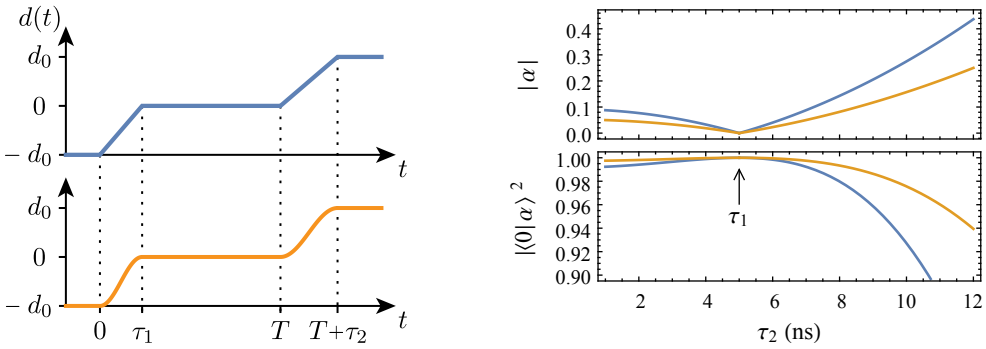

Figure 7.3: (left) Position of the potential minimum as a function of time during transport. The transitions between $t = 0$ and τ_1, and between T and $T + \tau_2$ will be given by the experimental setup. Here the examples of linear (blue line) and sinusoidal (orange line) ramps are depicted. (right) The coherent-state amplitude (top) and probability of overlap of the final state with the ground state (bottom) are plotted versus the second transition time, τ_2, for the two ramp shapes (same color code). The assumed situation is the transport of a $^{40}Ca^+$ ion over a distance $2d_0 = 100\,\mu m$ in a harmonic potential at frequency $\omega_m = (2\pi)\,1\,\mathrm{MHz}$. The transition time of the first ramp was set to $\tau_1 = 5\,\mathrm{ns}$. At $\tau_2 = \tau_1$, the ion can be recovered in the ground state for $T = \pi/\omega_m$.

according to Equation (7.3), it will evolve into a coherent state of amplitude

$$\alpha(T+\tau_2) = -\mathrm{e}^{-\mathrm{i}\omega_m(T+\tau_2)}\left[\int_0^{\tau_1} \mathrm{d}t\,\dot{\tilde{d}}(t)\,\mathrm{e}^{\mathrm{i}\omega_m t} + \int_0^{\tau_2} \mathrm{d}t\,\dot{\tilde{d}}(T+t)\,\mathrm{e}^{\mathrm{i}\omega_m(T+t)}\right] \tag{7.4}$$

with respect to the frame centered at $d(T + \tau_2)$. The main experimental control parameter is T. With the positions of the three potential wells given above but undefined $\dot{\tilde{d}}$ during the transitions, it is in general not possible to catch the ion in the ground state. If one assumes that the transitions are arbitrary but equivalent, $\dot{\tilde{d}}(t) = \dot{\tilde{d}}(T + t)$, which also implies $\tau_1 = \tau_2$, the final coherent-state amplitude can be made zero for $T = \pi/\omega_m$,

$$\alpha(T+\tau_2) = \mathrm{e}^{-\mathrm{i}\omega_m(\tau_2)}\int_0^{\tau_1} \mathrm{d}t\left[\dot{\tilde{d}}(t) - \dot{\tilde{d}}(T+t)\right]\mathrm{e}^{\mathrm{i}\omega_m(t)} = 0.$$

Without that assumption, the final state depends on the transition shapes and durations τ_1 and τ_2. We have calculated the effects of finite switching times for the case of linear and sinusoidal transitions for the parameters $\omega_m = (2\pi)\,1\,\mathrm{MHz}$, $d_0 = 50\,\mu m$ and $\tau_1 = 5\,\mathrm{ns}$. Figure 7.3 illustrates how the coherent-state size in the final potential (Equation (7.4)) and the probability of overlap of it with the ground state depend on τ_2. The time T that minimizes $\alpha(T + \tau_2)$ is in both cases given by

$$T \approx \frac{\pi}{\omega_m} + \frac{\tau_1}{2} - \frac{\tau_2}{2}.$$

As long as τ_1 and τ_2 are similar (less than a factor of 2 different), the probability for catching

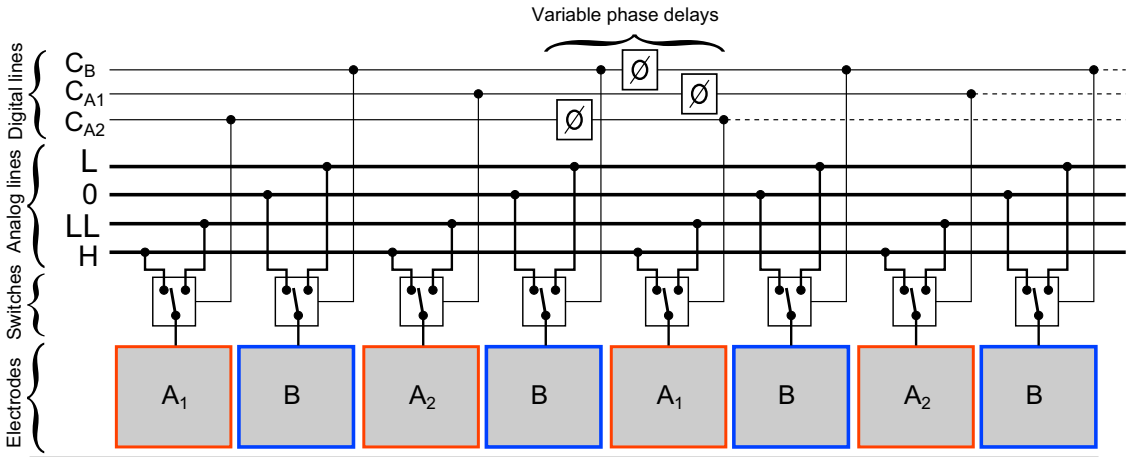

Duration	A1	B	A2	B	A1	B	A2	B
Δt_0	H	0	H	0	H	0	H	0
π/ω	H	L	LL	L	H	L	LL	L
Δt_1	H	0	H	0	H	0	H	0
π/ω	LL	L	H	L	LL	L	H	L
Δt_2	H	0	H	0	H	0	H	0
π/ω	H	L	LL	L	H	L	LL	L
Δt_3	H	0	H	0	H	0	H	0
π/ω	LL	L	H	L	LL	L	H	L
Δt_4	H	0	H	0	H	0	H	0

Figure 7.4: (top) Connections required to switch multiple trapping regions in an ideal case. One row of electrodes and connections to the bus are shown. The ions are separated by three electrodes in this scheme. Electrodes $A_{1,2}$ are switched between voltages H and LL, and electrodes B between 0 and L, with H>0>L>LL. Control lines $C_{A1,2}$ and C_B switch the voltages applied to the pairs of electrodes A and B, respectively. (bottom) Switching steps for the transport operations. The ions' positions (centered above an electrode) are indicated by shaded cells. It allows an ion to be moved by two electrode widths to the right with a time period of π/ω. The Δt_i account for time delays during which the ions are kept above the B electrodes for possible qubit operations.

the ion in the ground state is above 90 %, even higher for the smoother and more realistic case of a sinusoidal transition.

If in an experimental situation T as a free parameter is not sufficient for catching the ion in the ground state, the constraint on the position of final potential should be relaxed. Varying T and $d(T+\tau_2)$, the form of $\alpha(T+\tau_2)$ in Equation (7.4) suggests that motional excitations in the final potential can always be canceled out.

7.5. Extended transport throughout an array

In a large-scale trapped-ion quantum information processor based on the architecture described by Kielpinski et al. [Kie02], it is necessary to move ions between many remote trapping regions. Therefore, it would be useful to extend the scheme outlined above and

implement it in a repeated fashion. With experimental simplicity in mind, it is desirable to minimize the number of electric connections. In Figure 7.4, we give a simplified outline of a switch fabric that could be used to wire up electrodes in order to implement transport between a number of adjacent zones of a multi-zone trap. Though this does not include all electrodes required to control transport over any single zone, it illustrates that increasing the number of zones does not imply a direct increase in the number of digital and analog control lines as repeated transport in this scheme is realized by a total of four analog voltages controlled by three digital lines.

In a real experiment, it is likely that fabrication imperfections and stray environmental electric fields would require additional electrodes which could be used to tune the trap frequency of the ion. In addition, switch timing could be controlled by adding phase-shifting elements such as varactors, which have previously been proven to work in cryogenic ion trap settings [Sch12a].

With a chain of ions of equal mass, it should be possible to shunt the whole string along by one trap zone by switching the electrodes in the same manner as for a single ion. This is due to the fact that, as long as the curvature of the potential seen by the ions during the transport process remains the same, no motional modes will be affected other than the center-of-mass mode, which is excited exactly as a single ion would be [Jam98]. In addition to transport, in a large-scale processor it is likely that the ability to separate and deterministically re-order ion strings will be necessary. It is conceivable that methods similar to those we have described above could be used for these tasks.

7.6. Conclusion

We have proposed a method to transport an ion within a single oscillation cycle based on the ability to control the trapping potentials on timescales much faster than the ion's secular oscillation frequency. We have shown that this is experimentally challenging but should be possible for transporting a single $^{40}Ca^{+}$ ion at an axial angular frequency $\omega_{\mathrm{m}} = (2\pi)\,1\,\mathrm{MHz}$ over a distance of 100 µm in 500 ns.

As the fast-switching control has already been implemented and successfully tested (Chapter 6), the experimental demonstration of the proposed transport protocol should be within reach and will be attempted in the near future.

8. Summary and Outlook

This thesis covers work on quantum state engineering and towards fast transport of trapped ions through quasi-instantaneous changes to the trapping potential. The enabling technological step consists of placing electronic Complementary Metal–Oxide–Semiconductor (CMOS) switches close to the ion trap inside a cryogenic vacuum system. We have demonstrated the functionality of this approach and performed first characterization experiments. As such, we created coherent oscillator states in the motion of a trapped $^{40}Ca^{+}$ ion of phase-space sizes beyond $|\alpha| \approx 100$. These allowed us to map out the Franck-Condon coefficients for the laser–ion interaction in previously unexplored regimes.

Necessary prerequisites for these experiments were the design, fabrication and implementation of the experimental platform (Chapter 4). At its core is a microfabricated planar ion-trap chip mounted inside an Ultra-High Vacuum (UHV) chamber, which is attached to and cooled to $\approx 4\,\mathrm{K}$ by a liquid-helium recondenser cryostat. The oscillating voltage for ion trapping is stepped up by a quarter-wave helical resonator with a resonance frequency of 93.4 MHz and a quality factor of $Q \approx 110$ when loaded and at cryogenic temperature. The thermal atom beam from which atoms are ionized and loaded into the trap is created by a resistively heated oven. This heats the trap region during ion loading but was necessary after several laser-heated oven designs were unsuccessfully tested. The laser light for PhotoIonization (PI) and ion manipulation is exclusively obtained from (partially frequency-doubled) diode lasers. The relevant lasers are frequency-stabilized against Fabry-Perot cavities and computer-controllable via Acousto-Optic Modulators (AOMs). The PI, detection and repump beams are delivered to the trap through a single Photonic-Crystal Fiber (PCF). They can be independently tilted and translated for simple beam pointing. A cryo-compatible single-component purely reflective objective was designed for simultaneous imaging of $^{40}Ca^{+}$ and $^{9}Be^{+}$ ions without additional optics. It has a magnification factor of 81 and, at a numerical aperture of 0.55, it yields a total photon detection efficiency of $\approx 0.7\,\%$. The computer-control system was adapted to our needs and now controls the laser pulses via Direct Digital Synthesizers (DDSs), the trap-electrode voltages, and the fast voltage switches, and registers fluorescence-photon counts from a PhotoMultiplier Tube (PMT).

With the experimental setup basically operational, fluorescence from the neutral atom beam was observed and ions were loaded into the trap. At axial oscillation frequencies between 2.0 and 2.7 MHz, Doppler cooling reduced the motional excitation well into the Lamb-Dicke regime. Ground-state cooling was subsequently achieved using Electromagnetically Induced Transparency (EIT) cooling of the axial mode. The lowest mean phonon

number we could achieve this way is $n_{\mathrm{th}} = 0.13(6)$ at an axial frequency of 2.35 MHz, which corresponds to a ground state population of 88(4) %. We measured the heating from the ground state to be 1/ms for a trap frequencies of 2.7 MHz. We believe that this comparatively high heating rate is caused by surface contaminants and is the reason that prevents us from cooling closer to the motional ground state. Excess micromotion is reduced by minimizing motional heating due to parametric driving by amplitude-modulating the pseudopotential.

We used the active electronic switches close to the trap for bang-bang-control experiments. These entailed two displacements of the trap potential, forth by some distance and back. In a first set of experiments, we varied the timing of the second displacement, which allowed us to map the evolution of the ion in the displaced potential over several oscillation periods onto coherent-state sizes in the final potential. We extracted the latter from the experimental data by analyzing the Rabi oscillations from coherently driving on the first blue sideband, and observe the coherent-state amplitude oscillate between 0 and 10.

We examined how well a large coherent state ($|\alpha| \approx 85$) created by the first displacement can be returned to the initial state by precisely timing the second displacement. While the final state did not show excitation due to residual phase-space displacements, it had a larger thermal excitation ($n_{\mathrm{th}} = 0.22$ instead of $n_{\mathrm{th}} = 0.16$). We suspect that this results from jitter in the timing of the second displacement.

In a slightly modified experimental sequence, we created coherent states of phase-space sizes up to $|\alpha| \approx 100$ in the displaced potential by varying the displacement distance. After probing the states by coherently driving on the carrier and blue sidebands up to fifth order, we de-excited the motion with the second displacement for reliable spin-state detection. We could well reproduce the obtained experimental data in simulations by taking into account AC Starks shifts resulting from the coupling of the laser to the sidebands of both possible quadrupole transitions. Note that driving on higher-order sidebands was only observable due to the high coherent excitation. The dependence of the coupling strength on the number state is given by the Franck-Condon coefficients. We found that the mean Rabi frequency of the flopping curves for a given displacement agrees well with the Franck-Condon factor averaged over the corresponding number state distribution.

As part of a publication [Alo13], we have proposed applying bang-bang control to ion transport in a microtrap array. This could speed up the processing time of a trapped-ion quantum information processor that relies on transporting information encoded in the internal states of ions between different processing zones. The scheme would consist of two consecutive displacements of the trapping potential by the same distance. As long as the potential remains harmonic and the trap frequency constant, an ion in the ground state can be returned to the ground state in the final potential by precisely timing (on the order of tens of picoseconds) the second displacement . Adverse effects due to anharmonicities of trap potential and finite switching times depend on the specific experimental situation but seem to be manageable.

8.1. Future plans and improvements

The technology we have implemented extends the control over the oscillator state of trapped ions to a new regime, that is, large displacements at fast timescales compared to the characteristic length and frequency of the oscillator. Exploring this regime is a significant short-term goal. After, or in parallel to, improvements to the current setup, we will further characterize the bang-bang control schemes we have already applied, with a focus on spin and motional coherence throughout the sequence [Bow12; Wal12]. Later, we will attempt short-distance (over a few micrometers) and long-distance (several tens of micrometers) transport.

Immediate improvements to the setup will add EIT cooling of the radial motional modes. This should give us longer spin-coherence times (smaller decay rates γ in the fitting models) and allow us to examine changes in the radial excitations due to potential displacements. Furthermore, we will implement more precise and accurate Digital-to-Analog Converters (DACs). With the current voltage supplies, we observed significant displacements of the trapping potential when the displacement distance was nominally set to zero.

The latter is a requirement for producing squeezed states of the motion. When the trap frequency is nonadiabatically risen or dropped without a displacement of the potential minimum, a ground-state wave function immediately turns into a squeezed state. Repeatedly changing the trap frequency at suitable times increases the squeezing further (Figure 8.1) [Alo13]. In 2009, Serafini et al. showed theoretically that quickly changing the trapping potentials for chains of ions can yield a subsequent evolution into squeezed and entangled states [Ser09]. The obtainable degrees of squeezing and entanglement in the continuous-variable quadratures in this scheme are expected to be higher than what has previously been obtained in any technology to date. The generation of entanglement using these methods could make a first test of quantum non-locality for degrees of freedom describing the motion of massive particles become feasible.

In a more long-term perspective, we are going to replace the current microtrap chip with a new one designed by Chi Zhang [Zha15] and fabricated at a CMOS foundry. Metha et al. have recently reported a heating rate of 81(9) quanta/s for a similarly fabricated trap where $^{88}Sr^{+}$ ions were trapped at an axial frequency of 1.3 MHz and a distance of 50 µm from the surface [Meh14]. A comparable or even lower value (since ions will be confined at 80 µm from the surface in our design) would mean a significant improvement to our current heating rate. Since we believe surface contaminants are the main cause for our high heating rate, we will try to reduce them by loading ions from the back side through a slit in the trap chip [Lei09; Dor12], and by heating the trap during the cool down to prevent background gas from freezing onto the surface [Nie14; Thi14].

Another issue we will try to tackle is the building up of light-diffusing coatings on the windows on the UHV chamber. We will probably not be able to improve the isolation vacuum in the cryostat fundamentally, except for cleaning all vacuum seals and pumping it out more regularly. So one solution would be to remove the windows entirely, but that

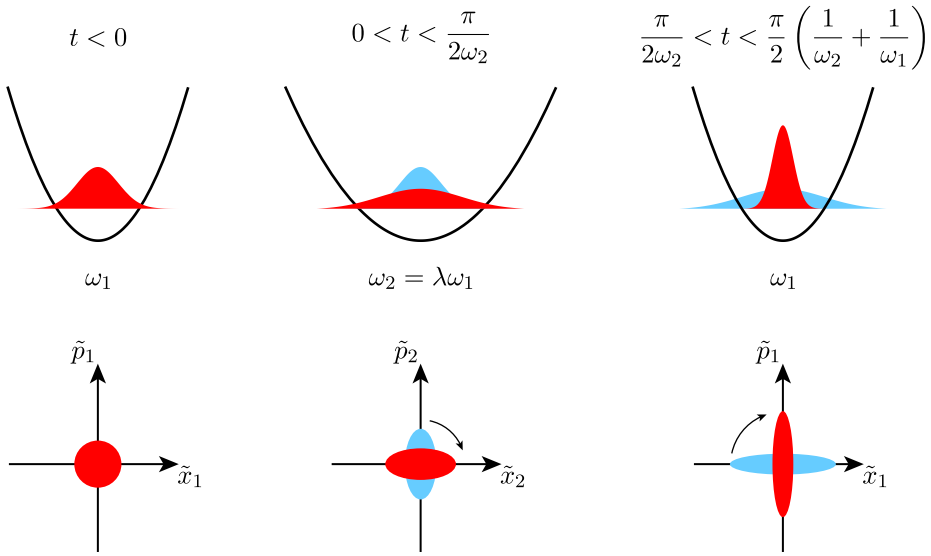

Figure 8.1: Routine for squeezing a ground state by nonadiabatic changes to the trap frequency, depicted in real and in phase space. (left) An ion is cooled to the ground state in a potential with trap frequency ω_1. (middle) At $= 0$, the trap frequency is abruptly risen to $\omega_2 = \lambda\omega_1$, which corresponds to a squeezing along the position quadrature by $1/\lambda$ (wave function in blue). Until $t = \pi/\omega_2$, the state rotates in phase space by an angle of $\pi/2$ (red), seen in real space as a "breathing" of the wave function. (right) Then the frequency change is inverted, which puts the wave function in a squeezed state with a squeezing of $1/\lambda^2$ along the momentum quadrature, and along the position quadrature time period of $\pi/(2\omega_1)$ later.

would certainly reduce ion lifetimes drastically. Another solution might be to use windows coated with electrically conducting Indium Tin Oxide (ITO). Thin films of ITO deposited on aircraft windshields are used to defrost them by running a current through the coating. Low-temperature vacuum compatibility of ITO was indirectly proven by Eltony et al. who have fabricated and operated a transparent ion trap with electrodes from ITO at $\approx 4\,\mathrm{K}$ [Elt13]. These facts combined, using ITO-coated windows on the UHV chamber for removing adsorbed background gas might be feasible.

A. Time-Evolution Pictures in QM

The dynamics of a closed quantum mechanical system represented by the state $|\psi\rangle$ is captured by the Schrödinger equation (SE),

$$\mathrm{i}\hbar\,\partial_t|\psi(t)\rangle = H(t)\,|\psi(t)\rangle,$$

which is a homogeneous partial differential equation, linear and only to first order in t. So an initial state $|\psi(0)\rangle$ at $t = 0$ evolves deterministically for all later times. All observable quantities are then predicted by the scalar product of a bra and a ket, or by matrix elements of operators. These predictions are therefore invariant under unitary transformations of the kets and operators.

Sometimes it is a matter of taste, but often of practicality, to transform $|\psi(t)\rangle$ and solve for the dynamics in a different "picture". Below I illustrate this for the Schrödinger, Heisenberg and interaction pictures. For clarity, kets and operators are marked with superscripts, none for Schrödinger, H for Heisenberg, and I for interaction picture.

A.1. Schrödinger picture

In the Schrödinger picture, operators (observables and others) are generally constant in time while the state vectors evolve. The unitary *time evolution operator* $U(t)$ relates initial and later states, $|\psi(t)\rangle = U(t)|\psi(0)\rangle$. It is determined by the Schrödinger equation for the time evolution operator, $\mathrm{i}\hbar\,\partial_t U(t) = H(t)\,U(t)$, and the initial condition $U(0) = 1$. In the case that the Hamiltonian commutes with itself at different times, the solution is given by

$$U(t) = \exp\left(\int_0^t \mathrm{d}t'\mathcal{H}(t')\right) \tag{A.1}$$

with $\mathcal{H}(t) = H(t)/(\mathrm{i}\hbar)$. Otherwise, if the Hamiltonian does not commute with itself at different times, the differential equation can be formally solved by a Dyson series [Sak94,

Section 2.1] or perturbatively by a Magnus expansion [Bla10],

$$U(t) = \exp\left\{ \int_0^t \mathrm{d}t_1\, \mathcal{H}_1 + \frac{1}{2} \int_0^t \mathrm{d}t_1 \int_0^{t_1} \mathrm{d}t_2 \left[\mathcal{H}_1, \mathcal{H}_2\right] \right.$$
$$\left. + \frac{1}{6} \int_0^t \mathrm{d}t_1 \int_0^{t_1} \mathrm{d}t_2 \int_0^{t_2} \mathrm{d}t_3 \left(\left[\mathcal{H}_1, \left[\mathcal{H}_2, \mathcal{H}_3\right]\right] + \left[\mathcal{H}_3, \left[\mathcal{H}_2, \mathcal{H}_1\right]\right] \right) + \dots \right\}$$

with the abbreviation $\mathcal{H}_i = \mathcal{H}(t_i)$.

A.2. Heisenberg picture

The Heisenberg picture is a formulation in which the operators incorporate a dependency on time, but the state vectors are time-independent. It differs from the Schrödinger picture only by a basis change with respect to the time-evolution operator:

$$|\psi^{\mathrm{H}}\rangle = U^\dagger(t)\,|\psi(t)\rangle = |\psi(0)\rangle \qquad \text{for kets, and}$$
$$A^{\mathrm{H}}(t) = U^\dagger(t)\,A(t)\,U(t) \qquad \text{for operators.}$$

The time-dependence of $A^{\mathrm{H}}(t)$ is given by the *Heisenberg equation*,

$$\mathrm{i}\hbar \frac{\mathrm{d}}{\mathrm{d}t} A^{\mathrm{H}}(t) = [A^{\mathrm{H}}(t), H^{\mathrm{H}}(t)] + \mathrm{i}\hbar \left(\partial_t A(t)\right)^{\mathrm{H}}. \tag{A.2}$$

The fact that the Hamiltonian is invariant under this transformation directly implies energy conservation within the closed system.

A.3. Interaction picture

The interaction picture (also known as the Dirac picture) is an intermediate representation between the Schrödinger and the Heisenberg picture in the sense that here both, state vectors and operators, carry part of the time dependence. It is useful in dealing with changes to the wave functions and observables of a composite system that are only due to the interactions.

The Schrödinger-picture Hamiltonian is split as $H = H_0 + H_1(t)$, typically that is into a part H_0 containing the single-system terms, and a part $H_1(t)$ containing the (possibly time-dependent) interaction terms. Transformation with respect to $U_0(t) = \exp(-\mathrm{i}H_0 t/\hbar)$ yields

$$|\psi^{\mathrm{I}}(t)\rangle = U_0^\dagger(t)\,|\psi(t)\rangle \qquad \text{for kets, and}$$
$$A^{\mathrm{I}}(t) = U_0^\dagger(t)\,A(t)\,U_0(t) \qquad \text{for operators.}$$

States in the interaction picture evolve according to a transformed SE,

$$\mathrm{i}\hbar\,\partial_t|\psi^{\mathrm{I}}(t)\rangle = \mathrm{i}\hbar\,\partial_t\Big[U_0^\dagger(t)\,|\psi(t)\rangle\Big] = \Big[\mathrm{i}\hbar\,\dot{U}_0^\dagger(t)\,U_0(t) + U_0^\dagger(t)\,H\,U_0(t)\Big]|\psi^{\mathrm{I}}(t)\rangle, \tag{A.3}$$

which upon evaluating for $U_0(t)$ yields the *Schwinger-Tomonaga equation*

$$\mathrm{i}\hbar\,\partial_t|\psi^{\mathrm{I}}(t)\rangle = H_1^{\mathrm{I}}(t)\,|\psi^{\mathrm{I}}(t)\rangle, \qquad H_1^{\mathrm{I}}(t) = U_0^\dagger(t)\,H_1(t)\,U_0(t). \tag{A.4}$$

That the interaction picture is somewhat halfway between the two previous pictures can be seen from the limiting cases: it contains the Schrödinger picture in the case of $H_1 = 0$, and the Heisenberg picture in case of a vanishing free Hamiltonian, $H_0 = 0$.

A.4. General unitary transformation

The formalism used in the interaction picture can be generalized to any (possibly time dependent) unitary transformation $T(t)$, $|\psi^{\mathrm{T}}(t)\rangle = T(t)\,|\psi(t)\rangle$ for kets. In full analogy to Equation (A.3), the dynamics of the system are then described by the

$$\mathrm{i}\hbar\,\partial_t|\psi^{\mathrm{T}}(t)\rangle = H^{\mathrm{T}}(t)\,|\psi^{\mathrm{T}}(t)\rangle$$

with the transformed Hamiltonian

$$H^{\mathrm{T}}(t) = T(t)H(t)T^\dagger(t) + \mathrm{i}\hbar\dot{T}(t)T^\dagger(t). \tag{A.5}$$

The Schwinger-Tomonaga Equation (A.4) results from $T(t) = U_0^\dagger(t)$.

B. Density Matrix Formalism

The definition of an *expectation value* of an operator A acting on a system is considered the averaged outcome of measurements performed on many quantum systems all prepared in the same state $|\psi\rangle$,

$$\langle A\rangle = \langle\psi \,|\, A \,|\, \psi\rangle.$$

Such an ensemble of quantum systems all prepared in an identical quantum state is known as a *pure state* ensemble. Note that $|\psi\rangle$ contains complete information of the system and incorporates quantum uncertainties.

There are many practical situations where the collection of quantum systems are not all in the same quantum state, for example a system in thermal equilibrium at finite temperature. In such a *mixed state* ensemble, where the quantum states $|\psi_i\rangle$ are represented with statistical probability p_i, the expectation value of A is the weighted average

$$\langle A\rangle = \sum_i p_i \,\langle\psi_i \,|\, A \,|\, \psi_i\rangle = \mathrm{Tr}[A\rho].$$

Classical and quantum uncertainties are now combined in the density matrix

$$\rho = \sum_i p_i \,|\psi_i\rangle\langle\psi_i|,$$

which is Hermitian and normalization requires $\mathrm{Tr}[\rho] = 1$. It is a signature of mixed states that $1/d \leq \mathrm{Tr}[\rho^2] < 1$. The lower bound stems from the fact that the density matrix of a fully mixed state in a Hilbert space of dimension d is a diagonal matrix with entries $1/d$.

B.1. Fidelity for mixed quantum states

A widely used, though not unique, fidelity measure, that is, a measure of the degree of similarity, between two quantum states is their transition probability [Men08]. For two pure states, it is given by $\mathcal{F} = |\langle\psi_1 \,|\, \psi_2\rangle|^2$, and for the similarity between a pure and a certain mixed state by $\mathcal{F} = \langle\psi_1 \,|\, \rho_2 \,|\, \psi_1\rangle$.

The *Uhlmann-Josza fidelity* extends this concept to two mixed states,

$$\mathcal{F} = \left(\mathrm{Tr}\left[\sqrt{\sqrt{\rho_1}\,\rho_2\,\sqrt{\rho_1}}\right]\right)^2.$$

This definition satisfies Josza's axioms for a fidelity measure: The fidelity lies between 0 and 1 and equals unity if and only if the two states are identical. It is symmetric with respect to the two states. And finally, $\mathcal{F}$ is invariant under unitary transformation on the state space [Jos94].

B.2. Closed-system dynamics

An isolated system undergoes reversible evolution generated by the Hamiltonian. In the Schrödinger picture ρ evolves as

$$\rho(t) = U(t)\,\rho(0)\,U^\dagger(t)$$

with the time-evolution operator from Equation (A.1). Differentiation with respect to time gives the *von Neumann equation*,

$$\mathrm{i}\hbar\,\partial_t\rho(t) = [H, \rho(t)]. \tag{B.1}$$

From Equation (A.4) one can readily write down its form in the interaction picture as

$$\mathrm{i}\hbar\,\partial_t\rho^{\mathrm{I}}(t) = [H_1^{\mathrm{I}}(t), \rho^{\mathrm{I}}(t)].$$

B.3. Open-system dynamics

Often one is interested in the dynamics of a quantum system, S, that is coupled to a reservoir, R. Suppose the total system is initially in an uncorrelated state, $\rho_{\mathrm{S}}(0)\otimes\rho_{\mathrm{B}}$, and evolves according to the von Neumann equation. The state of the system at a later time t is then obtained from the partial trace over the bath,

$$\rho_{\mathrm{S}}(t) = \mathrm{Tr}_{\mathrm{B}}\Big[U(t)\Big(\rho_{\mathrm{S}}(0)\otimes\rho_{\mathrm{B}}\Big)U^\dagger(t)\Big].$$

More desirable is capturing the state change of the open system via a *dynamical map*

$$V(t): \quad \rho_{\mathrm{S}}(0) \longrightarrow \rho_{\mathrm{S}}(t) = V(t)\rho_{\mathrm{S}}.$$

Performing the partial trace over the bath's basis states $|b\rangle$ in the equation above yields the operator-sum representation

$$V(t)\rho_{\mathrm{S}} = \sum_b \Big\langle b\Big|\,U(t)\Big(\rho_{\mathrm{S}}(0)\otimes\rho_{\mathrm{B}}\Big)U^\dagger(t)\,\Big|\,b\Big\rangle = \sum_b W_b\rho_{\mathrm{S}}W_b^\dagger,$$

where the *Kraus operators* fulfill the completeness relation $\sum_b W_b^\dagger W_b = \mathbb{1}_{\mathrm{S}}$. Note that the Kraus map resembles a projective measurement. In fact, projectors can be considered a special case of Kraus operators.

Evaluating the dynamical map for varying times is valid under the Markovian assumption that memory effects in the reduced system dynamics can be neglected, which means that reservoir correlations decay much faster than the characteristic time scale of the system evolution. In this case, starting from

$$\partial_t \rho_\mathrm{S} = \lim_{t\to 0} \frac{V(t)\rho_\mathrm{S} - \rho_\mathrm{S}}{t},$$

the *master equation in Lindblad form* can be derived, [Bre02, p. 119ff]

$$\partial_t \rho_\mathrm{S} = \frac{1}{\mathrm{i}\hbar}\,[H, \rho_\mathrm{S}] + \sum_k \gamma_k \Big(L_k \rho_\mathrm{S} L_k^\dagger - \frac{1}{2}\, L_k^\dagger L_k \rho_\mathrm{S} - \frac{1}{2}\, \rho_\mathrm{S} L_k^\dagger L_k \Big).$$

The first part represents the coherent evolution analogous to the von Neumann equation. But in this case $H = H_\mathrm{S} + H_\mathrm{LS}$, that means H not only consists of the Schrödinger picture system Hamiltonian, H_S, but also of a *Lamb shift* Hamiltonian, H_LS, due to the interaction with the reservoir, which commutes with the first, $[H_\mathrm{S}, H_\mathrm{LS}] = 0$.

The *Lindblad operators* L_k in the first term of the sum induce dissipative decay at rates γ_k while the last two terms ensure normalization. While one can microscopically derive these operators (see for example [Bre02, p. 130ff]), they are often more axiomatically guessed and a posteriori justified by their correct action.

C. Wigner Distribution

In 1932, Wigner formulated quantum mechanics in terms of a distribution function $W(x,p)$. It provides a re-expression of quantum mechanics in terms of classical concepts such that quantum mechanical expectation values are expressed as averages of phase-space distribution functions. Statistical information is transferred from the density operator ρ to the quasi-classical function [Har06, p. 573]

$$W(\tilde{x},\tilde{p}) = \frac{1}{\pi}\int \mathrm{d}\tilde{u}\, \mathrm{e}^{\mathrm{i}2\tilde{p}\tilde{u}}\, \langle \tilde{x}-\tilde{u}/2 \,|\, \rho \,|\, \tilde{x}+\tilde{u}/2\rangle,$$

where $\tilde{x}$ and $\tilde{p}$ are the dimensionless quadratures defined analogously to Equation (2.14). It originates from the Weyl transform, which is defined for any operator A as [Cas08]

$$\mathcal{A}(\tilde{x},\tilde{p}) = \mathfrak{W}[A] = \int \mathrm{d}\tilde{u}\, \mathrm{e}^{\mathrm{i}2\tilde{p}\tilde{u}}\, \langle \tilde{x}-\tilde{u}/2 \,|\, A \,|\, \tilde{x}+\tilde{u}/2\rangle.$$

The Wigner function is the Weyl transform of the density matrix, $W(\tilde{x},\tilde{p}) = \mathfrak{W}[\rho]/\pi$.

The trace of the product of two operators is given by the integral over phase space of the product of their Weyl transforms,

$$\mathrm{Tr}[AB] = \frac{1}{\pi}\iint \mathrm{d}\tilde{x}\,\mathrm{d}\tilde{p}\, \mathcal{A}(\tilde{x},\tilde{p})\, \mathcal{B}(\tilde{x},\tilde{p}). \tag{C.1}$$

The expectation value of an operator A can then be calculated as

$$\langle A\rangle = \mathrm{Tr}[A\rho] = \iint \mathrm{d}\tilde{x}\,\mathrm{d}\tilde{p}\, \mathcal{A}(\tilde{x},\tilde{p})\, W(\tilde{x},\tilde{p}).$$

Even though the Wigner function is normalized, it differs from a regular probability distribution because it can be negative in some areas of phase space. This can be seen from

$$\mathrm{Tr}[\rho_a\rho_b] = \pi \iint \mathrm{d}\tilde{x}\,\mathrm{d}\tilde{p}\, W_a(\tilde{x},\tilde{p})\, W_b(\tilde{x},\tilde{p}) = 0$$

for the case of two orthogonal states ρ_a, ρ_b.

A particularly appealing feature of the Wigner function is that its marginal distributions are the true probability distributions, that is

$$\int \mathrm{d}\tilde{p}\, W(\tilde{x},\tilde{p}) = \langle \tilde{x} \,|\, \rho \,|\, \tilde{x}\rangle \qquad \text{and} \qquad \int \mathrm{d}\tilde{x}\, W(\tilde{x},\tilde{p}) = \langle \tilde{p} \,|\, \rho \,|\, \tilde{p}\rangle.$$

It hence allows for visualizing a quantum state simultaneously in the quadratures $\tilde{x}$ and $\tilde{p}$.

The Wigner function of a particle subject to a potential of maximally quadratic order evolves according to the classical Liouville equation. The phase-space motion of a harmonic oscillator is therefore purely classical; each point of the Wigner function moves in elliptical paths. Thus if the Wigner function of an oscillator with angular frequency ω_m is $W(\tilde{x}, \tilde{p}, 0)$ at time $t = 0$, the Wigner function at a future time t is given by [Cas08]

$$W(\tilde{x}, \tilde{p}, t) = W\Big(\tilde{x}\cos(\omega t) - \tilde{p}\sin(\omega t), \tilde{p}\cos(\omega t) + \tilde{x}\sin(\omega t), 0\Big).$$

C.1. Examples of Wigner functions

Some examples of Wigner functions are [Har06, p. 576ff]:

- Number states (see Equation (F.13) for generalized Laguerre polynomials)

$$W_n(\tilde{x}, \tilde{p}) = \frac{2}{\pi}\,(-1)^n\,\mathrm{e}^{-2\tilde{x}^2}\,\mathrm{e}^{-2\tilde{p}^2}\,L_n^{(0)}\Big(4\tilde{x}^2 + 4\tilde{p}^2\Big)$$

- Coherent states

$$W_\alpha(\tilde{x}, \tilde{p}) = \frac{2}{\pi}\,\mathrm{e}^{-2(\tilde{x}-\alpha_\mathrm{r})^2}\,\mathrm{e}^{-2(\tilde{p}-\alpha_\mathrm{i})^2} \tag{C.2}$$

- Squeezed states (for $\zeta = r$)

$$W_\zeta(\tilde{x}, \tilde{p}) = \frac{2}{\pi}\,\mathrm{e}^{-2\mathrm{e}^{2r}\tilde{x}^2}\,\mathrm{e}^{-2\mathrm{e}^{-2r}\tilde{p}^2}$$

- Thermal states

$$W_{n_\mathrm{th}}(\tilde{x}, \tilde{p}) = \frac{2}{\pi}\frac{1}{2n_\mathrm{th}+1}\,\mathrm{e}^{-2\tilde{x}^2/(2n_\mathrm{th}+1)}\,\mathrm{e}^{-2\tilde{p}^2/(2n_\mathrm{th}+1)} \tag{C.3}$$

The number states are the only ones with negative Wigner function values, which can be seen as signature of a non-classical state. The squeezed state has a reduced variance in one quadrature at the expense of a higher variance in the other. The thermal state is broader compared to the coherent state.

D. Gaussian Beam Propagation

Derivations of the information given here in a condensed form for every-day use can be found in [Sie86].

The fundamental TEM_{00} mode of a laser beam as well as the light mode coming out of a single-mode fiber are beam modes with a Gaussian cross section profile. The complex phasor amplitude[1] of the electric field of a beam with waist size w_0 (see figure D.1 for notation) and planar wavefront at $z = 0$ propagating into the z-direction can be described by

$$\tilde{E}(x, y, z) = E_0 \frac{\tilde{q}_0}{(\pi/2)^{1/2} w_0 \tilde{q}(z)} \exp\left[-jk\frac{x^2 + y^2}{2R(z)} - \frac{x^2 + y^2}{w^2(z)}\right],$$

which is a paraxial spherical wave as solution to the paraxial wave equation. The complex radius of curvature $\tilde{q}(z)$ is related to the spot size $w(z)$ and the radius of curvature $R(z)$ at any plane z by

$$\frac{1}{\tilde{q}(z)} = \frac{1}{R(z)} - \frac{\mathrm{i}\lambda}{\pi w^2(z)},$$

where $\lambda = 2\pi/k$ is the wavelength of the radiation. In free space this parameter evolves as

$$\tilde{q}(z) = \tilde{q}_0 + z = z + \mathrm{i}z_R.$$

The so-called *Rayleigh range* $z_R = \pi w_0^2/\lambda$ is the distance from the waist where the beam area doubles. The beam shape at all other positions then follows from

$$w(z) = w_0 \sqrt{1 + \left(\frac{z}{z_R}\right)^2}, \qquad R(z) = z + \frac{z_R^2}{z}. \tag{D.1}$$

Therefore, a Gaussian beam with wavelength λ is characterized entirely by w_0 at the beam waist, see figure D.1 for an example.

If the total power in the beam is $P = \int \mathrm{d}A |\tilde{E}|^2$, where $\mathrm{d}A$ integrates over the cross-sectional area, the radial intensity variation is given by

$$I(r, z) = I_0(z)\, \mathrm{e}^{-2r^2/w^2(z)}, \qquad I_0(z) = \frac{2P}{\pi w^2(z)}. \tag{D.2}$$

[1] Complex or imaginary quantities are marked with a tilde in this section.

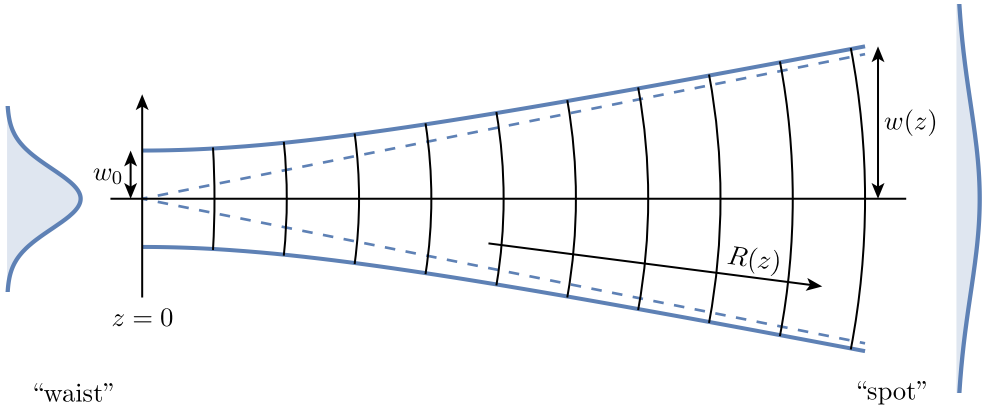

Figure D.1: Gaussian beam diverging away from its waist. The spot size w_0 at the beam waist determines the spot size $w(z)$ and wavefront radius $R(z)$ at all planes z. Adapted from [Sie86, p. 664].

At $r = w$ the intensity has dropped by a factor of $1/e^2$. And an aperture with diameter $d = 2w(z)$ transmits $\approx 86\,\%$ of the total beam power.

From Equations (D.1) follows that the smaller the beam waist, the shorter the Rayleigh range and the more rapidly the beam expands. Conversely, a beam with a Rayleigh range large compared to other experimental parameters can be considered collimated. A strongly expanding beam (for example coming out of a fiber) can be collimated by a lens of focal length f in the far field at $z \approx f$ and then has a spot size of $w(f)$ given by

$$w_0 \times w(f) \approx \frac{f\lambda}{\pi} \qquad (z \gg z_R).$$

This approximation also applies to the reverse process of focusing a collimated beam with spot size $w(f)$ to a beam waist radius of w_0.

The propagation of a beam through more complex optical systems can be analyzed with the help of ray transfer matrices (or ABCD matrices). In paraxial geometrical optics, a beam is characterized at a given plane perpendicular to the optical axis by the transverse displacement r from the optical axis and the slope $r' = \partial_z r$. How it is altered between the input and output planes of an optical system can be expressed in the form

$$\begin{bmatrix} r_\mathrm{o} \\ r'_\mathrm{o} \end{bmatrix} = \begin{bmatrix} A & B \\ C & D \end{bmatrix} \cdot \begin{bmatrix} r_\mathrm{i} \\ r'_\mathrm{i} \end{bmatrix} = M \cdot \begin{bmatrix} r_\mathrm{i} \\ r'_\mathrm{i} \end{bmatrix}, \tag{D.3}$$

where M is the *ray matrix* for the optical system. It is the product of the ray matrices of all optical elements that it contains, $M = M_n \dots M_1$. The ray matrices we need most are the ones for propagation in free space over a distance d and refraction at thin lens with

focal length f,

$$M_d = \begin{bmatrix} 1 & d \\ 0 & 1 \end{bmatrix}, \qquad M_f = \begin{bmatrix} 1 & 0 \\ -1/f & 1 \end{bmatrix}.$$

We can use this result for spherical waves with radius of curvature R by noting that they can be viewed as a collection of rays all diverging from or converging to a common point. The quotient of slope and displacement of each of these rays at a plane z then equals the radius of curvature, $R = r/r'$. A positive R indicates a diverging spherical wave, a negative R a converging spherical wave. From Equation (D.3) follows the transformation relation

$$R_\mathrm{o} = \frac{AR_\mathrm{i} + B}{CR_\mathrm{i} + D}$$

for the radii of curvature before and after the optical system. The complex radius of curvature $\tilde{q}$ of a Gaussian beam is transformed in the exact same way,

$$\tilde{q}_\mathrm{o} = \frac{A\tilde{q}_\mathrm{i} + B}{C\tilde{q}_\mathrm{i} + D}.$$

This result is extremely useful. It permits a Gaussian beam to be propagated through multiple paraxial elements in sequence, using only the cascaded $ABCD$ matrices for those elements.

Position and spot sizes of a beam waist can, for example, be found via the condition $\Re[\tilde{q}] = 0$ and $w_0 = \sqrt{\lambda z_R/\pi}$. Alternatively, the required lenses and their positions can be determined for given input and output beam parameters.

E. Data Analysis and Error Estimation

Consider a data set $\{\boldsymbol{x}_i, y_i\}$ consisting of n measurements where y was measured as function of the m independent $\boldsymbol{x} = (x_1, \ldots, x_m)$. This data set shall be fitted with a model $f(\boldsymbol{x})$ that includes p parameters a_k. An estimate of the parameters can be obtained by minimizing the objective function

$$S = \sum_{i+1}^{n} w_i (y_i - f(\boldsymbol{x}_i))^2$$

with statistical weights $w_i = 1/\sigma_{y_i}^2$ corresponding to the uncertainties σ_i in the measurements y_i [Wol06, p. 34]. A robust approach, particularly when the model function is time-consuming to evaluate, are brute-force grids: the objective function is evaluated at grid points of a rectangular grid in parameter space and subsequently minimized via interpolation [And10].

After the least squares solution was found the unbiased estimates of the uncertainties in the parameters can be found from

$$\sigma_{a_k}^2 = \frac{S}{n-p} C_{kk}^{-1}$$

where C_{kk}^{-1} is the inverse of the matrix

$$C_{jk} = \sum_{i=1}^{n} w_i \frac{\partial f(\boldsymbol{x}_i)}{\partial a_j} \frac{\partial f(\boldsymbol{x}_i)}{\partial a_k},$$

evaluated for the best-fit parameters [Wol06, p. 51f].

F. Useful Formulas

Commutator algebra

- Commutators of operator functions in case $[A,[A,B]] = [A,[A,B]] = 0$

$$[A, F(B)] = [A, B]\, F'(B)$$

- Hadamard-Lemma for two arbitrary operators A and B

$$e^{A} B e^{-A} = \sum_{m=0}^{\infty} \frac{1}{m!} [A, B]_m \tag{F.1}$$

  with $[A,B]_m = [A,[A,B]_{m-1}]$ and $[A,B]_0 = B$.

- Baker-Campbell-Hausdorff formulae in case $[A,[A,B]] = [B,[A,B]] = 0$

$$\begin{aligned} \mathrm{e}^{A+B} &= \mathrm{e}^{A}\, \mathrm{e}^{B}\, \mathrm{e}^{-[A,B]/2} \\ \mathrm{e}^{A}\, \mathrm{e}^{B} &= \mathrm{e}^{B}\, \mathrm{e}^{A}\, \mathrm{e}^{[A,B]} \end{aligned} \tag{F.2a}$$

Quantum harmonic oscillator

- Commutator of harmonic oscillator operators

$$[a, a^\dagger] = 1, \qquad [a^\dagger a, a^\dagger] = a^\dagger$$

- Lowering operator in the interaction picture (using Equation (F.1))

$$\mathrm{e}^{\mathrm{i}\omega_\mathrm{m} t (a^\dagger a)}\, a\, \mathrm{e}^{-\mathrm{i}\omega_\mathrm{m} t (a^\dagger a)} = a\, \mathrm{e}^{-\mathrm{i}\omega_\mathrm{m} t} \tag{F.3}$$

- Displacement of oscillator amplitudes (using Equation (F.1))

$$D(\alpha)\, a\, D(-\alpha) = a - \alpha, \qquad D(\alpha) = \mathrm{e}^{\alpha a^\dagger - \alpha^* a} \tag{F.4}$$

- Consecutive displacements and scalar product of coherent states (using Equation (F.2a))

$$D(\alpha)\, D(\beta) = \mathrm{e}^{(\alpha\beta^* - \alpha^*\beta)/2}\, D(\alpha+\beta) \qquad \Rightarrow \qquad \langle \beta \,|\, \alpha \rangle = \mathrm{e}^{\alpha\beta^* - (\alpha\alpha^* + \beta\beta^*)/2} \tag{F.5}$$

- Squeezing by $\zeta = r\mathrm{e}^{\mathrm{i}\phi}$ of oscillator amplitudes (using Equation (F.1))

$$S(\zeta)\, a\, S(-\zeta) = a\cosh(r) + a^\dagger \sinh(r)\mathrm{e}^{\mathrm{i}\phi/2}, \qquad S(\zeta) = \mathrm{e}^{\left(\zeta^* a^2 - \zeta a^{\dagger 2}\right)/2} \tag{F.6}$$

Spin system

- Pauli spin matrices are usually defined as

$$\sigma_x = \begin{pmatrix} 0 & 1 \\ 1 & 0 \end{pmatrix} \qquad \sigma_y = \begin{pmatrix} 0 & -\mathrm{i} \\ \mathrm{i} & 0 \end{pmatrix} \qquad \sigma_z = \begin{pmatrix} 1 & 0 \\ 0 & -1 \end{pmatrix} \tag{F.7}$$

  and have the properties

$$\sigma_i\sigma_j = \epsilon_{ijk}\mathrm{i}\sigma_k + \delta_{ij}\mathbb{1}, \qquad \mathrm{Tr}(\sigma_i) = 0, \qquad \det(\sigma_i) = -1$$

- Pauli ladder operators in the interaction picture

$$\mathrm{e}^{\mathrm{i}\frac{\omega_\mathrm{a} t}{2}\sigma_z}\, \sigma_{eg}\, \mathrm{e}^{-\mathrm{i}\frac{\omega_\mathrm{a} t}{2}\sigma_z} = \sigma_{eg}\, \mathrm{e}^{\mathrm{i}\omega_\mathrm{a} t}, \tag{F.8}$$

Angular-momentum coupling

- The Clebsch-Gordan coefficients can be related to the Wigner 3-j symbols as

$$\langle j_1, m_1; j_2, m_2 \,|\, j_3, m_3\rangle = (-1)^{j_1 - j_2 + m_3}\, [j_3]^{1/2} \begin{pmatrix} j_1 & j_2 & j_3 \\ m_1 & m_2 & -m_3 \end{pmatrix} \tag{F.9}$$

  where the abbreviated notation $[j] = 2j + 1$ was introduced. Both are real and only non-zero, when $m_3 = m_1 + m_2$, $j_1 + j_2 + j_3$ is an integer, and the triangle relation $|j_1 - j_2| \leq j_3 \leq j_1 + j_2$ is fulfilled [Coh99b, Section 10.5]. The Wigner 3-j symbols are invariant under cyclic permutations of the columns.

- Sum rule of Wigner 3-j symbols [Cow81, Section 5-1]

$$\sum_{m_1}\sum_{m_2} [j_3] \begin{pmatrix} j_1 & j_2 & j_3 \\ m_1 & m_2 & m_3 \end{pmatrix} \begin{pmatrix} j_1 & j_2 & j_3' \\ m_1 & m_2 & m_3' \end{pmatrix} = \delta_{j_3 j_3'}\, \delta_{m_3 m_3'}\, \delta(j_1 j_2 j_3) \tag{F.10}$$

  The symbol $\delta(j_1 j_2 j_3)$ gives $+1$ if the triangle relation (s.a.) is fulfilled and zero otherwise.

- Product of spherical harmonics [Cow81, Section 5-1]

$$Y_{l_1}^{m_1} Y_{l_2}^{m_2} = \sum_{l_3, m_3} (-1)^{m_3} \sqrt{\frac{[l_1][l_2][l_3]}{4\pi}} \begin{pmatrix} l_1 & l_2 & l_3 \\ 0 & 0 & 0 \end{pmatrix} \begin{pmatrix} l_1 & l_2 & l_3 \\ m_1 & m_2 & -m_3 \end{pmatrix} Y_{l_3}^{m_3} \tag{F.11}$$

- Wigner-Eckart theorem for the qth component T^k_q of the rank k spherical tensor operator T^k [Cow81, Section 11-4]

$$\langle \alpha_1, j_1, m_1 \,|\, T^k_q \,|\, \alpha_2, j_2, m_2 \rangle = (-1)^{j_1 - m_1} \begin{pmatrix} j_1 & k & j_2 \\ -m_1 & q & m_2 \end{pmatrix} \langle \alpha_1, j_1 \,||\, T^k \,||\, \alpha_2, j_2 \rangle \quad \text{(F.12)}$$

Various

- Generalized Laguerre polynomials

$$L_n^{(\alpha)}(x) = \sum_{i=0}^{n} (-1)^i \binom{n+\alpha}{n-i} \frac{x^i}{i!}, \qquad \binom{n+\alpha}{n-i} = \frac{(n+\alpha)!}{(n-i)!(\alpha+i)!} \quad \text{(F.13)}$$

- Fourier transform

$$\hat{f}(\omega) = \int_{-\infty}^{\infty} \mathrm{d}t \, f(t) \, \mathrm{e}^{-\mathrm{i}\omega t} \qquad \Leftrightarrow \qquad f(t) = \frac{1}{2\pi} \int_{-\infty}^{\infty} \mathrm{d}\omega \, \hat{f}(\omega) \, \mathrm{e}^{\mathrm{i}\omega t} \quad \text{(F.14)}$$

- Dirac delta distribution expressed as Fourier transform

$$\delta(x) = \frac{1}{2\pi} \int_{-\infty}^{\infty} \mathrm{d}k \, \mathrm{e}^{\mathrm{i}kx} \quad \text{(F.15)}$$

- Heaviside function as the integral of the Dirac delta function

$$\Theta(t) = \int_{-\infty}^{t} \mathrm{d}s \, \delta(s), \qquad \Theta(0) \equiv 0 \quad \text{(F.16)}$$

- Integral representation of the Bessel function

$$J_n(x) = \frac{1}{2\pi} \int_{0}^{2\pi} \mathrm{d}\tau \, \mathrm{e}^{\mathrm{i}(n\tau - x\cos(\tau))} \quad \text{(F.17)}$$

Bibliography

[All10] D. T. C. Allcock, J. A. Sherman, D. N. Stacey, A. H. Burrell, M. J. Curtis, G. Imreh, N. M. Linke, D. J. Szwer, S. C. Webster, A. M. Steane, and D. M. Lucas. "Implementation of a symmetric surface-electrode ion trap with field compensation using a modulated Raman effect". *New J. Phys.* **12**, 053026 (2010). Cited on page 97.

[Alm09] M. Almendros, J. Huwer, N. Piro, F. Rohde, C. Schuck, M. Hennrich, F. Dubin, and J. Eschner. "Bandwidth-Tunable Single-Photon Source in an Ion-Trap Quantum Network". *Phys. Rev. Lett.* **103** (2009). Cited on page 104.

[Alo13] J. Alonso, F. Leupold, B. C. Keitch, and J. P. Home. "Quantum control of the motional states of trapped ions through fast switching of trapping potentials". *New J. Phys.* **15** (2013). Cited on pages 2, 132, 133.

[Ami10] J. M. Amini, H. Uys, J. H. Wesenberg, S. Seidelin, J. Britton, J. J. Bollinger, D. Leibfried, C. Ospelkaus, A. P. VanDevender, and D. J. Wineland. "Toward scalable ion traps for quantum information processing". *New J. Phys.* **12**, 033031 (2010). Cited on page 123.

[Ami11] J. M. Amini, J. Britton, D. Leibfried, and D. J. Wineland. "Micro-Fabricated Chip Traps for Ions". In: *Atom Chips*. Edited by J. Reichel and V. Vuletic. Wiley-VCH Verlag GmbH & Co. KGaA, 2011, pages 395–420. Cited on page 52.

[And10] R. Andrae. "Error estimation in astronomy: A guide". *arXiv* (2010). Cited on page 149.

[Ant09] P. B. Antohi, D. Schuster, G. M. Akselrod, J. Labaziewicz, Y. Ge, Z. Lin, W. S. Bakr, and I. L. Chuang. "Cryogenic ion trapping systems with surface-electrode traps". *Rev. Sci. Instrum.* **80**, 013103 (2009). Cited on pages 47, 57, 61.

[Art00] I. A. Artioukov and K. M. Krymski. "Schwarzschild objective for soft x-rays". *Optical Engineering* **39**, 2163–2170 (2000). Cited on page 77.

[Bak06] W. S. Bakr. "Towards a Cryogenic Planar Ion Trap for Sr-88". PhD thesis. Massachusetts Institute of Technology, 2006. Cited on page 58.

[Bar03] M. D. Barrett, B. Demarco, T. Schaetz, V. Meyer, D. Leibfried, J. Britton, J. Chiaverini, W. M. Itano, B. Jelenkovic, J. D. Jost, C. E. Langer, T. Rosenband, and D. J. Wineland. "Sympathetic cooling of Be-9(+) and Mg-24(+) for quantum logic". *Phys. Rev. A* **68** (2003). Cited on pages 2, 123.

[Bar04] M. D. Barrett, J. Chiaverini, T. Schaetz, J. Britton, W. M. Itano, J. D. Jost, E. Knill, C. E. Langer, D. Leibfried, R. Ozeri, and D. J. Wineland. "Deterministic quantum teleportation of atomic qubits". *Nature* **429**, 737–739 (2004). Cited on page 1.

[Bar97] S. M. Barnett and P. M. Radmore. *Methods in Theoretical Quantum Optics*. Oxford: Clarendon Press, 1997. Cited on page 18.

[Ben08] J. Benhelm, G. Kirchmair, C. F. Roos, and R. Blatt. "Towards fault-tolerant quantum computing with trapped ions". *Nat Phys* **4**, 463–466 (2008). Cited on page 1.

[Ber86] J. C. Bergquist, R. Hulet, W. M. Itano, and D. J. Wineland. "Observation of quantum jumps in a single atom". *Phys. Rev. Lett.* **57**, 1699–1702 (1986). Cited on page 90.

[Ber98] D. J. Berkeland, J. D. Miller, J. C. Bergquist, W. M. Itano, and D. J. Wineland. "Minimization of ion micromotion in a Paul trap". *Journal of Applied Physics* **83**, 5025–5033 (1998). Cited on page 97.

[Bla01] E. Black. "An introduction to Pound–Drever–Hall laser frequency stabilization". *Am. J. Phys.* **69**, 79 (2001). Cited on pages 69, 71.

[Bla08] R. Blatt and D. J. Wineland. "Entangled states of trapped atomic ions". *Nature* **453**, 1008–1015 (2008). Cited on pages 1, 5.

[Bla09] B. R. Blakestad, C. Ospelkaus, A. P. VanDevender, J. M. Amini, J. Britton, D. Leibfried, and D. J. Wineland. "High-fidelity transport of trapped-ion qubits through an X-junction trap array". *Phys. Rev. Lett.* **102**, 153002– (2009). Cited on page 123.

[Bla10] S. Blanes, F. Casas, J. A. Oteo, and J. Ros. "A pedagogical approach to the Magnus expansion". *Eur. J. Phys.* **31**, 907–918 (2010). Cited on page 136.

[Bla11] B. R. Blakestad, C. Ospelkaus, A. P. VanDevender, J. H. Wesenberg, M. J. Biercuk, D. Leibfried, and D. J. Wineland. "Near-ground-state transport of trapped-ion qubits through a multidimensional array". *Phys. Rev. A* **84**, 32314 (2011). Cited on page 123.

[Bow12] R. Bowler, J. P. Gaebler, Y. Lin, T. R. Tan, D. Hanneke, J. D. Jost, J. P. Home, D. Leibfried, and D. J. Wineland. "Coherent Diabatic Ion Transport and Separation in a Multizone Trap Array". *Phys. Rev. Lett.* **109**, 80502 (2012). Cited on pages 2, 123, 133.

[Bre02] H.-P. Breuer and F. Petruccione. *The Theory of Open Quantum Systems*. Oxford University Press, 2002. Cited on pages 29, 32, 141.

[Bro11] K. R. Brown, C. Ospelkaus, Y. Colombe, A. C. Wilson, D. Leibfried, and D. J. Wineland. "Coupled quantized mechanical oscillators". *Nature* **471**, 196–199 (2011). Cited on page 49.

[Bro15] M. Brownnutt, M. Kumph, P. Rabl, and R. Blatt. "Ion-trap measurements of electric-field noise near surfaces". *Rev. Mod. Phys.* **87**, 1419–1482 (2015). Cited on pages 102, 103.

[Cas08] W. B. Case. "Wigner functions and Weyl transforms for pedestrians". *Am. J. Phys.* **76**, 937–946 (2008). Cited on pages 143, 144.

[Che11] X. Chen, E. Torrontegui, D. Stefanatos, J.-S. Li, and J. G. Muga. "Optimal trajectories for efficient atomic transport without final excitation". *Phys. Rev. A* **84**, 43415 (2011). Cited on page 2.

[Chi05] J. Chiaverini, B. R. Blakestad, J. Britton, J. D. Jost, C. E. Langer, D. Leibfried, R. Ozeri, and D. J. Wineland. "Surface-electrode architecture for ion-trap quantum information processing". *Quantum Inform Compu* **5**, 419–439 (2005). Cited on pages 1, 49.

[Cir95] J. I. Cirac and P. Zoller. "Quantum Computations with Cold Trapped Ions". *Phys. Rev. Lett.* **74**, 4091–4094 (1995). Cited on page 1.

[Coh99a] C. Cohen-Tannoudji, B. Diu, and F. Laloë. *Quantenmechanik, Teil 1.* 2nd edition. Walter de Gruyter, 1999. Cited on page 16.

[Coh99b] C. Cohen-Tannoudji, B. Diu, and F. Laloë. *Quantenmechanik, Teil 2.* 2nd edition. Walter de Gruyter, 1999. Cited on pages 32, 152.

[Cow81] R. D. Cowan. *The Theory of Atomic Structure and Spectra.* University of California Press, 1981. Cited on pages 32, 33, 152, 153.

[Day06] C. Day. "Basics and applications of cryopumps". In: *CERN Accelerator School Proceedings on Vacuum in Accelerators.* 2006. Cited on page 61.

[dCle15] L. E. de Clercq. "Transport Quantum Logic Gates for Trapped Ions". PhD thesis. ETH Zürich, 2015. Cited on page 71.

[Deh68] H. G. Dehmelt. "Radiofrequency Spectroscopy of Stored Ions I: Storage". *Adv. At. Mol. Phys.* **3**, 53–72 (1968). Cited on page 10.

[Die89] F. Diedrich, J. C. Bergquist, W. M. Itano, and D. J. Wineland. "Laser cooling to the zero-point energy of motion." *Phys. Rev. Lett.* **62**, 403–406 (1989). Cited on page 35.

[DiV00] D. P. DiVincenzo. "The Physical Implementation of Quantum Computation". *Fortschr. Phys.* **48**, 771–783 (2000). Cited on page 1.

[Dor12] S. C. Doret, J. M. Amini, K. Wright, C. Volin, T. Killian, A. Ozakin, D. Denison, H. Hayden, C. S. Pai, R. E. Slusher, and A. W. Harter. "Controlling trapping potentials and stray electric fields in a microfabricated ion trap through design and compensation". *New J. Phys.* **14** (2012). Cited on page 133.

[Dre83] R. Drever, J. Hall, F. V. Kowalski, J. Hough, G. M. Ford, A. J. Munley, and H. Ward. "Laser phase and frequency stabilization using an optical resonator". *Applied Physics B Photophysics and Laser Chemistry* **31**, 97–105 (1983). Cited on page 69.

[Eki06] J. Ekin. "Experimental Techniques for Low-Temperature Measurements". In: *Cryostat Design, Material Properties and Superconductor Critical-Current Testing*. Oxford University Press, 2006, page 704. Cited on pages 55, 59.

[Elt13] A. M. Eltony, S. X. Wang, G. M. Akselrod, P. F. Herskind, and I. L. Chuang. "Transparent ion trap with integrated photodetector". *Appl. Phys. Lett.* **102** (2013). Cited on page 134.

[Esc03] J. Eschner, G. Morigi, F. Schmidt-Kaler, and R. Blatt. "Laser cooling of trapped ions". *J. Opt. Soc. Am. B* **20**, 1003–1015 (2003). Cited on pages 24, 37.

[Fad13] M. Fadel. "Cryogenic Setup for Fast Manipulation of the Quantum Motional States of Trapped Ions". Master's thesis. ETH Zürich, 2013. Cited on pages 53–55, 116, 127.

[Fic92] F. R. Fickett. "Low temperature magnetic behavior of "nonmagnetic" materials". *Advances in cryogenic engineering- Materials.* **38**, 1191–1197 (1992). Cited on page 59.

[Foo05] C. J. Foot. *Atomic Physics*. Oxford University Press, 2005. Cited on page 43.

[Fuj07] S. Fujiyoshi, M. Fujiwara, C. Kim, M. Matsushita, A. M. van Oijen, and J. Schmidt. "Single-component reflecting objective for low-temperature spectroscopy in the entire visible region". *Appl. Phys. Lett.* **91**, 051125 (2007). Cited on pages 77, 79.

[Fuj09] M. Fujiwara, S. Fujiyoshi, and M. Matsushita. "Single-component reflecting objective for ultraviolet imaging and spectroscopy at cryogenic temperature". *J. Opt. Soc. Am. B* **26**, 1395–1399 (2009). Cited on page 78.

[Fuj11] M. Fujiwara, S. Fujiyoshi, and M. Matsushita. "Single-component reflecting objective for low-temperature imaging and spectroscopy of single nano objects". *Physics Procedia* **13**, 38–41 (2011). Cited on page 78.

[Gab90] G. Gabrielse, X. Fei, L. A. Orozco, R. L. Tjoelker, J. Haas, H. Kalinowsky, T. A. Trainor, and W. Kells. "Thousandfold improvement in the measured antiproton mass". *Phys. Rev. Lett.* **65**, 1317–1320 (1990). Cited on page 60.

[Gui14] N. D. Guise, S. D. Fallek, H. Hayden, C. S. Pai, C. Volin, K. R. Brown, J. T. Merrill, A. W. Harter, J. M. Amini, L. M. Lust, K. Muldoon, D. Carlson, and J. Budach. "In-vacuum active electronics for microfabricated ion traps". *Rev. Sci. Instrum.* **85**, 063101 (2014). Cited on page 47.

[Gul01] S. Gulde, D. Rotter, P. Barton, F. Schmidt-Kaler, R. Blatt, and W. Hogervorst. "Simple and efficient photo-ionization loading of ions for precision ion-trapping experiments". *Appl. Phys. B* **73**, 861–863 (2001). Cited on page 87.

[Hab12] R. Hablützel. "Novel Atom Sources and Ultra-fast Electronic Switches for Trapped-Ion Quantum-Information Experiments". Master's thesis. ETH Zürich, 2012. Cited on pages 54, 57, 58.

[Häf08] H. Häffner, C. F. Roos, and R. Blatt. "Quantum computing with trapped ions". *Physics Reports* **469**, 155–203 (2008). Cited on page 1.

[Han10] D. Hanneke, J. P. Home, J. D. Jost, J. M. Amini, D. Leibfried, and D. J. Wineland. "Realization of a programmable two-qubit quantum processor". *Nat Phys* **6**, 13–16 (2010). Cited on page 123.

[Har06] S. Haroche and J.-M. Raimond. *Exploring the Quantum*. Atoms, Cavities and Photons. Oxford University Press, 2006. Cited on pages 143, 144.

[Hec02] E. Hecht. *Optics*. 4th edition. Addison Wesley, 2002. Cited on pages 69, 70.

[Hem14] C. Hempel. "Digital quantum simulation, Schrödinger cat state spectroscopy and setting up a linear ion trap ". PhD thesis. University of Innsbruck, 2014. Cited on page 41.

[Hen06] W. K. Hensinger, S. Olmschenk, D. L. Stick, D. Hucul, M. Yeo, M. Acton, L. Deslauriers, C. Monroe, and J. Rabchuk. "T-junction ion trap array for two-dimensional ion shuttling, storage, and manipulation". *Appl. Phys. Lett.* **88**, 034101 (2006). Cited on page 123.

[Hom06] J. P. Home and A. M. Steane. "Electrode configurations for fast separation of trapped ions". *Quantum Inform Compu* **6**, 289–325 (2006). Cited on page 126.

[Hom09a] J. P. Home, D. Hanneke, J. D. Jost, J. M. Amini, D. Leibfried, and D. J. Wineland. "Complete methods set for scalable ion trap quantum information processing". *Science* **325**, 1227–1230 (2009). Cited on pages 2, 123.

[Hom09b] J. P. Home, M. J. McDonnell, D. J. Szwer, B. C. Keitch, D. M. Lucas, D. N. Stacey, and A. M. Steane. "Memory coherence of a sympathetically cooled trapped-ion qubit". *Phys. Rev. A* **79** (2009). Cited on page 123.

[Hug11] M. D. Hughes, B. Lekitsch, J. A. Broersma, and W. K. Hensinger. "Microfabricated ion traps". *Contemporary Physics* **52**, 505–529 (2011). Cited on page 49.

[Iba11] Y. Ibaraki, U. Tanaka, and S. Urabe. "Detection of parametric resonance of trapped ions for micromotion compensation". *Appl. Phys. B* **105**, 219–223 (2011). Cited on pages 97, 98, 100.

[Jac62] J. D. Jackson. *Classical Electrodynamics*. New York: John Wiley & Sons, 1962. Cited on pages 23, 55.

[Jam98] D. F. V. James. "Quantum dynamics of cold trapped ions with application to quantum computation". *Appl. Phys. B* **66**, 181–190 (1998). Cited on pages 22, 32, 130.

[Jos94] R. Josza. "Fidelity for Mixed Quantum States". *J. Mod. Opt.* **41**, 2315–2323 (1994). Cited on page 140.

[Kei07] B. C. Keitch. "A Quantum Memory Qubit in Calcium-43". PhD thesis. University of Oxford, 2007. Cited on page 71.

[Kie01] D. Kielpinski. "Entanglement and decoherence in a trapped-ion quantum register". PhD thesis. University of Colorado, 2001. Cited on page 108.

[Kie02] D. Kielpinski, C. Monroe, and D. J. Wineland. "Architecture for a large-scale ion-trap quantum computer". *Nature* **417**, 709–711 (2002). Cited on pages 1, 123, 129.

[Kie15a] D. Kienzler. "Quantum Harmonic Oscillator State Synthesis by Reservoir Engineering". PhD thesis. ETH Zürich, 2015. Cited on page 91.

[Kie15b] D. Kienzler, H.-Y. Lo, B. C. Keitch, L. E. de Clercq, F. Leupold, F. Lindenfelser, M. Marinelli, V. Negnevitsky, and J. P. Home. "Quantum harmonic oscillator state synthesis by reservoir engineering". *Science* **347**, 53–56 (2015). Cited on page 2.

[Kot11] S. Kotler, N. Akerman, Y. Glickman, A. Keselman, and R. Ozeri. "Single-ion quantum lock-in amplifier." *Nature* **473**, 61–65 (2011). Cited on page 45.

[Kot13] S. Kotler, N. Akerman, Y. Glickman, and R. Ozeri. "Nonlinear Single-Spin Spectrum Analyzer". *Phys. Rev. Lett.* **110** (2013). Cited on page 45.

[Lad10] T. D. Ladd, F. Jelezko, R. Laflamme, Y. Nakamura, C. Monroe, and J. L. O'Brien. "Quantum computers". *Nature* **464**, 45–53 (2010). Cited on page 1.

[Lan06] C. E. Langer. "High Fidelity Quantum Information Processing with Trapped Ions". PhD thesis. University of Colorado, 2006. Cited on page 108.

[Lau11] H.-K. Lau and D. F. V. James. "Decoherence and dephasing errors caused by the dc Stark effect in rapid ion transport". *Phys. Rev. A* **83** (2011). Cited on page 110.

[Lei03a] D. Leibfried, R. Blatt, C. Monroe, and D. J. Wineland. "Quantum dynamics of single trapped ions". *Rev. Mod. Phys.* **75**, 281–324 (2003). Cited on pages 2, 10, 25, 39, 96.

[Lei03b] D. Leibfried, B. Demarco, V. Meyer, D. M. Lucas, M. D. Barrett, J. Britton, W. M. Itano, B. Jelenkovic, C. E. Langer, T. Rosenband, and D. J. Wineland. "Experimental demonstration of a robust, high-fidelity geometric two ion-qubit phase gate." *Nature* **422**, 412–415 (2003). Cited on page 1.

[Lei09] D. R. Leibrandt, J. Labaziewicz, R. J. Clark, I. L. Chuang, R. J. Epstein, C. Ospelkaus, J. H. Wesenberg, J. J. Bollinger, D. Leibfried, D. J. Wineland, D. L. Stick, J. Sterk, C. Monroe, C. S. Pai, Y. Low, R. Frahm, and R. E. Slusher. "Demonstration of a Scalable, Multiplexed Ion Trap for Quantum Information Processing". *Quantum Inform Compu* **9**, 901–919 (2009). Cited on page 133.

[Lim86] C. C. Lim. "Indium Seals for Low-Temperature and Moderate-Pressure Applications". *Rev. Sci. Instrum.* **57**, 108–114 (1986). Cited on page 60.

[Lin11] F. Lindenfelser. "Laser stabilisation for quantum information experiments with trapped ions". Master's thesis. ETH Zürich, 2011. Cited on page 69.

[Lo15] H.-Y. Lo, D. Kienzler, L. E. de Clercq, M. Marinelli, V. Negnevitsky, B. C. Keitch, and J. P. Home. "Spin-motion entanglement and state diagnosis with squeezed oscillator wavepackets." *Nature* **521**, 336–339 (2015). Cited on page 2.

[Lou01] R. Loudon. *The Quantum Theory of Light*. 3rd edition. Oxford University Press, 2001. Cited on page 32.

[Lou92] B. Lounis and C. Cohen-Tannoudji. "Coherent Population Trapping and Fano Profiles". *J. Phys. II* **2**, 579–592 (1992). Cited on page 40.

[Mac59] W. W. Macalpine. "Coaxial resonators with helical inner conductor". In: *Proceedings of the IRE*. 1959. Cited on pages 54, 55.

[Mar94] I. Marzoli, J. I. Cirac, R. Blatt, and P. Zoller. "Laser cooling of trapped three-level ions: Designing two-level systems for sideband cooling". *Phys. Rev. A* **49**, 2771–2779 (1994). Cited on page 102.

[McL64] N. W. McLachlan. *Theory and Applications of Mathieu Functions*. New York: Dover Publications Inc., 1964. Cited on pages 7, 8.

[McM04] T. McMillan, P. Taborek, and J. E. Rutledge. "A low drift high resolution cryogenic null ellipsometer". *Rev. Sci. Instrum.* **75**, 5005–5009 (2004). Cited on pages 61, 62.

[Mee96] D. M. Meekhof, C. Monroe, B. E. King, W. M. Itano, and D. J. Wineland. "Generation of nonclassical motional states of a trapped atom". *Phys. Rev. Lett.* **76**, 1796–1799 (1996). Cited on pages 2, 91, 102.

[Meh14] K. K. Mehta, A. M. Eltony, C. D. Bruzewicz, I. L. Chuang, R. J. Ram, J. M. Sage, and J. Chiaverini. "Ion traps fabricated in a CMOS foundry". *Appl. Phys. Lett.* **105** (2014). Cited on page 133.

[Men08] P. E. M. F. Mendonça, R. d. J. Napolitano, M. A. Marchiolli, C. J. Foster, and Y.-C. Liang. "Alternative fidelity measure between quantum states". *Phys. Rev. A* **78**, 052330–11 (2008). Cited on page 139.

[Miz13] J. Mizrahi, C. Senko, B. Neyenhuis, K. G. Johnson, W. C. Campbell, C. W. S. Conover, and C. Monroe. "Ultrafast Spin-Motion Entanglement and Interferometry with a Single Atom". *Phys. Rev. Lett.* **110** (2013). Cited on page 2.

[Moe11] D. L. Moehring, C. Highstrete, D. L. Stick, K. M. Fortier, R. A. Haltli, C. Tigges, and M. G. Blain. "Design, fabrication and experimental demonstration of junction surface ion traps". *New J. Phys.* **13**, 075018 (2011). Cited on page 123.

[Mon13] C. Monroe and J. Kim. "Scaling the Ion Trap Quantum Processor". *Science* **339**, 1164–1169 (2013). Cited on page 1.

[Mon95] C. Monroe, D. M. Meekhof, B. E. King, W. M. Itano, and D. J. Wineland. "Demonstration of a fundamental quantum logic gate". *Phys. Rev. Lett.* **75**, 4714–4717 (1995). Cited on page 1.

[Mor03] G. Morigi. "Cooling atomic motion with quantum interference". *Phys. Rev. A* **67**, 033402 (2003). Cited on page 30.

[Nie14] M. Niedermayr, K. Lakhmanskiy, M. Kumph, S. Partel, J. Edlinger, M. Brownnutt, and R. Blatt. "Cryogenic surface ion trap based on intrinsic silicon". *New J. Phys.* **16**, 1–11 (2014). Cited on page 133.

[Obe99] H. Oberst. "Resonance fluorescence of single Barium ions". Master's thesis. University of Innsbruck, 1999. Cited on page 88.

[Oli01] M. H. Oliveira and J. A. Miranda. "Biot-Savart-like law in electrostatics". *Eur. J. Phys.* **22**, 31–38 (2001). Cited on page 11.

[Osp11] C. Ospelkaus, U. Warring, Y. Colombe, K. R. Brown, J. M. Amini, D. Leibfried, and D. J. Wineland. "Microwave quantum logic gates for trapped ions". *Nature* **476**, 181–184 (2011). Cited on page 2.

[Pau90] W. Paul. "Electromagnetic traps for charged and neutral particles". *Rev. Mod. Phys.* **62**, 531–540 (1990). Cited on pages 5, 11.

[Raz98] M. A. N. Razvi, X. Z. Chu, R. Alheit, G. Werth, and R. Blümel. "Fractional frequency collective parametric resonances of an ion cloud in a Paul trap". *Phys. Rev. A* **58**, R34–R37 (1998). Cited on page 99.

[Roh09] F. Rohde. "Remote ion traps for quantum networking: Two-photon interference and correlations". PhD thesis. Universitat Politecnica de Catalunya, 2009. Cited on page 55.

[Roo00a] C. F. Roos. "Controlling the quantum state of trapped ions". PhD thesis. University of Innsbruck, 2000. Cited on pages 34, 97.

[Roo00b] C. F. Roos, D. Leibfried, A. Mundt, F. Schmidt-Kaler, J. Eschner, and R. Blatt. "Experimental demonstration of ground state laser cooling with electromagnetically induced transparency." *Phys. Rev. Lett.* **85**, 5547–5550 (2000). Cited on page 38.

[Roo06] C. F. Roos, M. Chwalla, K. Kim, M. Riebe, and R. Blatt. "'Designer atoms' for quantum metrology". *Nature* **443**, 316–319 (2006). Cited on page 106.

[Roo99] C. F. Roos, T. Zeiger, H. Rohde, H. C. Nagerl, J. Eschner, D. Leibfried, F. Schmidt-Kaler, and R. Blatt. "Quantum state engineering on an optical transition and decoherence in a Paul trap". *Phys. Rev. Lett.* **83**, 4713–4716 (1999). Cited on page 102.

[Rot97] A. Roth. "Vacuum Sealing Techniques". In: American Inst. of Physics, 1997, page 845. Cited on page 60.

[Row02] M. A. Rowe, A. Ben-Kish, B. Demarco, D. Leibfried, V. Meyer, J. Beall, J. Britton, J. Hughes, W. M. Itano, B. Jelenkovic, C. E. Langer, T. Rosenband, and D. J. Wineland. "Transport of quantum states and separation of ions in a dual RF ion trap". *Quantum Inform Compu* **2**, 257–271 (2002). Cited on pages 2, 123.

[Sak94] J. J. Sakurai. *Modern Quantum Mechanics*. Revised Edition. Addison Wesley, 1994. Cited on page 135.

[Šaš02] M. Šašura and V. Bužek. "Cold trapped ions as quantum information processors". *J. Mod. Opt.* **49**, 1593–1647 (2002). Cited on page 23.

[Sch03] F. Schmidt-Kaler, H. Häffner, M. Riebe, S. Gulde, G. P. T. Lancaster, T. Deuschle, C. Becher, C. F. Roos, J. Eschner, and R. Blatt. "Realization of the Cirac-Zoller controlled-NOT quantum gate." *Nature* **422**, 408–411 (2003). Cited on page 1.

[Sch06] S. A. Schulz, U. G. Poschinger, K. Singer, and F. Schmidt-Kaler. "Optimization of segmented linear Paul traps and transport of stored particles". *Fortschr. Phys.* **54**, 648–665 (2006). Cited on page 123.

[Sch09] R. Schmied, J. H. Wesenberg, and D. Leibfried. "Optimal Surface-Electrode Trap Lattices for Quantum Simulation with Trapped Ions". *Phys. Rev. Lett.* **102**, 233002 (2009). Cited on page 11.

[Sch10] R. Schmied. "Electrostatics of gapped and finite surface electrodes". *New J. Phys.* **12**, 023038 (2010). Cited on page 11.

[Sch11] R. Schmied, J. H. Wesenberg, and D. Leibfried. "Quantum simulation of the hexagonal Kitaev model with trapped ions". *New J. Phys.* **13**, 115011 (2011). Cited on page 12.

[Sch12a] B. Schabinger, S. Sturm, A. Wagner, J. Alonso, W. Quint, G. Werth, and K. Blaum. "Experimental g factor of hydrogenlike silicon-28". *The European Physical Journal D* **66**, 71 (2012). Cited on page 130.

[Sch12b] R. Schmied. *SurfacePattern software package, version 2.4*. 2012. URL: `https://atom.physik.unibas.ch/people/romanschmied/code/SurfacePattern.php`. Cited on page 11.

[Sch15] P. Schindler, D. J. Gorman, N. Daniilidis, and H. Häffner. "Polarization of electric field noise near metallic surfaces". *arXiv* (2015). Cited on page 104.

[Sch52] E. Schrödinger. "Are there quantum jumps? Part II". *The British Journal for the Philosophy of science* **3**, 233–242 (1952). Cited on page 1.

[Scu08] M. O. Scully and M. S. Zubairy. *Quantum Optics*. Cambridge University Press, 2008. Cited on page 18.

[Sei06] S. Seidelin, J. Chiaverini, R. Reichle, J. J. Bollinger, D. Leibfried, J. Britton, J. H. Wesenberg, B. R. Blakestad, R. J. Epstein, D. B. Hume, W. M. Itano, J. D. Jost, C. E. Langer, R. Ozeri, N. Shiga, and D. J. Wineland. "Microfabricated surface-electrode ion trap for scalable quantum information processing." *Phys. Rev. Lett.* **96**, 253003 (2006). Cited on pages 5, 49.

[Ser09] A. Serafini, A. Retzker, and M. B. Plenio. "Generation of continuous variable squeezing and entanglement of trapped ions in time-varying potentials". *Quantum Inf Process* **8**, 619–630 (2009). Cited on page 133.

[Sie86] A. E. Siegman. *Lasers*. Mill Valley, California: University Science Books, 1986. Cited on pages 145, 146.

[Sim94] N. J. Simon. "Cryogenic properties of inorganic insulation materials for ITER magnets: a review". (1994). Cited on page 49.

[Siv12] J. D. Siverns, L. R. Simkins, S. Weidt, and W. K. Hensinger. "On the application of radio frequency voltages to ion traps via helical resonators". *Appl. Phys. B* **107**, 921–934 (2012). Cited on page 56.

[Sla58] J. C. Slater. "Interaction of Waves in Crystals". *Rev. Mod. Phys.* **30**, 197–222 (1958). Cited on page 71.

[Sta03] J.-P. Stacey. "Stabilization and Control In a Linear Ion Trap". PhD thesis. University of Oxford, 2003. Cited on page 55.

[Ste10] M. D. Stewart, G. Koutroulakis, N. Kalechofsky, and V. F. Mitrović. "A reusable, low-profile, cryogenic wire seal". *Cryogenics* **50**, 50–51 (2010). Cited on page 60.

[Ste86] S. Stenholm. "The Semiclassical Theory of Laser Cooling". *Rev. Mod. Phys.* **58**, 699–739 (1986). Cited on pages 36–38.

[Suz93] M. Suzuki. "Improved Trotter-like formula". *Physics Letters A* **180**, 232–234 (1993). Cited on page 125.

[Tan11] U. Tanaka, K. Masuda, Y. Akimoto, K. Koda, Y. Ibaraki, and S. Urabe. "Micromotion compensation in a surface electrode trap by parametric excitation of trapped ions". *Appl. Phys. B* **107**, 907–912 (2011). Cited on page 98.

[Thi14] T. Thiele, S. Filipp, J. A. Agner, H. Schmutz, J. Deiglmayr, M. Stammeier, P. Allmendinger, F. Merkt, and A. Wallraff. "Manipulating Rydberg atoms close to surfaces at cryogenic temperatures". *Phys. Rev. A* **90**, 013414 (2014). Cited on pages 68, 133.

[Tom04] G. Tommaseo, P. Paasche, C. Angelescu, and G. Werth. "Subharmonic excitation of the eigenmodes of charged particles in a penning trap". *Eur. Phys. J. D* **28**, 39 (2004). Cited on page 99.

[Tur00] Q. A. Turchette, D. Kielpinski, B. E. King, D. Leibfried, D. M. Meekhof, C. J. Myatt, M. A. Rowe, C. A. Sackett, C. S. Wood, W. M. Itano, C. Monroe, and D. J. Wineland. "Heating of trapped ions from the quantum ground state". *Phys. Rev. A* **61** (2000). Cited on pages 43, 103.

[Wal12] A. Walther, F. Ziesel, T. Ruster, S. T. Dawkins, K. Ott, M. Hettrich, K. Singer, F. Schmidt-Kaler, and U. G. Poschinger. "Controlling Fast Transport of Cold Trapped Ions". *Phys. Rev. Lett.* **109**, 80501 (2012). Cited on pages 2, 123, 133.

[Wan10] C. Wang and J. G. Hartnett. "A vibration free cryostat using pulse tube cryocooler". *Cryogenics* **50**, 336–341 (2010). Cited on pages 47, 64, 67.

[Win78] D. J. Wineland, R. Drullinger, and F. L. Walls. "Radiation-Pressure Cooling of Bound Resonant Absorbers". *Phys. Rev. Lett.* **40**, 1639–1642 (1978). Cited on page 35.

[Win98] D. J. Wineland, C. Monroe, W. M. Itano, D. Leibfried, B. E. King, and D. M. Meekhof. "Experimental issues in coherent quantum-state manipulation of trapped atomic ions". *J. Res. Natl. Inst. Stand. Technol.* **103**, 259–328 (1998). Cited on pages 43, 97.

[Wis10] H. M. Wiseman and G. J. Milburn. *Quantum Measurement and Control*. Cambridge University Press, 2010. Cited on page 16.

[Wol06] J. Wolberg. *Data Analysis Using the Method of Least Squares*. Extracting the Most Information from Experiments. Springer Science & Business Media, 2006. Cited on page 149.

[Wün91] A. Wünsche. "Displaced Fock states and their connection to quasiprobabilities". *Quantum Opt.* **3**, 359–383 (1991). Cited on page 19.

[Zäh10] F. Zähringer, G. Kirchmair, R. Gerritsma, E. Solano, R. Blatt, and C. F. Roos. "Realization of a quantum walk with one and two trapped ions." *Phys. Rev. Lett.* **104**, 100503– (2010). Cited on page 2.

[Zha15] C. Zhang. "CMOS fabrication for scalable trapped-ion quantum information processing". Master's thesis. ETH Zürich, 2015. Cited on page 133.